LOAN DOCUMENT

AD-A267 971

DTIC ACCESSION NUMBER

LEVEL

INVENTORY

①

AFOSR-TR-93-0489

DOCUMENT IDENTIFICATION

Aug 91

DISTRIBUTION STATEMENT A

Approved for public release;
Distribution Unlimited

DISTRIBUTION STATEMENT

DTIC
S ELECTE
AUG 9   1993
C   D

DATE ACCESSIONED

DATE RETURNED

DTIC QUALITY INSPECTED 5

93 8 05 148

DATE RECEIVED IN DTIC

93-18095

HANDLE WITH CARE

LOAN DOCUMENT

DISCLAIMER NOTICE
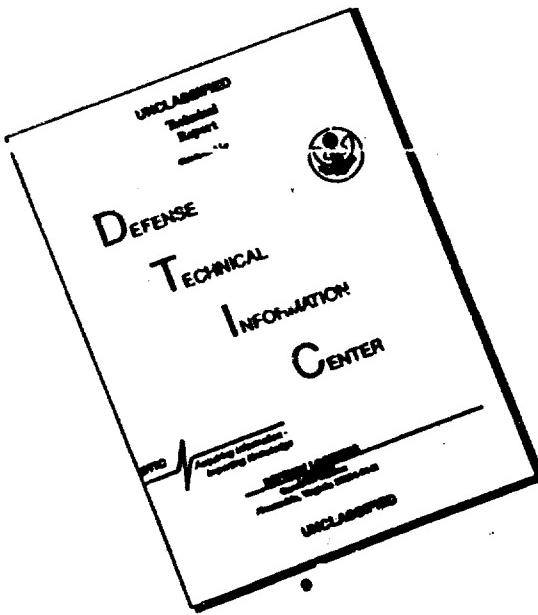
THIS DOCUMENT IS BEST QUALITY AVAILABLE. THE COPY FURNISHED TO DTIC CONTAINED A SIGNIFICANT NUMBER OF PAGES WHICH DO NOT REPRODUCE LEGIBLY.

VOLUME 217

Advanced Tomographic Imaging Methods For The Analysis Of Materials

EDITORS

Jerome L. Ackerman

William A. Ellingson

REPORT DOCUMENTATION PAGE

Public reporting burden for this collection of information is estimated to average 1 hour per response, including the time for reviewing instructions, searching existing data sources, gathering and maintaining the data needed, and completing and reviewing the collection of information. Send comments regarding this burden estimate or any other aspect of this collection of information, including suggestions for reducing this burden, to Washington Headquarters Services, Directorate for Information Operations and Reports, 1215 Jefferson Davis Highway, Suite 1204, Arlington, VA 22202-4302, and to the Office of Management and Budget, Paperwork Reduction Project (0704-0188), Washington, DC 20503.

1. AGENCY USE ONLY (Leave blank)	2. REPORT DATE	3. REPORT TYPE AND DATES COVERED
	August 1991	Final 15 Nov 90 – 14 Nov 91

4. TITLE AND SUBTITLE

MRS Symposium on Advanced Tomographic Imaging Methods for the Analysis of Materials

5. FUNDING NUMBERS

61102F   2306/A2

6. AUTHOR(S)

Jerome L. Ackerman, and William A. Ellingson

7. PERFORMING ORGANIZATION NAME(S) AND ADDRESS(ES)

Materials Research Society
Pittsburgh, PA   15237-6005

8. PERFORMING ORGANIZATION REPORT NUMBER

AFOSR-TR· 93 0409

9. SPONSORING/MONITORING AGENCY NAME(S) AND ADDRESS(ES)

AFOSR/NC
Bolling AFB, DC   20332-6448

10. SPONSORING/MONITORING AGENCY REPORT NUMBER

AFOSR-91-0087

11. SUPPLEMENTARY NOTES

12a. DISTRIBUTION/AVAILABILITY STATEMENT

Approved for public release; distribution is unlimited

12b. DISTRIBUTION CODE

13. ABSTRACT (Maximum 200 words)

See Back

14. SUBJECT TERMS

15. NUMBER OF PAGES

226

16. PRICE CODE

17. SECURITY CLASSIFICATION OF REPORT	18. SECURITY CLASSIFICATION OF THIS PAGE	19. SECURITY CLASSIFICATION OF ABSTRACT	20. LIMITATION OF ABSTRACT
UNCLASSIFIED	UNCLASSIFIED	UNCLASSIFIED	SAR

Advanced Tomographic Imaging Methods For
The Analysis Of Materials

Advanced Tomographic Imaging Methods For The Analysis Of Materials

Symposium held November 28-30, 1990, Boston, Massachusetts, U.S.A.

EDITORS:

Jerome L. Ackerman
Massachusetts General Hospital, Charlestown, Massachusetts, U.S.A.

William A. Ellingson
Argonne National Laboratory, Argonne, Illinois, U.S.A.

Single article reprints from this publication are available through University Microfilms
Inc., 300 North Zeeb Road, Ann Arbor, Michigan 48106

CODEN: MRSPDH

Contents

*Invited Paper

PART II: X-RAY

PART III: DIFFRACTION

*Invited Paper

*Invited Paper

Preface

The development of methods to noninvasively, nondestructively "see" (image) the interior of structures—for example, mechanical components to be used in large or small power generation systems, electronic components, special material test pieces used in process development or biological systems including the human body—is a research area to which the medical community has given extensive attention. X-ray "CAT" scanning and Magnetic Resonance Imaging (MRI) are two cases in point. The development of new structural materials for advanced industrial needs, such as new energy-efficient engines, new materials such as superconductors, as well as the study of materials involving advanced chemical processing, have driven the need for high sensitivity, high spatial resolution non-destructive characterization methods such as computed tomography. The purpose of this symposium was to present the most advanced work in this technological area.

The present volume contains the edited papers of the first Materials Research Society symposium devoted to the topic of tomographic imaging applied to materials research. The symposium was held during the MRS Fall Meeting, Boston, November 28-December 2, 1990. Sponsorship of the symposium was provided by the Air Force Office of Scientific Research, Battelle-Pacific Northwest Laboratory, Bruker Instruments, Inc., Spectroscopy Imaging Systems and General Electric NMR Instruments.

The papers are organized by the tomographic modality (i.e., X-ray, NMR, etc.). However, because the modalities provide different information, a session on multi-modality imaging is provided. Each section of this volume provides the most current information available on the applications to materials.

The editors would like to thank the Materials Research Society for their assistance in getting this first volume together.

William A. Ellingson
Jerome L. Ackerman

July 1991

MATERIALS RESEARCH SOCIETY SYMPOSIUM PROCEEDINGS

Earlier Materials Research Society Symposium Proceedings listed in the back.

PART I

Nuclear Magnetic Resonance

NMR IMAGING OF ELASTOMERS
AND POROUS MEDIA

RICHARD A. KOMOROSKI AND SUBHENDRA N. SARKAR
  University of Arkansas for Medical Sciences, Departments of
Radiology and Pathology, 4301 West Markham St., Little Rock, AR
72205.

ABSTRACT

NMR imaging has been applied to some elastomeric materials
of industrial interest. The T_2s of common elastomers,
particularly after filling and curing, are sufficiently short
that spin-echo sequences at submillisecond echo times cannot
produce T_2-independent images. The sensitivity to T_2
potentially makes spin echo imaging a good probe of elastomer
blend composition, as demonstrated for a series of filled and
cured cis-polybutadiene, styrene-butadiene rubber blends. The
technique can be used to distinguish good and bad carbon black
dispersion in actual tire tread samples. The configuration of
polyester tire cord, voids, rubber layer boundaries, differences
of molecular mobility and composition, and other inhomogeneities
can be detected in end-product tire samples. The value of
isotropic voxels at 80-100 um and the effect of resolution
relative to pore size are demonstrated on a model, H_2O-saturated
porous glass disk of 200-um average pore size. The feasibility
of multinuclear NMR imaging for fluid-specific characterization
of porous materials such as oil cores is demonstrated for ^7Li
and ^{19}F.

INTRODUCTION

Nuclear magnetic resonance (NMR) imaging is being
vigorously pursued as a nondestructive characterization tool
for materials. The promise of measuring spin concentration,
molecular mobility [via the spin-lattice (T_1) and spin-spin (T_2)
relaxation times], and chemical structure (by largely unrealized
localized spectroscopy techniques) at various locations within a
sample has resulted in initial applications in a wide variety of
nonmedical areas.[1] Sizes have ranged from tree trunks of 25-
cm diameter [2] to "microscopic" studies on millimeter-sized
objects at 50-100 um resolution.[3,4]

Because standard NMR imaging techniques are limited to
observing molecularly mobile components, applications to date
have concentrated on bulk elastomers [5], solvent diffusion [6],
and liquids in porous inorganic materials such as ceramics and
oil cores.[7,8] Techniques are being developed for imaging of
highly rigid materials [9], which is the subject of other papers
in this proceedings.

For standard NMR imaging techniques, the primary
requirement for increased resolution is powerful gradients. For
medical imaging, gradients typically never exceed 1 G/cm.
Figure 1 shows plots of gradient strength G vs. acquisition time
AT for various image resolutions. The significance of the
acquisition time is that in echo imaging, it is limited by (and
often equal to) the echo time TE. For materials, T_2 can be
quite short, and hence TE or AT cannot be lengthened without

4
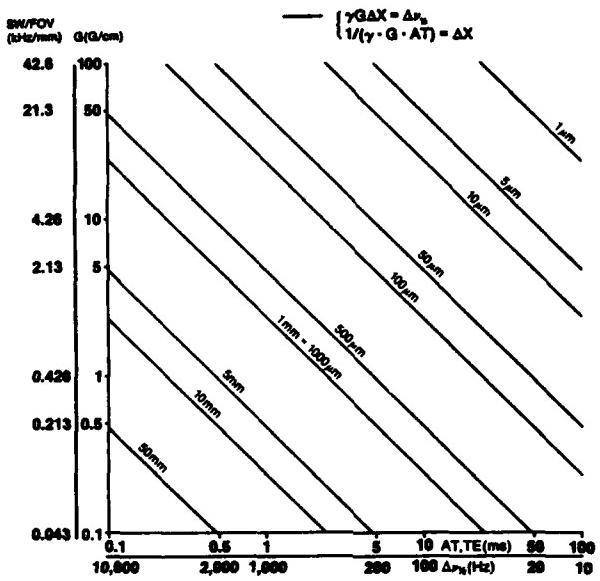
Figure 1.   Plots of G and spectral width (SW)/field of view
(FOV) versus AT (TE) or line width for various resolutions.

Figure 2.   NMR image of a series of 2-mm sheets of cured, filled
CB/SBR blends.   Polymer compositions (CB:SBR) are from bottom:
100:0, 80:20, 60:40, 40:60, 20:80, 0:100.

loss of echo signal. Another consideration is the resonance line width of the material. The spread of frequencies caused by the gradient must be larger than the spread inherent in the line width. This relationship is also shown in Figure 1 for the limiting case where gradient spread equals the line width. Hence the relatively large line widths seen for materials also necessitate powerful gradients, typically 10 G/cm or larger.

In this report we explore applications of NMR imaging to direct analysis of bulk elastomeric materials of industrial interest and porous media. Current limitations and new directions of research are discussed.

EXPERIMENTAL METHODS

The ^{1}H NMR images were acquired at 200.1 MHz on a General Electric Omega CSI-4.7 system with Acustar shielded gradients and available bore size of 120 mm. The maximum gradient strength was 20 G/cm. Either a standard single-plane, spin-echo sequence with slice-selective 90 and 180° pulses [5] or a 3D volume imaging sequence was used. The 3D volume sequence employed a hard, initial 90° excitation pulse of 15-70 us (depending on the coil) to excite spins in the entire object. Phase encoding was performed in the slice-select direction and one transverse direction, with frequency encoding in the remaining direction. For small objects at higher resolution, a commercial, single-turn surface coil of 2-cm diameter was used for both excitation and detection. For larger objects and oil cores, a 6.0-cm diameter, home-made birdcage coil was used. Lithium-7 and ^{19}F images were acquired on the same instrument at 77.8 and 188.2 MHz, respectively. For ^{7}Li a 5.5-cm birdcage coil was used, whereas for ^{19}F a 2-cm, single-turn surface coil provided both excitation and detection.

Carbon-13 NMR spectra were acquired at 75 MHz and 90°C on a General Electric GN-300 WB high resolution spectrometer with proton scalar decoupling in spinning 10-mm NMR tubes.

RESULTS AND DISCUSSION

Elastomer Composition and T$_2$

We previously demonstrated that standard spin-echo techniques at TEs of 10 ms or greater could be used successfully to image favorable cases of cured elastomers.[5] Many common elastomers have T_2s of 0.5-2 ms [10], making it necessary to use short TE sequences such as 3D volume imaging described above to capture sufficient signal intensity. We have imaged elastomeric materials at TEs as low as 500 us. However, even at submillisecond TEs it is not possible to obtain images for typical pure elastomers without T_2 affecting signal intensity and contrast. Of course, the filling and curing that impart the desired mechanical properties further reduce T_2 from that of the pure elastomer.

Figure 2 shows an NMR image (200 x 200 x 500 um voxels) from a 3D volume dataset for a phantom composed of 2-mm sheets of a common series of cured, carbon-black filled cis-polybutadiene, emulsion styrene-butadiene rubber (CB/SBR) blends. Although all the blends have approximately the same hydrogen content, image intensity varies dramatically among the

6

blends. As the SBR (T_g = -70°C) content increases relative to CB (T_g = -102°C), T_2 decreases and image intensity decreases at a TE of 1.2 ms, as in Figure 2, or even at a TE of 500 us. This is also apparent from the image profile on the right in Figure 2.

Conversely, the results in Figure 2 illustrate that NMR imaging can be a sensitive measure of polymer blend composition in well defined situations. Differences as small as 10% may be detectable. Such an approach may provide a substitute for localized spectroscopy techniques, which currently seem of limited use for complex, short T_2 materials.

Tire Materials

Inhomogeneities in elastomers have been imaged directly [5,11] and by solvent swelling.[12] Detection of an [1]H-rich, relatively mobile swelling agent in a polymeric material produces images of high quality. However, spatially dependent differential swelling and dimensional changes make interpretation of such images problematic. Direct imaging at short TE of cured, filled elastomer blends such as tire sections is preferred and can be highly informative. Figure 3 shows NMR images (250 x 250 x 500 um voxels, TE = 4 ms) of actual finished tire tread sections. The section in Figure 3A was from a tire tread with a good, homogeneous carbon black dispersion, whereas that in Figure 3B had a poor dispersion. The samples appeared visually similar. The images are dramatically different and reflect the degree of filler dispersion. The good dispersion image has a relatively even distribution of NMR intensity, whereas the poor dispersion image appears spotty and highly heterogeneous, even in higher resolution (200^3 um^3) images of thinner slices throughout the sample. Tread grooves are seen in both images. Numerous local inhomogeneities of a lesser nature are also seen in Figure 3A. We have routinely observed such inhomogeneties in a variety of elastomer compounds, both cured and uncured.

Figure 4 is an NMR image (100 x 100 x 200 um voxels at TE of 2 ms) of a transverse section of a simple tire containing polyester fiber tire cord. The arrangement and shape of the cord fibers, as well as numerous irregularities, are clearly visible. The laminate structure of the section is well defined. This consists of a 2-mm wide layer on the left which corresponds to the tread. This is bonded to the 5.5 mm layer containing the cords in the center, with a barely visible 2-mm layer on the right. The right-hand layer is the inner liner of the tire, and it appears to consist of two layers from the image and profile although visually this is not apparent.

Carbon-13 NMR spectra of samples taken from the left (closest to the cord) and right sides of the right hand layer show the elastomeric components of these to consist of an isoprene rubber, butyl rubber blend, and probably pure butyl rubber, respectively. This is not unexpected as butyl rubber is commonly used as an air barrier on the inner surface of tubeless tires. It also explains the difficulty in observing this layer by NMR imaging. Butyl rubber is very difficult to image by standard techniques [5] because of its uncharacteristically short T_2, which is a consequence of reduced chain segmental mobility.[13] The addition of isoprene rubber to butyl would increase segmental mobility in the blend, making that layer more
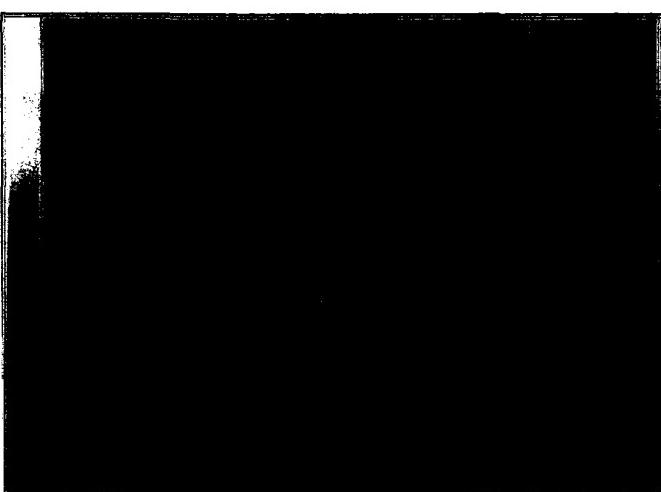
Figure 3. NMR images of actual finished tire tread sections. Tread grooves are seen in each image. A) Good dispersion of carbon black; B) bad dispersion of carbon black. TE = 4 ms. 250 x 250 x 500 mm voxels.
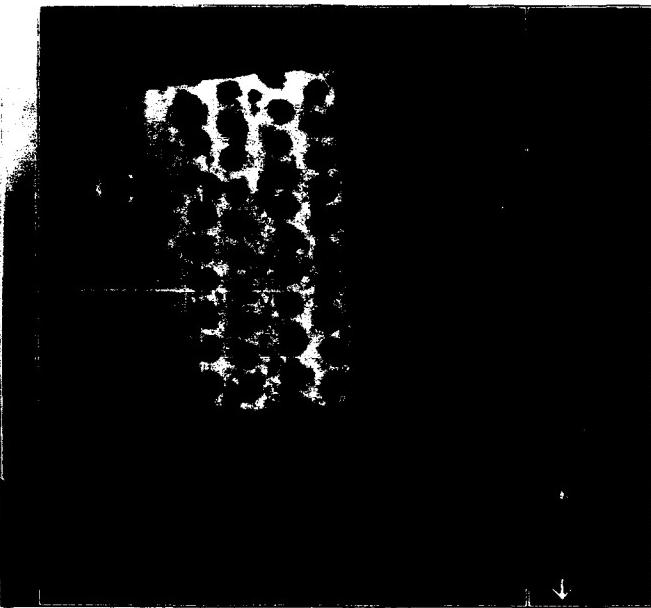
Figure 4. NMR image (slice #9 of 16, 100 x 100 x 200 um voxels, TE = 2 ms) of a tire section with polyester cord belts. The FOV is 12.8 x 12.8 mm. One two-component layer, due to the inner liner of the tire, is barely visible on the right side of the image.
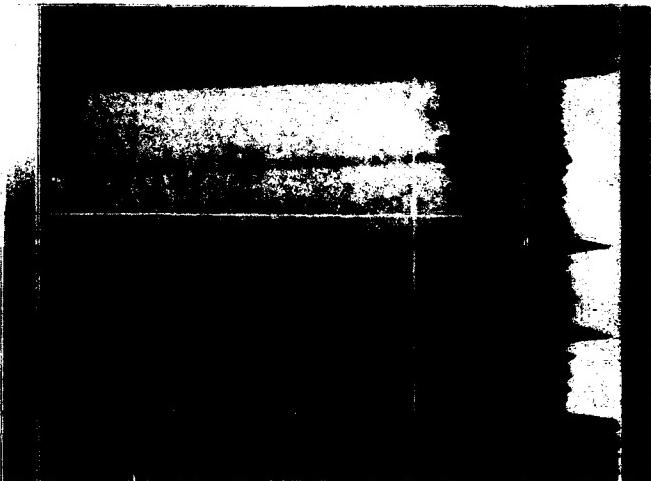
Figure 5. Image (80 x 80 x 500 um voxels, TE = 4.3 ms) of 4 cured, filled 2-mm CB sheets. The bottom three sheets are separated by glass spacers of 180-um thickness. The top two sheets have no spacer.

visible than pure butyl in the image. This sample has a
material feature that might have gone undetected without NMR
imaging.

The relatively large feature in the left layer consists of
a low-intensity region surrounded by three spots of higher
intensity. This is apparently a solid particle or agglomerate
of carbon black or other material. The bright spots are
probably magnetic susceptibility artifacts associated with the
particle, and appearing along the readout (horizontal)
direction, as was confirmed by imaging the object in several
orientations. We see such artifacts routinely in carbon-black-
filled rubbers, both cured and uncured.

In the image in Figure 4 the rubber layer boundaries are
well defined because the layers have different combinations of
T_2 and mobile hydrogen densities. For layers of identical
material, detection of layer boundaries may be less straight-
forward. We previously demonstrated that in model elastomers
boundaries beyond the image resolution can be detected by
reduction of voxel intensity at that point.[5] Under the
relatively poor resolution and long TE conditions of the
previously published images [5], it was not clear if such sub-
resolution boundary detection was from depletion of hydrogen
content, lower T_2 at the surface, or both. Figure 5 shows
higher resolution (80 x 80 x 500 um) images of the same sheets
as before [5] with 180-um spacers at two boundaries and with no
spacer at the third boundary. The sheets were firmly pressed
together and secured for this experiment to eliminate the
possibility of casual air space between the sheets. As
expected, the spacers were well resolved. However, the boundary
without spacer was also detected. Examination of image profiles
at higher resolution suggests that this arises (under these
conditions) from a slightly reduced amount of NMR visible rubber
in the 200-um region at the surface of the sheet. Hahn spin-
echo experiments between 3 and 10 ms measure essentially the
same T_2 at the surface as in the bulk rubber.[10] These results
suggest that laminate boundaries may be more readily detectable
for separately cured sheets than for uncured or co-cured
materials.

Model Porous Materials

To date, most NMR imaging of materials has been with highly
anisotropic voxels and poor resolution perpendicular to the
slice. The advantage of isotropic voxels for visualizing
complex 3D structures and minimizing confusing partial volume
effects has been recognized.[14] Although 3D volume imaging may
ultimately be the method of choice for obtaining isotropic
voxels, it is possible to use the single-slice technique at
moderately good resolution. Figures 6A-C show images of a 7 x 7
mm piece of a water-saturated, porous glass disk (35% porosity,
pore size 170-220 um) at three different isotropic resolutions-
less than, at, and greater than the nominal pore size. As
expected, the images are dramatically different and, in
particular, display how features in the low resolution image
arise from different planes in the slice. In the 100-um
isotropic-voxel image, there are a few small and intense spots
whose size is about 190 um x 190 um in plane and are either
single pores or collections of smaller pores. Longer spots may
be pores connected in plane. Small and weak spots may be from

A

B
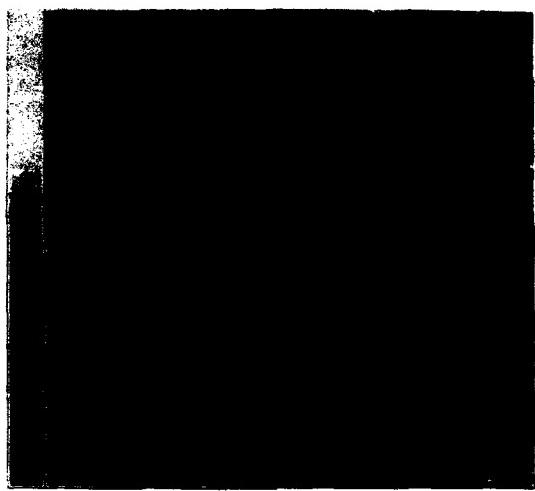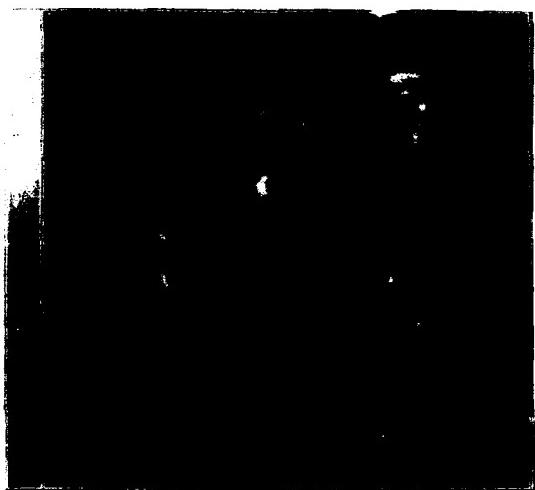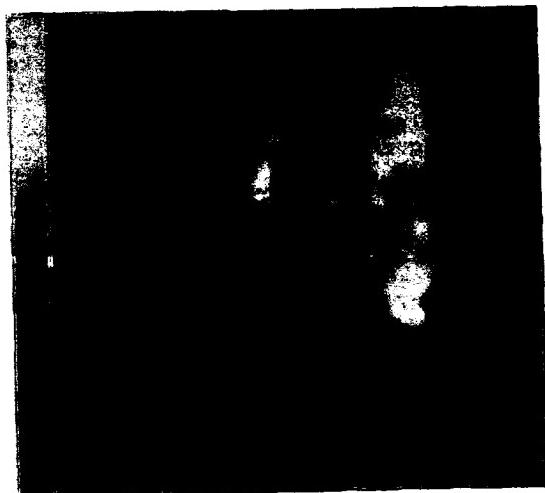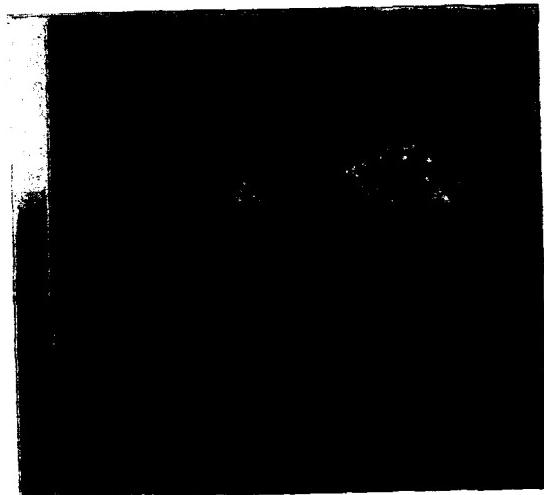
Figure 6. NMR images of a 7 x 7 mm portion of a sintered glass disk of 35% porosity and nominal pore size 170-220 um at three isotropic resolutions: A) 100 um; B) 200 um; and C) 400 um; D) 100 x 100 x 2000 um voxels.

pores of about 100-um size or less and fully included in the
slice, or from larger pores partially cut by the 100-um slice.
For the 200-um and 400-um isotropic resolution images (Figures
6B and 6C, respectively), a few intense spots become larger as
the resolution becomes coarser. Some of the spots remain
bright, implying perhaps collections of water-filled pores from
various planes. Images of other porous glass disks of 5-50 um
pore size suggest that the image appearance is dominated by the
large-pore tail of a pore size distribution.[10]

The higher-resolution appearance of Figure 6A is retained
to some extent in Figure 6D, an image with 100 x 100 x 2000
um voxels, even though features from the equivalent of twenty
100-um slice thicknesses contribute to the latter image. This
arises from the fact that the majority of the object volume in
this case is occupied by glass or air, and hence many of the
anisotropic voxels have little or no signal. For porous
materials of low-to-medium porosity and relatively large pore
size, thick slices may provide more useful information than for
relatively homogeneous materials such as polymers.

The results of Figure 6 also demonstrate that obtaining
isotropic voxels at high resolution will not exact too severe a
penalty in S/N ratio for porous materials. Although the voxel
volume in the 100-um image is 1/64th that of the 400-um image,
it took only 16 times (4x S/N penalty) as long to obtain the
100-um image. This arises from the "dilution" of the signal in
a single voxel by glass as the resolution becomes coarser.

Multinuclear Imaging of Porous Materials

NMR imaging is being used increasingly to study the fluid
distribution in oil cores.[8,15] Since such imaging is usually
concerned with the distribution of two or more fluids such as
oil and water in the rock, methods for separate observation of
the components must be developed. For cases where individual
resonances can be resolved for the oil and water components, we
have used a radiofrequency presaturation pulse and dephasing
gradient to produce component-selective images.[15] When
resonance lines are broad and the individual components cannot
be resolved, a multinuclear approach is necessary. Edelstein et
al. [8] have used the ^{1}H and ^{13}C isotopes to analyze for the
amounts of water and oil in whole cores. We have indirectly
imaged a third fluid (isopropanol as a model miscible injectant)
in a core by profiling the disappearance of signal in the ^{1}H NMR
image when the third fluid is deuterated.[15]

Direct multinuclear imaging of isotopes confined to a
single phase should provide unambiguous separation of two or
more components in model systems. Possible nuclei include ^{19}F
(fluoride or fluorinated organics), ^{13}C (organics, CO_2), ^{23}Na
(brine), ^{7}Li (brine), ^{2}D (D_2O or deuterated organics), and ^{17}O
(H_2O), in addition to ^{1}H. As an example, Figure 7A shows the
^{7}Li NMR image of a Li brine in a model porous glass filter disk
of nominal pore size of 200 um. The ^{7}Li isotope is favorable
for such studies, with a sensitivity about 27% that of ^{1}H,
relatively narrow lines, T_2s of 10-500 ms, and T_1s of 0.5-4 s
in motionally restricted systems. Figure 7A shows that a
resolution on the order of 1 x 1 x 5 mm^3 can be expected.
Figure 7B shows a comparable image for ^{19}F of 50% hexafluoro-
benzene in porous glass taken using a surface coil. We have
obtained preliminary ^{7}Li and ^{19}F images on actual oil cores.
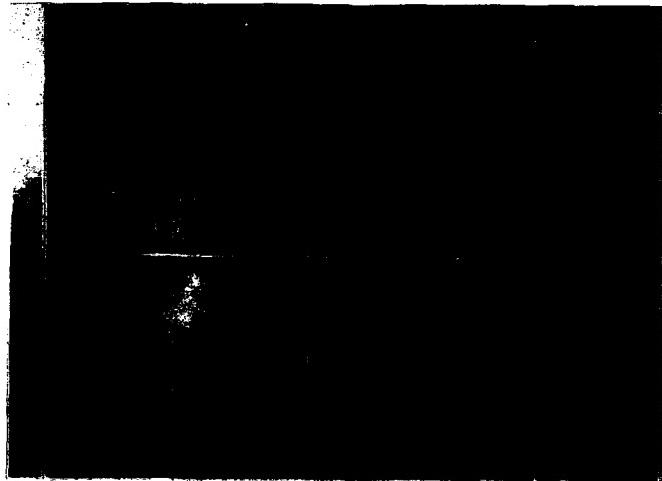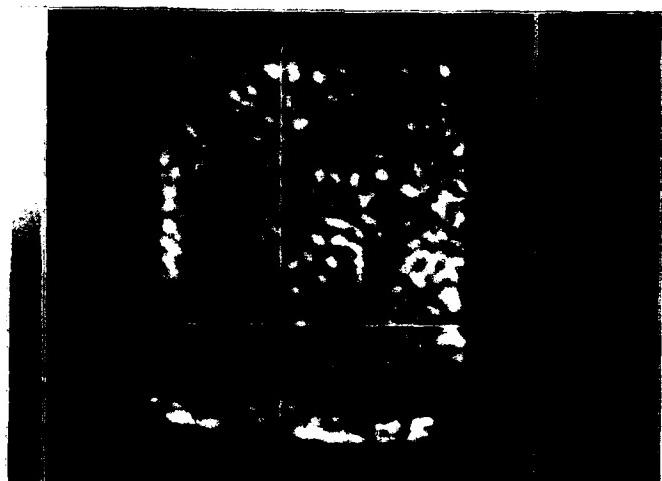
Figure 7. A) ^{7}Li NMR image of a portion of a sintered glass disk (35% porosity, 170-220 um pore size) with 2 M LiCl. (1 x 1 x 5 mm voxels; TE = 2 ms; FOV, 64 x 64 mm) B) ^{19}F NMR image of a sintered glass disk (40% porosity, 4-5.5 um pore size) with 50% hexafluorobenzene. (200 x 200 x 2000 um voxels; TE = 2.8 ms; FOV, 12.8 x 12.8 mm)

Resolution better than ^{7}Li can be expected for ^{19}F in comparable cases (Figure 7B). The ^{19}F T_2 may be short, on the order of 2 to 10 ms. For both ^{7}Li and ^{19}F it will be necessary to use short TE sequences such as whole-core 3D volume imaging.

ACKNOWLEDGEMENTS

REFERENCES

1. J.M. Listerud, S.W. Sinton, and G.P. Drobny, Anal. Chem. 61, 23A (1989).

2. S.J. Chang, J.R. Olson, and P.C. Wang, For. Prod. J. 39, 43 (1989).

3. C.F. Jenner, Y. Xia, C.D. Eccles, and P.T. Callaghan, Nature 336, 399 (1988).

4. W. Kuhn, Angew. Chem. Int. Ed. Eng. 29, 1 (1990).

5. C. Chang and R.A. Komoroski, Macromolecules 22, 600 (1989).

6. L.A. Weisenberger and J.L. Koenig, Appl. Spectrosc. 43, 1117 (1989).

7. L. Garrido, J.L. Ackerman, and W.A. Ellingson, J. Magn. Reson. 88, 340 (1990).

8. W.A. Edelstein, H.J. Vinegar, P.N. Tutunjian, P.B. Roemer, and O.M. Mueller, SPE Paper 18272, 63rd Annual Technical Conference and Exhibition, Houston, TX, Oct. 2-5, 1988.

9. D.G. Cory, J.B. Miller, R. Turner, and A.N. Garroway, Mol. Phys. 70, 331 (1990).

10. S.N. Sarkar and R.A. Komoroski, unpublished results.

11. A.G. Webb, P. Jezzard, L.D. Hall, and S. Ng, Polym. Commun. 30, 363 (1989).

12. R.S. Clough and J.L. Koenig, J. Polym. Sci. Polym. Lett. 27, 451 (1989).

13. R.A. Komoroski and L. Mandelkern, J. Polym. Sci. Polym. Symp. 54, 201 (1976).

14. X. Zhou, C.S. Potter, P.C. Lauterbur, and B. Voth, Abstracts, Eighth Annual Meeting, Soc. Magn. Reson. Med., 286 (1989).

15. J.J. Dechter, R.A. Komoroski, and S. Ramaprasad, Proc. Soc. Core Analysts, paper #8903, 1989.

NMR IMAGING OF SOLIDS USING IMAGING INSTRUMENTATION DESIGNED FOR LIQUIDS

D. G. CORY* AND S. J. GRAVINA
Bruker Instruments, Fortune Drive, Manning Park, Billerica, MA 01821, USA

ABSTRACT

The possibilities of acquiring NMR images of solids with conventional imaging apparatuses are explored. To this end a multiple-pulse line-narrowing sequence is introduced which averages both homonuclear dipolar couplings and time independent linear I_z interactions such as chemical shifts and susceptibility shifts. For imaging the multiple-pulse cycle is accompanied by an oscillating magnetic field gradient which phase encodes the spatial location of each spin. The period of the gradient oscillation is matched to the period of effective field toggling such that the multiple-pulse cycle does not average to zero the gradient induced spin evolution. A small radio frequency coil of 3.0 mm i.d. is used since then only modest radio frequency (RF) power is sufficient to generate a strong RF field, and the RF homogeneity is quite good over the sample volume. The resolution of the image is not spatially uniform, but near the center the resolution is better than 100 μm and the resolution at the edges of the image is degraded by only a factor of 3 to 5. Images of solids with acceptable resolution and sensitivity can be collected by this method with minimal setup time and difficulties.

INTRODUCTION

Although the principles of NMR imaging are well established [1,2] and imaging techniques are routinely used for mapping the distribution of the liquid fractions of a sample, it has proven difficult to translate these same methods into a usable method for imaging the solid fractions of materials. On the other hand, a large number of approaches for NMR imaging of solids have been demonstrated but so far none can be considered to be routine since they all require very special instrumentation and experimental skills. Here we wish to introduce an imaging method which uses the instrumentation of solution state imaging as far as is possible while implementing selected solid state techniques and modifications thereof to allow the best possible NMR images of solids to be obtained with the least pain, cost and setup time.

The foundation of NMR imaging is that the Larmor frequency of a spin is directly proportional to the applied magnetic field strength and therefore a profile of a sample's spin density is obtained simply by observing the NMR spin evolution of the sample in the presence of a magnetic field gradient. To resolve two spatially distinct volume elements requires the application of a magnetic field gradient of sufficient strength such that the elements one wishes to resolve are shifted in resonance frequency from each other by an amount greater than the natural linewidth. Stated more simply,

$$\text{resolution} = \text{linewidth}/\text{gradient strength}.$$

Herein lies the difficulties of solid state imaging since the solid state linewidth is approximately 1000 times broader than its solution counterpart. The gradient strength can be increased by a factor of 1000, but increasing the gradient strength leads to a broader spread in resonance frequencies which must be accommodated by a proportionally wider receiver bandwidth. Noise enters the receiver in proportion to the square-root of the receiver bandwidth resulting in the experimental time to acquire an image scaling as the natural linewidth,

$$\text{imaging time} \approx \text{linewidth}.$$

Acquiring a high resolution image of a small sample is already a time consuming

procedure so a factor of 1000 in experiment time is a huge price to pay and most approaches to solid state imaging have involved some means of line-narrowing rather than relying on increases in gradient strength.

Many approaches to solid state imaging have been successfully demonstrated with line-narrowing approaches including magic angle sample spinning with synchronized rotating gradients [3-5], multiple-pulse line narrowing to eliminate homonuclear dipolar couplings [6-8], combinations of these (CRAMPS) [9], and rotating frame line-narrowing [10].

While the homonuclear dipolar broadening is generally the dominant linebroadening mechanism, chemical shift and susceptibility shifts may still be a factor of 100 broader than the typical water linewidth and can not be ignored. Since the gradient and chemical shift Hamiltonians have the same spin dependence, these two interactions can only be differentiated by manipulating the gradient (i.e. making the gradient strength time-dependent). This has been incorporated into a number of solid state imaging schemes in the form of pulsed gradient [11,12], oscillating gradients [13,14], and in two-dimensional experiments by stepping the gradient strength in a controlled fashion between successive data points [15,16]. Provided that the offending chemical shift and susceptibility shifts may be assumed to be constant throughout the image, deconvolution of the image with the known spectral information [17,18] is also useful, but susceptibility shifts are by nature spatially varying, and noise seriously complicates the deconvolution process.

We have been interested in developing and implementing a solid state imaging method using conventional micro-imaging instrumentation designed for liquid state imaging while retaining as many of the desirable features of the more complex solid state imaging schemes as is possible. The method described below can be implemented on most micro-imaging systems with minimal modifications of the hardware and yields quite good images of rigid solids. To accomplish this we have sacrificed some in sample size (the sample is constricted to fit inside a 3 mm i.d. rf coil) and the resolution across the image is not as uniform as it would be with pulsed gradient methods [12]. This approach is very similar to the refocussed gradient imaging approach which was introduced by Miller and Garroway [13], but the multiple-pulse line-narrowing sequence is a new more forgiving cycle which allows the method to be implemented on systems where more pulse imperfections are likely to be found than would be tolerated by traditional multiple-pulse cycles.
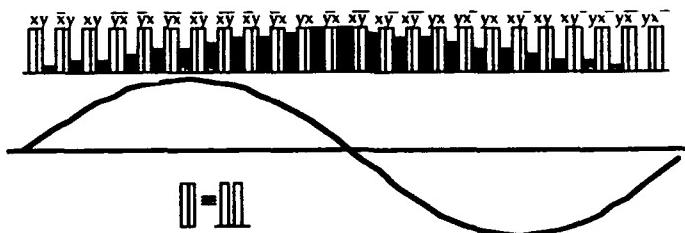
Figure 1. A 48-pulse multiple-pulse cycle which averages to zero homonuclear dipolar couplings as well as time independent I_z interactions. The gradient oscillates with a period equal to the cycle time of the multiple-pulse cycle and this time dependence prevents the cycle from averaging the gradient induced spin evolution to zero. The gradient strength is shown as a sinusoidal modulation, but in practice a more square wave looking modulation was employed and the shape of the modulation is not critical. A phase shift of the RF which occurs between solid echo pulse pairs is shown as building up over the first half of the cycle and then slowly decreasing again during the second half. This introduces a spatially homogeneous resonance offset which may be used to shift the center of the image. As shown in the key below the figure, each pair of RF pulses is a standard solid echo pulse pair with the normal pulse spacing.

IMAGING METHOD

The imaging method is outlined in Fig. 1. The experiment consists of three parts, a 48 pulse imaging cycle which averages homonuclear dipolar broadenings, chemical shifts and susceptibility shifts; a magnetic field gradient which is time dependent such that the multiple-pulse cycle does not average gradient induced shifts; and a stepped rf phase shift which acts as a spatially homogeneous offset of the image. In the scheme's simplest implementation the magnetization is sampled once at the end of the cycle and the experiment is repeated to map out the accumulated phase evolution induced by a combination of the gradient and the phase offset.

The 48 pulse cycle is very similar to a 48 pulse cycle [19] which was previously used for solid state imaging with pulsed gradients intercalated into selected windows. Both of these cycles are constructed from set of 6-pulse dipolar decoupled inversion pulses which in terms of the Magnus expansion are dipolar decoupling to zero order including the effects of finite pulses and to second order in a delta function rf pulse approximation. The properties of these composite inversion pulses has been investigated by Wietekamp and coworkers [20,21]. The cycle used here is distinguished from previous cycles by having the effective fields of each composite pulse point in the same direction in the transverse plane for half of the cycle, and then point anti-parallel to this for the second half of the cycle. The effective field picture for this experiment is outlined in Table 1.

Table I. Effective fields of the experiment outlined in Fig. 1.

Hamiltonian	effective field	sign
chemical shift	I_x-I_y	+/-
susceptibility	I_x-I_y	+/-
gradient	I_x-I_y	+/+
phase toggle	I_x-I_y	+/+

In Table I for each of the linear I_z Hamiltonians which are considered, the direction of the effective field is given along with the sign of the spin evolution over the first half and remainder of the multiple-pulse cycle. From this it is clear that the net effect of the chemical shift and susceptibility spin evolution is zero when averaged over the cycle, but that both the gradient and phase toggle terms remain.

Multiple-pulse methods are generally very demanding of RF field strengths, RF homogeneity and pulse imperfections; so much so in fact that solution state spectrometers can normally not perform these experiments. By using a small (3 mm i.d.) transverse solenoid RF coil, the first two problems are avoided by the high efficiency of the coil and its inherent high homogeneity. The pulse imperfections of the spectrometer must also be considered and for these we choose to use a multiple-pulse cycle which is more forgiving than traditional cycles rather than attempting to modify the spectrometer for multiple-pulse spectroscopy. As an example of the forgiving nature of this cycle consider the first half of the cycle shown in Fig. 1. This multiple-pulse cycle may be employed for spectroscopy since it does not average chemical shift evolution and Fig. 2 shows a comparison of the cycle to two commonly employed multiple-pulse cycles for a CRAMPS [22,23] experiment on para-dimethoxybenzene. Clearly the new cycle has superior line-narrowing properties in this example even though the scaling factor is smaller than that for either of the other cycles.

The final problem that is typically encountered when attempting to perform a solid state experiment on a solution state spectrometer is that the receiver bandwidth of the spectrometer is too narrow to allow the full bandshape of the response to be accurately reproduced. Many modern spectrometers have receivers with settling times of under the 4 µs required for this experiment, but if not this is one modification which will need to be made prior to attempting these experiments. The results shown here were obtained on an MSL-400 which is certainly a solid state spectrometer, however the probes and amplifiers which were used were designed for solution state studies and the solid state capabilities of the spectrometer were not fully utilized. It

18

still remains to be shown how far these methods can be pushed in implementing them on other less sophisticated spectrometers.
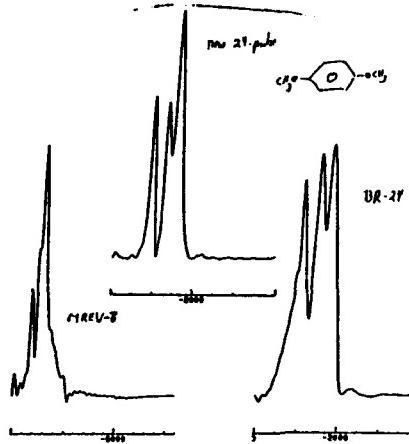
Figure 2. CRAMPS results for dimethoxybenzene acquired with three different multiple-pulse cycles, MREV-8, BR-24, and a new 24-pulse cycles corresponding to the first half of the cycle shown in Fig.1. The resolution of the new cycle is superior to either of the other two under these conditions. This improvement over BR-24 is most likely a result of the forgiving nature of the cycle to pulse imperfections rather than any inherent greater efficiency.
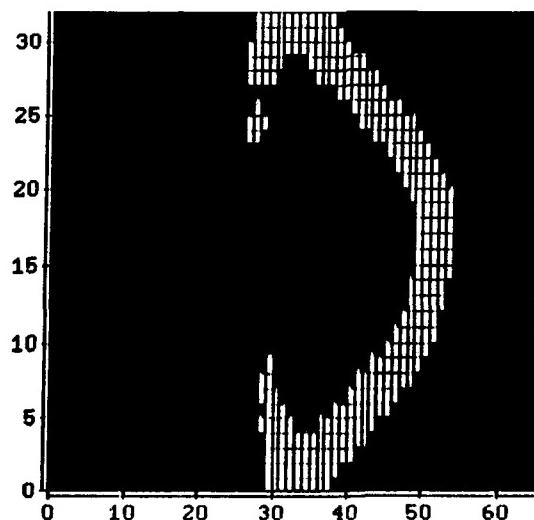
Figure 3. A grey scale plot of the data as acquired with the imaging method described above of a sample consisting of two pieces of adamantane contained in a 2 mm i.d. tube and placed approximately 3 mm apart. The data were acquired by varying the direction of the magnetic field gradient electrically between successive acquisitions.
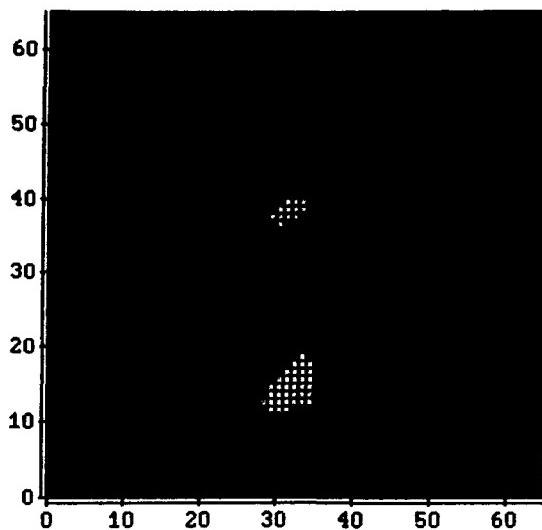
Figure 4. The image resulting from a filtered back projection reconstruction of the data shown in figure 3. Filtering was performed in the spatial domain and sharp glitches (one data point wide) were removed by hand prior to deconvolution to avoid large artifacts. These glitches were the result of spin-locking a small portion of the magnetization along the effective field, and are common in multiple-pulse experiments.

Figures 3 and 4 show an example of applying this imaging method to a phantom consisting of two pieces of adamantane. The two pieces of adamantane are well resolved in this image which is a reasonable representation of the actual spin density distribution.

As we have applied this method a conventional NMR imaging microscopy probe performs well, and there is no need for either fast or strong magnetic field gradients. Of course the restriction to samples which fit inside of a 3 mm RF coil is severely limiting, but there is amply space inside microscopy gradient coil sets to accommodate a sample of up to 2 cm or more. Clearly, to apply these methods at this scale will require that the RF portion of the probe be modified to withstand the much higher power levels, along with using a high power amplifier and a new RF coil insert. These modifications are easily made if the imaging spectrometer is already capable of solid state studies as is the case for the MSL-400 which was employed here. Such modifications may represent a next step in evolving solid state imaging techniques which are robust and simple to apply. Although the approaches which promise the best results are multiple-pulse imaging with intercalated short gradient pulses [11-13], and MAS methods [3-5] where the isotropic chemical shift is of interest, these techniques are still being developed and the simpler methods described above may find some use today.

CONCLUSIONS

We have introduced a method of solid state imaging which can be easily implemented on most existing micro-imaging instruments. To accomplish this the sample size has been restricted to fit within a 3 mm i.d. sample holder, and the reduction of resolution at the edges of the image has been accepted. A multiple-pulse sequence which eliminates homonuclear dipolar broadenings, as well as chemical shift and susceptibility shifts has been used which is forgiving of small pulse imperfections, and an oscillating magnetic field gradient is employed to preserve gradient encoding. It is hoped that this or similar experiments will allow a wider range of potential users to explore the possibilities of solid state NMR imaging without requiring a large investment in both time and research funds.

REFERENCES

1. P. Mansfield, and P. G. Morris, *"Advances in Magnetic Resonance,"* Vol. 12, Suppl. 2, ed. J. S. Waugh (Academic Press, New York 1982).
2. P. G. Morris , *"Nuclear Magnetic Resonance Imaging in Medicine and Biology,"* (Clarendon Press 1986).
3. D. G. Cory, J. W. M. van Os, and W. S. Veeman, *J. Magn. Reson.* 76 543 (1988).
4. D. G. Cory, J. C. de Boer,, and W. S. Veeman, *Macromolecules* 22 1618 (1989).
5. W. S. Veeman, and D. G. Cory, *"Advances in Magnetic Resonance,* Vol. 14, Suppl. 2, ed. W. Warren, (Academic Press 1989).
6. P. Mansfield, and P. K. Grannell, *Phys. Rev.* B12 3618 (1975).
7. G. C. Chingas, J. B. Miller, and A. N. Garroway, *J. Magn. Reson.* 66 530 (1986).
8. S. L. Dieckman, N. Gopalsami, and R. E. Botto, *Energy and Fuels,* 4, 417 (1990).
9. D. G. Cory, A. M. Reichwein, J. W. M. van Os, and W. S. Veeman, *Chem. Phys. Lett.* 143 467 (1988).
10. F. De Luca, B. C. De Simone, N. Lugeri, B. Maraviglia, and C. Nuccetelli *J. Magn. Reson.,* 90, 124 (1990).
11. J. B. Miller, D. G. Cory, and A. N. Garroway, *Chem. Phys. Lett.* 164, 1 (1989).
12. D. G. Cory, J. B. Miller, R. Turner, and A. N. Garroway, *Molecular Physics* 70, 331 (1990).
13. J. B. Miller, and A. N. Garroway, *J. Magn. Reson.* 82, 529 (1989).
14. P. J. McDonald, and P. F. Tokarczuk, *J. Phys. E: Sci. Instrum.* , 22, 948 (1989).
15. S. Emid, and J. H. N. Creyghton, *Physica B,* 128, 81 (1985).
16. P. Bendel, M. Davis, E. Berman, and G. W. Kabalka, *J. Magn. Reson.,* 88, 369 (1990).
17. Busse, L. J., Thomas, S. R., Pratt, R. G., Clark, Jr., L. C., Ackerman, J. L., Samaratunga, R. C., and Hoffman, R. E.,1986, *Med. Phys.* 13 518.
18. D. G. Cory, A. M. Reichwein., and W. S. Veeman, *J. Magn. Reson.* 80 259 (1988).
19. D. G. Cory, J. B. Miller, and A. N. Garroway, *J. Magn. Reson.* 90, 205 (1990).
20. M. H. Werner, T. J. Lenosky, D. N. Shykind, and D. P. Weitekamp, 31st Experimental NMR Spectroscopy Conf. Abstracts p. 189 (1990).
21. D. P. Weitekamp (private communication, 1990)
22. U. Haeberlen, *"Advances in Magnetic Resonance,"* Vol. 12, Suppl. 1, ed. J. S. Waugh (Academic Press 1982).
23. G. E. Maciel, C. E. Bronnimann, and B. L. Hawkins, *Advances in Magnetic Resonance,* Vol. 14, p. 125 ed. W. Warren (Academic Press 1990).

THREE DIMENSIONAL (3D) ELECTRON PARAMAGNETIC RESONANCE IMAGING TECHNIQUE FOR MAPPING POROSITY IN CERAMICS

G. KORDAS and Y.H. KANG
NSF Center for Advanced Cement-Based Materials, Department of Materials Science and Engineering, University of Illinois at Urbana-Champaign, Urbana, IL 61801. USA

ABSTRACT

A three dimensional (3D) Electron Paramagnetic Resonance Imaging (EPRI) method has been developed to probe the structure and size of pores in ceramic materials. A computer control current source and magnetic field gradient coil assembly were added on the conventional EPR instrument as imaging devices. This added-on facility was tested using a phantom sample having cavities filled with DPPH (2,2-diphenyl-1-picrylhydrazyl) particles. Pumice was then used to demonstrate the feasibility of the technique. Porous pumice stone was immersed in a 0.5mM ^{15}N-PDT-water solution to introduce the spin labels into the open volume of the sample. A two-dimensional image was reconstructed from a set of 1-D projections using a filtered back-projection technique. A three-dimensional image was derived from 22 2-D images each constructed by 22 1-D projections. At present, the facility allows a resolution of 69 and 46 μm for 2-D and 3-D imaging.

INTRODUCTION

Magnetic resonance imaging has been announced by Lauterbur [1] for the first time. Since that time, the development of imaging capability of EPR spectroscopy has been attempted in such various fields as studies on paramagnetic impurities in solid materials [2,3], diffusion of radicals in tissues [4,5], and those in adsorbents [6,7]. Unlike the NMR imaging, EPR imaging technique has not found a wide application yet partially due to infrequent occurrence of unpaired electrons with suitable concentration in ceramics. However, by using stable nitroxide radicals as an imaging substance, EPR imaging can provide useful informations about the internal geometry of the solid materials.

The linear spatial resolution along the field gradient depends on the linewidth of the spin label, ΔH_i, and the magnitude of field gradient, $G = dH/dz$ ($G(=10^{-4}T)/cm$) [8]:

$$\delta_z = \Delta H_i / k \cdot G \qquad (1)$$

where k is equal to 1.73 and 1.18 for Lorentzian and Gaussian lineshape, respectively. A reasonable linewidth of 0.6 G from 0.5 mM ^{15}N-substituted perdeutereted Tempone(2,2,6,6-tetramethylpiperidine-d$_{16}$-N-oxyl-4-one, ^{15}N-PDT) and field gradient of 100 G/cm can easily be realized at present. This conditions results in a spatial resolution of 34 μm. The resolution of this technique was improved by a setup generating a field gradient of 3300 G/cm [9]. Electron Spin Echo (ESE) spectroscopy with a pulsed field gradient can enhance the spatial resolution of a CW-EPRI by three orders of magnitude [10].

In our present paper, we prove the potential of EPRI method to image the pores in pumice that served as a model material for this feasibility study. The EPRI setup was tested using a phantom sample.

EXPERIMENTAL

Instrumentation

The gradient coils shown in Figure 1 consist of a set of anti-Helmholtz coils and of a set of rectangular coils. The coils are tightly attached to the surface of the main magnet for efficient cooling. The anti-Helmholtz coils produce a linear magnetic field gradient along the z axis of the cavity. The x/y gradient is produced by another pair of rectangular coils placed inside of the z coils. Gradients at different angles were produced by changing the current through the z coils

and x/y coils. Different imaging planes can be selected by rotating the x/y coils around the z axis. As a result, the projection can be oriented at any angle.
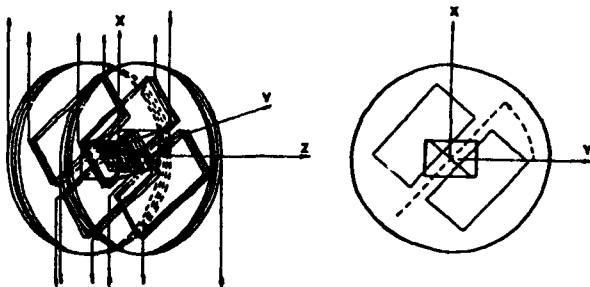
Figure 1. Gradient coils assembly for EPRI (imaging plane is shadowed)

Data collection and image reconstruction

Pumice stones were used for this feasibility study that is known to contain large pores. Samples with known dimensions were cut from the stone and were soaked in 0.5 mM ^{15}N-PDT for 5 hours to introduce the nitroxide radicals into the internal open empty volume. The phantom sample consists of four plexy glasses with cavities having known radii and depths. Figure 2 shows the schematic diagram of the DPPH phantom sample.
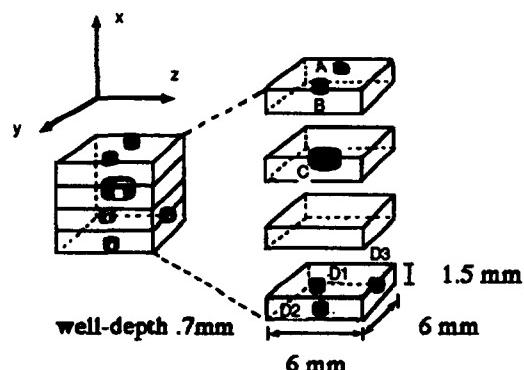
Figure 2. Schematic diagram of DPPH phantom sample

The experiments were performed at 9.5 GHz using a Varian E112 spectrometer with a conventional TE-102 cavity. For two-dimensional imaging, a set of 33 projections over 180° was measured. The spectra were integrated and integrals of the low-field line of the nitroxide hyperfine spectrum were used as the data to generate the image. A two-dimensional image was reconstructed by the filtered back-projection technique, using enhanced projections by Blackman filter [11]. For three-dimensional imaging, a set of 22 projections were obtained for 22 imaging planes equally spaced between 0° and 171°. Two-stage filtered back-projection [12] technique was used for 3-D image reconstruction. Stage one produced a set of 22 two-dimensional image using a three point filter [13], and stage two created the final three dimensional image array (65^3) from 2-D images.

RESULTS

Figure 3 shows surface plots of planes selected from 3-D image arrays of the DPPH phantom sample. These surface plots shows the position of the DPPH particles in good agreement with the geometrical location of the holes in the phantom sample. Irregularities in the shape and intensity of the peaks are due to the nonuniformity of the distribution of DPPH particles in the holes. However, the image qualitatively provides a good description of the internal and external geometries of the sample.

Figure 4 shows a typical 2-D image of the central plane of the pumice sample. The color tones in this figure vary from white to dark blue. White is the highest density of spin labels in the sample corresponding to the holes. The dark blue area of the figure corresponds to the background signal of the sample holder. The light blue tones conforms with the solid pumice sample. This figure clearly shows how the pores are interconnected with each other. It becomes evident from this figure that this figure reveals the structure and size of the pores in a material.

Figure 5 shows a sequence of 15 intensity plots out of 65 imaging planes along the external magnetic field. The bright area in each imaging plane represents the strong EPR signal intensity from the spin labels localized in the internal open volume of the sample and therefore corresponds to the porosity. From this figure, it is well shown how the porosity and complexity of the sample are changing throughout the sample.
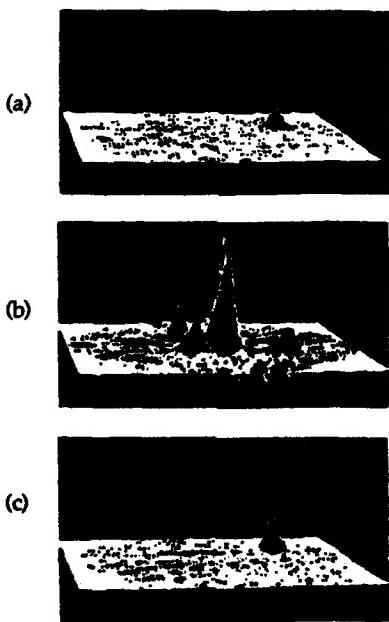
Figure 3. Surface plots of planes from the 3-D image array of the DPPH phantom: (a) plane z=24 (D1 hole), (b) z=34 (A,B,C, and D2 holes), and (c) z=44 (D3 hole)

CONCLUSIONS

With these experiments, we demonstrated the accuracy and applicability of EPRI for porosity measurement in ceramics. Obviously, modification should be made to improve the performance of the imaging device. Also, a larger field gradient and more projections will be required to improve the resolution. An imaging substance exhibiting a single line with a narrow line width would increase the resolution of the technique considerably. For such spin labels, the compatibility of the imaging substance with the sample must be considered before measurement.

24

ACKNOWLEDGMENTS

Figure 4. 2-D image of x-z plane
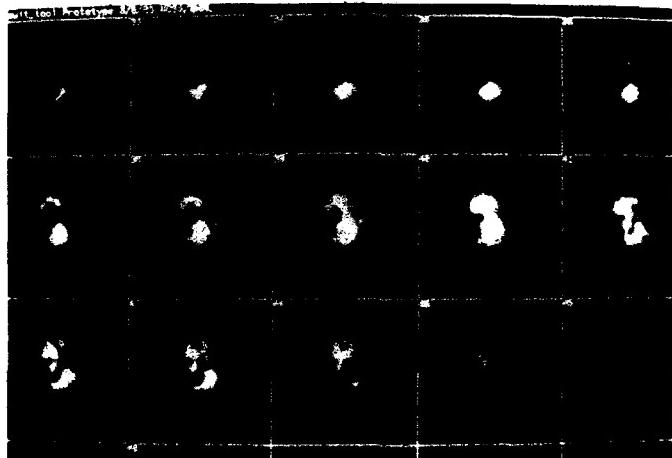
Figure 5. 15 x-y planes out of 65 3-D image planes of pumice along the z-axis

REFERENCES

1.   P.C. Lauterbur, Nature. 242, 190 (1974) .
2.   M.J.R. Hoch, J. Phys. C. 14, 5659 (1981) .

3.   M.J.R. Hoch and A.R. Day, Solid State Commun. 30, 211 (1979) .

4.   F. Demsar, P. Cevc, and M. Schara, J. Magn. Reson. 69, 258 (1986) .

5.   E.V. Galtseva, O.Y. Yakimochenko, and Y.S. Lebedov, Chem. Phys. Lett. 99, 301 (1983) .

6.   B. Ebert, T. Hanke, and N. Klimes, Stud. Biophys. 103, 161 (1984) .

7.   B. Ebert, T. Herrling, U. Ewert, and B. Ebert, Colloids Surf. 11, 19 (1984) .

8.   W. Karthe and E. Wehrsdorfer, J. Magn. Reson. 33, 107 (1979) .

9.   K. Ohno and T. Murakami, J. Magn. Reson. 79, 343 (1988) .

10. A.D. Milov, A. Yu Pusep, S.A. Dzuba, and Yu.D. Tsvetkov, Chem. Phys. Lett. 119 (5), 421 (1985) .

11. J.G. Wade, Signal Coding and Processing (Ellis Horwood Limited, Chichster, 1987), p. 199.

12. C.M. Lai and P.C. Lauterbur, J. Phys. E. 13, 747 (1980) .

13. R.B. Marr, C.N. Chen, and P.C. Lauterbur, in Mathematical Aspects of Computerized Tomography, edited by G.T. Herman and F. Natterer (Springer -Verlag, Berlin/New York, 1981), p. 225.

IMAGING OF DIFFUSION PROCESSES IN DIFFERENTLY CROSSLINKED POLYSTYRENES BY ^{1}H AND ^{19}F-MICROSCOPY

M.Ilg, B.Pfleiderer*, K.Albert, W.Rapp, E.Bayer
University of Tuebingen, Institute of Organic Chemistry, Tuebingen, Germany.
* Massachusetts General Hospital, NMR Center, Charlestown, MA, USA

Polymeric beads are valuable tools for a variety of applications in chemistry, e.g. separation and synthesis support. A common property of all applications is, that diffusion processes and mass transport balances play an important part and are heavily dependent upon matrix parameters such as crosslinking. We have applied ^{1}H and ^{19}F-microscopy to monitor diffusion processes in differently crosslinked polystyrene beads (CL-PS). MRI is used primarily as a medical diagnostic method, but has begun to find increasing application in material science, including studies of fluids in polymers [1,2].

Although it is possible to image the beads (diameter 200 mm) themselves, the monitoring of diffusion behavior and matrix homogeneity requires bigger samples. For this reason, we prepared cylindrical shapes specimens with a diameter of 8mm using the same materials and methods as for preparation of the beads. These samples were then exposed to slightly doped dioxane (4 mg/ml $Cr(Ac)_2$) in test tubes at 50°C and imaged on a Bruker MSL 200 spectrometer equipped with a micro-imaging accessory We used a FLASH gradient echo imaging sequence [3], because we found it offered the best contrast and we could adjust parameters to get exclusively spin-density weighted images.

Fig.1 shows four stages of the dioxane penetration in 2.5% CL-PS. The solid unswollen polystyrene (PS) appears black due to its extremely short T_2. The surrounding bulk dioxane is bright ,with the penetrating diffusion front showing up in differently grey levels corresponding to the dioxane concentration in the matrix. The absence of inner voids and stress cracks indicates a high quality of the material. The penetration takes place with a remarkable geometric homogeneity, the front remaining circular in shape until reaching the core of the sample. Fig.2 is a stacked plot of the signal intensity of semi-profiles stretching from the center of the cylinder to bulk dioxane in the test tube. CL-PS values were 1%, 2.5% and 5% respectively. The figures indicate the time (in minutes) elapsed after exposure to dioxane. The plateau to the right is the signal of bulk dioxane, the inverted spike is a susceptibility change due to a local concentration of Cr-ions at the surface of the swollen polymer. The diffusion gradient is to the left of the plateau. The low plateau of untouched PS is the extreme left. The stacked plots demonstrate the consequences of cross-linking: the 1% CL-PS sports a steep gradient advancing with time but keeping its slope throughout the process and followed by a concentration

plateau. This can be correlated to a type of diffusion which is referred to as CASE II. 5% CL-PS in the beginning shows a steep gradient starting at the surface of the sample, gradually flattening with time, which is the normal fickian way of diffusion. The behavior of 2.5% CL-PS lies between these two extremes, showing elements of both types.
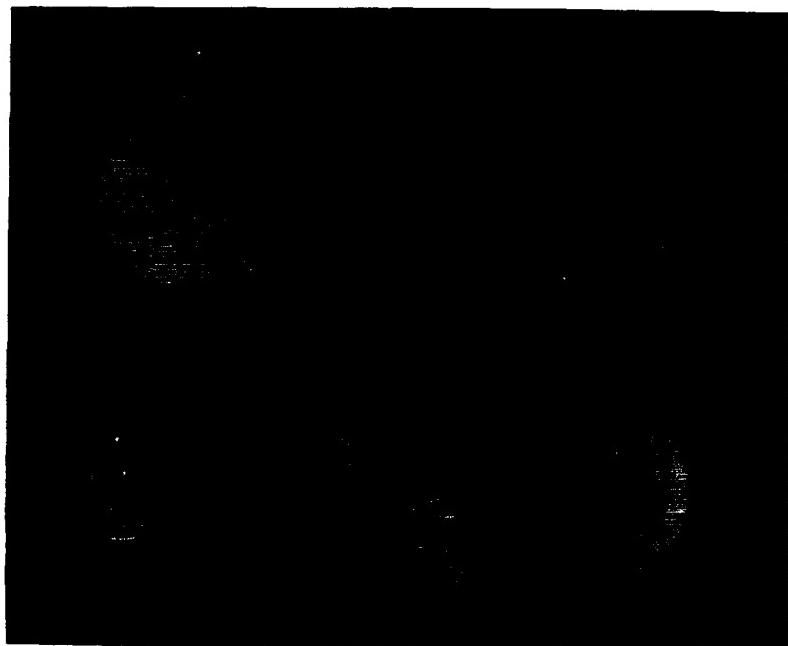
Fig.1 Cross-sectional FLASH-Images of PS-cylinders. Four stages of diffusion after exposure to dioxane.
the imaging parameters used are: $\alpha = 15^0$, TE = 4ms, TR = 50ms, gradient strength = 50mT/m, data matrix = 256*256, slice thickness = 1.5mm, FOV = 15mm, pixel resolution = 115 μm.

Fig.3 is the diffusion distance plotted versus time. We defined a distinct threshold intensity value and monitored its spatial advance, by taking the difference between the original diameter of the cylinder and the radius of the unswollen part of the sample (this convention is necessary due to the swelling). As expected, the velocity of the advancing front depends on the cross-linking, with the 1% CL-PS being the fastest.
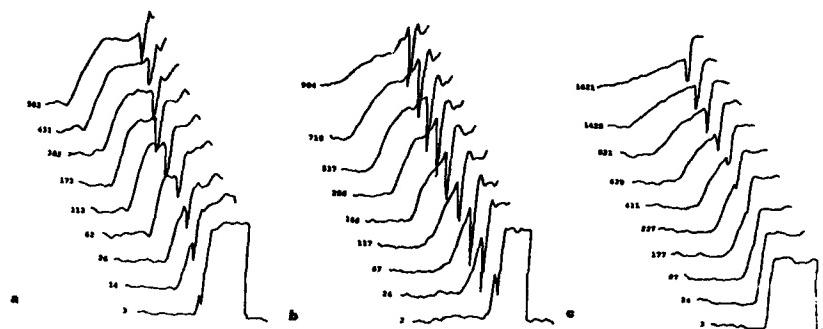
Fig.2 Stacked plot of the intensity profiles. Note the different time scales.
a. 1% crosslinks, b. 2.5% crosslinks and c. 5% crosslinks.
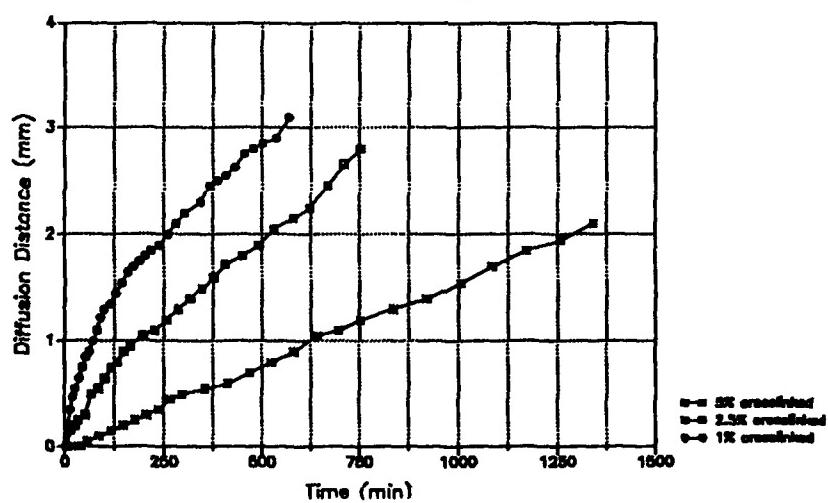
Fig.3 Diffusion distance with time.

Fig.4 reveals the swelling of the cylinders during uptake of fluid with time, measured as the difference between actual and original diameter. The swelling curves indicate somewhat similar results to the velocities. In summary, a qualitative interpretation of the data reveals the fact that a slight variation in cross-linking results in a complete change of the diffusion type. The use of the extended Darcy-equation, which has been sucessfully applied to similar systems [4], failed, mostly probably due to the extreme swelling of the specimens. So other algorithms have to be found. A quantitative evaluation is currently under way.

Swelling of Polystyrene in Dioxane
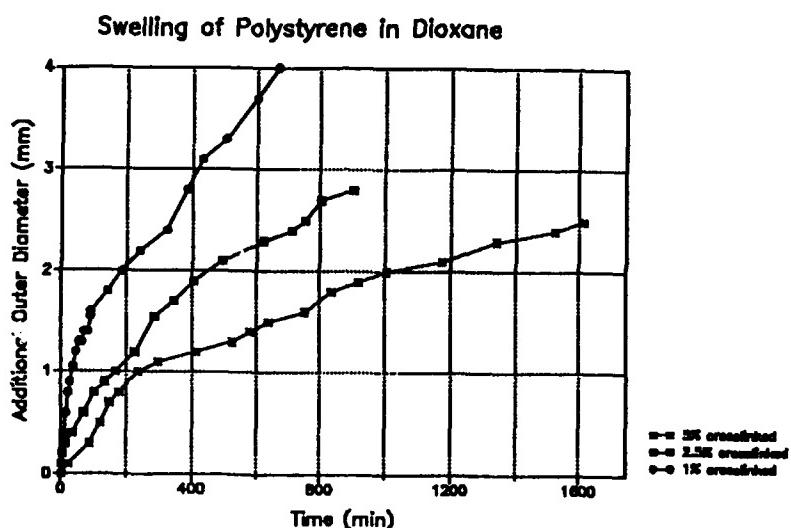
Fig.4   Radial swelling dynamics.

^{19}F-MRI has found limited application in biomedical problems, but it promises to be a useful technique in material science [5]. ^{19}F is second only to the proton in terms of sensitivity. Fluorine can be attached to organic compounds either by direct substitution or by derivatization. Fluorinated compounds are employed in technical processes as solvents and for extraction, swelling and foaming agents for polymers.

In analogy to the well-established use of chemical shift ^{1}H-MRI it should be possible to track diffusion processes and liquid-liquid displacement mechanics with ^{19}F-microscopy. Using the same set-up as for the ^{1}H-images above, we could visualize the penetration of C_6F_6 into polystyrene, resulting in images quite similar to Fig.1. A liquid-liquid displacement process in the same polymer, with the PS preswollen in benzene and then exposed to C_6F_6, is shown in Fig.5. In contrast to

the combined diffusion-swelling process above, the pure diffusion tracked here occurs without the formation of a well-defined front, but seemingly moves through channels and irregularities in the mesh. It seems that the material does not have the degree of homogeneity one would consider when looking at Fig.1.
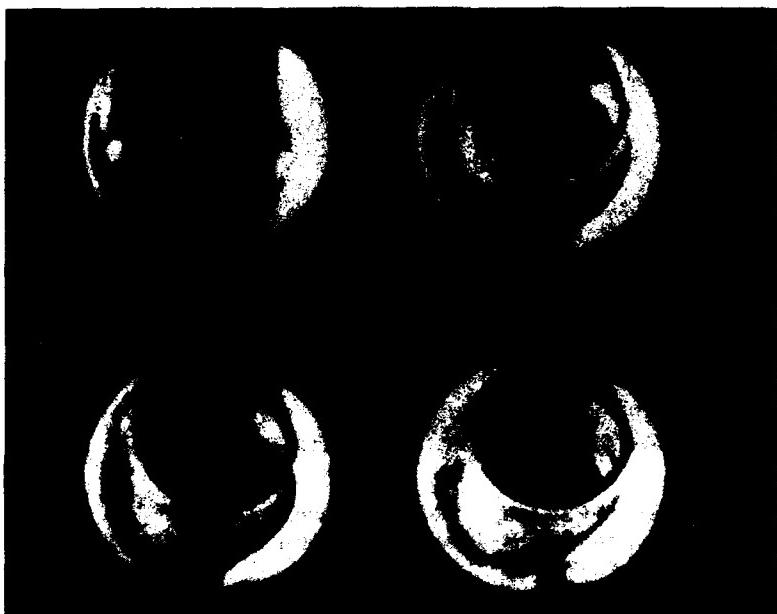
Fig.5 ^{19}F-Microscopy: Displacement of C_6F_6 in already swollen PS sample. FLASH Sequence with the same parameters as in Fig.1.

Fig.6 depicts the migration of an amino acid over PS-beads, which are swollen in tetrahydrofurane. Such systems are used for the separation of peptides. The beads have an an enormous inner surface consisting of microchannels. Separation is controlled by diffusion between in bead and bulk volume. The amino acid was derivatized with pentafluorophenol, a common substrate for such compounds. The figure shows a longitudinal section of a test tube filled with such beads (single beads are not resolved). Following are three ^{19}F-images: after addition of the amino acid (b), when penetrating the "column" (c) and when reaching the bottom (d). The images show for the first time, that the amino acid is capable of unhindered diffusion in the bead pores and therefore does not remain within the beads.
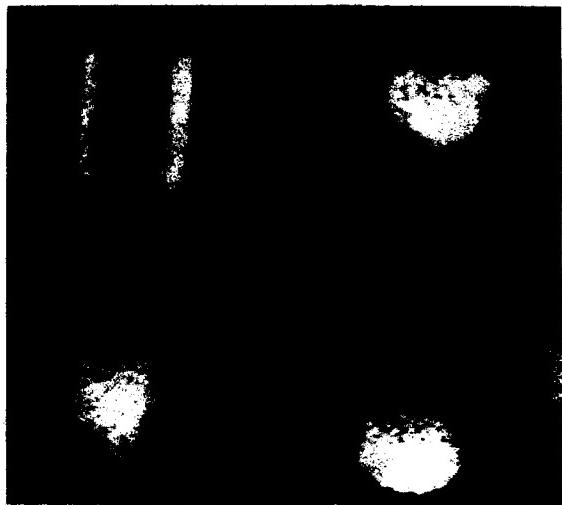
Fig.6 a. ^{1}H image of PS beads in tetrahydrofurane.
b. - d. corresponding ^{19}F images after addition of derivatized glycine.
Spin-Echo sequence.

Additionally, we are investigating diffusion processes in polystyrene beads on a more macroscopic scale by looking at packing homogeneity and shape of chromatographic bands in real chromatographic columns. Results are presented elsewhere.

REFERENCES

1. W.P.Rothwell and P.P.Gentempo, Bruker Report 1, 46 (1985).
2. L.A.Weisenburger and J.Koenig, Polym.Prepr. 29, 98 (1988).
3. A. Haase, J.Frahm, D.Matthaei, K.D.Merboldt and W.Haenicke,
   J.Magn.Reson. 67, 217 (1989).
4. C.Blackband and P.Mansfield, J.Phys.C, L49 (1986).
5. M.Ilg, K.Albert, W.Rapp and E.Bayer, J.Magn.Reson. in press.
6. M.Ilg, J.Maier-Rosenkranz, W.Mueller and E.Bayer, J.Chromatogr. 517,
   263 (1990).

Characterization of Stressed and Crosslinked Polymers by 13C-CP/MAS and NMR Imaging

Winfried Kuhn, Isolde Theis and Elmar Koeller
Fraunhofer-Institute for Nondestructive Testing, Magnetic Resonance
Division, Ensheimer Str. 48, D-6670 St. Ingbert

1. Introduction

Aging of polymers and elastomers is a time dependent alteration of the chemical composition and physical properties depending on the aging conditions. Chemical reactions and hence changes in the chemical composition result in many cases from influence by oxygen or solvents and treatment of the bulk material at high temperatures. Aging of the materials by mechanical strain as well as in an oxidative manner can alter the ratio of amorphous to crystalline portions in the polymer, break chemical bondings and hence can alter the physical behavior of the materials.

Aging processes have been studied in the past by the measurement of macroscopic parameters such as mechanical and dielectric relaxation and thermal and electrical conductivity. From these experiments only a phenomenological understanding of the aging process is possible.

The basis of aging processes on the molecular level is up to now not known and not well studied. Since the development of high resolution solid state NMR spectroscopy exists a tool to study both the chemical composition as well as the molecular dynamics of polymers and elastomers. By means of 13C-MAS the chemical composition can be determined quantitatively and 13C-CP/MAS the dynamic properties of the polymer chains can be studied by variation of the cross polarization contact time and the determination not only of the spin lattice and spin spin relaxation times of the protons, which are sensitive to molecular motions in the MHz range but also the relaxation times for protons and 13C nuclei in the rotating frame, which are sensitive to motions in the kHz range. (1,2)

High field NMR imaging recently developed and known as NMR microscopy, (3), can in addition to spectroscopy give important information on the morphology of the bulk material and inhomogeneous regions of different molecular mobility, caused either by crosslink-inhomogeneities or aging of the material. Inhomogeneities in molecular mobility can be detected by relaxation imaging, which allows the spatially resolved determination of the spin lattice relaxation time T_1 the spin spin relaxation time T_2 and the relaxation time $T_{1\rho}$ in the rotating frame. From such experiments images can be calculated where the contrast is proportional to the local relaxation times which are finally pure relaxation images. Such measurements can be performed on the bulk material as well as on material which is swollen in a protonated or deuterated solvent (4). The swelling behavior depends on the crosslink density and several other factors such as e.q. brittleness, caused by oxydative aging. Due to the swelling behavior T_2 becomes longer and T_1 is to expected shorter because the increased mobility of the polymer chains. If the swelling is caused

by protonated solvents it is expected that only solvent distribution and their relaxation times in the swollen polymer can be determined. The diffusion process itself and its time dependence can also be characterized because the high mobility and concentration of solvent protons. In case deuterated solvents have been used the protons of the polymer itself and their relaxation times can be detected. This should result in a more detailed information about the mobility of the polymer chains itself.

The aim of this study was to find a correlation between NMR parameters such as the relaxation times $T_{1\rho H}$ and T_{CH} determined by ^{13}C-CP/MAS and T_1 from ^{1}H spectroscopy. Detection of inhomogeneities caused by different curing and aged by mechanical stress and oxidation on mono- and polysulfidic crosslinked natural rubber of the bulk material as well as swollen polymers is possible by ^{1}H-imaging.

2. Materials and Methods

2.1 Materials

Natural rubber samples treated by mechanical and oxidative aging were used for the study. The samples contained carbon black, stearic acid, zinc oxide, antioxidant, sulfur and accelerator for crosslinking and were mono- and polysulfidic crosslinked and cured for 80 min at 150° C. The mechanical stress occured in a Monsanto fatique tester with 100 % elongation and a cycle time of 1 s until break. The material from the broken region was taken for spectroscopy and imaging. Oxidative aging occured at 90° C for 4 days in an air stream. The control experiments were performed on untreated samples manufactured at the same curing and crosslinking conditions. The following scheme shows the program under work.

crosslinking	monosulfidic		polysulfidic	
curing conditions	80'/150°		80'/150°	
untreated	S	I	S	I
mechanical stressed	S	I	S	I
oxidative aged	S	I	S	I

S: ^{13}C-CP/MAS with contact time variation and ^{13}C-MAS spectroscopy was performed

I: Spin-echo imaging and T_1-imaging on both the non swollen as well as swollen samples were performed.

For imaging rubber samples with a size of about 1.0 x 2 x 4 mm^3 were used. To study the swelling behavior and the diffusion of solvents in the samples a rod of a length of 2.5 cm were stored for 3 min in deuterated cyclohexane (99,9 %). To make sure that a two dimensional diffusion occured a piece from the center of this rod with the same dimensions as described above was taken and measured at 22° C. The weight of the sample was measured before and after

the NMR experiment to determine the loss of solvent during the measuring time.

To determine the diffusion behavior of the deuterated as well as protonated cylohexane 2D images were taken every 9 min with a recovery time TR=250 ms and a spin echo time TE=1.7 ms. The evaluation of the diffusion time constants occured according to fig. 1. Two orthogonal profiles were plotted and the ratio between the flat region of the profile and the profile maxima was calculated and averaged. This value was then plotted versus the diffusion time.

Fig. 1

$$I = \frac{MAX1 + MAX2}{2 \, MIN}$$
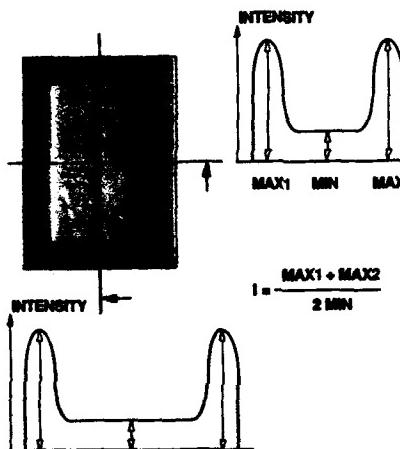
Schematic draw of analyzing the diffusion experiments. Two perpendicular intensity plots across the sample were taken. The average value of the measured intensities was used for the calculation of the diffusion behavior.

2.2   Spectroscopy

^{13}C-CP/MAS spectroscopy was applied at a sample rotation frequency of 5.0 kHz using a 7 mm rotor and a conventional high power broadband MAS probehead. The contact time was varied between 1 ms and 40 ms in 32 steps at different CP-times. From the resulting contact time curve we could determine the position of the maxima and relaxation times in the rotating frame by means of a mono-and double exponential fitting routines. The experiments were performed on a Bruker MSL 400 spectrometer equipped with a microimaging accessory.

2.3   Imaging

Imaging experiments were performed to localize the inhomogeneities in the observed slice, the size of the aged part of the material and to determine spatially resolved the spin lattice relaxation time T_1.

For this studies images without any slice selection were taken from both the unswollen as well as swollen samples with a slice thickness between 300 μm and 2 mm. To reduce the spin echo time TE only hard pulses with a typical pulse length of 8 μs for a 90 degree pulse were applied. Gradient strengths of 150 mT/m were used for the in plane gradients to achieve a calculated pixel resolution of 30 x 30 μm^2. The linewidth of the proton signal was about 1500 Hz

which limits the spatial resolution in the images for the applied gradient strength of 150 mT/m to 230 μm. For data processing the time domain data were filtered with a gaussian filter, baseline corrected and 2D transformed. The images are represented by a 256^2 data matrix. No other data manipulation was applied. The T_1 images were analyzed with a self-written program (SUNRISE) using an algorithm described by Dietrich et.al. (5). T_1 values, according magnetization M_o in the thermal equilibrium and the saturation pulse angle were calculated for each pixel. From this calculation each of them can be choosen as selection parameter and for each of them a parameter selective window can be adjusted. The image display shows then only such regions, where the choosen parameter fits in. This parameter selective image analysis programm (SUNRISE) works for monoexponential T_1 and multiexponential T_2 analysis using five different algorithms, is written in C and runs on Bruker X32 as well as SUN4 workstations. T_1 imaging was performed by application of a 90 degree aperiodic pulse saturation sequence (fig. 2) (6) followed by variable delays in a range between 50 ms and 3 s and a spin echo imaging sequence described above.

Fig. 2
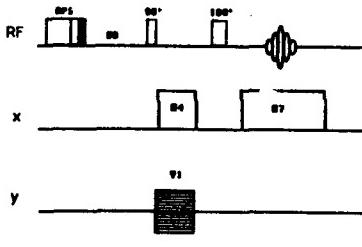
T_1-imaging pulse sequence with an aperiodic saturation pulse train (APS) prior the spin echo imaging sequence. Imaging without slice selection (profile imaging) was applied. Between two variable delays VD the entire image was completely taken in 256 phase encoding steps. 8 variable delays between 50 ms and 3 s were choosen. The APS sequence started with 512 ms, next value was 256 ms, than 128 ms etc. until 16 μs.

3. Results and Discussion

3.1 ^{13}C-MAS and -CP/MAS-Spectroscopy

^{13}C-MAS measurements of all samples (untreated, mechanical and oxidative aged) show the same well known spectra for natural rubber with no specific characteristics (fig. 3). From CP/MAS-spectra the contact time constant T_{CH} and the proton spin lattice relaxation time in the rotating frame. $T_{1\rho H}$ could be determined for each spectral line in the ^{13}C spectra. The monosulfidic crosslinked spectra show at a CP-time of 12 ms a signal at 46.4 ppm which could be assigned according to (7) to C-C bridges but could not be observed without CP and in the polysulfidic samples.

Monosulfidic crosslinks

Same trend is found by the determination of $T_{1\rho H}$. For oxidative aged material the T_{CH} as well as $T_{1\rho H}$ values show the same behavior for normal and overcured material. The evaluation of the C=C signal at 125.3 ppm in the spectra of the stressed overcured sample showed some difficulties and was not interpretable. Aliphatic signals at 25 ppm show longer T_{CH} after
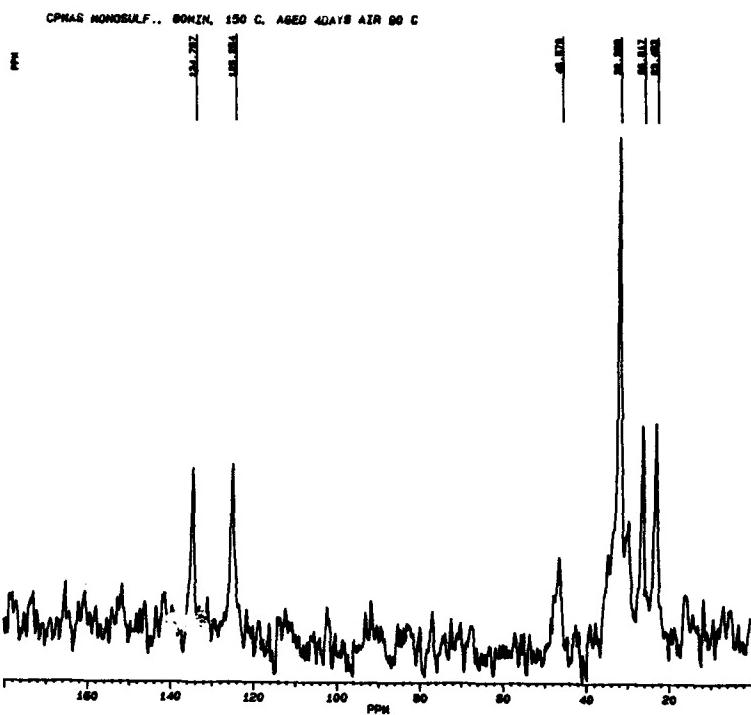
Fig. 3

^{13}C-CP/MAS spectrum of a monosulfidic cured oxidatively aged natural rubber sample. Contact time was 12 ms

mechanical stress and oxidation of the sample which could be a result of a higher mobility of the polymer chains caused by changing the crosslink structure through breaks of the crosslink knots. The same behavior isobserved for $T_{1\rho H}$ (table 1a and 1b)

Polysulfidic crosslinks

In comparison to monosulfidic crosslinks are in general remarkable shorter T_{CH} values observed which are caused by a lower mobility of the polymer chains. The same behavior is observed for $T_{1\rho H}$. T_{CH} becomes shorter in oxidative aged samples compared to nontreated material. The $T_{1\rho H}$ values show the same behavior (table 2a and 2b).

Table 1

a) T_{CH} - values [ms]

chemical shift [ppm]	untreated	stressed	aged 4 d/90° C
134.6	11.9	11.4	13.1
125.3	6.8	4.3	7.9
32.4	1.5	2.5	2.5
26.6	2.0	5.8	4.5
23.5	3.2	9.6	8.7

b) $T_{1\rho H}$ - values [ms]

chemical shift [ppm]	untreated	stressed	aged 4 d/90° C
134.6	23.2	26.9	46.5
125.3	20.1	26.9	27.7
32.4	19.1	25.2	26.7
26.6	20.2	22.0	25.5
23.5	21.9	27.5	27.7

Table 2

a) T_{CH} - values [ms]

chemical shift [ppm]	untreated	stressed	aged 4 d/90° C
134.6	6.5	3.8	5.5
125.3	4.5		1.9
32.4	2.0	1.4	1.8
26.6	3.4	1.3	2.0
23.5	5.8	4.0	4.8

b) $T_{1\rho H}$ - values [ms]

chemical shift [ppm]	untreated	stressed	aged 4 d/90° C
134.6	15.4	15.7	20.0
125.3	14.3	20.1	20.2
32.4	12.5	13.5	18.3
26.6	14.6	17.4	19.2
23.5	19.8	18.4	20.0

3.2 Imaging

Strong T_1 weighted images were taken from all samples to show relaxation and spin density dependent contrast. The T_1 weighted images from untreated (fig. 4a), and oxidative aged (fig. 4b) monosulfidic unswollen material show similar structures. This structures can either be caused by inhomogeneties in spin density or by inhomogeneous crosslinked regions. There is no characteristic difference between aged and untreated material observable. T_1 imaging on monosulfidic crosslinked samples shows also no characteristic differences between untreated and stressed samples, but slightly lower T_1-values in the oxidative aged sample.

From the swollen material the diffusion behavior of the solvent can be derived. The images of the swollen untreated as well as treated material look qualitativly very similar but the diffussion time constant is quite different. The diffusion can be detected by changes in the molecular mobility of the polymer chains during the swelling process. Fig. 5a shows an intensity plot according to fig. 2. In fig. 5b the same plot is shown for the oxidative aged material. The signal decays to 50% intensity in the untreated sample after 52 min while it falls down to the same intensity in the aged sample after 73 min. Hence the diffusion of the solvent is remarkable slower in the aged sample compared to the untreated material. This may be caused by brittleness of the aged material. This results indicate that the diffusion time constant could be a sensitive parameter to characterize the oxidative aging of monosulfidic crosslinked material.

Fig. 5
a) Intensity plot of the diffusion of deuterated cyclohexane into an untreated monosulfidic cured natural rubber sample. b) Same plot as shown in fig a) but of an oxidatively aged material.

From the T_1 analysis no significant differences in the T_1 values of untreated and aged materials could be derived.

Fig. 6a shows a T_1 weighted image of the unswollen polysulfidic crosslinked overcured material. No remarkable difference between mono- and polysulfidic crosslinked material is visible. Fig. 6b shows the image of the oxidative aged unswollen sample. A region of about 300 µm thickness on each side of the sample can be very clear observed and results from the oxidative aging. Parameter selective T_1 image analysis shows the differences in T_1 in the nonaged (fig. 7a) and aged region (fig. 7b) of the sample. The T_1 values of the

Fig. 4

T_1 weighted images taken from unswollen monosulfidic crosslinked overcured material. (a) untreated, (b) aged by air. The pixel resolution is 30 x 30 μm, slice thickness is 500 μm, TR = 250 ms, TE = 1ms.
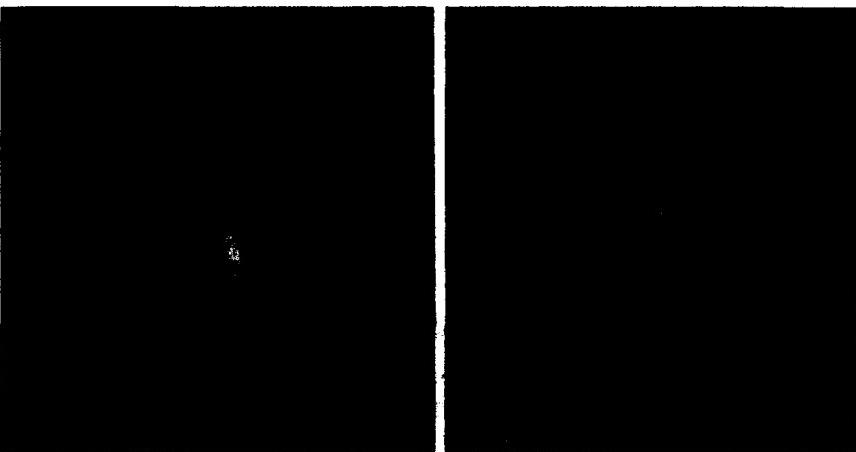
Fig. 6
a) T_1 weighted spin echo image of polysulfidic cured untreated material. The image shows similar structures as the image taken from monosulfidic cured sample.
b) T_1 weighted spin echo image of polysulfidic cured oxidatively aged material. The aging conditions were the same as for monosulfidic cured aged material. Very clear visible are the aged regions and the nonaged region in the center of the sample.
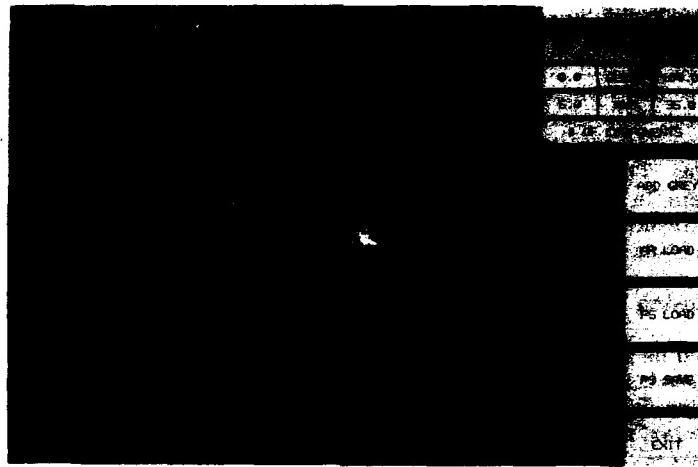
Fig. 7a
Results of the parameter selective T_1 image analysis of the images from the sample shown in fig. 6b. The T_1 window is in the range between 700 ms and 1050 ms. Only the magnetization in the aged region of the sample contributes to the signal in the image.

Fig. 7b
Same sample as in fig. 7a, but the T_1 window is now adjusted so that only magnetization with relaxation timed between 500 ms and 700 ms contribute to the image. Only the nonaged part of the sample is visible due to the higher mobility of the molecules in this region.

nonaged region are significantly shorter (500-700 ms) than in the aged region where they are in a range between 700 ms and 1.2 s. The differences in contrast are still greater in the images of the swollen polysulfidic crosslinked sample. The T_1 image analysis confirms the results obtained on the unswollen material. The mechanical stressed polysulfidic crosslinked unswollen and swollen samples show surprisingly similar structures as the oxidative aged samples. The same is observed by T_1 image analysis. The T_1 values are comparable to the values determined for the oxidative aged material. This could result from the warming up of the sample during mechanical stress which leads to oxidative aging on the sample surface at the same time.

Conclusion

It could be shown that high field imaging is a very promising method for the characterization of aged and nonaged elastomers. By means of parameter selective T_1 imaging regions with different crosslink densities or different molecular mobility caused either by the crosslinking process, aging by mechanical stress or in an oxidative manner can be clearly identified in unswollen as well as swollen polysulfidic crosslinked material. Not only the differences in molecular mobility can be detected by parameter selective imaging but also the size of the aged regions in the sample can be measured. Moreover inhomogeneities in the bulk material caused by any kind of defects such as voids or crazes can be resolved if there size is in the order of 50 μm to 100 μm. The determination of the diffusion time constant of solvents diffusing into the bulk material can also give valuable information about crosslink density and aging of elastomers. It could be shown that the diffusion of deuterated cyclohexane and the change in molecular mobility of the polymer chains occur for aged and unaged samples in monosulfidic crosslinked material quite differently. The ^{13}C-CP/MAS measurements can also be applied to characterize aging processes in elastomers and prove the results obtained by imaging experiments.

References

(1) R. A. Komoroski, High Resolution NMR Spectroscopy of Synthetic Polymers in Bulk, VCH 1986
(2) J. Schaefer, E. O. Stejskal, R. Buchdahl, Macromolecules 10, 384 (1977)
(3) W. Kuhn, Angew. Chemie, Int. Ed. Engl. 28, 1 (1990)
(4) T. H. Mareci, S. Doenstrup, A. Rigamonti, J. Mol. Liqu. 38, 185 (1988)
(5) R. Gerhards, W. Dietrich, J. Magn. Res. 23, 21 (1976)
(6) W. Dietrich, G. Bergmann, R. Gerhards, Zeitschr. f. Analyt. Chemie 279, 177 (1976)
(7) W. Gronski, A. Hasenhindl, B. Freund, S. Wolff, in press

FAST RADIAL NMR IMAGING OF TRANSPORT PROCESSES

PAUL D. MAJORS*·**, DOUGLAS M. SMITH*, AND ARVIND CAPRIHAN**
*UNM/NSF Center for Micro-Engineered Ceramics, University of New Mexico, Albuquerque, NM 87131
**Lovelace Medical Foundation, Research Division, 2425 Ridgecrest Dr. SE, Albuquerque, NM 87108

ABSTRACT

Fast NMR imaging techniques for the study of objects with circular or spherical symmetry are introduced. Quantitative, radially-resolved information for an object with circular symmetry is obtained by Abel inversion of a single one-dimensional (1D) NMR image or equivalently by Hankel transformation of the 1D time domain NMR signal. With adequate sensitivity, the entire image information is obtained in a single experimental iteration, providing snapshot temporal resolution. Thus these techniques are useful for the study of transport phenomena. Spherical objects can also be radially resolved from a 1D projection image by applying two sequential Abel inversions, or in one simple differentiation step. These radial imaging techniques are easy to implement and the computational and data storage requirements are nominal. These procedures are also applicable to microscopic and solids NMR imaging, as well as to X-ray CAT and other projective imaging techniques. Noise effects, and the detection and handling of distortions from circular symmetry are also considered.

INTRODUCTION

Nuclear Magnetic Resonance Imaging (NMRI or MRI) is a non-invasive method for obtaining static distributions of nuclear spins which, while well-established in the biomedical field, is becoming a popular tool for basic sciences and engineering research [1,2]. It is also an important tool for the study of transport phenomena. NMRI is noninvasive and so may be used to follow the time evolution of the sample. Another advantage of NMRI is that can readily be combined with NMR spectroscopic, relaxation and flow measurements to provide spatially resolved chemical and physical information.

Because transport phenomena are dynamic processes, the NMRI data must be collected *quickly* to obtain temporal resolution. Unfortunately, the inherently low S/N ratio and long T_1 values for NMR as compared to other spectroscopies often necessitates long experiment times. Only for very slow transport mechanisms will these experiment times result in information with sufficient time resolution to obtain accurate transport parameters. Gaigalas, et al. [3] showed (using a model system with circular symmetry) that

conventional two-dimensional (2D) NMRI of fast transport processes can lead to blurred images. One solution is to employ fast 2D NMRI schemes such as FLASH [4] and echo planar imaging [5]. These techniques (which are based on gradient echoes) are often inappropriate for materials imaging because they do not refocus T_2^* effects, which are often significant for heterogeneous materials and solids.

Another solution is to impose high symmetry upon the sample and use 1D NMRI (several researchers use the term projection imaging, which we use synonymously with 1D NMRI). Gummerson, *et al.* [6], studied unsaturated flow in porous media by imposing axial symmetry upon the sample and imaging in the axial direction. Guillot, et al. [7], monitored the drying process of a cube-shaped limestone rock using 1D (and 3D) NMRI. Blackband and Mansfield [8] demonstrated the Fickian diffusion behavior of water in nylon at 100^0C using 1D NMRI.

Radially symmetric (*i.e.*, circular and spherical) systems are also convenient for the study of transport processes. First, only one or two spatial parameters are involved, which makes for simpler modeling. These systems also experience reduced pressure gradients (and lower strain) [9]. Many systems, *e.g.*, drying porous solids [7], naturally take on a spherical profile at advanced stages for this reason.

We have recently developed a fast 1D *radial imaging* (or, if one prefers, radially averaged profiling) scheme for studying systems with circular or spherical symmetry [10]. For a circular object, a 1D NMR image signal $f_c(t)$ is obtained in a magnetic field gradient G_l aligned transverse to the sample symmetry axis. This signal is converted to a radial image F(r) by using a Hankel transform **HT**, or equivalently in two steps by a Fourier transform **FT** followed by a inverse Abel transform **IAT** [11], *i.e.*,

$$F(r) = HT[f_c(t)] = IAT\{FT[f_c(t)]\}. \tag{1}$$

1D NMRI yields the highest signal-to-noise (S/N) ratio [12] for a fixed experiment time, because all of the spins in the sample are refocussed at each repetition, and all repetitions are added. HT or IAT[FT] processing yields a radial profile with spatially invariant resolution.

The enhanced S/N ratio makes radial imaging useful for studying small samples, or for imaging less sensitive nuclei. Thus radial imaging is applicable to microscopic imaging transport studies [13]. Fast imaging is also useful for NMRI experiments which involve the collection and processing of much data. For example, we are currently using radial imaging to characterize the evolution of pore structure and connectedness in cylindrically cast sol-gels during aging and drying processes [14]. The determination of pore size *distributions* involves the collection of many (20 or more) T1 or T2-weighted datasets [15], followed by a point-for-point inversion of the data. Radial imaging yields the data in compact form in the shortest time.

The noise in NMR data presents special considerations for radial imaging. Whereas FT processing of random noise returns random noise, Abel inversion distributes noise in an envelope which has an approximately $1/r$ radial dependence [16], yielding a higher S/N ratio at the edge of the sample. This is because the integration limits for the IAT transform vary with radius over the projection image. Thus, radial imaging yields a less noisy signal at the outer edge of a radially symmetric object, at the expense of features at the center.

Radial imaging requires true radial (circular or spherical) symmetry. Sample imperfections such as point defects or eccentricity will yield incorrect results. Radial symmetry is inferred by mirror symmetry (a necessary though not sufficient condition) in the transverse 1D NMR images. This can be checked by comparing projection images obtained at several transverse angles. If the images vary in shape, width, or symmetry, then the object is asymmetric. One can collect as many independent image angles as the kinetics of the transport process allows, which (if equivalent) can be added to enhance the S/N ratio.

In the presence of one or a few point defects, i.e., sites of high or low spin density, one can sometimes minimize or avoid image distortions by moving the defect(s) to the center (where the S/N ratio is poor anyway) or to one side of the projection image and the IAT procedure applied exclusively to the other half. Such distortions can often be eliminated by careful sample preparation and alignment (perpendicular to the imaging gradient, and parallel to the gravity vector if important).

We have tested the radial imaging procedure by measuring the effective diffusivity and time-resolved radial concentration profile of water in a model porous solid [17]. An ultra-fine zirconia powder with fairly narrow particle size distribution (Toyo Soda Chemical) was pelleted (1.27 cm OD vs. 1.33 cm in length) at 7,000 psia without a binder, and subsequently calcined at 1173 K in air. Before imaging, the sample ends were sealed with silicone and the pellet was concentrically placed within a cylindrical bottle (2.54 cm i.d.) and saturated with distilled water. The bottle was then filled with ^2H_2O to the height of the pellet and intermittent ^1H NMR images were obtained at 1-10 minute intervals over eight hours.

One dimensional ^1H spin echo (90^0-τ-180^0-τ-acquire) NMRI measurements were performed at a Larmor frequency of 80.34 MHz. The interpulse spacing $\tau = 5$ msec. One hundred twenty-eight complex points were acquired with a dwell time of 50 μsec in the presence of a 2 Gauss/cm magnetic field gradient which was aligned transverse to the sample symmetry axis, yielding a spatial resolution of approximately 184 μm. Thirty-two, 0.5 second repetitions were performed to enhance the S/N ratio, yielding an experiment time of approximately 17 seconds.

The data was Fourier transformed and the 1D magnitude image

was retained. The first moment of the image was assigned to the origin for the Abel inversion (r=0), and data points equidistant from the origin were averaged to further enhance the S/N ratio. Abel inversion yielded the temporally resolved radial images. The initial change of average proton concentration was used to determine the effective diffusivity of water in the pellet ($D_E = 6.7 \cdot 10^{-6}$ cm^2/sec). This value was used to calculate a time-resolved radial concentration profile, which was compared withthe experimental images as shown in Fig. 1.
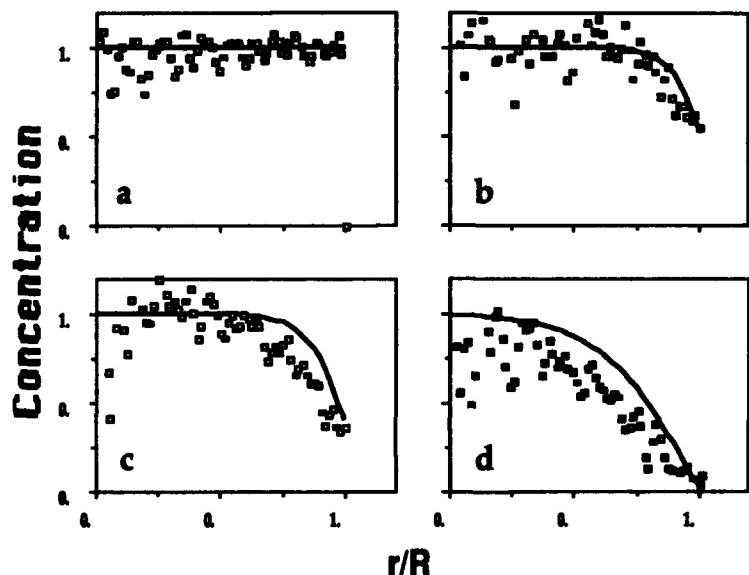
Figure 1. ^{1}H NMR radial images (points) and calculated profiles (solid curves) showing the normalized concentration of [1]H$_2$O for a porous cylindrical zirconia pellet which was saturated in H$_2$O and immersed in [2]H$_2$O. The images were collected (a) 0s; (b) 600s; (c) 900s; and (d)3400s after adding the [2]H$_2$O. The radial resolution is 184 μm. See text for details.

ACKNOWLEDGEMENTS

REFERENCES

1. W.A. Ellingson, P.S. Wong, S.L. Dieckman, J.L. Ackerman, and L. Garrido, *Ceram. Bull.* **68**, 1180 (1989).
2. J.M. Listerud, S.W. Sinton, and G.P. Drobny, *Anal. Chem.* **61**, 23A (1989).
3. A.K. Gaigalas, A.C. VanOrden, B. Robertson, T.H. Mareci, and L.A. Lewis, *Nucl. Techn.* **84**, 113 (1989).
4. A. Haase, J. Frahm, D. Matthaei, W. Hanicke, and K.D. Merboldt, *J. Magn. Reson.* **67**, 258 (1986).
5. P. Mansfield, *J. Phys. C: Solid State Phys.* **10**, L55 (1977).
6. R.J. Gummerson, C. Hall, W.D. Hoff, R. Hawkes, G.N. Holland, and W.S. Moore, *Nature,* **281**, 56 (1979).
7. G. Guillot, A. Trokiner, L. Darrasse, and H. Saint-Jaimes, *J. Phys. D: Appl. Phys.* **22**, 1646 (1989).
8. S. Blackband, and P. Mansfield, *J. Phys. C.* **19**, L49 (1986).
9. G.W. Scherer, *J. Am. Ceram. Soc.* **73**, 3 (1990).
10. P.D. Majors, and A. Caprihan, Fast radial imaging of circular and spherical objects by NMR, submitted to *J. Magn.Reson.* July 1990.
11. R.N. Bracewell, The Fourier Transform and Its Applications, 2nd ed. revised, (McGraw-Hill, New York, 1986) pp. 262-266.
12. A. Kumar, D. Welti, and R.R. Ernst, *J. Magn. Reson.* **18**, 69 (1975).
13. M. Neeman, P.D. Majors, and L.O. Sillerud, (unpublished).
14. P.D. Majors, and D.M. Smith, (unpublished).
15. K. Munn, and D.M. Smith, *J. Colloid Interface Sci.* **119**, 117 (1987).
16. L.M. Smith, *IEEE Trans. Inform. Theory* **34**, 158 (1988).
17. P.D. Majors, P.J. Davis, and D.M. Smith, submitted to Chemical Engineering Science, August 1990.

CHARACTERIZATION OF BIOMATERIALS WITH NMR

LEONCIO GARRIDO, BETTINA PFLEIDERER, JEROME L. ACKERMAN AND
JOHN MOORE
NMR Center, Massachusetts General Hospital and Harvard Medical School, 149 13th St.,
Charlestown, MA 02129.

ABSTRACT

Silicone based biomaterials are characterized with NMR. Bulk spin–lattice (T_1) and spin–spin (T_2) relaxation times are measured in polydimethylsiloxane (PDMS) model networks and various types of implants. The T_2 results seem to indicate that crosslink densities of these biomaterials are lower than those of the PDMS model networks studied. ^{1}H chemical shift NMR imaging techniques are developed to investigate the aging (e.g., migration of free polymer, rupture due to mechanical stress, etc.) of biomaterials *in vivo*.

INTRODUCTION

Over the past 30 years, plastic and reconstructive surgical procedures have experienced significant changes, in part because of the development of new or improved synthetic substances for the replacement of tissues [1,2]. Although these materials are biocompatible, the prosthetic device lifetime is often found to be very short. The improvement of the biomaterial properties and performance requires the understanding of the chemical and structural changes induced in the material after implantation.

Silicone (PDMS) oil and rubber are the most widely used mainly because of their inertness, oxidative and thermal stability at high temperatures, flexibility and elasticity at low temperatures and nonadhesiveness to tissues [3,4]. Although, some studies indicate that PDMS has practically no adverse tissue reactions, toxic effects are often found due to migration of free PDMS molecules (oil and unreacted materials in the rubber) [5-7] and filler particles (SiO_2) [8,9] from the implant. Moreover, the implant function is frequently deteriorated because of absorption of body fluid components [10] and chemical reactions with them [11,12].

The sensitivity of the NMR signal to the environment of a given nuclear spin is well known. Such environmental features include chemical composition and structure, which are reflected in the details of the chemical shift spectrum, as well as molecular and chain dynamics, which affect relaxation parameters such as T_1 and T_2. NMR can produce chemically specific images in which the contrast between different regions will be related to differences in their T_1, T_2 and concentration of the nuclei being observed, and it will depend upon the imaging sequence parameters (flip angle, echo time, etc.).

Previous studies on PDMS have shown the effects of radiation [13], presence of filler [14] and solvents [15], on proton T_1 and T_2. It is found that only T_2, which is affected by low frequency motions involving large portions of the macromolecule, is altered significantly. The presence of crosslinks and physical or chemical polymer–filler interactions hinder molecular motions, reducing T_2 values. The opposite occurs for swollen networks with T_2 increasing as the degree of swelling increases. The degradation of the network structure after implantation may increase molecular mobility (i.e., break-down of polymer chains, reduction in polymer–filler interactions, absorption of lipids) and, therefore, T_2 may increase as well. Thus, by T_2–weighted imaging it will be possible to map changes in T_2 that will be related to the implant molecular structure, the degree of swelling and the extend of these changes. Also, T_2–weighted images will allow the measurement of the amount of unreacted material present in the implant when the crosslinking reaction takes place partially or totally *in situ* [16].

However, in order to study the chemical or structural changes induced in implanted silicones by ^{1}H NMR imaging it is necessary to separate the contribution of the PDMS protons to the

NMR signal from that of the two major components present in animal and human tissues: water and fat. Different techniques have been proposed to enable spatial resolution of spectra [17-19] and, in particular, the separation fat-water has captured wide attention. The presence of a third resonance which corresponds to silicone protons makes it necessary to develop and optimize chemical shift sensitive pulse sequences that will enable the acquisition of the desired information, i.e., the distribution of silicone in implant and tissue.

The aim of this work is to develop NMR spectroscopic and imaging methods for the characterization of silicone based biomaterials, in particular, to study *in vivo* the migration of free material (e.g., polymer, reactants, particles, etc.) *from* the implant to adjacent tissue and the biomaterial aging.

EXPERIMENTAL

Materials.

PDMS model networks were prepared by end-linking reaction of divinyl-terminated PDMS chains having a number-average molecular weight between 3,000 and 18,000 g mol^{-1} with $Si[O-Si(CH_3)_2H]_4$ in the usual manner [20].

Various unused silicone biomaterials from different manufacturers were studied including chins, tissue expanders, breast implants, finger joints, etc.

Animal model.

Sprague-Dawley male rats (250 g) were used. Under general anesthesia (pentobarbital, 60 mg kg^{-1}) sterilized implants containing silicone oil with a viscosity of 1,000 cp were surgically placed in the rat's lower back. The imaging was performed on animals at different time points beginning a week after the implantation. During the imaging procedure, general anesthesia was maintained by delivering nitrous oxide:oxygen gas (1:4 v:v) via face mask to the animal.

Instrumentation and techniques.

The NMR relaxation measurements and the *in vitro* NMR imaging of PDMS model networks and silicone implants were performed on an MSL 400 spectrometer/imager (Bruker Instruments, Billerica, MA) equipped with an Oxford 9.4 T (proton frequency at 400.13 MHz) 8.9 cm vertical bore superconducting magnet.

Bulk T_1 and T_2 measurements were carried out using inversion recovery (IR) and spin echo (SE) sequences, respectively. The results are shown in Table I. The inversion time in the IR sequence was varied between 0 and 10 s. The echo time (TE, time between the 90° RF pulse and the center of the echo) in the SE sequence ranged from 10^{-3} to 1 s. The repetition time, TR, was 10 s in both cases, more than five times T_1.

^{1}H NMR images of the silicone implants were obtained using two-dimensional Fourier transform (2DFT) SE techniques with TEs on the order of 3 to 10 ms. The selective excitation of a slice throughout the sample 500 μm thick was achieved with a 1 ms wide sinc-function amplitude modulated RF pulse. The pulse sequence TR was typically 1 s.

The *in vivo* NMR imaging of implants was performed in an Omega system (General Electric, Fremont, CA) 4.7 T (proton frequency at 200.15 MHz) with an 20 cm horizontal bore superconducting magnet. The pulse sequence used is shown in Fig. 1. It combines IR with chemical shift selective excitation in order to discriminate the PDMS proton signal from that of fat and water present in animal tissues.

RESULTS AND DISCUSSION

As expected, the T_1 dependence on crosslink density in the PDMS model networks is very small, showing a slight decrease as the molecular weight between crosslinks decreases (see Table I).

Table I: T_1 and T_2 values of PDMS and silicone biomaterials

Sample	M^a (g mol^{-1})	T_1 (s)	$T_{2s}{}^b$ (ms)	$f_s{}^c$	$T_{2l}{}^d$ (ms)
Polymer	7,400	1.42	437	—	—
Network	3,700	1.19	0.80	—	—
	7,400	1.25	1.31	—	—
	18,000	1.34	2.88	—	—
finger	—	1.18	4.24	—	—
	—	1.25	3.38	—	—
chin	—	1.10	7.71	—	—
	—	1.14	4.75	—	—
breast (gel)	—	1.35	57.6	0.43	248
tube	—	1.29	3.62	—	—
sheet	—	1.24	2.08	—	—
expander	—	1.21	1.00	0.61	4.79

[a] Molecular weight number–average (uncrosslinked) or molecular weight between crosslinks.
[b] Component with short spin-spin relaxation time.
[c] Fraction of the component with short T_2 contributing to the NMR signal ($f_s + f_l = 1$).
[d] Component with long spin-spin relaxation time.

The T_2 changes are more pronounced. As mentioned above, the molecular mobility is reduced as the molecular weight between crosslinks decreases, shortening T_2. The T_2 values of the biomaterials are larger than those found in the model networks studied which suggest that implants have lower crosslink densities. There are two exceptions: the sheet and the tissue expander have values within the range of T_2s of the networks.

It is notable that the ^{1}H NMR spectra of the finger joints and chin implants have two main resonances resolve, with a small difference in their T_2s (see Table I). This might be attributed to the presence of, at least, two types of side groups attached to the Si atoms in the backbone. Only two of the biomaterials studied give the best fit to the experimental results with a biexponential function (two component model). This may be interpreted as the result of two contributions to
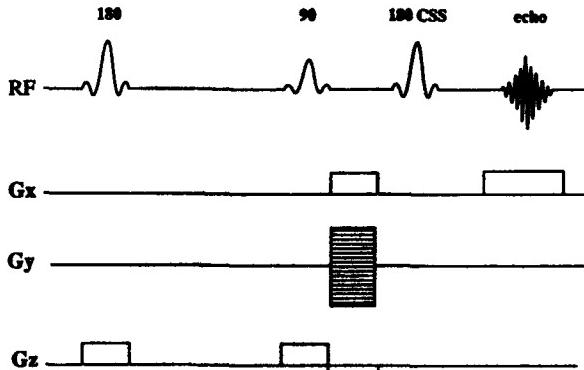
Figure 1. Hybrid pulse sequence for *in vivo* NMR imaging experiments. It exploits the differences between T_1s of the fat protons and those of water and silicone, and the ^{1}H chemical shift of tissue and PDMS. Typically the inversion time (TI) is about 150 ms, TE is 20 ms and the repetition time (TR) is 500 ms. The chemical shift selective excitation is achieved with a 3 ms wide sinc–function amplitude modulated 180° RF pulse.

the NMR signal, each fraction with a different degree of molecular mobility. In particular, the results for the gel in the breast implants seem to indicate that the polymer is slightly crosslinked to an extent of 40 %. The uncrosslinked material is likely to migrate to the implant surface or to adjacent tissues if it is implanted. This and other aspects related to biomaterials (i.e., mechanical degradation, homogeneity) could be investigated with NMR imaging.

In Fig. 2 is shown the ^{1}H NMR image of a chin implant. Several dark spots can be seen throughout the 500 μm thick section. The lack of NMR signal in these areas could be attributed to the presence of air bubbles or, perhaps, paramagnetic impurities. At the moment, a more detailed understanding requires further studies.

To assess the migration of free silicone from the implant to adjacent tissue or fat infiltration into it in vivo by ^{1}H NMR imaging, it is necessary to discriminate the PDMS proton NMR signal from those of fat and water (main components of animal tissues). We have achieved it by using the pulse sequence described in Fig. 1. The results obtained with a rat model are shown in Fig. 3. The image on the left shows a cross section at the rat's lower back obtained with a conventional SE sequence. All three components (water, fat and silicone) are visible. An arrow points to the silicone implant. In the image on right only the silicone distribution is mapped. In this case, the data was acquired using an IR–chemical shift selective excitation pulse sequence. The tissue and subcutaneous fat are completely suppressed. Some residual fat mainly in the digestive tract is visible (fat in food might have different NMR relaxation behavior). At this early stage, two weeks after implantation, no significant changes are observed in the implant nor in the surrounding tissue. Work on the long time effects on biomaterial NMR properties and tissue-silicone interactions are in progress.

CONCLUSIONS

The results obtained in this work demonstrate that ^{1}H NMR imaging is an effective tool for the characterization of silicone implants both in vitro and in vivo. The images of unused chin implants show spatial inhomogeneities that might be a possible cause of unwanted complications. We have developed a pulse sequence that allows the separation of the proton NMR signals of fat, water in tissue and silicone. This sequence will enable the in vivo study of implant aging. The NMR relaxation measurements, in particular T_2, of the biomaterials studied indicate that there
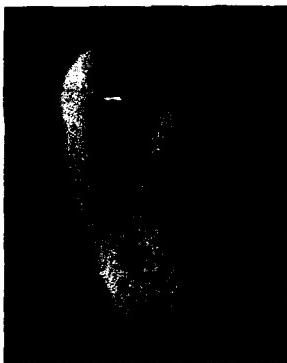
Figure 2. ^{1}H NMR image of a chin implant obtained using 2DFT spin echo technique with TE of 2.8 ms and TR of 1 s at 9.4 T. The imaging time was 17 min. The slice thickness is 500 μm. The in-plane resolution is 128 X by 128 Y pixels of 150 by 130 μm, respectively. Heterogeneities are readily visible.
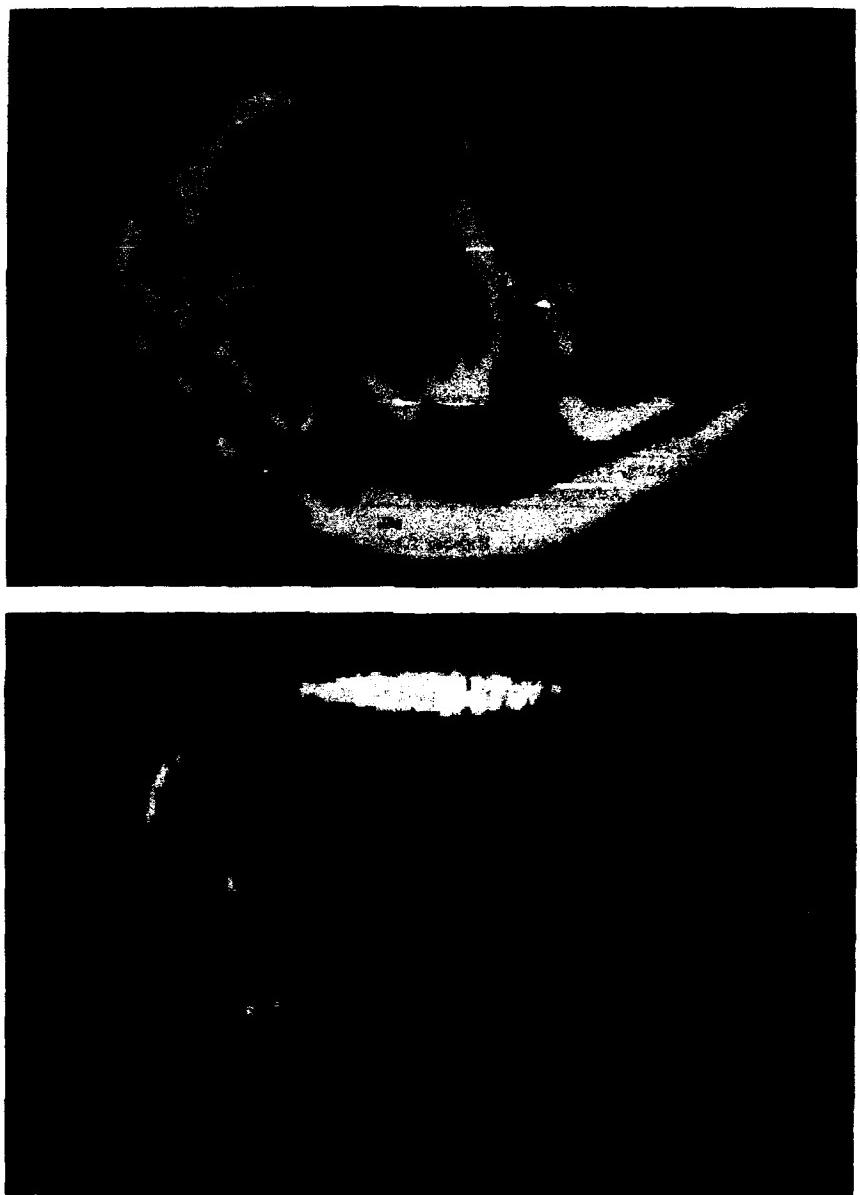
Figure 3. Transverse ^{1}H NMR images of a rat wearing a silicone implant two weeks after implantation. The image at the top was obtained using standard 2DFT spin echo technique with TE of 20 ms and TR of 500 ms at 4.7 T. Fat, tissue and silicone (arrow) are visible. The imaging time was 4.3 min. The slice thickness is 3 mm. The in-plane resolution is 256 X by 128 Y pixels of 390 by 781 μm, respectively. The image at the bottom shows only the silicone distribution (fat in digestive tract is seen). The data was acquired using the pulse sequence shown in Fig. 1. The other parameters are the same to those in top image.

is no free polymer present in them except in the breast implants. In the later case more than half of the contribution to the ^{1}H NMR signal is from free PDMS which might migrate out of the implant.

Although additional investigations are required to fully understand the origin of the heterogeneities observed in some implants, it is clear that NMR imaging will be extremely useful as a nondestructive tool for monitoring the uniformity of these and other types of implants. Also, by offering the possibility of studying *in vivo* the interaction tissue–biomaterial, this technique will allow better design and improvement of implants.

ACKNOWLEDGEMENTS

REFERENCES

1. Biomedical Materials, edited by J. M. Williams, M.F. Nichols, W. Zingg (Mater. Res. Soc. Proc., 55, Pittsburg, PA, 1986).

2. C.G. Gebelein, in Advances in Biomedical Polymers (Polym. Sci. Technol., 35, Plenum Press, NY, 1987).

3. E.L. Warrick, O.R. Pierce, et al., Rubber Chem. Technol., 52, 437 (1979).

4. R. van Noort and M.M. Black, in Biocompatibility of Clinical Implant Materials, edited by D.F. Williams (2, CRC Press, Boca Raton, FL, 1981) p. 79-98.

5. O. Winding, et al., Scand. J. Plast. Reconstr. Surg., 22, 127 (1988).

6. T.J. Sergott, J.P. Limoli, et al., Plast. Reconstr. Surg., 78, 104 (1986).

7. M.F. Refojo, M. Roldan, et al., J. Biomed. Mat. Res., 19, 643 (1985).

8. L.C. Hartman, R.W. Benette, et al., J. Biomed. Mat. Res., 22, 475 (1988).

9. W.S. Pierce, J.W. Boretos, J. Biomed. Mat. Res., 17, 389 (1983).

10. H.P. Chin, E.C. Harrison, et al., Circulation Suppl., 43, 51 (1971).

11. S. Chan, J. Biomed. Mat. Res., 7, 485 (1973).

12. R. van Noort, M.M. Black and B. Harris, J. Mat. Sci., 14, 197 (1979).

13. R. Folland, et al., J. Polym. Sci., Polym. Phys. Ed., 16, 1041 (1978).

14. J.P. Cohen-Addad, A. Viallat and P. Huchot, Macromolecules, 20, 2146 (1987).

15. J.P. Cohen-Addad, J. Chem. Phys., 76, 2744 (1982).

16. T.J. Sergott and L.M. Vistnes, Plast. Reconstr. Surg., 79, 331 (1987).

17. W.T. Dixon, Radiology, 153, 189 (1984).

18. I.L. Pykett and B.R. Rosen, Radiology, 149, 197 (1983).

19. P.A. Bottomley, et al., Proc. Natl. Acad. Sci. USA, 81, 6856 (1984).

20. J.E. Mark, Adv. Polym. Sci., 44, 1 (1982).

A STUDY OF CHANGES IN POLY(METHYL METHACRYLATE) (pMMA) RESULTING FROM THE ADSORPTION OF METHANOL USING NMR IMAGING.

NORBERT SCHUFF, PHILLIP A. HORNUNG AND EVAN H. WILLIAMS,
Varian Associates Nuclear Magnetic Resonance Instruments, 3120 Hansen Way, Palo Alto CA 94304. USA

ABSTRACT

The understanding of the adsorption of solvents into materials is of great interest in different fields of material science. NMR imaging techniques can be used to follow the process of solvent adsorption by obtaining spatial and chemical information in a nondestructive way. We report here a study of the uptake of methanol (a non-solvent) into poly(methyl methacrylate) beads produced by suspension polymerization and into compression mouldings. In both cases, the uptake is far faster than the rate of diffusion measured elsewhere. We also illustrate the nonreversible nature of this uptake with respect to temperature cycling.

INTRODUCTION

The effects of methanol on poly(methyl methacrylate) (pMMA) are of considerable interest and importance. In fabricated items, exposure causes problems; methanol is a potent agent for stress-crazing [1,2] and cracking [3]. The distribution of methanol in pMMA as a function of morphology has been reported, both as a diffusion study in homogeneous samples using imaging techniques [4] and in samples that had spatial heterogeneity [5].

This work extends that of [5] and investigates the spatial distribution of methanol both in pMMA beads and in pressure moulded samples as a function of time and of temperature.

EXPERIMENTAL PROCEDURES

The pMMA used was that designated as LMW (table 1, [6]). This is a low molecular weight pMMA purchased from Polyscience and was prepared by suspension polymerization.

Pressure moulded samples of this polymer were prepared by filling a 3 mm diameter mould and then subjecting this to 90 tonnes pressure in a press, until the resulting cylinder of polymer became completely transparent.

NMR imaging was performed on a Varian Associates Unity-300 spectrometer operating at 7.04 T and equipped with microimaging and with complete solids modules.

Imaging was performed using 2 techniques. Backprojection images of the actual pMMA beads was performed in a Varian 5 mm wideline probe in which the $\pi/2$ pulsewidth was 1.2 μsec. TE used was 200 μsec and the gradient strength was up to 70 G/cm. Reconstruction was performed in a phase sensitive mode. Spin warp images of the methanol surrounding pMMA samples were obtained on the same spectrometer using a 5 mm 1H/19F high resolution probe inside the standard external gradient set. The TE (15 msec) used was selected to give maximum contrast for each phase of the experiment. The TR used was 1 second. Pixel resolution was 30 μm and slice thickness 400 μm. The displayed images were threshold equalized and photographed on an Agfa-Matrix 6000 camera system.

Images were obtained under thermostated conditions at the temperatures indicated. Temperature stability was typically ±0.1 °C

The spin warp imaging protocol used both for the beads and for the mouldings was the same and followed the following course. Beads were placed in a 5 mm NMR tube and methanol was added to cover them with an excess depth of approximately 4 mm. The tube was quickly agitated to remove as many air bubbles as possible and then placed in the spectrometer. Images were obtained at ambient temperature (22 °C) every 30 minutes for 2 hours or until the methanol was evenly distributed. The sample was then raised to 40 °C and then equilibrated

after which a further image was obtained. Finally the temperature was dropped to 25 °C, equilibrated and then an image taken immediately and a further image taken after 30 minutes.

RESULTS

Backprojection images

Although good images of the beads could be obtained using this methodology, no internal structure could be discerned. The average bead diameter was observed to be of the order of 300 μm. Any internal voids were therefore estimated to be less than the pixel resolution which was 30 μm.

Spin warp imaging of beads in water

A typical image obtained is shown in the left hand image of figure 1. Although there is some variation in intensity within various beads, this was seen to be invariant with time and so was not indicative of diffusion into the beads. As with the backprojection images the average bead size was observed to be 300 μm, indicating that there were no major artifacts contributing to apparent size.
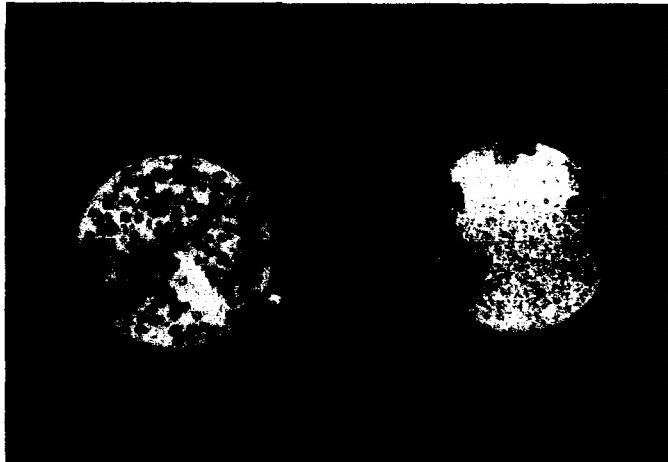
Figure 1. Images of pMMA beads in water (left) and in methanol (right) after 180 minutes.

<u>Spin warp imaging of beads in methanol</u>

Uptake of methanol leads to a loss of definition of the beads. This is illustrated by the right hand image of figure 1.
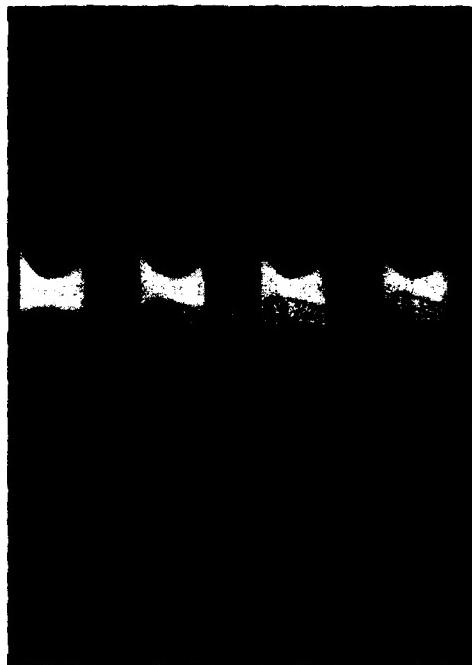
<u>Figure 2.</u> Time course of uptake of methanol into pMMA beads. Times shown are (from left to right) 30, 60, 90 and 120 minutes.

Figure 2 shows a typical set of images taken during the equilibration phase of the protocol. The bottom (120 minute) image shows that the intensity of the methanol signal is uniform over a far larger proportion of the sample than would be expected for diffusion through solid pMMA. As can be seen, the methanol intensity increases over the period of 120 minutes with the sample losing differentiation of structure. This is illustrated in graph 1 in which we have plotted the uptake of methanol against time. Uptake is simply reported as the loss in column height of the supernatant methanol.
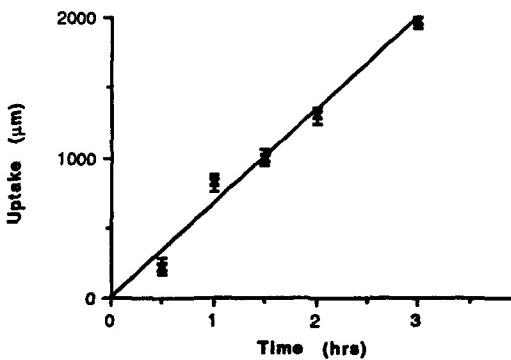
Graph 1. A plot of methanol uptake against time for pMMA beads. Uptake is measured as the loss of supernatant methanol height. The data are shown with resolution as the Y axis error and a simple line of best fit is included.

The left hand side of figure 3 shows the effect of raising the sample temperature to 40 °C. The two large voids are air bubbles. This image shows a nearly uniform distribution of methanol throughout the sample, with little bead structure visible. Little free methanol is visible above the beads.
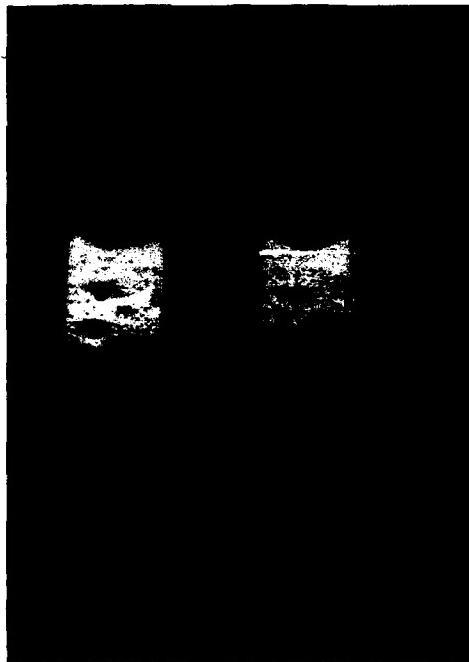
Figure 3. Comparison of the methanol distribution in pMMA beads at 40 °C (left) and subsequently at 25 °C (right).

An image obtained after the temperature drop to 25 °C is shown in the right hand side of figure 3. There is far more visible structure in the sample although not of the expected spherical nature. Furthermore, there is considerably more free methanol visible above the pMMA.

As reported earlier [5], the optical and other physical properties of these samples change during the methanol uptake and change again during the temperature cycle.

During uptake the beads swell and become transparent. They rapidly become stuck together so that it is impossible to shake them about in the tube. With the increase in temperature, samples held in a waterbath lose all discernable structure and appear as one homogeneous, transparent mass.

Immediately upon subsequent equilibration at 25 °C the samples became white in appearance and could be readily agitated, settling in the tube and leaving an upper la · : of free methanol. As shown earlier, the process was irreversible.

Spin warp imaging of compression moulding in methanol

Little apparent uptake of methanol was observed in the mouldings at ambient temperature.

On increasing the sample temperature to 40 °C irregular uptake was observed as shown in the time course series of figure 4.
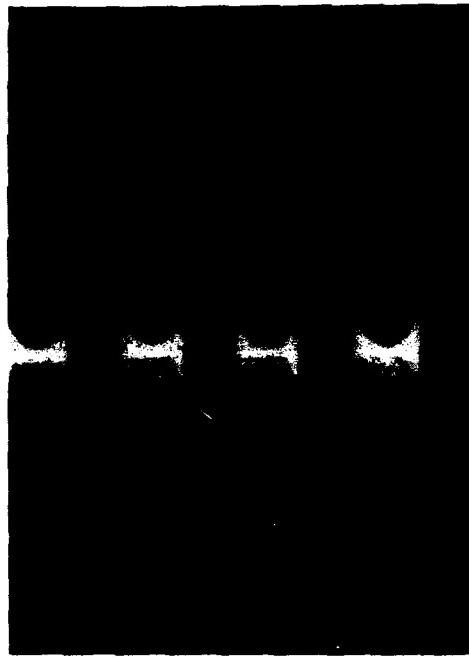
Figure 4. Images of a moulding in methanol. From left to right the images are - after 180 minutes at ambient temperature, then subsequently after 30, 60 and 120 minutes at 40 °C.

After return to 25 °C, the samples showed a reduced methanol intensity, with a loss in contrast. Visual inspection revealed that the mouldings had become opaque.

DISCUSSION

Beads in methanol

From the results on these beads presented elsewhere [5], it is evident that the suspension polymerization used produces a sphere which is honeycombed with voids. The size distribution of these voids is continuous as is evidenced by the backprojection images and by the uniform uptake of methanol at ambient temperature by the beads. The speed of uptake throughout the sample is indicative of channels in the pMMA, as postulated by Allen *et al.* [5].

Weisenberger *et al.* [4] have studied the diffusion of methanol into pMMA and have found it to be linear with time (case II) rather than being Fickian in nature. They report a front velocity of 5 nm/s. From this it can be seen that the extent of penetration of methanol into a solid bead of pMMA would be 18 μm in 1 hour - a rate far slower than that observed in the experiments reported here.

The change in appearance and in the methanol distribution after temperature cycling, strongly suggests that the beads have fractured and, in addition, changed in some way so as to preclude further methanol uptake. Allen *et al.* [5] argue that the larger voids may have filled with methanol as well as the space between the beads. Furthermore the loose packing of pMMA in the beads permits chain conformational changes in response to methanol penetration.

However, this work suggests rather that upon cooling methanol is excluded from the pMMA that remains after fracture of the beads.

Thus it appears likely that during the initial equilibration, methanol is rapidly taken up into the beads and fills the voids in them. As the temperature is raised, chain reorientation may indeed occur, allowing swelling of the beads which may also be facilitated by plasticization by the methanol [7]. Diffusion may also be a contributing process as the methanol front velocity is sufficient to penetrate much of a spongy interior structure. When the temperature is lowered, the methanol in the voids contracts faster than new methanol can be taken up, resulting in a partial collapse of the voids with concomitant fracturing of the pMMA structure surrounding. Once fractured, the beads disintegrate sufficiently to allow release of methanol. The void structure is also destroyed and so the uptake process is irreversible.

Moulding in methanol

Here the process is similar to that seen in the beads except that the compression moulding process would appear to effectively remove the internal voids in the beads. However, there are considerable channels left in the moulding and it is these channels that take up the methanol. This process is far slower than that in the beads at ambient temperature and it is possible that this is primarily due to to viscosity effects.

The movement of the methanol front was measured to be 255 nm/s, clearly far faster than that expected for diffusion through homogeneous pMMA.

Temperature cycling had the expected result - the structure of the sample altered, excluding methanol. Although the sample was opaque, it maintained structural integrity, but was easy to crush.

REFERENCES

1. Van Tan Truong, P.E.M. Allen and D.R.G. Williams, *Eur. Polym. J.*, **23**, 181 (1987).
2. Van Tan Truong, P.E.M. Allen and D.R.G. Williams, *Eur. Polym. J.*, **23**, 595 (1987).
3. Van Tan Truong, D.R.G. Williams and P.E.M. Allen, *Eur. Polym. J.*, **23**, 41 (1987).
4. L.A. Weisenberger and J.L.Koenig, *J. Polym. Sci.*, C27, 55 (1989).
5. P.E.M. Allen, S. Hagias, D.R.G. Williams and E. H. Williams, *Eur. Polym. J.*, **26**, 841 (1990).
6. P.E.M. Allen, D.M. Host, Van Tan Truong and D.R.G. Williams, *Eur. Polym. J.*, **21**, 603 (1985).
7. L.A. Belfiore, P.M.Henrichs, D.J.Massa, N.Zumbulyadis, R.P.Rothwell and S.L.Cooper. *Macromolecules*, **16**, 1744 (1983).

OXYGEN-17 AND PROTON MR MICROSCOPY IN MATERIALS ANALYSIS

G.D. MATEESCU,[†] R.A. KINSEY[‡] AND G.M. YVARS[†]
†Department of Chemistry, Case Western Reserve University
Cleveland, Ohio 44106, USA
and
‡B.F. Goodrich Research & Development Center
Brecksville, Ohio 44141 USA

ABSTRACT

Preliminary results of two applications of $^{17}O/^1H$ NMR microimaging (MRμI) are described. In the first case, it is shown that oxygen-17 MRμI presents a unique advantage in situations where a strong proton background hinders the analysis of water ingress in polymeric materials. This is illustrated with ^{17}O-enriched water diffusion into an agar gel from a central well. While proton imaging cannot readily distinguish between exogenous and endogenous water, ^{17}O imaging makes a clear differentiation, due to the fact that the natural abundance gel has virtually no ^{17}O background. In the second case, proton MRμI was used to analyze the structure and performance of commercial time-release pellets (ProMac[R]) containing an active ingredient (surfactant) dispersed into an inert matrix. This was done after leaching the detergent with natural abundance water or after drying the leached sample and refilling the pores with water. Pores ranging in size from 25 to 325 μm diameter are clearly visual ized. The ^1H images have been quantitated with commercial image analysis software in terms of the total porosity and the individual pore characteristics. Two types of water can be separately imaged: "bound" water with restricted mobility (interacting with the polymer matrix), and "free" water (in large pools). The majority of water is in the bound state. It is possible to evaluate the control-release performance of the product from the size of the pores, the uniformity of dispersion and the time course of detergent-water exchange.

INTRODUCTION

The oxygen-17 nucleus is generally regarded as "unfavorable" for NMR experiments for two principal reasons: quadrupolar line broadening and very low natural abundance. Until recently, its use in MR imaging has not even been considered.

However, the feasibility of ^{17}O MRI and localized spectroscopy has been demonstrated during the past three years. Indeed, it has been shown[1-11] that the "unfavorable" magnetic resonance properties of ^{17}O can actually be turned into advantages: the fast relaxation allows much shorter pulse intervals than with proton, and even modest isotopic enrichment dramatically increases the signal-to-contrast ratio. Thus, an enrichment of 3.7 atom % increases the concentration by a factor of 100 and decreases the measurement time by a factor of 10,000. In fact, in vivo detection of local (mouse brain) concentrations as low as 0.5% $H_2^{17}O$ has been recently reported.[9]

The low gamma of ^{17}O leads to the necessity of increasing the gradient strength by a factor of 7.37 (the γ_H/γ_O ratio) in

order to achieve a resolution comparable to that of proton MRI. This is quite feasible with high performance NMR instruments generally employed for materials characterization.

Perhaps, the most important atribute of ^{17}O MR$_\mu$I resides in the possibility to detect labeled water molecules in a large pool of water. This opens a unique avenue towards precise determination of net transport of water in systems that naturally contain water and/or mobile protons (e.g., elastomers, biopolymers, etc). The specific example presented in this communication refers to migration of water through an agar gel.

With regard to proton imaging, it is shown here that an adequate resolution can be obtained by employing small sample size in a microscope accessory attached to a high performance NMR system. This is illustrated by the measurement of pore sizes in a ProMac^R material,[12] a low density polyethylene (LDPE) coextruded with a surfactant (LAS, linear alkylbenzene sulfonate) to form a time-release system.[12] The surfactant is a bactericide used to enhance the reclamation of land after surface mining. It inhibits the growth of acid-producing bacteria which hinder revegetation.

MATERIALS AND METHODS

Oxygen-17 and proton images were obtained on a Bruker MSL 400 system equipped with a double resonance ($^{17}O/^{1}H$) microimaging probe which also incorporates the gradient coils. Gradient strengths in excess of 100 Gauss/cm can be obtained. Proton spectra were taken with a Bruker AM-200 instrument.

NMR micrographs were taken employing two kinds of spin warp sequences: one with a soft 90° (single lobe sinc) pulse for slice selection followed by a hard 180° pulse, in order to obtain short echo times (TE) for imaging of "bound" water; the other, with both soft pulses, for imaging "free" water. Specific parameters are given in the text or in Figure captions.

Oxygen-17 enriched (40 atom %) water was purchased from the Monsanto-Mound laboratories. Natural abundance water was distilled and deionized.

The agar gel (0.7%) was prepared with hot (80 °C) water, poured in two identical 18 mm I.D. NMR tubes, each containing a concentrical 5 mm O.D. tube. After cooling, the 5 mm tubes were removed to obtain the wells in which the natural abundance or ^{17}O-labeled water was placed at the beginning of each diffusion experiment.

Two kinds of ProMac^R (42.5 % LAS)/LDPE) rods were investigated: one having a 7 mm diameter (PRO1) and the other having a 4 mm diameter (PRO2).

A rod of PRO1, 2 cm long, was extracted by stirring in 600 ml of distilled water at ambient temperature for 10 days. The water was changed twice a day. After removing external excess water with filter paper, the leached sample was imaged for both bound and free water. A control consisting of unleached PRO1 was wrapped in wet filter paper in order to show that, in our conditions, both the surfactant (LAS) and LDPE did not yield an image.

After leaching, rods of PRO2 were dried in the oven at 70 °C. They were then placed in NMR tubes containing a quantity of water which was approximately twice the volume of the rod. The tubes were sealed and kept in a bath at 70 °C for 20 hours. Since there was very little indication of water ingress

the tubes were removed from the bath and stored 100 days at room temperature to allow completion of the diffusion process. The samples were imaged after removal of excess external water with filter paper. All images were performed in 10 mm inserts.

The percent porosity and pore size parameters (length, width, area, perimeter, shape function) were determined using the stored image analysis (SIA) software on a Tracor Northern Energy Dispersive X-ray Analyzer.

RESULTS AND DISCUSSION

Water Diffusion in Agar Gel

A comparison of proton and oxygen-17 images taken at the beginning and the end of parallel studies of water transport within a mass of agar gel is shown in Figure 1. It is obvious
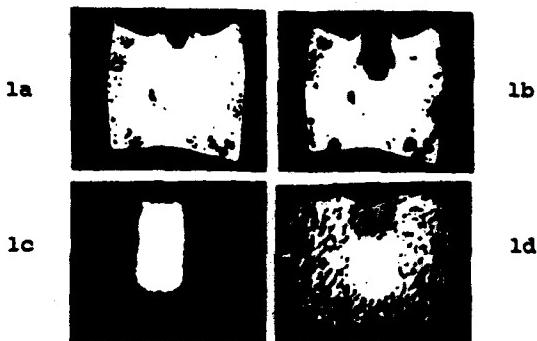

Figure 1. a&b: proton images of a 500 μm slice trough the agar gel phantom described in the Materials and Methods section. A spin warp sequence with soft 90 and 180° pulses was employed with echo times (TE) of 12 ms, field of view 26 mm and 113 μm/pixel resolution. a: Image taken approximately one hour after gel preparation and adding natural abundance water in the central well; time of repetition (TR) 1s, total experiment time (ET)= 8 min. b: Image after 20 hr; ET = 16 min. c&d: oxygen-17 images of a similar phantom as above, but after adding 5 atom % ^{17}O-water in the central well. A hard 180° pulse was used to shorten the echo time. c: i-mage at five minutes. d: image at 108 minutes. TE = 2 ms, TR = 28 ms, ET = 4 min, ST = 14 mm, resolution 157 μm/pixel.

that the evaluation of a diffusion coefficient from proton data is virtually impossible. In dramatic contrast, the ^{17}O images provide unambiguous data for the calculation of H_2O diffusion. Work is in progress for the adaptation of Fick's law to three dimensional NMR determination of the diffusion coefficient. Performing parallel experiments with D_2O will contribute to the understanding of this complicated process. We emphasize here the strong difference between the behavior of oxygen and hydrogen as representatives of a given water molecule. Indeed, while oxygen will be permanently attached to the originally labeled molecule, hydrogen or deuterium will be rapidly separated from it by intermolecular exchange processes.

Proton MR Microscopy of Porous Polyethylene

In preparation for MRμI, one dimensional ^{1}H spectroscopy was performed on the samples. Initial attempts to hydrate ProMac^R rods for study of the water or surfactant were unsuccessful. After equilibration to a relative humidity of 74% a broad featureless line is observed with a linewidth of ~1300 Hz. There is no chemical shift resolution, so this signal may be from either water or surfactant. Attempts were made to induce proton mobility by raising the temperature. At 90 °C the linewidth was 430 Hz. These preparations were not judged to yield samples suitable for imaging.

Exchanging the LAS for water by soaking the material in water for ten days yielded 200 Hz (water) linewidths. A small
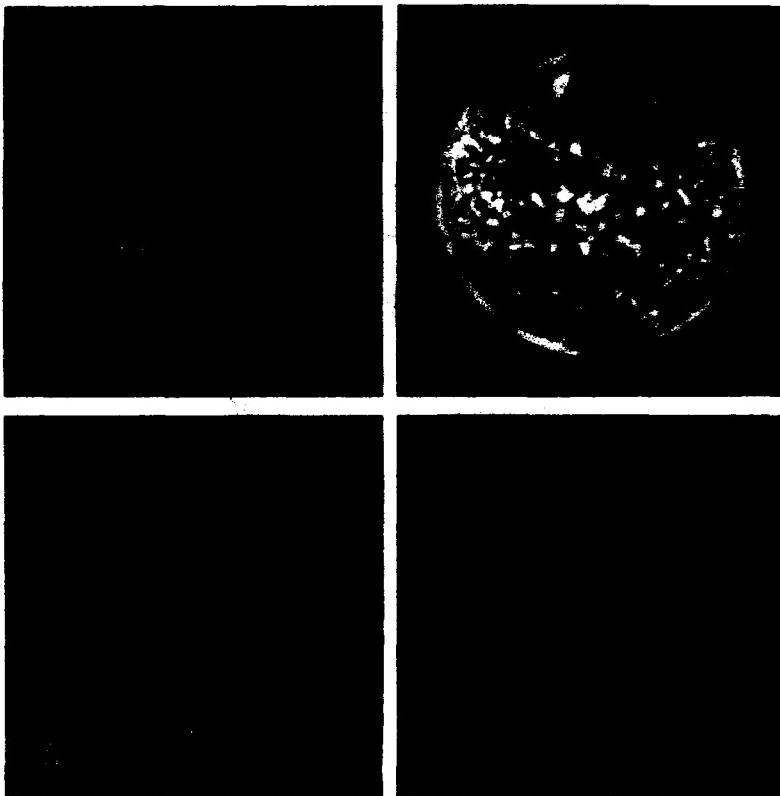

Figure 2

shoulder at high field was detected. This could be interpreted either as a susceptibility effect or as due to residual surfactant. The water that fills the voids left by the leached LAS constitutes the source of signal for imaging.

Figure 2 (upper left) shows a transverse NMR microimage yielded by the leached LDPE (7 mm diameter, 300 μm slice

thickness). The in-plane pixel resolution is 10μm. The echo time (TE=6 ms) was adjusted to emphasize the free water in "large" pores. This image indicates there are no significant areas devoid of signal, and hence a uniform surfactant distribution.

An image emphasizing the bound water (TE=3ms) is shown in Figure 2 (upper right). Again, the pixel resolution is 10 μm and the slice thickness is 300 μm. This image was taken of a rod wrapped in filter paper which absorbed excess water at the exterior of the sample, thus defining its perimeter. The bound water covers nearly the entire cross section except for several areas, the largest (~800 μm) being situated on the left side, close to the horizontal diameter. Careful examination of the image reveals a circular feature without water, particularly visible in the upper two quadrants which could be interpreted as a result of the extrusion process.

Figure 2 (lower right) shows a slice through a control (unexchanged) LDPE rod wrapped in wet filter paper. No signal appears in the interior due to lack of visible water and immobility of the LAS and LDPE protons.

PRO2 samples (not shown here) revealed a more dense pore distribution which corresponds to a much slower (hence, efficient) LAS release. Indeed, it took up to 100 days to extract the surfactant.

Image Analysis

The lower left of Figure 2 represents an expansion of a small region from the first quadrant of the image above. This area was scanned and digitized into a binary image by a Tracor Northern energy dispersive x-ray analyzer. As with comparing images, care must be taken when adjusting the image threshold for the digitization. Stored Image Analysis (SIA) software allows for quantitative evaluation of the pores. Each pore is defined in terms of location, diameter, length, width, area, perimeter, and orientation. Averages of each of these parameters are calculated as well as total porosity (the percentage of area covered by pores). Histograms can be produced for the distribution of the pore parameters. The calculated porosity of this region is 8.3%. The particles range in diameter from 25-300 μm within two major pore size distributions, 25-70 and 170-300 μm.

Table I. Characteristics for Pores Larger than 100 μm

Part.	Av.diam.	Area	Perim.	Cntr-x	Cntr-y	Length	Width
1	100	8,700	340	140	90	130	100
2	180	23,440	580	1,900	130	200	160
3	170	23,070	560	610	270	200	150
4	230	38,630	730	1,160	280	270	200
5	210	28,210	670	750	490	220	190
6	285	57,160	910	1,560	600	310	250
7	170	17,420	550	160	660	220	110
8	270	53,360	880	1,970	700	290	250
9	210	27,690	650	140	1,350	220	180
10	260	49,940	840	890	1,440	290	220
11	198	23,820	620	60	1,780	240	130
12	300	63,490	960	2,070	1,750	350	270

However, pores smaller than 70 μm may be indistinguishable

from noise. Table I contains data for the pores larger than 70 μm in diameter.

CONCLUSIONS

When a proton background hinders the ^{1}H MRI analysis of diffusion of water in a polymeric system, employing ^{17}O-enriched water and ^{17}O MRI brings an elegant and efficient solution. Use of other ^{17}O labeled liquids (alcohols, phenols, ethers etc.), is also deemed possible.

Proton microscopy of porous materials constitutes a valuable means for characterization of inner structures, voids and defects. Exploiting differences in relaxation parameters results in establishing the extent of tight or weak interactions between the matrix and the incorporated liquid. In addition, determining the time course of water (or other solvent) ingress is an invaluable means to evaluate the performance of time-release products.

NOTES AND REFERENCES

1. G.D. Mateescu and Terri Dular, Oxygen-17 NMR Imaging, ENC (Experimental NMR Conference) 28, 73a (1987).
2. G.D. Mateescu, G.M. Yvars and T. Dular, Oxygen-17 MRI, Soc.Magn.Res.Med. (SMRM), 6, 929a. (1987).
3. G.D. Mateescu, G.Yvars, D. Pazara and N. Alldridge, ^{17}O/^{1}H NMR Microscopy, ENC, 29, 189, (1988).
4. G.D. Mateescu, G.M. Yvars, D. Pazara, J. LaManna, D. Lust, K. McKracken, M. Mattingly and W. Kuhn, Oxygen-17: A Physiological, Biochemical and Anatomical MRI Contrast Agent, SMRM 7, 600 (1988).
5. G.D. Mateescu, G.M. Yvars and Terri Dular, Water, Ions and ^{17}O MRI, Water and Ions in Biological Systems, edited by P. Lauger (Birkhauser Publishers, Basel, 1988), p.239-250.
6. G.D. Mateescu, G.M. Yvars, D.I. Pazara, N.A. Alldridge, J.C. LaManna, W.D. Lust, M. Mattingly and W. Kuhn, Combined ^{17}O/^{1}H MR Microscopy in Plants, Animals and Materials, Synthesis and Applications of Isotopically Labeled Compounds, Baillie & Jones, Eds. (Elsevier, 1989) 499-508.
7. G.D. Mateescu, G. Yvars, L. Maylish-Kogovsek, J. LaManna, W.D. Lust and D. Sudilovsky, ^{17}O MRI and MRS of the Brain, the Heart and Coronary Arteries, SMRM 8, 659 (1989).
8. G.D. Mateescu and G.M. Yvars, Oxygen-17 MR Imaging: Theory and Experiment, ENC 30, 197a (1989).
9. G.D. Mateescu, G. M. Yvars, J.C. LaManna, W.D. Lust and D. Sudilovsky, Oxygen-17 MRS:in vivo Evaluation of Water Uptake and Residence Time in the Mouse Brain after Injection of O-17 Labelled Water, SMRM 9, 1236 (1990).
10. G.D. Mateescu, G.M. Yvars, J.C. LaManna, D.W. Lust and D. Sudilovsky, Volume Selected ^{17}O Spectroscopy in Experimental Cerebral Ischemia, ENC, 31, 205a (1990).
11. G.D. Mateescu, Oxygen-17 Imaging of Non-Biological Materials, FACSS 17, 127a (1990).
12. a) ProMac^R is a registered trade mark of B.F. Goodrich Co.
    b) A.A. Sobek, D.A. Benedetti, V.J. Rastogi, Proc. Mining and Reclamation Conf., Vol. 1, 33-42 (1990).

NMR IMAGING AND THE ELECTRIC QUADRUPOLE
INTERACTION IN SOLID MATERIALS

B. H. Suits, Physics Department
Michigan Technological University
Houghton, MI 49931

ABSTRACT

Nuclei with a spin, $I > \frac{1}{2}$, possess a nuclear quadrupole moment which can couple to the electric field gradients in a material. They can be static, leading to NMR frequency shifts, or dynamic, which can influence relaxation times. In either case, an NMR image can be made which is sensitized to changes in the electric quadrupole interaction to provide a sensitive measure of the macroscopic spatial dependence of the microscopic changes in the material. Several examples are presented. Special considerations need to be given in the case when the strength of the Zeeman interaction between the nucleus and the magnetic field and/or the rf field is small compared to the electric quadrupole interaction.

INTRODUCTION

Small distortions in materials such as impurities, dislocations, and thermal fluctuations, are predominant factors when determining the mechanical and electrical behavior of materials. The sensitivity of quadrupole perturbed NMR to the presence of static and dynamic distortions is well known [1-3]. It is only natural to use the non-destructive, non-invasive techniques of NMR imaging in a way which can utilize the sensitivity of the NMR response to electric field gradients.

NMR imaging in solids is not easy [4,5]. Several articles have been written describing methods to approach the problem. One of the most common difficulties with solids NMR is the dipole-dipole interaction which causes broadening on the signal and may limit the time available for a measurement. Various elegant techniques can be used, with varying degrees of success, to partially eliminate the effects of the dipole-dipole coupling from the image. Most involve rapid switching of high power gradient coils and use sensitive multipulse NMR techniques which also tend to eliminate quadrupole broadening. Another, perhaps less elegant, method, used for the NMR images presented here, reduces the effects of the dipole-dipole broadening on image quality in a simple way by using large static magnetic field gradients (10 to 50 g/cm) to form the image. Numerical techniques can also be used to reduce the effects of broadening *ex post facto*. One must also realize that the most common nuclei used for NMR studies, ^1H and ^{13}C, have spin $I = \frac{1}{2}$ and hence do not couple (directly) to electric field gradients.

ELECTRIC QUADRUPOLE INTERACTIONS

The electric quadrupole interaction is discussed at great length elsewhere [2,3] and is due to the presence of an electric field gradient which couples to the electric quadrupole moment of the nucleus. The electric field gradient can be described using a symmetric traceless second rank tensor, V, with components V_{ab} ($a,b = x,y,z$). The field gradient represented in one coordinate system, (x_1,x_2,x_3), can be transformed to another, (x_1',x_2',x_3'), using the rotation

$$V' = T^{-1} V T \tag{1}$$

where the elements of T, T_{ij}, are the cosines of the angles between x_i' and x_j. It is always possible to find a coordinate system for which $V_{ab} = 0$ if $a \neq b$ which is referred to as a principal axis system. In the principal axis system the quadrupole interaction can be expressed using the Hamiltonian,

$$\mathcal{H}_Q = \frac{eQ}{6I(2I-1)} \sum_{a=X,Y,Z} V_{aa}(3I_a^2 - I^2) \tag{2}$$

where I is the angular momentum operator for the nucleus in question, I_a is the operator for the a-th component of the angular momentum, I is the spin of the nucleus (a number), Q is the quadrupole moment of the nucleus and e is the magnitude of the charge of an electron.

It is useful to estimate the size of the quadrupole couplings for various nuclei. For any particular nucleus the quadrupole field can vary from zero to very large values. However, what is desired is a measure of the sensitivity of different nuclei to the presence of distortions in the lattice. Charges in a crystal will be roughly one electronic charge in magnitude and typical interatomic spacings are roughly 0.2 nm. Thus we calculate the field gradient due to a charge e, 0.2 nm away on the z-axis. Taking into account the redistribution of the electrons on the atom which contains the nucleus using a linear response theory [6] and calculating the resulting frequency splittings gives the results shown in Table I. The values in Table I are for comparison purposes only but serve as an indication of the relative sensitivity of the NMR signal to the presence of distortions.

The total interaction, which determines the frequency of response of the nucleus, will include both the field gradient interaction and the Zeeman interaction, $\mathcal{H}_z$, with applied magnetic fields.

TABLE I

Relative Sizes of the Quadrupole Interaction for Selected Ions Under Similar Conditions*

Ion	I	$<H_Q>/h$ (MHz)
^2H	1	0.018
$^7Li^+$	3/2	0.22
$^{14}N^{+3}$	1	0.37
$^{23}Na^+$	3/2	2.50
$^{27}Al^{+3}$	5/2	0.45
$^{35}Cl^-$	3/2	19
$^{63}Cu^+$	3/2	8.6
$^{79}Br^-$	3/2	200
$^{127}I^-$	5/2	260

* Frequency shift of 3/2 to 1/2 or 1 to 0 transition, as appropriate.

HIGH MAGNETIC FIELDS

When the Zeeman interaction, $\mathcal{H}_z = -\gamma H \cdot I$, where γ is the gyromagnetic ratio for the nucleus under study and H is the applied magnetic field, is large compared to the quadrupole interaction $\mathcal{H}_Q$, the effects of $\mathcal{H}_Q$ can be calculated using perturbation theory. The convention used here defines the magnetic field, H, to be along the z-axis of the reference frame (x,y,z) in the lab frame and the principal axes of the electric field gradient define a crystal reference frame (x',y',z'). To first order in perturbation theory one has an effective Hamiltonian

$$\mathcal{H} = -\gamma H I_z + \frac{eQ}{4I(2I-1)} V_{zz}(3I_z^2 - I^2) \tag{3}$$

where, using the rotation (Eq. 2) expressed using Euler angles,

$$V_{zz} = V_{z'z'} \cos^2\theta + V_{x'x'} \sin^2\theta \cos^2\phi + V_{y'y'} \sin^2\theta \sin^2\phi \qquad (4)$$

which yields 2I magnetic dipole transition frequencies which depend on the relative orientation of the magnetic field and the quadrupole field principal axes.

Note that the transition $m = -\frac{1}{2}$ to $m = +\frac{1}{2}$ (present for nuclei with half integer spin) is not sensitive to the presence of the electric field gradient to first order.

In imaging applications a spatially dependent magnetic field is applied which is often (assumed to be) linear. That is the magnetic field depends on position, x, via $H(x) = H(0) + G \cdot x$, where the elements of G, G_{ab}, are the derivatives of the a-th component of the magnetic field with respect to the b-th coordinate, e.g. $G_{zx} = dH_z/dx$. Note that Maxwell's equations require that (in a vacuum) $G_{ab} = G_{ba}$. If one assumes the magnitude of the field due to the gradients is small compared to $H(0)$, then the gradients can also be treated using perturbation theory so that effectively, $H(x) = (H(0) + g \cdot x)2$, where $g = (G_{zx}, G_{zy}, G_{zz})$ is a vector. That is, in the high field case, aside from a possible splitting of the NMR lines by the quadrupole field, the effects of the gradient are the same as those for nuclei with no quadrupole interaction.

Images using the $+\frac{1}{2} \to -\frac{1}{2}$ transition of a quadrupole split NMR spectrum were presented some time ago for the Na signal in Na-β-alumina [5]. The Na resonance in that case was partially motionally narrowed by two-dimensional diffusional motion (the line width was about 1 kHz). Images can also be made using the satellite transitions of a quadrupole split line. The satellites have the potential to be much more sensitive to the presence of defects. An example of an NMR image of a thin crystal of $NaClO_3$ made using one of the Na satellite lines is shown in Figure 1. The sample is rotated from the main magnetic field, also the direction of view, to obtain a large splitting between the satellite line used and other lines present. Orientation would not be so important for pulsed gradient (phase encoded) imaging methods.

Figure 1. Image made using a Na quadrupole satellite line of a thin, square $NaClO_3$ crystal rotated 53° about the horizontal axis.

The transient response to rf pulses of a quadrupole perturbed NMR system in the high field limit also needs to be briefly considered. For simplicity assume that a short rf pulse is applied along the y-axis with a constant amplitude, H_1, over a bandwidth $\Delta\omega$. Two situations are easily discussed: when all of the transitions from a given nucleus have resonant frequencies within the bandwidth, $\Delta\omega$, and when all but one of the transitions are outside the bandwidth.

If all the resonance frequencies are within the bandwidth $\Delta\omega$ the effect of the rf pulse is simply a rotation. On the other hand, in the opposite limit where only one of the many transitions is within $\Delta\omega$ then the problem can be treated in the "fictitious spin-$\frac{1}{2}$" formalism [3,7]. In this case the effective strength of the applied rf field is multiplied by $[I(I+1) - m(m+1)]^{1/2}$ for the observed transition (from m to m+1) and by zero for the others. That is, the pulse length which gives a maximum signal for a given transition will depend on the presence of other transitions within the bandwidth of the rf pulse. These results are summarized nicely by Fukushima and Roeder [7].

For samples which contain the same nucleus in sufficiently different electric field gradients, one can use the different transient response of a split line compared to an unsplit line as a contrast mechanism to distinguish the two

species. This contrast mechanism is unique to nuclei with an electric quadrupole moment. An example of pulse length contrast is shown in Figure 2 which shows a one-dimensional projection (a 1-d image) using the Na signal in the presence of a static field gradient for two different pulse lengths. The sample contains both NaCl which has no quadrupole splitting and $NaClO_3$ which has a modest splitting. Note that the differences in resonant frequencies of the central line between the two materials is small compared to the dipolar linewidths. Even better contrast may be possible by Fourier transforming many measurements made as a function of pulse length, a process described as "nutation spectroscopy" for NQR measurements [8]. The name is appropriate here as well, though the details are actually quite dissimilar. Such measurements may be appropriate to study the change from a cubic (or higher symmetry) environment to an environment with a lower than cubic symmetry.

Figure 2. 1-d projections of Na NMR intensity for a sample, illustrated in the inset, containing NaCl and $NaClO_3$, for two different pulse lengths showing "pulse length contrast."

The Influence of Defects

Associated with any defect is a strain field, the nature of which depends on the particular type of defect, which may be quite long range. In the region of the strain field, the lattice varies significantly from the host lattice and the quadrupole field will reflect this difference.

It is quite difficult to treat the nuclei which are very close to the defect where elastic theory does not apply. However, outside this "core" region elastic theory can be used in a very general way. Estimates of the size of the core region for a dislocation, for example, show it is only a few lattice constants in diameter [9].

Just outside the core region is a region where the quadrupole interaction is large enough to cause shifts which are large compared to the bandwidth of the rf pulse. Outside that region is a region where the shifts are smaller than the bandwidth of the pulse, but still large compared to the NMR line width. Finally, if one is far enough away, the effects are small compared to the NMR line width. To gain an appreciation for the range of the lattice distortion, for a simple single dislocation in NaCl, Na nuclei up to about 100nm from the dislocation can have shifts large compared to their undistorted line width.

An example of an NMR image showing the effects of mechanical damage on a single crystal of NaCl is shown in Figure 3. The sample was struck off center with a drop hammer with the left portion in the figure outside the region of the strike. Further details can be found in Ref [10].


Figure 3. An image of an undamaged (top) and damaged (bottom) NaCl crystal showing loss of intensity for the Na signal in the damaged region.

Relaxation

Though the presence or absence of a quadrupole splitting can have an effect on the spin-spin relaxation time, T_2, by changing "like-nuclei" into "unlike nuclei," the effects on the spin-lattice relaxation time, T_1, can be quite significant. In many materials containing a quadrupole nucleus, T_1 is determined predominantly by the coupling of the nucleus to the fluctuating electric field gradient from its surroundings. Of course if there are large scale motions due to diffusion or rotation, the fluctuating fields are dominated by the large scale motion. But even in simple solids such as the alkali halides, the nuclear quadrupole moment coupling to the changing electric field gradient due to lattice vibrations (phonons) dominates the relaxation.

Except at very low temperatures the relaxation due to phonons is dominated by the second order two phonon (Raman) process. For temperatures above the Debye temperature of the solid, the number of phonons present is proportional to temperature and so the relaxation rate, $1/T_1$, is proportional to the square of the temperature. The temperature dependence of the relaxation time can be used to measure thermal distributions in solids as was shown in Ref. [11] where the changes in the T_1 for the Bromine resonance were used to image a small thermal gradient in a single crystal sample of KBr.

LOW MAGNETIC FIELDS

When the quadrupole interaction is particularly large compared to the applied magnetic field, the magnetic field is treated as the perturbation. It is most useful to express the Hamiltonian in the crystal reference frame

$$\mathcal{H} = A \ (3I^2_{z'} - I^2 + \eta \ (I^2_{x'} - I^2_{y'})) \ +$$

$$\gamma H(\cos\theta \ I_{z'} + \sin\theta\cos\phi \ I_{x'} + \sin\theta\sin\phi \ I_{y'}) \tag{4}$$

where $\eta = (V_{x'x'} - V_{y'y'})/V_{z'z'}$ and the unique set of axis is chosen with $0 \leq \eta \leq 1$, and where θ and ϕ express the orientation of the magnetic field using Euler angles. The first order (degenerate) perturbation theory results are calculated using the eigenvalues and eigenfunctions of the quadrupole coupling. The resulting transition frequencies are complicated functions of orientation and for many cases can be found in Ref. [2].

As discussed for $H = 0$ in Ref [8], the signal amplitude will also be a complicated function of pulse length and the orientation of the rf field relative to the electric field gradient. The method of "nutation spectroscopy" [3] can be used to separate out different orientations of the electric field gradient by measuring the strength of the coupling between the applied rf field and the magnetic dipole moment of the nucleus.

As before, the magnetic field gradient used for imaging is assumed to be linear so that the total magnetic field is $H = H(0) + G \cdot x$. Note that in general if $H(0)$ is small enough both the magnitude and the orientation of H vary significantly with position.

If NMR imaging methods are used in carefully aligned single crystals in which only one electric field gradient tensor is present, standard imaging techniques may be possible. A small uniform (~100g) field might be helpful to separate the transitions.

Many samples of interest are either powders or have multiple electric field gradient tensors. An example is the prototype used for many NQR studies, $NaClO_3$, which has four chlorine atoms per unit cell. The electric field gradient for each has $\eta = 0$ and are oriented along each of the four body diagonals of a cube.

The key is to realize that what is needed is some information about the orientation of the electric quadrupole principal axes and that that information can be acquired using nutation spectroscopy. Using an rf field oriented along an axis one can find (or select) the orientation of the principal axes relative

72

to that laboratory axis. Once the principal axis are known, an image can be formed using a small uniform magnetic field with gradients superimposed. The purpose of the uniform field is to separate lines which move in opposite directions but are otherwise identical and to minimize the changes in θ with position.

References

1. G.D. Watkins and R. V. Pound, Phys. Rev. 89, 658 (1953).
2. T.P. Das and E.L. Hahn, *Solid State Physics, Supplement 1* (Academic Press, New York, 1958), Vol. 1, P. 3ff.
3. A. Abragam, *Principles of Nuclear Magnetism* (Oxford, London, 1961).
4. For example, see G.C. Chingas, J.B. Miller, and A.N. Garroway, J. Magn. Reson. 66, 530 (1986), and references therein.
5. B.H. Suits and D. White, Solid State Commun. 50, 291 (1984).
6. F.D. Feiocle and W.R. Johnson, Phys. Rev. 187, 39 (1969).
7. E. Fukushima and S.B.W. Roeder, *Experimental Pulse NMR*, (Addison-Wesley, MA, 1969).
8. G.S. Harbison, A. Slokenbergs, and T.M. Barbara, J. Chem. Phys 90, 5292 (1989).
9. J.J. Gilman, General Electric Research Laboratory Report 59-RL-2194, 1959.
10. B.H. Suits and J.L. Lutz, J. Appl. Phys. 65, 3728 (1989).
11. B.H. Suits and D. White, J. Appl. Phys. 60, 3772 (1986).

NMR IMAGING OF INDUSTRIAL FLOW PROCESSES.

S. W. SINTON, J. H. IWAMIYA, AND A. W. CHOW
Lockheed Palo Alto Research Laboratory, 3251 Hanover St., Palo Alto, CA 94304

ABSTRACT

The application of nuclear magnetic resonance flow imaging to the study of Poiseuille flows of solid/liquid suspensions is described. The basic imaging method is presented along with results on suspensions with solid particle loading levels up to 52 vol. % and viscosities up to 7 kPoise. The most concentrated suspensions are non-Newtonian, and the NMR flow data show evidence for deviations from a simple parabolic velocity profile in straight pipes. Cross-sectional intensity images derived from the flow image data on concentrated suspensions are non-uniform. Possible explanations for these results are discussed in terms of current rheological understanding of suspension flow and relaxation weighting phenomena in the NMR imaging experiments.

INTRODUCTION

Nuclear magnetic resonance imaging (NMRI) is proving to be a powerful tool for rheological and processing studies of polymers. Because of its unique ability to non-invasively provide spatial mappings of spin density, spin relaxation times, flow velocities, and molecular diffusion - all potentially from the same experiment - NMRI can be effectively used in a variety of situations where information about the composition or distribution of properties in a process stream is desired. Some recent examples are the determination of flow lines and microscopic homogeneity in extruder-processed polymer suspensions [1] and flow velocity imaging of non-Newtonian polymer solutions [2,3] and highly filled solid suspensions [3,4].

In this paper, we describe a study of Poiseuille flow of solid-filled suspensions of varying particle filling levels. Each suspension consisted of a solution of a low-molecular-weight (~12,000 Dalton) polyether oil and plastic spheres on the order of 100 μm in diameter. These materials are designed to mimic some important rheological characteristics encountered in actual processing industries, the most relevant being solid-rocket-motor propellant manufacturing. This paper is primarily concerned with details of the NMRI flow imaging technique and special considerations in data interpretation for suspensions. The physical characterization of the suspensions and the rheological issues addressed by the NMRI experiments are covered elsewhere [3].

EXPERIMENTAL APPROACH

Figure 1 shows the NMR flow-imaging timing sequence used in this work. This sequence is designed to give a 3D image while compensating for the effects of steady-state flow along one direction. The basis of the method was first published by Kose, et al. [5], and the pulse sequence of Figure 1 was later used by Majors, et al. [6]. Application of a selective RF pulse at the same time as a gradient at the start of the sequence excites a slice of magnetization in the stream. The slice plane is perpendicular to the flow direction (Z), and the thickness of the slice is determined by the RF bandwidth and gradient strength in the usual manner. Slice excitation is followed by two broadband π pulses and two Z-gradient pulses which have the effect of refocusing the phases of different isochromats in the sample, regardless of their position or Z velocity. Thus, at 4τ seconds after the selective pulse an echo is detected. Incremented X and Y gradients are used to generate phase encoding in the transverse direction in the usual manner of spin-warp imaging. The RF phase of the last π pulse is toggled between zero and 180 degrees with each phase encode increment to shift any interference from a stimulated echo to the Nyquist edges of the image [6]. Three-dimensional Fourier transformation leads to an image of the slice which has changed shape as a result of flow during the sequence and the distribution of velocities across the pipe. Velocities are computed by measuring Z displacements from the
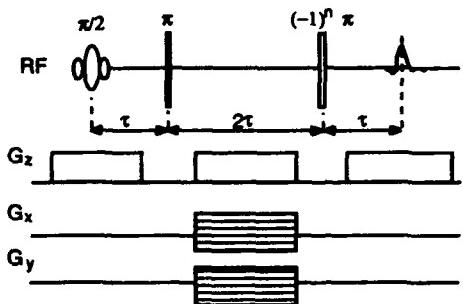
Figure 1. Time-of-flight spin-echo flow imaging pulse sequence

image for each (X,Y) location and dividing by the flight time (4τ). To minimize the effects of noise, displacements in the flow direction are determined by computing the first moment of each Z trace [6].

All NMR data were collected using a Bruker Model MSL spectrometer with a 4.7 T magnet and a large volume "mini-imaging" probe operating at the proton resonance (200 MHz). Gradient switching capabilities are somewhat limited with this equipment, necessitating a fairly long flight time of 30.7 ms. A 6-lobe, sinc-shape RF pulse of 3 ms duration in the presence of a Z gradient of 32 mT/m was used to excite a 3-mm slice across the pipe. Three-dimensional data set dimensions were 32 X 32 X 128 (X,Y,Z) pixels, and 1 to 4 repetitions of each acquisition were averaged to improve signal to noise. The recycle delay to allow for thermal spin equilibration was 600 ms ($3 * T_1$), resulting in acquisition times from 10 to 41 min.

RESULTS

Flow images were collected for a range of flow rates and pipes with inner diameters from 15 mm to 50 mm. The liquid portion of the suspensions studied consisted of a low-molecular-weight polyether oil, water, and sodium iodide (added to match the solution density to that of the suspended particles). Particles were PMMA spheres with median diameter of

131 μm. The particles do not contribute to image intensity since proton spin-spin relaxation of PMMA is very short compared to the flight time in the experiment. Suspensions with particle loading levels from 21% to 52% were imaged, and velocities up to 45 cm/s were measured without difficulty. At low particle concentration these suspensions are Newtonian, while at the highest concentrations they are moderately shear-thinning. Complete rheological characterizations of the suspensions are given elsewhere [3], but for comparison we note here that a 21% suspension has a low-shear viscosity of 400 Poise while the viscosity of a 52% suspension is about 7000 Poise (measured in Couette geometry at a shear rate of 100 s^{-1}).

Figure 2 shows stack plots of the calculated velocity images for two suspensions at different particle concentrations. Figure 3 shows gray-scale renditions of the cross-sectional (XY) intensity formed by summing along the Z direction of the 3D flow image file for the two cases corresponding to Figure 2. Drawn above each image is a trace of pixel intensity along a row passing approximately through the center of each pipe.

A detailed examination of the velocity profile for the 21% suspension in Figure 2 shows it to be parabolic whereas the profile for the 52% suspension is "blunted" (velocities slower in the center than predicted for a parabolic profile which fits the velocities at the outer edge). Likewise, there are remarkable differences in the intensity images of Figure 3. Intensity is relatively uniform across the pipe in the case of the low-concentration suspension while it varies in a smooth fashion, peaking at the center, for the 52% suspension. Results with other suspensions and pipe sizes indicates that this behavior is a function of suspension concentration, pipe diameter, and flow rate [3]. For example, a 40% suspension flowing in a 15-mm pipe gave similar results to the 52% suspension shown in Figures 2 and 3, while the same suspension flowing in a 50-mm pipe at a lower flow rate showed no unusual intensity features and had a parabolic velocity profile.

21% SUSPENSION   52% SUSPENSION
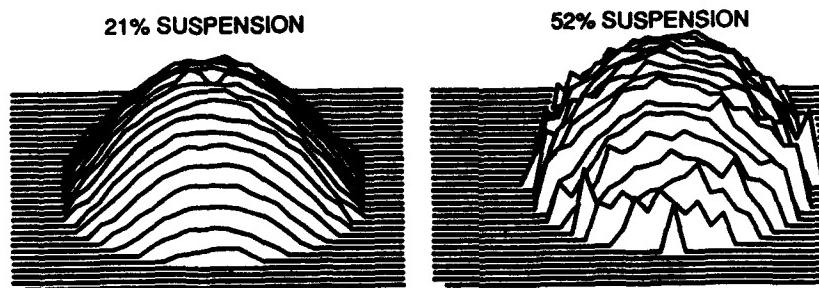
Figure 2. Left: Z velocity image for 21% suspension of PMMA spheres in oil solution. Pipe diameter=25 mm, max velocity=25.9 cm/s. Right: 52% suspension. Pipe diameter=15 mm, max. velocity=29.1 cm/s.

Figure 3. Projections of XY intensity from 3D flow images. Left: 21% suspension. Right: 52% suspension.

Figure 4 is an image of the 52% suspension taken immediately after flow was stopped. The standard spin-warp method with an echo delay of about 10 ms was used to collect this image. The intensity distribution within the pipe is much more uniform in this image than that in the XY image during flow (Fig. 3). (The bright arcs outside the pipe in Figure 4 are features folded over from material clinging to the wall of a larger pipe which was concentric with the flow pipe and outside the image field of view.) Because of the high viscosity of the suspension, it is unlikely that any particle concentration gradients set up during flow would have dissipated through Brownian motion in the time lapse between collecting the flow and static images. Thus, the difference between Figures 3 and 4 for the 52% suspension cannot be explained by differences in particle concentrations.

Possible explanations for the non-uniform intensity pattern for the flowing 52% suspension must involve relaxation weighting of the image. Relaxation weighting due to diffusion effects can be eliminated since the diffusion constants are small ($\sim 10^{-7}$ cm^2/s) and the gradient magnitudes relatively weak. The rate of NMR relaxation for some types of suspensions is in-

Figure 4. XY image of 52% suspension in 15-mm pipe immediately after cessation of flow.

creased due the presence of surface paramagnetic electron sites or reduced motion of molecules in the vicinity of the surface [7,8]. The observed relaxation decay in this case depends on the magnitude of the surface-to-volume ratio, and hence, particle concentration, and the rate of exchange of spins between surface and bulk sites. To assess this possibility, we measured T_2 and T_1 for suspensions with a wide range of particle concentrations. T_1 was found to be insensitive to particle concentration with an average value of around 200 ms. The T_2 decays (measured by the Carr-Purcell-Meiboom-Gill method) had to be fit with a biexponential function for each sample since there was clear evidence for at least two relaxation components. The results are presented graphically in Figure 5. That the base fluid by itself has T_2 relaxation components much less than T_1 is an indication that extreme-narrowing conditions do not apply for this viscous material. The presence of more than one exponential decay component is due to either unresolved chemical shifts or the existence of more than one characteristic correlation time for molecular motion.
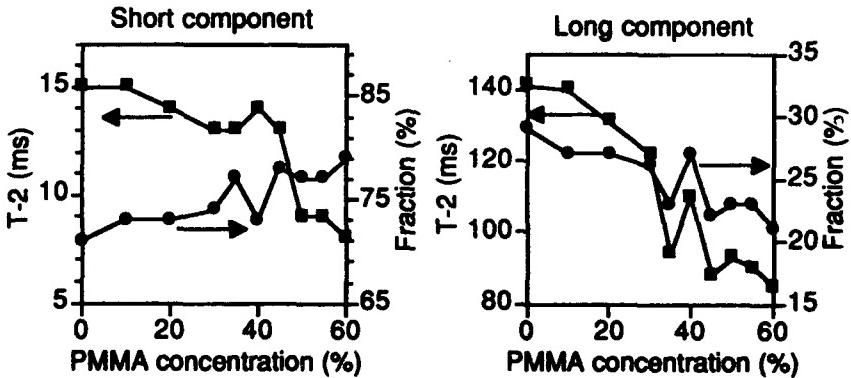
Figure 5. Left: Relaxation times and fraction for short component of biexponential fit to T_2 data. Squares are the relaxation times and circles are the fraction. Right: same for long component.
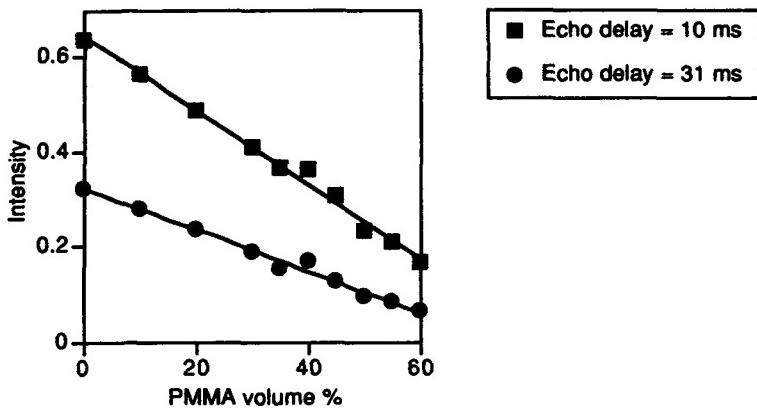
Figure 6. Calculated image intensity versus PMMA concentration. The intensity axis is normalized to 1 for 0% PMMA and an echo delay of 0 seconds.

Figure 5 indicates that there is little change in relaxation times of static samples as concentration increases until about 35% when both the short and long components decrease significantly. The data in Figure 5 was used to calculate the dependence of image intensity on concentration for different echo delays. Figure 6 shows the results for two echo delay times corresponding to our static and flow imaging parameters. In both cases the intensity correlates linearly with particle concentration, and the slopes indicate less variation for the longer echo time. If T_2 decay times are the same in a flowing and stationary suspension, Figure 6 implies that the intensity pattern observed from the longer echo time used in the flow imaging sequence should be similar to that of Figure 4 with only a slight attenuation of the intensity variations. Since this is not what is observed, we deduce that flow must alter T_2 under certain conditions of concentration and shear rate. This statement is supported by other relaxation data not shown here and tests which confirm that the imaging sequences were working correctly in all cases. Our data indicate that above 40% PMMA concentration a non-uniform shear field can result in a non-uniform flow-image intensity pattern.

DISCUSSION

The observed blunting of the velocity profile of concentrated suspensions in Poiseuille flow is consistent with predictions calculated by Leighton [9] based the on the shear-induced particle migration mechanisms proposed by Leighton and Acrivos [10]. Trends in the velocity behavior with particle concentration, particle size, and pipe size are in accord with the predicted parametric dependences [3]. In addition to a blunted profile, theory predicts that particles will migrate along a gradient in shear rate, i.e. from the region of high shear near the wall towards the center of the pipe. The static image of the 52% suspension shows a very slight decrease in intensity in the center of the pipe which, since T_2 weighting has been shown to be relatively insensitive to particle concentration near the nominal concentration, implies a slightly increased particle concentration in the pipe center in agreement with theory.

Intensity in the flow images is more difficult to interpret. At low particle concentration or shear rate, the images appear to faithfully reflect proton density of the fluid component. For higher concentrations in small-diameter pipes, XY image intensity derived from the flow data is non-uniform and seems to follow the velocity profile. We have eliminated several possible explanations and are drawn to the conclusion that there must be some mechanism whereby shear induces a decrease in T_2 for our highly concentrated suspensions. Strain-induced changes in NMR relaxation are known for some crosslinked elastomeric systems and semicrystalline polymers, but those mechanisms are not operative in our suspensions. Nakatani, et al. [11] have recently reported evidence for shear-induced increases in proton NMR relaxation rates in

polymer melts and have proposed a mechanism based on modified averaging of residual direct dipole-dipole coupling constants caused by changes in the average chain conformation in a shear field compared to the at-rest coil configuration. However, their observations were for entangled polymer chains of much higher molecular weight than the polyether oil used in our study.

In the absence of suspended particles and at the shear rates encountered in this study molecular motions in the base fluid would probably not be altered sufficiently to affect NMR relaxation. However, when PMMA particles are present, particle-polymer interactions might become important and their importance would increase in the more concentrated suspensions where the fluid is confined in smaller spaces. Moreover, the effective shear rates applied to the fluid existing between particles can be much higher than the bulk shear rate and extensional-type flow may exist between particles when the average velocities of the two phases are not the same. If present, this extensional flow might alter molecular motion sufficiently to affect T_2. Clearly, more experiments are needed to investigate the possibility of flow-induced relaxation effects in these suspensions and the mechanism for any observed dependence.

ACKNOWLEDGEMENT

REFERENCES

1.   S. W. Sinton, J. C. Crowley, G. A. Lo, D. M. Kalyon, and C. Jacob, "Nuclear Magnetic Resonance Imaging Studies of Mixing in a Twin-Screw Extruder", Proceedings of Soc. Plastic Eng./ANTEC Conf., Dallas, 1990. pp. 116-119.

2.   Y. Xia and P. T. Callaghan, Makromol. Chem., Macromol. Symp. 34, 277 (1990).

3.   S. W. Sinton and A. W. Chow, "NMR Flow Imaging of Fluids and Solid Suspensions in Poiseuille Flow" submitted to J. Rheology and presented at the Soc. of Rheology Meeting, Santa Fe, October, 1990.

4.   S. A.Altobelli, P. D. Majors, E. Fukushima, and R. C. Givler "NMR Measurement of Fluid Concentration in Two-Phase Flows." presented at the Soc. of Rheology Meeting, Santa Fe, October, 1990.

5.   K.Kose, K. Satoh, T. Inouye, and H. Yasuoka, J. Phys. Soc. Japan 54, 81 (1985).

6.   P. D.Majors, R. C. Givler, and E. Fukushima, J. Magn. Reson. 85, 235 (1989).

7.   J. A. Glasel and K. H. Lee, J. Amer. Chem. Soc. 96, 970 (1974).

8.   B. M. Fung and T. W. McGaughy, J. Magn. Reson. 43, 316 (1981).

9.   D. Leighton, "Migration Arising from Gradients in Shear Stress: Particle Distributions in Poiseuille Flow", NASA Conf. Publ. #3006, Mixing and Demixing Processes in Multiphase Flows with Applications to Propulsion Systems, Marshall Space Flight Center, Alabama, 1988.

10.   D. Leighton and A. Acrivos, J. Fluid Mech. 181, 415 (1987).

11.   A. I. Nakatani, M. D. Poliks, and E. T. Samulski, Macromolecules, 23, 2686 (1990).

PART II

X-Ray

NONDESTRUCTIVE IMAGING OF MATERIALS MICROSTRUCTURES USING X-RAY TOMOGRAPHIC MICROSCOPY

J.H. KINNEY*, M.C. NICHOLS**, U.BONSE†,S.R. STOCK††, T.M. BREUNIG††, A. GUVENILIR†† AND R.A. SAROYAN*

*Chemistry and Materials Sciences Department, Lawrence Livermore National Laboratory, Livermore CA 94550
**Sandia National Laboratories, Livermore CA 94550
†Department of Physics, University of Dortmund, Dortmund Germany
††School of Materials Engineering, Georgia Institute of Technology, Atlanta GA 30332

ABSTRACT

A technique for nondestructively imaging microstructures of materials *in situ*, especially a technique capable of delineating the time evolution of chemical changes or damage, will greatly benefit studies of materials processing and failure. X-ray tomographic microscopy (XTM) is a high resolution, three-dimensional inspection method which is capable of imaging composite materials microstructures with a resolution of a few micrometers. Because XTM is nondestructive, it will be possible to examine materials under load or during processing, and obtain three-dimensional images of fiber positions, microcracks, and pores. This will allow direct imaging of microstructural evolution, and will provide time-dependent data for comparison to fracture mechanics and processing models.

INTRODUCTION

The spatial resolution of x-ray CT has been improved by several orders of magnitude during the past decade. It is now possible, using x-ray CT, to three-dimensionally image materials microstructures with a resolution of a few micrometers in millimeter-size samples. Efforts are underway to improve this resolution and, at the same time, to increase the sample dimensions which can be imaged with this technique. Nevertheless, the resolution and sensitivity of x-ray CT are sufficient to make significant inroads into our understanding of how mechanical properties are affected by changes in microstructure. The impact of x-ray CT methods will be especially felt in the study of processing and failure in advanced composite materials. Noninvasive, *in-situ* CT observations of advanced composites will provide time-resolved information regarding the evolution of microstructure—information which currently is only indirectly inferred from *post-mortem* examinations and large statistical sampling of as-prepared material.

This paper provides details about a CT technique we have been developing these past several years. We call this technique x-ray tomographic microscopy (XTM) to distinguish it as a form of x-ray microscopy which utilizes tomographic reconstruction techniques to form three-dimensional images. The paper is presented in three parts. The first part discusses critical issues involved in performing XTM, such as the optimization of the detector and the x-ray energy. The second part discusses

three examples of the application of XTM to imaging fiber composite microstructures. These examples represent progressively more complicated fiber geometries beginning with uniaxially aligned fibers and concluding with woven (balanced plain weave) fibers. The third part discusses our present efforts to perform *in–situ* materials studies, and outlines future directions of research. Throughout this paper, the emphasis is placed on imaging advanced composites which have technological importance. XTM is a powerful technique, however, and its application to other areas such as electronic materials, biomaterials, and geology can be anticipated.

X–RAY TOMOGRAPHIC MICROSCOPY

X–ray tomographic microscopy (XTM) using synchrotron radiation has been shown to be an effective, high–resolution, three dimensional imaging technique for nondestructive characterization of materials [1,2]. XTM differs from conventional optical and electron–beam microscopy in that the sample need not be harmed prior to characterization of internal microstructure. There is no requirement for flat optical surfaces or thin sections; materials are examined in their unaltered state. XTM measures the x–ray attenuation coefficient, μ, at a point $r_{x,y,z}$ in a material from a finite set of x–ray attenuation measurements (projection data) taken at different angles through the sample. The projection data is the transmitted x–ray intensity reaching a position sensitive detector after passing through the sample. The absorption data is directly related to the materials microstructure, and is given, for a single point on the detector, by

$$I = \int S(E)[\exp{-\int \mu(x,y,z,E)dl}\ ]\ dE,\tag{1}$$

where $S(E)$ is the energy spectrum of the x–ray source and $\mu(x,y,z,E)$ is the energy dependent attenuation coefficient at a single point along the projection. The integral is taken along a straight path dl through the sample. If the x–rays are made nearly monochromatic with photon energy E_0, the energy spectrum can be approximated by a delta function and Equation 1 reduces to the familiar form of the Radon transform [3]:

$$\ln\left(\frac{I_0}{I}\right) = \int \mu(x,y,z,E_0)dl\ .\tag{2}$$

Measurements of the attenuation through the sample as a function of angle and position are used to numerically invert Equation 2 to solve for $\mu(x,y,z,E_0)$. The number of angular views considered sufficient for this inversion (reconstruction) is approximated using simple geometric arguments by

$$R\Delta\Theta = W\tag{3}$$

where R is the maximum outward extent of the sample from the center of rotation, $\Delta\Theta$ is the suggested angular increment and W is the projection width. A typical value for R with the present XTM is 2 mm and W is 5 μm. The angular increment sufficient for the reconstruction using these dimensions is approximately 0.2 degrees, although increments of 0.5 degrees are generally used in practice.

Conventional CT measurements involve collecting absorption information for a single cross-sectional slice through a material. Spatial resolution is achieved either by collimating the incident beam using a pinhole, and then rastering the beam across the sample for every angular setting, or by using a position sensitive detector to measure all of the projection data for a single angular view in parallel. Aside from its relative simplicity, the advantage of the pinhole technique is that the resolution, to first order, is determined only by the size of the collimator. Elliott and Dover have successfully used pinhole scanning with a standard x-ray generator to perform tomography on mineralized tissues [4] and composites [5]. An energy dispersive detector is used to count photons of only a single energy, thereby satisfying the requirement for nearly monochromatic radiation.

The primary disadvantage using the pinhole is that most of the incident radiation is thrown away. The rastering technique, therefore, is extremely time consuming. Acquiring the data for the reconstruction of a single cross section of a sample takes upwards of 12 or more hours depending on the size of the pinhole collimator and the sample. This limits the utilization of the pinhole approach for three-dimensional analysis and precludes real time studies.

Linear photodiode arrays have been used in a number of CT devices designed to operate on conventional x-ray sources [6,7]. The widespread application of linear photodiode arrays results from both their ease of use and ability to acquire upwards of a thousand projected rays simultaneously. The parallel acquisition of data improves the speed of the measurements nearly a thousandfold, and the accumulation of enough data to reconstruct a single slice becomes measured in minutes rather than days. In spite of these advantages, however, there are drawbacks to the use of the photodiode array for ultrahigh resolution characterization. The first of these drawbacks is that the photodiode array is noisy and is subject to nonlinearities. This noise limits the dynamic range and therefore the maximum contrast which can be studied in a sample. The nonlinearities introduce ring-like artifacts in the reconstructions which can further reduce the usefulness of the information obtained, although these effects can be partially reduced by using a combination translate-rotate design. Finally, even with reducing the data acquisition times for a single slice from days to hours, it still requires days to obtain enough information for three-dimensional sample visualization.

Clearly, a two-dimensional array which records projection data for many contiguous slices simultaneously is essential for practical three-dimensional imaging [8]. Feldkamp uses a vidicon array as a two-dimensional detector [9]. Because a vidicon is continuously read out at video rates, the integration times are too short to detect an x-ray image using a laboratory x-ray source. Therefore, Feldkamp relies on an image intensifier which converts the x-ray photons into visible photons and then amplifies the light signal by orders of magnitude. Because image intensifiers have relatively low spatial resolution, it is necessary to use a microfocus source in a magnifying geometry, and a "cone-beam" algorithm is necessary to reconstruct the three-dimensional image from the x-ray projection data[10]. CT systems run in this manner are limited in spatial resolution by the source spot size (~20-25 μm), and in sensitivity by the photon statistics and linearity of the image intensifier. Good photon statistics are difficult to

achieve because signal averaging with vidicons is limited by excessive read-out noise. Nevertheless, the image intensifier with vidicon detector has been adopted by others [11], and images of 20–30 μm resolution have been demonstrated when imaging high contrast features.

Our group has developed an XTM instrument which uses a thermoelectrically–cooled charge coupled device detector (CCD) in place of a vidicon array [12]. The CCD provides superior spatial resolution and noise properties, and can be integrated over time periods of several minutes with little buildup of dark current noise. Because of this, imaging can be performed without the complications and image degradation of an intensifier. Furthermore, the detecting system we have configured can be operated successfully using standard focus x–ray tubes as well as microfocus sources and synchrotron radiation. With the standard focus source, the sample is placed in close proximity to the scintillator to minimize the penumbral blurring due to the diverging beam. In this configuration, a parallel beam reconstruction algorithm is used. With a microfocus source, the sample can be placed much closer to the source in order to take advantage of an x–ray magnifying geometry using a cone–beam reconstruction algorithm. Since its development, XTM using CCD arrays has been successfully tested using synchrotron radiation at the Stanford Synchrotron Radiation Laboratory 13,14], at the DORIS storage ring at the Hamburg Synchrotron Radiation Laboratory [15], at the National Synchrotron Light Source [16], at the Cornell High Energy Synchrotron Source (CHESS), and most recently using laboratory x–ray sources.

The sample positioning hardware currently consists of translation stages, a rotary stage, and the stage controllers and driver electronics. The hardware now in use is from Klinger Scientific. All stages have stepper drive motors, incremental position encoders and an origin signal. The linear stages also have plus– and minus– limit signals. The stage controller provides both user and computer interfaces to up to eight separate stages. The user interface consists of front panel displays of position with a separate button for each axis. Also, there are front panel buttons which allow the user to independently position each axis or to home each axis to its origin position. The computer interface, as it is used here, is an IEEE–488 port, through which the controller can accept commands from a computer telling it how and where to position the eight axes and through which it can report back to the computer its success or failure at executing the commands.

In operation, the sample is removed from the beam with a linear translation stage. A reference image ($I_0(x,y)$ in Eq. 1) is recorded and the sample is moved back into the beam. A radiograph of the sample is taken ($I(x,y)$ in Eq. 1), and the image data are stored in the computer memory. This procedure is incrementally repeated until a full 180 degrees of sample rotation has been recorded. The reason for the reference images is to monitor the incident beam profile. For a very stable source, the frequency at which reference images are taken can be reduced.

A single crystal scintillator screen converts x–rays into visible light which is imaged with the CCD. Initially, the scintillator consisted of ball-milled sub-micron particles of phosphor. The phosphor layer was thin with respect to the optical path length, and suspended on a glass substrate with a transparent binder. Though great care was taken in fabricating the phosphor, the spatial resolution was no better than 20 μm because of optical

scatter caused by differences in the indices of refraction between the phosphor and the binder, and between the binder and the substrate.

In the present configuration, we use a single crystal $CdWO_4$ scintillator. $CdWO_4$ is not hygroscopic and has a very high x-ray stopping power. Optical scatter off of the free surface is minimized by using an anti-reflective coating. Measurements using synchrotron radiation sources at 20 keV indicate that the spatial resolution of the scintillator is better than 5 μm.

The resolution of a single crystal scintillator is not perfect, however. First, x-rays have a finite depth of penetration, and this depth increases with increasing energy. Second, secondary events such as fluorescence, photoelectron production and scatter act to blur the image within the scintillator. The first effect, a finite depth of penetration, reduces the image contrast. The secondary effects reduce the resolution. Unfortunately, both of these problems increase with increasing energy, and are related to each other by the modulation transfer function, MTF, of the system.

Figure 1 shows the depth of x-ray penetration in $CdWO_4$ as a function of incident x-ray energy. The depth has been calculated as the path length over which 90% of the scintillation events occur. As x-ray energy rises above 20 keV, the penetration becomes significant, and the loss of subtle contrast variations in a sample becomes unavoidable. Also plotted in Fig. 1 is the depth of x-ray penetration in CsI, a widely used scintillator material.

Two approaches have been developed to improve the resolution of scintillator screens. The first approach is to decrease the thickness of the scintillator. The second approach is to segment the scintillator into very small optically isolated pieces[17,18]. In this manner, light produced by x-ray absorption is confined to a single region of the scintillator. Making the scintillator thinner reduces the amount of contrast loss, but greatly decreases
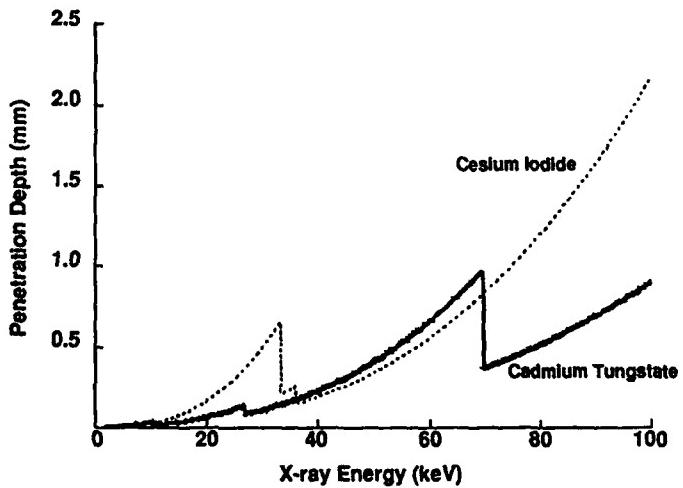
Figure 1:   X-ray penetration depth (90% absorption) in single crystal scintillators.

the light output of the scintillator. Segmentation, on the other hand, offers the advantage that as the x-ray energy increases, the scintillator can be made thicker, thereby allowing more efficient use of the x-ray flux. The difficulty of segmentation lies in fabricating very small elements and in keeping them optically isolated. Exxon has had some success in growing 1μm columns of CsI crystals for a high resolution scintillator. Though the isolated columns are 1 μm and less in diameter and roughly 1 μm apart, a careful examination of Exxon's published radiographs indicates that the spatial resolution is not as high as the segmentation would lead us to believe. Though it is difficult to speculate on the cause for this poorer than expected performance, two possibilities are worth considering. The first possibility is that the scintillator face plate (the substrate upon which the CsI is grown) has a different index of refraction than the CsI, thereby leading to optical scatter. The second possibility is that the individual segments of the scintillator are not isolated from secondary x-ray effects.

X-ray scatter (defined here as including all secondary processes) may be the ultimate limiting factor in the resolution of scintillator screens. At the x-ray energies considered here (< 100 keV), an x-ray photon can either be absorbed or scattered. In high Z materials the incoherent scattering probability is small at these energies; hence, the predominant interaction is through absorption. When an x-ray photon is absorbed, the excited atom can decay by emitting fluorescent radiation. The fluorescent radiation is emitted into a 4π solid angle, and can travel for considerable distances before being absorbed. This fluorescent radiation creates additional scintillation events which can be far removed from the original photon path. Also, the absorption of x-rays leads to the production of energetic photoelectrons. The energy of the photoelectron is given by $E_e = h\nu - \phi_b$, where ϕ_b is the binding energy of the electron and $h\nu$ is the energy of the absorbed x-ray. The photoelectrons are sufficiently energetic to travel for considerable distances in the scintillator, creating scintillation events all along their path. Each of these events lead to a loss of spatial resolution and an increase in noise.

We have calculated the effects on resolution due to secondary events in $CdWO_4$ as a function of x-ray energy using the Monte Carlo code COG [19]. COG follows all primary and subsequent generations of photons until they are either absorbed or leave the scintillator. Photoelectric processes and incoherent and coherent scattering processes are considered in the calculations. The results of these calculations suggest that the largest contributor to secondary scintillation events is the emission of photoelectrons during the stopping of the x-rays.

The photoelectron range depends strongly on the incident x-ray energy. Photoelectrons have much greater penetration in CsI than in $CdWO_4$, principally because the electron binding energy increases with Z and the photoelectron range decreases with increasing density. The large range of the photoelectrons in CsI (>1 μm) makes it impossible to isolate scintillator segments on the micron scale. It is important to note, however, that the spatial resolution of the scintillator is optimal immediately above an absorption edge where the depth of x-ray penetration and photoelectron energy are at their lowest.

Though laboratory x-ray sources can be used for XTM, synchrotron radiation is the optimal source. Synchrotron radiation provides a broad

Though laboratory x–ray sources can be used for XTM, synchrotron radiation is the optimal source. Synchrotron radiation provides a broad banded source of x–rays which range in energy from a few eV to several tens of keV. Because synchrotron radiation can be continuously tuned using a single crystal monochromator, it is possible to select the optimum x–ray energy for the sample being characterized. Frequently, it is desired to choose an x–ray energy which optimizes the *signal–to–noise for the sample*. The optimum energy is given by the well known relationship

$$D = \frac{2}{\mu} \qquad (4)$$

Figure 2 shows the optimum sample diameter, D, as a function of x–ray energy for three important classes of materials used in composite manufacture: aluminum, silicon carbide, and titanium aluminide. Also depicted in Fig. 2 are the energy intervals which can reasonably be spanned with present and proposed synchrotron radiation sources. Test panels of metal matrix composites are typically 1.5mm thick. Assuming that the aspect ratio of a rectangular gauge *tensile specimen should be at least three* to one, then the largest dimension through the gauge section will be about 5mm. In ceramic matrix composite (CMC) specimens, for example Nicalon fibers (Nicalon is an amorphous SiC fiber) in a SiC matrix, the panel thickness is typically 3mm, giving a largest dimension through the gauge of approximately 10mm.

Using Fig. 2, the optimal x–ray energy for imaging Al–matrix material will be 27 keV, for imaging SiC material will be 37 keV and for imaging higher Z intermetallics such as Ti_3Al will be 52 keV. Although the National Synchrotron Light Source (NSLS) does not provide adequate x–ray flux at
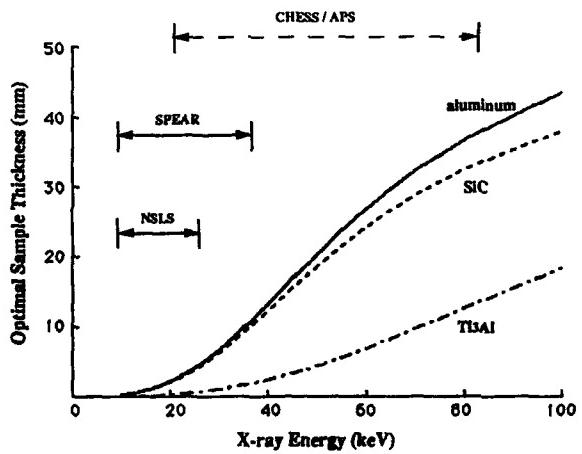
Figure 2: The optimal x–ray energy for imaging typical composite materials as a fuction of thickness.

88
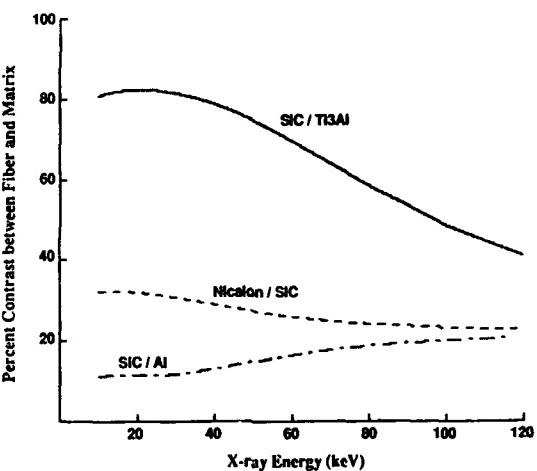
Figure 3: X–ray contrasts ($100 \times |\mu_f - \mu_m|/\mu_m$) between fiber and matrix for three typical composite systems.

the high energies required for penetrating composites with these gauge sections, the hard x–ray wiggler beamline on the SPEAR storage ring at Stanford is well suited for imaging the CMCs as well as the aluminum–based composites. For the more absorbing intermetallic composites, it will be necessary to use the wiggler beamlines at Cornell which can provide the required flux at high energies. The proposed Advanced Photon Source (APS) will also be well suited to imaging materials microstructures of the intermetallic composites.

In an x–ray image, contrast between features arises from differences in the x–ray attenuation coefficient. High contrast features occur when cracks and high Z or high density inclusions are present in the sample. Weak contrasts result from slight variations in material composition. Figure 3 represents the contrast between matrix and fiber as a function of x–ray energy for three cases: 1) SiC–fiber (SCS8) in an Al matrix, 2) Nicalon fiber in a SiC matrix, and 3) SiC–fiber (SCS6) in a titanium–aluminide matrix. The contrast between SiC and Al is only 10% over a broad energy range. Therefore, distinguishing the fiber from the matrix in this composite system requires excellent photon statistics. The higher contrast between SiC and CAS, on the other hand, relaxes the statistical constraints somewhat. The contrast is highest between the SiC an_ the intermetallic Ti_3Al. At low x–ray energy, the contrast is as high as 80%. Thus, in this composite system, the fibers are clearly identified in the presence of noise. However, the high contrast poses another problem; namely, it becomes difficult to distinguish broken fibers from voids and pores!

EXAMPLES

We consider three examples of the application of XTM to imaging composite microstructures. These examples have been chosen to represent progressively more complicated fiber geometries. All of the data were

acquired during a run at the Cornell High Energy Synchrotron Source (CHESS) using the 6–pole wiggler end station on beamline A2. Silicon monochromator crystals were used, with (111),(311), and (400) reflections chosen to cover the x-ray energy range from 20 to 60 keV used in the experiments.

The first example is that of an aluminum matrix—SCS8 silicon carbide fiber composite. SCS8 fibers consist of a 32-μm diameter carbon core surrounded by an approximately 140-μm diameter SiC sheath. An approximately 1-μm thick carbon coating is deposited onto the fiber to protect it from detrimental chemical reactions with the matrix phase during consolidation. The composite is approximately 1.5 mm thick and consists of 8 plies of uniaxially aligned fibers. The composite has failed in tension, and XTM was performed from the fracture surface down about 2 mm along the long axis of the composite. The pixel sampling size was 5.6 μm, and 0.5 degree angular increments were used. The x-ray energy was 20 keV.

Figure 4 shows an XTM slice taken in the vicinity of the fracture surface. It is important to emphasize that the cross section is taken through bulk material, and that no surface preparation was necessary. Hence, none of the artifacts frequently associated with polishing, such as fiber pull-out, need to be considered when interpreting the XTM image. The image in Fig. 4, therefore, is of the undisturbed region beneath and bordering the fracture surface. In Fig. 4 it is observed that the fibers have apparently failed at the graphite core–SiC interface in the fiber interiors, and not at the fiber–matrix interphase as we had expected. The impact of these observations on our understanding of mechanical failure in this composite system is presented in more detail later in these proceedings[20].

Figure 4: XTM image beneath the fracture surface in a SiC fiber / Al matrix composite failed in tension. Significant plastic deformation of the matrix is observed, as is the fracture behavior of the fibers (arrows marked A). Examination of the fiber fractures indicate that failure occured at the graphite core and not at the SiC/Al interphase.

The second example is a 1.5 mm CAS (calcium aluminum silicate) matrix—SCS6 fiber composite[21]. The fibers are arranged in a 0/90 cross-ply stacking sequence. Absorption data were acquired at 0.5 degree angular increments using an x-ray energy of 20 keV. The pixel sampling size was 5.6-μm, and 250 contiguous slices were imaged. Figure 5a is an XTM micrograph taken 0.9 mm beneath the surface of the composite panel at 50X magnification. Figure 5b is the corresponding SEM micrograph showing the same location. The SEM photomicrograph was obtained subsequent to the XTM examination by sectioning.

It is of interest to compare the two observations. The XTM image shows a crack running from left to right across the specimen approximately 12 μm (.0005") above a 90° fiber. This same crack is also observed in the optical micrograph. SEM examination of this crack reveals it to be less than 1.5 μm (.00004") across along its entire length. Even though the pixel sampling size is 5.6 μm, the high contrast provided by the crack makes it possible to image features much smaller. This is an important point: spatial resolution and feature detectability are not the same, and pixel size as a measure of system performance is a meaningless concept unless it is related to the overall resolution of all of the individual components in the system.

In addition to the crack, a small piece of broken fiber can be seen in both the XTM and the optical images. This broken fiber fragment lies between the second and third fiber plies from the top of the image. Broken pieces of fiber may act as stress concentrators for initiating cracks, and therefore, it is important to be able to detect these low contrast flaws.

Figure 5a: XTM micrograph of a CAS matrix/SCS6 fiber 0/90 composite. Arrows marked A highlight a microcrack running across the width of the sample. This crack is 1.5 μm at its widest extent. Arrow marked B shows a broken fiber fragment lodged between fiber plies. Arrow marked C shows another microcrack in the composite.
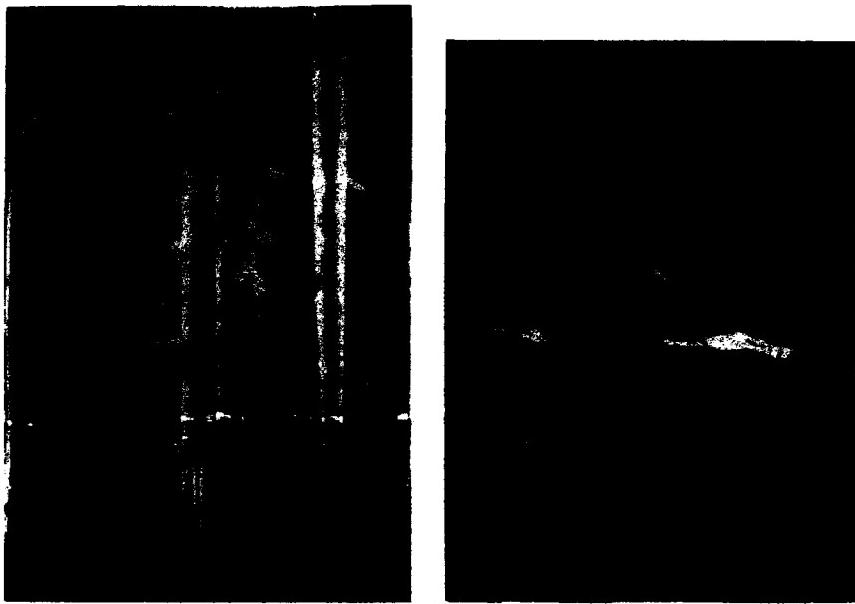
Figure 5b: SEM photomicrograph showing the CAS composite described in Fig. 5a. This
              SEM micrograph was obtained after sectioning the sample to the same slice
              plane as the XTM image. The SEM shows the same crack (marked with arrow
              A) as displayed in the XTM image. In addition, the SEM image shows the crack
              continuing across a fiber ply (arrow B). This crack extension was not seen in
              the XTM image, and therefore we believe it to be a result of stress relief upon
              polishing. On the right side of 5b is a high magnification image (5000X) of the
              crack imaged by the XTM, indicating that it is less than 1.5μm.

The final example is a SiC matrix—Nicalon fiber (amorphous SiC)
composite. The Nicalon fibers vary in diameter from 10–20 μm. The fibers
are organized into bundles called tows (containing approximately 500 fibers),
and these tows are in turn woven into a cross–ply cloth. The fiber
cloth is formed into a near net shape component, and then a SiC matrix is
grown around the fibers by infiltrating a reactive gas mixture at high
temperature[22]. Several types of porosity can be left behind from the
chemical vapor infiltration (CVI) process. The porosity is generally broken
down, however, into two types: microporosity, consisting of pores within a
tow, and macroporosity, consisting of any type of porosity lying outside of
the tow. The type, size and interconnectedness of the porosity directly
influence the permeability of the chemical vapor into the composite. The
pores may also act as nucleation sites for cracks. Because of the geometric
complexity of this type of composite, a three–dimensional imaging technique
has a great advantage over two–dimensional techniques in studying the
origin of pores, their interconnectedness, and their subsequent influence on
mechanical properties.
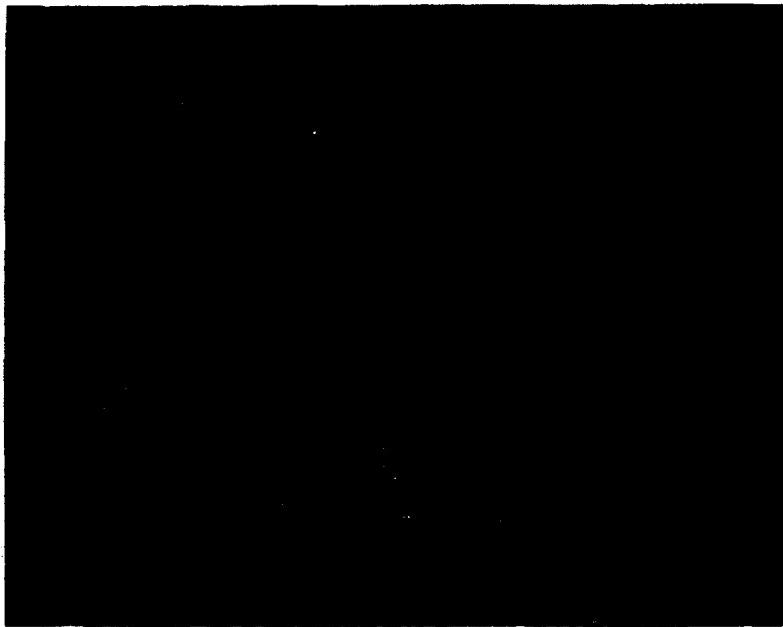
Figure 6: XTM image of a Nicalon fiber/SiC woven composite. The fully–dense SiC is marked with arrow A. A fiber tow oriented perpendicular to the cross section is marked with arrow B. A fiber tow oriented in the plane of the cross section is marked with arrow C. Individual fibers (arrow D) can be seen in the tow peripheries. Also resolved are macropores (arrow E) and micropores (arrow F).

Figure 6 is an XTM image of a fully reacted SiC–Nicalon woven composite. This preliminary study was designed to determine whether or not XTM can image micro– and macroporosity, and also whether the present contrast sensitivity and spatial resolution of the technique is adequate for imaging the fiber tows in the SiC matrix. The XTM image in Fig. 6 clearly distinguishes between the Nicalon and SiC, and shows both types of porosity. Near the peripheries of the tow, it is possible to identify individual fibers (10–20 μm). The magnification will need to be increased to resolve individual fibers in the tow interiors.

FUTURE DIRECTIONS

It is highly unlikely that XTM will ever achieve the spatial resolution of SEM. XTM's principal advantage, an extremely important advantage, lies in its noninvasive, three-dimensional capability. Coupling XTM to other, more destructive techniques, will greatly expand our understanding of the time-evolution of materials microstructures. In order for XTM to realize this potential, however, in-situ inspection capabilities must be developed. These capabilities will include tensile load cells and high temperature stages.

We have recently tested a prototype load frame which allows XTM studies to be performed on samples while they are under tensile load[23]. In its prototype configuration, the load frame rests upon a single rotational stage—the load from the grips being suppoted by a semi–transparent x-ray window. Though the x-ray window alters the DC value of the XTM images due to incomplete normalization of the reference beam, we have demonstrated an ability to open up and image cracks using this cell up to 42ksi tensile load. It is important to note that vibration and drift in the sample position must be kept below a micrometer during the XTM measurements.

Figure 7 shows the load frame configured for use with a conventional x-ray generator. At the right in Figure 7 are shown longitudinal and transverse XTM sections through the notched region of an Al–Li alloy under 42ksi tensile load. The opened crack is easily visualized, whereas at 0 ksi load the crack is nearly invisible. The noise in the image is due to un–normalized absorption in the x-ray window. A second generation load cell is now being designed which will eliminate the x–ray window.
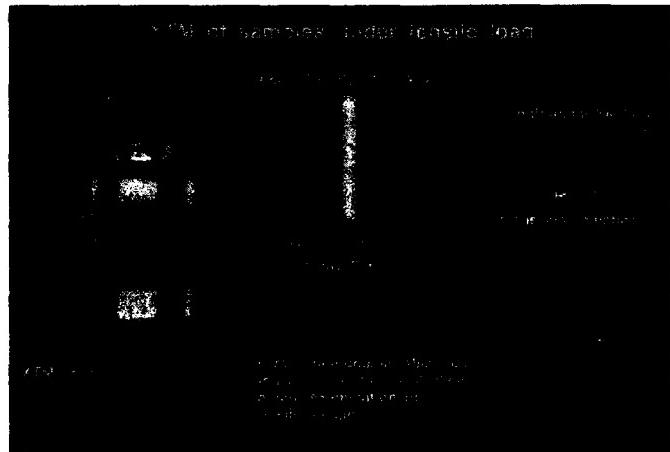
Figure 7:   *In–situ* load frame for perfoming XTM on samples under tensile load.

In addition to *in–situ* load frames, it will be necessary to image larger samples with at least the same spatial resolution, if not better, as that which we have already demonstrated. In the present XTM design, and in all commercially available systems, the sample is constrained to always remain within the field of view of the detector during rotation. The CCD detector used for these examples has approximately 1000 pixels (detector elements) across the field of view. This allows us to image a 1 cm wide sample with an equivalent 10 μm pixel. With a recently acquired 2k x 2k element CCD array, the same sample can be imaged using 5 μm pixels. An obvious approach is to obtain larger format CCDs as they become available. This approach is impractical, however, because the cost of these CCDs is high, and the availability is low. In addition, the data storage requirements become enormous with increasing format.

Two other options exist for increasing the sample size with the present XTM design. The first is to use translate–rotate geometries. In this manner, the sample is translated across the field of view. This method requires multiple exposures and an extremely tight tolerance on pixel registration. Though greatly increasing the acquisition time, the translate–rotate method will allow imaging larger samples with small format CCDs. However, data storage requirements will remain large using this method.

An alternative approach, and the one which we are pursuing, is the region of interest (ROI) method. Using the ROI method, the entire sample is no longer constrained to remain within the field of view; rather, only a region of interest needs to remain within view during rotation. We have been making progress with the ROI method, and success with the method has now been obtained with artificial data. Application of the ROI method to actual experimental data is now being undertaken.

CONCLUSIONS

We have described an x–ray tomographic microscope which has sufficient resolution and contrast sensitivity to provide valuable microstructural information on engineering materials. The microscope can operate using both conventional and synchrotron sources of radiation. The approach to x–ray microscopy outlined in this paper differs from other efforts in that we are developing the technique to image small features in large samples at high x–ray energy.

X–ray tomographic microscopy is beginning to be applied to materials science studies of composite materials. Efforts are underway to use XTM in studies of fatigue and failure in metal matrix composites and also to study chemical vapor infiltration of ceramic composites. Furthermore, a recently developed tensile loading frame has been used in initial studies of crack closure in high strength Al alloys[23].

The application of XTM to materials studies has only just begun. The use of XTM with other imaging modalities, for example ultrasound, MRI, and electron microscopy, promises to greatly improve our understanding of processing and failure in advanced materials.

ACKNOWLEDGEMENTS

REFERENCES

1. J.H. Kinney, et al., J. Mat. Res., 5, 1123 (1990).
2. U.Bonse, et al., accepted for publication in J. Mat. Science, (1990).
3. G.T. Herman, *Image Reconstruction from Projections: The Fundamentals of Computerized Tomography* (Academic Press, New York, 1980).
4. J.C. Elliott and S.D. Dover, J. Microscopy 126, 211 (1982).
5. S.R. Stock, A. Guvenilir, J.C. Elliott, P. Anderson, S.D. Dover and D.K. Bowen, in *Advanced Characterization Techniques for Ceramics* (American Ceramic Society, Westervill, Ohio, in press).
6. F.H. Seguin, P.Burstein, P.J. Bjorkholm, F. Homburger, and R.A. Adams, Appl. Opt. 24, 4117 (1985).
7. M.K. Cueman, L.J. Thomas, C. Trzaskos, and C. Greskovich, in *Review of Progress in Quantitative Nondestructive Evaluation*, D.O. Thompson and Dale E. Chimenti, eds. (Plenum Press, New York, 1989), Vol. 8A. p. 431.
8. U.Bonse, Q.Johnson, M.Nichols, R. Nusshardt, S. Krasnicki and J. Kinney, Nucl. Instrum. Methods A246, 644 (1986).
9. L. A. Feldkamp, G. Jesion, and D.J. Kubinski,in *Review of Progress in Quantitative Nondestructive Evaluation*, D.O. Thompson and Dale E. Chimenti, eds. (Plenum Press, New York, 1989), Vol. 8A., 381.
10. L.A. Feldkamp, L.C. Davis, and J.W. Kress, J. Opt. Soc. A1, 612 (1984).
11. H.E. Martz, S.G. Azevedo, J.M. Brase, K.E. Waltjen and D.J. Schneberk, Int. Jour. of Radiation Applications and Instrumentation Part A (UCRL - 98492 Livermore Report) to be published 1990.
12. J. Kinney, Q.Johnson, U.Bonse, R. Nusshardt,andM.C. Nichols, SPIE 691, 43 (1986).
13. J.H. Kinney, Q.C. Johnson, R.A. Saroyan, M.C. Nichols, U.Bonse, R. Nusshardt and R. Pahl, Rev. Sci. Instrum. 59, 196 (1988).
14. M.C. Nichols, et al. , Rev. Sci. Instrum. 60, 2475 (1989).
15. U.Bonse, et al., Rev. Sci. Instrum. 60, 2478 (1989).
16. B.P. Flannery, H.Deckman, W. Roberge, and K. D'Amico, Science 237, 1439 (1987).
17. H.W. Deckman, K.L. D'Amico, J.H. Dunsuir, B.P. Flannery and S.M. Gruner, in *Advances in X-ray Analysis* 32, 641 (Plenum Press, New York 1989).
18. M. Ito, M. Yamaguchi, K. Oba, and S.-Kanzo,IEEE Transactions on Nuclear Science NS-34, 401 (1987).
19. T.P. Wilcox, Jr. and E. M. Lent, in *COG- A Particle Transport Code Designed to Solve the Boltzmann Equation for Deep-Penetration Problems*, M-221-1 (Lawrence Livermore National Laboratory, Livermore California 1989).
20. T.M. Breunig, S.R. Stock, J.H. Kinney, A. Guvenilir, and M.C. Nichols, presented at the MRS Fall Meeting, Boston, November 1990 (to be published in these proceedings).
21. Sample provided by D. Copley, GE Aircraft Engines, Cincinnati,OH.
22. T.L. Starr, Ceramic Engineering and Science Proceedings, 8, 951 (1987).
23. T.M. Breunig, S.R. Stock, S.D. Antolovich, J.Kinney,W. Massey and M.C. Nichols, Proceedings of the 22nd National Symposium on Fracture Mechanics, June 1990, Atlanta GA (to be published in a STP by ASTM).

DEVELOPMENT OF QUANTITATIVE X-RAY MICROTOMOGRAPHY

H. W. Deckman, J. H. Dunsmuir, K. L. D'Amico, S. R. Ferguson, B. P. Flannery
Corporate Research Laboratory, Exxon Research and Engineering Co.,
Rt. 22 East Annandale, NJ 08801

ABSTRACT

We have developed several x-ray microtomography systems which function as quantitative three dimensional x-ray microscopes. In this paper we describe the evolutionary path followed from making the first high resolution experimental microscopes to later generations which can be routinely used for investigating materials. Developing the instrumentation for reliable quantitative x-ray microscopy using synchrotron and laboratory based x-ray sources has led to other imaging modalities for obtaining temporal and spatial two dimensional information.

Introduction

X-Ray tomography is a non-invasive imaging technique which produces maps of the internal structure of samples. It was first discovered [1] and developed [2-3] in the early 1970's and was originally employed as a medical diagnostic tool [4]. In medical applications [5], computed axial tomographic scanners map bone and tissue sections of human patients with .5-1 mm resolution on an image plane which usually contains fewer than 512 x 512 pixels. Several different protocols for acquiring the data in medical CAT scanners have evolved [4,5], however the attainable resolution is limited near .25 mm due to dose limitations to human patients and the physical detector design. Medical CAT scanning technology was extended to other applications by several groups in the late 1970's [5,6], resulting in devices which obtained ~50 μm resolution in planar crossectional images. Higher resolution planar scanners (obtaining ~5 μm resolution) were also produced [7] using a protocol which traded increased resolution for a several hundred fold decrease in throughput.

With the advent of intense high brightness synchrotron sources, the potential existed [8] to extend the technology with a plane parallel data acquisition protocol and develop a practical x-ray tomographic system which functions as a three dimensional x-ray microscope. X-ray flux available from a bending magnet beamline on the synchrotron in principle allows a millimeter sized sample to be scanned with micron resolution in less than 5 minutes. To capture this potential required innovations in the areas of ; (1) algorithms for reconstructing .1-1 gigabyte data sets, (2) computer graphics to display the enormous amount of reconstructed data, (3) x-ray detector technology to obtain quantitative micron resolution images, and (4) beamline x-ray optics to stably illuminate samples with a high flux x-ray beam. Since 1984 we have had an ongoing program which addressed all these issues and in 1986 [9] we obtained our first three dimensional micron resolution images. Since that time we have been working to evolve the prototype microscope into one which is a microscope for experiments rather than an experimental microscope. This has involved, (1) integrating advances in computer technology to speed up data reconstruction and display, (2) creating an improved detector which incorporates automatic alignment procedures, (3) constructing dedicated laboratory and synchrotron based x-ray sources and (4) developing user friendly menu driven software that controls data acquisition and reconstruction. In this paper we will review the evolutionary path of our microtomography program. Other groups have also been working on several of these issues [10,11] and describe their results in this volume.

Development Of Synchrotron and Laboratory X-Ray Sources

Principle attributes desired in x-ray sources for microtomography are ; (1) high flux levels in a narrow energy range, (2) nearly parallel collimation, and beam stability in position and intensity. Flux levels required for an accuracy , σ_F / F , in the reconstructed map of linear attenuation coefficients, F , in the target are given by

$$Flux \approx \frac{N\sqrt{2}\,n}{S\ A} \approx \frac{\omega^2\ e^\tau \sqrt{2}\ n}{\mathcal{D}\tau\,(\,\sigma_F\,/F\,)^2\ S\ \delta^2} \qquad \text{Eq. 1}$$

where , N, is the number of x-ray photons per pixel incident in a single view of the sample; A, is the area of each pixel; S, is the the live time for the scan during which the sample is actually exposed by x-rays; $\tau = \{\,F\ \cdot\ \text{Sample Size}\,\}$ is the optical density through the target; ω, is a noise amplification factor introduced by the reconstruction process [12]; n, is the number of pixels in the image spanned by the sample; δ, is the physical dimension of a pixel in the image, $\mathcal{D}$ is the detective quantum efficiency of the x-ray detector which is ~.5 for our detector [13]. In an optimal observational strategy [12], the x-ray energy is matched to the target so that optical depth through the target is τ=2. and the required flux is minimized. Under these conditions, the flux required for obtaining σ_F /F = .05 (5% accuracy) in the reconstruction with a relatively short live scan time, S, of 10 minutes is shown in Figure 1 below as a function of the number of pixels, n, and pixel's size, δ. A 5% accuracy in the reconstructed map of linear attenuation coefficients gives acceptable image quality for many materials. Inspecting Figure 1 it is seen that high resolution large format images have extremely demanding source requirements.
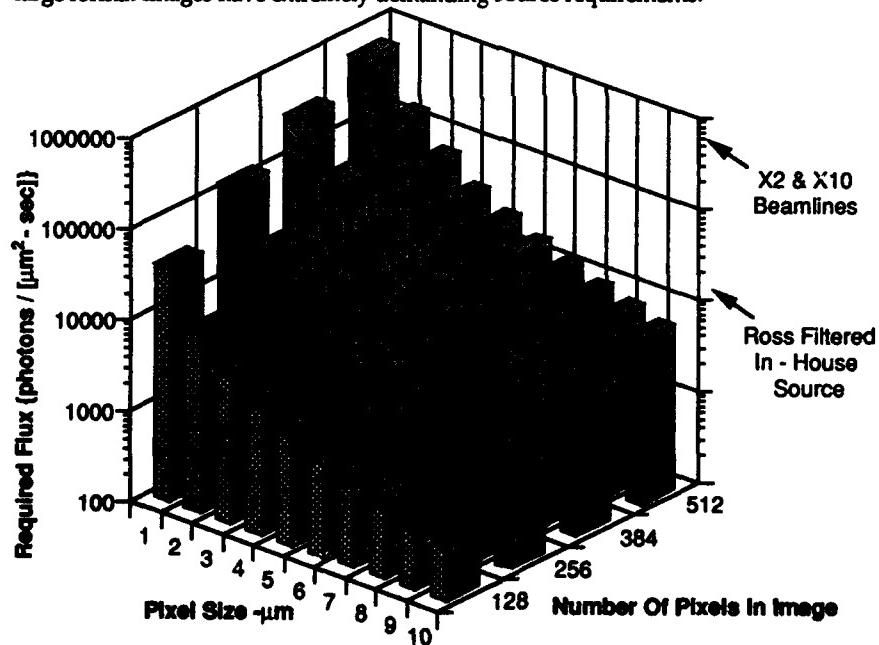
Figure 1. Plot of the x-ray flux required to obtain 5% accuracy in the reconstructed map of attenuation coefficients under optimal observational conditions in a 10 minute (live time) scan. Also shown are characteristic fluxes obtained with our available sources.

To deliver high fluxes needed for high resolution large format operation, we originally used Exxon's beamline X-10A at the National Synchrotron Light Source. Some of the key optical components in this beamline are shown in Figure 2 below. Fluxes as high as ~10^6 x-rays / (μm^2-sec) can be obtained with a 150 mA synchrotron beam current when the mirror located ~10 m along the line is focussed to relay a direct image of the bending magnet radiation to the sample. The focussed spot has a roughly Gaussian intensity profile with a width of less than ~400 μm which does not fully illuminate samples scanned with micron scale resolution. To fully illuminate samples, the beam was defocused to a ~1000 μm spot size with an average intensity of ~10^5 x-rays / (μm^2-sec). In initial operation, fluctuations in the position and intensity of the beam over the exposure period produced an unanticipated problem. Because the mirror delivers an image of a beam with Gaussian intensity profile, variations as small as ~250 Å in the position of the x-ray beam could lead to errors in detector calibration and artifacts in the reconstructed images. Changes in the beam position were due primarily to variations in the orbit of the synchrotron beam and thermally induced deformations of the mirror and monochromator. Often these variations were uncorrectable and ~33% of the data sets had to be rejected. Another ~33% of the data sets taken had severe ring artifacts due to uncorrectable calibration errors.

To overcome this problem and obtain reliable stable uniform high flux sample illumination, a new beamline was designed and constructed. The new beamline (X2) does not form an image of the source with a long working distance mirror, but rather has optical elements closely coupled to the sample. A white beam is brought from the synchrotron to within ~1 meter of the sample where it can be processed with a variety of optical elements and provide a uniform sample illumination over area greater than 6 mm . Figure 3 shows a schematic diagram of two different configurations of the X2 beamline. In one configuration (Figure 3A), a silicon monochromator provides a narrow bandpass. Higher harmonics (λ/N) reflected from the silicon monochromator are rejected with a flat grazing incidence x-ray mirror. A wider bandpass is obtained by using a multilayer monochromator which can be inserted in place of the silicon monochromator. Figure 3B shows the X2 beamline configured to operate at ~20 keV energies with the multilayer monochromator. At ~20 keV, the grazing incidence x-ray mirror is not needed to reject higher harmonics (λ/N) because of the relative absence of photons of these energies in the synchrotron spectrum. Fluxes of ~.5 · 10^6 x-ray photons /(μm^2-sec) can be obtained in a ~50 ev bandpass. This flux allows rapid large format high resolution scans of sample as quantitatively shown in Figure 1.
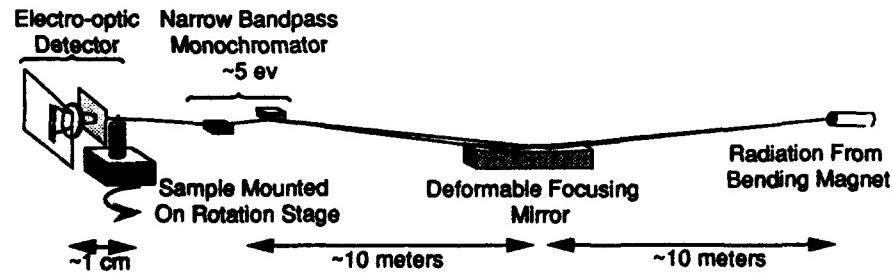
Figure 2. Schematic diagram of initial x-ray tomography experiment on beamline X-10A at the National Synchrotron Light Source. The detector is shown with a scale factor which is different from the rest of the drawing.

A) <u>X2 Beamline Optical Layout: Narrow Bandpass / Low Energy Configuration</u>

Focusing Silicon
Monochromator

White Beam
From
Synchrotron

θ

2θ

λ λ/N

λ

Grazing Incidence X-Ray Mirror
(.5 m Long)
(5 Å RMS Roughness)

Specimen
And
Rotation
Table

High
Resolution
Imaging
X-ray
Detector
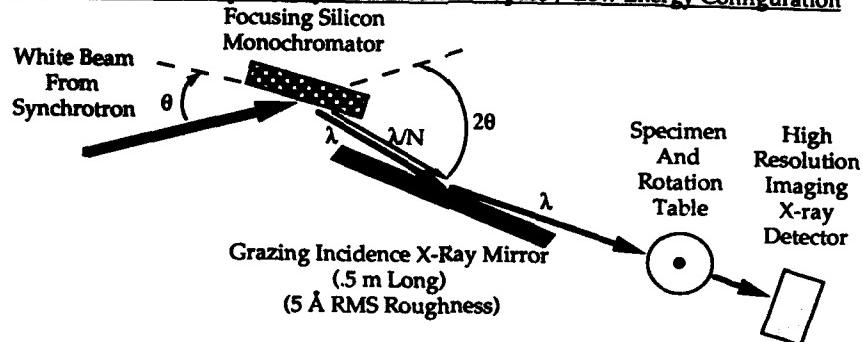
B) <u>X2 Beamline Optical Layout: ~50 ev Bandpass / High Energy Configuration</u>

White Beam
From
Synchrotron

θ

2θ

Multilayer
Monochromator

λ

~1 meter

~1 cm
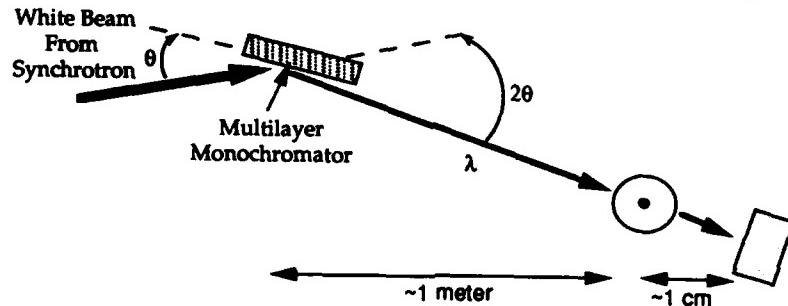
Figure 3.   Schematic diagram of two configurations   for x-ray tomography
experiments on beamline X-2. The configuration shown at the top
(Figure 3A) provides a ~8 ev bandpass while the configuration shown at
the bottom (Figure 3B) provides a ~20 ev bandpass. The sample rotation
stage and detector are represented with a scale factor different from the
rest of the drawing.

Laboratory based x-ray sources do not have the flux of synchrotron sources,
however they provide significantly better convenience and source stability.   As a
convenient in-house laboratory source we have been using a 3 kw Phillips x-ray
generator configured with commercial Cu, and Mo fine focus x-ray tubes commonly
used in x-ray diffraction experiments. The long fine focus tube produces a .4 x 12 mm
x-ray spot which is viewed at a 4 degree takeoff angle yielding an apparent .4 x .8 mm
source size. Even though radiation diverges from this source, plane parallel sample
illumination conditions can be attained by moving the sample far back from the source
[13].   For example plane parallel data acquisition protocols can be attained for
millimeter sized samples placed 30 cm from the source scanned at 2.5μm resolution.
This type of laboratory source cannot be directly used for quantitative x-ray
tomography because of polychromatic bremsstrahlung radiation which is emitted
along with characteristic line spectra.   To eliminate this problem a crystal
monochromator can be attached to the x-ray tube, however, it reduces the effective
flux of the line radiation at the sample by more than a factor of ten. We have adopted

a different technique which reduces x-ray flux at the sample by less than a factor of ~two but doubles the amount of data needed to reconstruct a sample. Quantitative data is obtained by digitally processing sequential scans of the sample with different filters imposed in the x-ray beam. The filters used are balanced using a technique described by Ross, [14] so that the digital subtraction of the two data sets results in an *effectively monochromatic* data set. Details of the application of the Ross balanced filtering technique to quantitative tomography are described elsewhere [15]. With this bandpass technique, the ~2 ev wide K line from copper can be isolated with an effective flux in the subtracted data set of ~.01 10^6 [x-rays/μm^2 -sec] as is indicated in Figure 1.

Development Of High Resolution Elector-Optic X-Ray Detectors

At the heart of the microtomography device is a detector that digitally records panoramic X-ray images with up to ~1μm resolution, and high accuracy over large dynamic range. Using electro-optic x-ray detector technology we have constructed two different generations of detectors which meet microtomographic resolution and accuracy requirements.

Electro-optic x-ray detectors function by converting the x-ray signal to an optical image which can be detected with a wide variety of TV sensors such as videcons, orthocons, charge injection devices (CID), and charge coupled devices (CCD). Both generations of electro-optic detectors were constructed to take advantage of the properties of cryogenically cooled solid state CCD sensors, which in recent years [16] have evolved to become the preeminent imaging electro-optic sensor technology . At cryogenic temperatures (-140 °C - -75 °C) a CCD is a nearly quantum limited device and each optical photon absorbed in a pixel is converted to an electron that is stored in a charge packet held in a silicon chip by fields from an electrode structure that defines a two dimensional array of pixels. The chip is read out by passing the charge packets in bucket brigade fashion from pixel to pixel to an onboard charge sensitive FET preamplifier. Only a small amount of noise is added in the CCD sensor because a double correlated sampling technique is used to read the charge in the preamplifier [17]. CCD sensors used in our detectors have a readout noise that is equivalent to less than 40 electrons per pixel and a dark noise that adds a signal less than 5 electrons per pixel per minute. The CCD's also have a dynamic range (saturation signal / RMS readout noise) which is greater than ~10^5 and a readout which is linear to better than .5% over the full dynamic range. Both generations of detectors use back illuminated CCD's which were manufactured by RCA . The first generation device had 320 x 512 defect free ~25 μm sized square pixels that could integrate up to ~800,000 electrons per pixel before saturating. The second generation device uses a sensor made with a 2X design rule and contains 640 x 1024 ~12.5 μm sized pixels that could integrate ~160,000 electrons per pixel before saturating.

Since pixel sizes in the CCD sensors do not match the desired 1 - 10 μm image resolution, the x-ray image format must be altered before it can be recorded by the CCD. Several different techniques have been used to alter image formats in electro-optic x-ray detectors and we have shown [18] that a carefully designed optical lens can be used for format alteration in demanding quantitative imaging applications. Lens coupled format alteration is used in both generations of electro-optic detectors and Figure 4 shows a schematic diagram of key elements in the detectors.

When a lens is used to couple the x-ray induced luminescence of a phosphor screen to a CCD sensor, careful optical engineering must be performed. Attention must be paid not only to the overall modulation transfer function of the system but also to the overall light gathering efficiency of the lens. If the light gathering efficiency of the lens is too large, the attainable accuracy in a single exposure will be dramatically reduced.
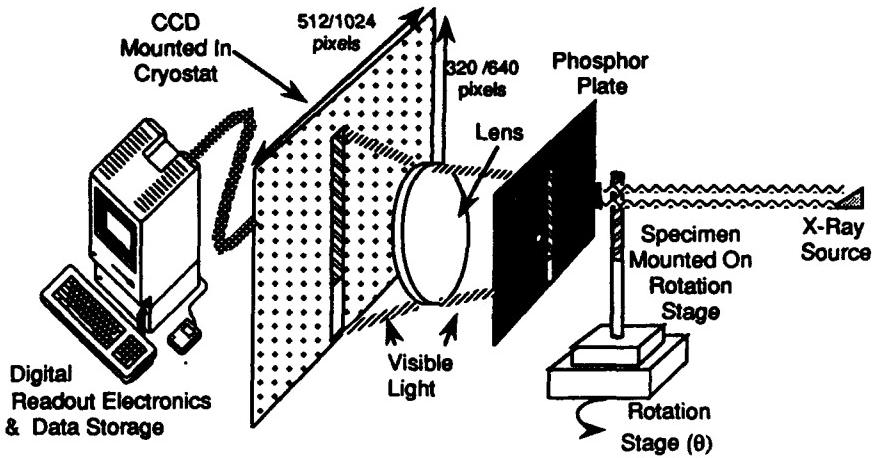
Figure 4.   Schematic diagram of the key elements in the electro-optic detector and
their relationship to the specimen and x-ray source

To quantify importance of properly tuning the lens light gathering efficiency, we
consider the detected accuracy or uncertainty, ρ , which is related to the detected
quantum efficiency, $\mathcal{D}$, for each pixel by

$$\rho = \frac{1}{\sqrt{\mathcal{D}N}}$$ Eq. 2

where N, is the number of photons per pixel incident on the detector.   The detected
quantum efficiency, $\mathcal{D}$, for a lens coupled electro-optic x-ray detector [18] is given by,

$$\mathcal{D} \approx \left[\frac{1}{t} + \frac{1}{t\ \varepsilon_p L_{\bullet}}\left(1+\frac{1}{\varepsilon_c}\right) + \frac{1}{N}\left(\frac{Q_n}{t\ \varepsilon_p L_{\bullet}\ \varepsilon_c}\right)^2 \right]^{-1}$$ Eq. 3

where $L_{\bullet}$ is the light gathering efficiency of the lens, ε_p is the number of optical
photons emitted by the phosphor for each absorbed x-ray, t is the absorption
probability of an x-ray in the phosphor, Q_n is the readout noise of the CCD
and ε_c =.8 is the overall quantum efficiency of the CCD.   The maximum number of
x-ray photons, which can be integrated by the detector is

$$N_{max} = \frac{h\ W}{t\ \varepsilon_p\ L_{\bullet}\ \varepsilon_c}$$ Eq. 4

where W is the number of electrons that saturate the CCD well and h is the
usable fraction of W which is typically 2/3.   Inspecting equations 2,3 and 4, it is
seen that for a phosphor which efficiently absorbs x-rays (t >.8) coupled with a low
readout noise CCD (Q_n <50 electrons), the attainable accuracy in a single exposure
depends primarily on the usable CCD well depth, $h\ W$, and the number of photons
per x-ray relayed from the phosphor to the CCD, $\varepsilon_p\ L_{\bullet}$. The best attainable single
exposure accuracies are plotted in Figure 5 as a function of the usable CCD well depth
and number of photons per x-ray relayed by the lens to the CCD. For large format
tomographic reconstructions (512 x 512 pixels) there is a large noise amplification (ω
~12.5) and the X-ray image must be recorded with better than .2-4% accuracy so that
the amplified noise in the reconstructed image is less than 5 - 10%.
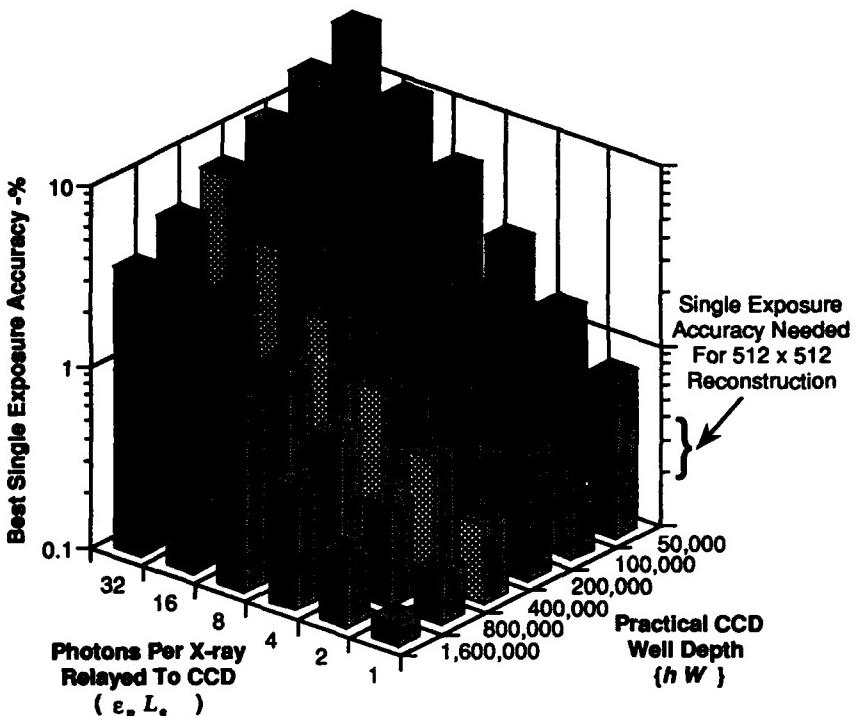
Figure 5. Plot of accuracy attainable in a single exposure for a phosphor which efficiently stops x-rays (t = .8) coupled by a lens to a CCD having a quantum efficiency of ε_c =.8.

Inspecting Figure 5, is is seen that even when the usable CCD well depth is greater than 200,000 electrons, fewer than 2 optical photons per x-ray can be relayed to the CCD by the lens if attainable single exposure accuracy has to be less than the ~.4% needed for large format tomography. Most phosphors have quantum efficiencies of .5-5% [18] and generate ~50-500 photons per absorbed hard (~10 keV) x-ray. To limit the number of x-rays arriving at the CCD, the light gathering efficiencies of most lens systems have to be restricted. A simple field aperture can be used to restrict the light gathering efficiency of many lenses. Averaging less accurate multiple exposures with more light per x-ray reaching the CCD is currently not viable. Most of the time in tomographic data acquisition is spent waiting for the CCD to be read out. Charge transfer considerations limit quantitative readout rates of CCD's to ~1-10 μsec per pixel. Operating with multiple exposures would significantly increase this overhead which consumes ~70-90% of the scan time. Future generations of CCD devices with multiple readout ports and other advances may eventually alter this situation, however presently the CCD readout rate limits scanner performance and data at each view angle must be acquired from single exposures.

Besides being able to measure the x-ray flux to an accuracy of better than .4%, stringent resolution requirements must be met by the lens coupled electro-optic x-ray detector. Usually it is difficult to achieve spatial resolutions in the micron range with

104

Phosphor Plugs
Deposited In
Cellular Matrix

Cell Lined
With Optical
Isolation Coating

Cellular Matrix
(Micron Sized Cells)
(> 100,000,000 Cells)

Cut Away View Of
X-Ray Transparent
Protective Hermetic
Overcoat On Phosphor
Screen
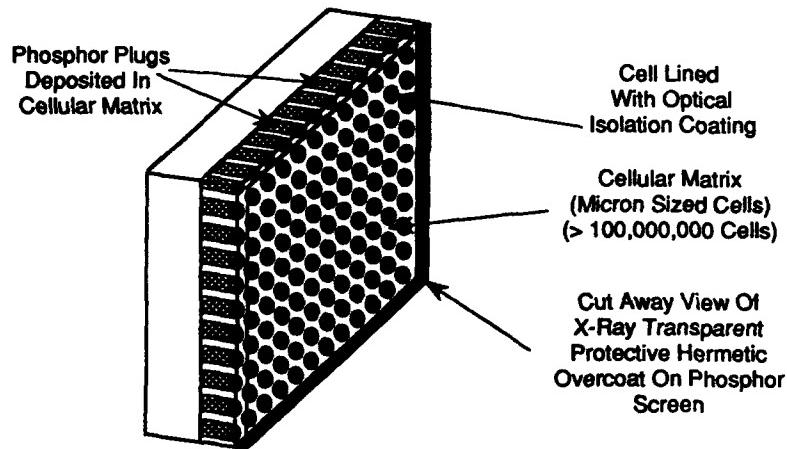
Figure 6. Schematic diagram of cellular phosphor used in first generation
electro-optic x-ray detector

lens coupled electro-optic detectors. Resolution is usually degraded by spreading of
light through the phosphor and lens so that the signal at each pixel is in part due to
x-rays incident on different pixels. To overcome this limitation, the first generation
detector used a novel cellular phosphor structure which is shown schematically in
Figure 6 above. The cellular phosphor screens were lithographically produced and
contained more than 100,000,000 optically isolated uniform sized CsI phosphor
columns having ~10:1 aspect ratios. The high aspect ratio CsI phosphor columns
stopped ~80% of ~8 keV x-rays entering each cell and acted as an optical
waveguide for the emitted optical photons. Waveguiding of light in the cell was
facilitated by gold and gold/palladium coatings sputter coated onto the cell wall.
Several different phosphor screens having cell sizes ranging from ~.5-3 µm were
produced by a variety of techniques which have been described in detail elsewhere
[19]. All fabrication procedures yielded relatively efficient phosphors because cell
walls that occluded less than 50% of the surface area. The lithographic fabrication
procedures only yielded defect free phosphor filled cell structures over a small
(5-10%) fraction of the screen. Screens were scanned for good areas before being
used for tomographic data acquisition. Even in good areas there were slight spatial
variations in the quantum efficiency of the cellular phosphor. The variations were
due to differences in cell sizes and depth of phosphor in the cells. Typically the
maximum variation of the quantum efficiency amongst cells in the screen was less
than 15%. Figure 7 shows an example of the type of spatial quantum efficiency
variations which can occur with lithographically fabricated cellular phosphors.
This type of spatial variation quantum efficiency can be tolerated if the x-ray source
is spatially uniform and is stable over the course of a tomographic scan, however
even slight positional or intensity changes in the x-ray source will lead to a ring
artifact in the reconstructed tomographic data set.

To overcome problems with ring artifacts appearing in reconstructed data sets, a
different phosphor has been used with the second generation detector. A flat
phosphor plate free from optical defects is integrated directly with a specially

Ratio Cal/Exp   Projection Image
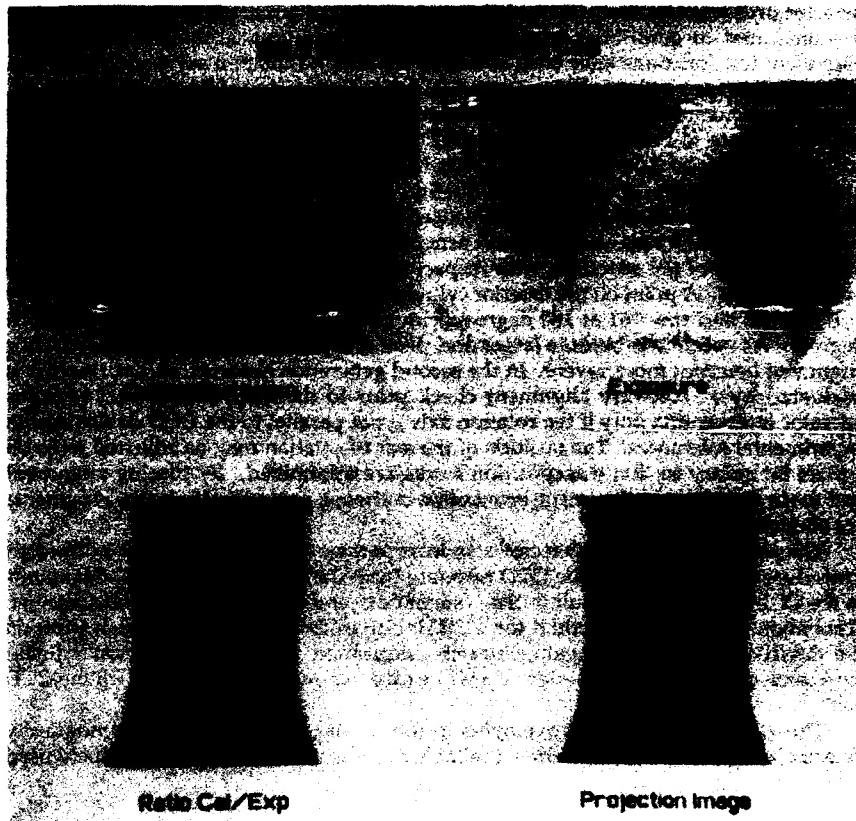
Figure 7. Example of raw and processed data taken with high spatial resolution
cellular phosphor used in first generation electro-optic detector. Spatial
variation of phosphor screen quantum efficiency can be clearly seen in the
calibration exposure and image through the sample. The fixed pattern
variations are removed by ratioing the calibration and sample
measurements. Also the inhomogeneous detector response is absent in
the projection (ln of the ratio) used for reconstruction.

designed lens. In designing this system care must be taken to avoid scattered light and
to minimize the effects from light generated out of the focal plane of the lens. Light is
generated out of the depth of field of the lens because x-rays are stopped over a ~10 μm
distance and micron resolution lens systems have a significantly smaller depth of field.
The optical engineering of this flat phosphor and lens system will be described
elsewhere [20].

Besides changes to the phosphor, lens and CCD, the second generation detector
incorporated several mechanical changes which improved the system reliability and
statistical accuracy. A redesigned CCD mounting in the cryostat and related imaging
optics provided substantially improved mechanical stability so that mechanical

detector drift was less than ~50 Å. Mechanical drift in the first generation camera was demonstrated to contribute to ring artifacts. In addition, autofocus and critical alignment test functions have been added to the data acquisition software. To obtain critically focussed images, focus control is automated and rapidly produces images focussed to quantitative criteria. The optical relay requires the image formed on the phosphor plate to be focussed on the CCD. Images that appear sharp may not be critically focussed. The resulting defocus MTF (Modulation Transfer Function) can have a detrimental effect on data quality. In a system test, contrast reversed reconstruction was obtainable from defocused images of a periodic test target.

Since the CCD forms an orthogonal array of detectors, slight misalignments in the axis of rotation of the specimen with respect to the CCD array results in errors in the projection data. A point on the exterior cylindrical specimen may appear in a row 160 at 0 degrees and row 161 at 180 degrees with an axis alignment error of less than .5 degrees. As specimens become larger and pixel arrays smaller, the sensitivity to this alignment becomes more severe. In the second generation detector, axis of rotation is evaluated by a software alignment check prior to data acquisition and requires operator intervention only if the rotation axis is not parallel to the CCD device within experimental tolerances. The position of the axis of rotation may be adjusted to lie on a pixel boundary so that transposition errors are minimized. By placing alignment and focus functions in the image acquisition software, subjective operator judgments are eliminated.

The second generation detector also incorporates an improved CCD calibration procedure to better remove the CCD response from the input signal. Small deviations in the CCD response can result in the systematic over / under estimation of specimen absorption. The revised method for CCD device calibration evaluates each pixel on the device for dark count, gain, linearity, saturation and noise based on a linear regression of each pixel in a series of a white card exposures that partially fill the CCD well.

The aforementioned improvements in the second generation microtomography detector x-ray sources have created a reliable microscope which can be routinely used to scan samples.

Development Of Data Reconstruction Algorithms And Display Software

To practice microtomography on even moderately sized samples requires a tremendous amount of computational analysis. For example, a cubic millimeter sized sample imaged at one micron resolution requires a gigabyte data set. Typically we analyze slightly smaller data sets containing .1 gigabytes. To handle this large amount of data we have developed [9,21] image reconstruction methods that are far more rapid than the conventional Filtered Back Projection methods. Our technique, called Direct Fourier Inversion has been developed specifically for data collected using the plane parallel acquisition protocol employed in the microtomography system. The technique provides an implementation of the fundamental theorem of tomography which states that the Fourier transforms of the sample and projection measurements are identical. The implementation adds two steps of padding the data set with zeros and appropriately filtering the transforms to successfully reconstruct complex targets. On relatively fast array processing computers, the technique reduces the amount of time needed to process data sets from ~ 1 month to hours. Typically the reconstructed maps of the sample consist of three hundred planar sections each containing 512 x 512 pixels.

Besides developing algorithms for reconstruction, techniques had to be perfected to visualize the enormous data sets. In our first generation system we were only able

to display individual planar images from the reconstructed data sets. More recently we employed computer graphic techniques which allow us more fully visualize three dimensional reconstructions. These computer graphic techniques are described elsewhere [22] and allow cube tool sliced viewing of the three dimensional structure, display of hidden surfaces within samples, and transparency rendering of phases within samples. Examples of the display of surfaces within sample reconstructions are shown in Figures 8 and 9 below as well as Figure 10 on the next page. An example of a cubetool rendering is shown in Figure 11. These visualization techniques can often be performed in real time.
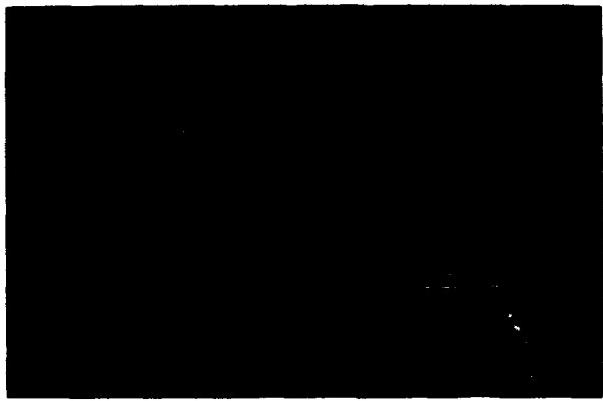
Figure 8.   Visualization of the interior and exterior surfaces of ~3 mm sized hollow aluminum shells provided by the Vanderbilt Microgravity Center. Surfaces were determined from 512 x 512 x 320 data sets taken at ~6 μm per pixel.

Figure 9.   Visualization of the surfaces of wires running inside ceramic packaging provided by IBM Research . The wire surfaces in the interior of the ceramic and are exposed by processing of the 512 x 512 x 320 data set taken at ~6 μm per pixel. Details of this investigation will be published elsewhere [23].

Figure 10. Visualization of surface inside a 1.5 mm piece of Berea sandstone. Sample was reconstructed on a 512 x 512 x320 mesh at 3 μm per pixel.

Figure 11. Rendering of the interior structure of a the piece of Berea sandstone shown above using cubetool. White regions are mineral matter, black regions are pores and gray areas are sand grains.

Discussions And Conclusions

This paper has reviewed the evolution of several key technological developments that led to creation of a reliable microtomography instrument. Currently the instrument can be routinely and reliably used as a three dimensional microscope in materials investigations. During the course of the development of this three dimensional x-ray microscope, a number of applications were implemented which utilize its ability to acquire quantitative microradiographic images. The ability to rapidly collect quantitative high resolution images of x-ray attenuation has allowed us to study dynamic changes in samples and rapidly map composition and porosity of samples. Dynamic changes, such a mapping flow patterns in porous materials, are typically studied using a digital subtraction radiography process. To visualize flow patterns, a radiographic image of the sample is subtracted from sequential images taken with fluid invading the pore structure. Similarly porosity can be mapped by subtracting radiographic images taken before and after the introduction of a suitable x-ray attenuating fluid into the pore network.

We have been applying the microtomography technique to study the structure of a variety of rocks, minerals, coals, catalysts and engineered materials. Samples can be scanned with monochromatic synchrotron radiation at .75 - 3 μm per pixel in less than 2 hours and reconstructed on a 512 x 512 x 320 grid in a similar amount of time. Scans times and reconstruction times as short as 10 minutes can be achieved when samples are scanned at the synchrotron on a 128 x 128 x 80 grid of 6 micron sized voxels. Currently scans covering a 1024 x 1024 x 640 grid represent the largest number of voxels which can be reconstructed and displayed. At this level of detail, samples can be scanned in less than 10 hours at .75 microns per pixel.

In the future, we expect to see microtomography applied to an increasing variety of subjects including those in materials science, biology and medicine.

References

1. G. N. Hounsfield, Br. J. Radiol. 46, 1016 (1973).
2. L. Shepp and B. F. Logan, IEEE Trans. Nucl. Sci. 21, 21 (1974).
3. R. M. Merseraeu and A. V. Oppenheim, Proc. IEEE 62,1319 (1974).
4. C. C. Jaffee, American Scientist, 70, 576 (1982).
5. W. Swindell, H. H. Barrett: Physics Today 30, 32 (1977).
6. L. A. Feldkamp, L. C. Davis, and J. Kress, J. Opt. Soc. Am. A1, 612 (1984)
7. G. T. Hermann, Image Reconstruction From Projections: The Foundations Of Computerized Tomography (Academic Press, New York, 1980).
8. L. Grodzins, Nucl. Instrum. Methods 206, 541 (1983).
9. B. P. Flannery, H. W. Deckman, W. G. Roberge, and K. L. D'Amico, Science 237,1389 (1987).
10. J. H. Kinney, Q. C. Johnson, R. A. Saroynan, M. C. Nichols, U. Bonse, R. Nusshardt, and R. Pahl, Rev. Sci. Instrum. 59, 196 (1988).
11. J. H. Kinney et. al., Applied Optics, 25, 4583 (1986).
12. B. P. Flannery,H. W. Deckman, P. M. Eisenberger, W. G. Roberge, U. S. Patent 4,833,698 (1989).
13. H. W. Deckman, K. L. D'Amico, J. H. Dunsmuir, B. P. Flannery and Sol M. Gruner, Advances In X-Ray Analysis 32, 641 (1988).
14. P. A. Ross, Phys. Rev. 28, 425(1926).
15. J. H. Dunsmuir (to be published)
16. Sol. M. Gruner, J. R. Milch, and G. T. Reynolds , Nucl. Instrum. Methods, 195, 287 (1982).
17. J. L. Lowrence, P Zucchino, G. Renda, and D. C. Long, Adv. Elect. Phys. 52, 441 (1979).
18. H. W. Deckman, B. Flannery, J. Dunsmuir, K. D'Amico, Proceedings Of The 46th Electron Microscopy Society Of America, 988 (1988).
19. H. W. Deckman, J. H. Dunsmuir, and Sol M. Gruner , J. Vac. Sci. Technol. B7, 1832 (1989).
20. J. Dunsmuir (to be published)
21. B. Flannery and W. Roberge U. S. Patent 4,907,129 (1990)
22. S. Ferguson and B. Flannery (to be published)
23. Jean Marc Halbout, G. B. Stephenson , K. L. D'Amico, J. H. Dunsmuir, H. W. Deckman, S. R. Ferguson, B. P. Flannery (to be published)

DETECTION OF FREE LIQUID IN CEMENT-SOLIDIFIED RADIOACTIVE WASTE DRUMS USING COMPUTED TOMOGRAPHY

J.S. STEUDE* AND P.D. TONNER
ARACOR, 425 Lakeside Drive, Sunnyvale, CA 94086

*now at Stone & Webster Engineering Corporation, PO Box 550, Richland, WA 99352

ABSTRACT

Acceptance criteria for disposal of radioactive waste drums require that the cement-solidified material in the drum contain minimal free liquid after the cement has hardened. Free liquid is to be avoided because it may corrode the drum, escape and cause environmental contamination. The DOE has requested that a nondestructive evaluation method be developed to detect free liquid in quantities in excess of 0.5% by volume. This corresponds to about 1 liter in a standard 208 liter (55 gallon) drum. In this study, the detection of volumes of free liquid in a 57 cm (2') diameter cement-solidified drum is demonstrated using high-energy X-ray computed tomography (CT). It is shown that liquid concentrations of simulated radioactive waste inside glass tubes imbedded in cement can easily be detected, even for tubes with inner diameters less than 2 mm (0.08"). Furthermore, it is demonstrated that tubes containing water and liquid concentrations of simulated radioactive waste can be distinguished from tubes of the same size containing air. The CT images were obtained at a rate of about 6 minutes per slice on a commercially available CT system using a 9 MeV linear accelerator source.

INTRODUCTION

The production of radioactive waste is a result of nearly five decades of nuclear energy and defense programs. During this time, many methods have been developed for disposal of radioactive wastes in a manner that reduces the risk of environmental contamination. One such method is to mix liquified radioactive waste with cement and allow the mixture to solidify in steel drums prior to disposal. As long as the radioactive waste is bound in the cement and the drum is properly disposed, there is little chance that the radioactive elements will be able to find a path to the biosphere.

Experience has shown that some types of liquid radioactive wastes produce residual free liquid when mixed with cement. The top surface of the solidified mixture may appear to be uniform but pockets below can contain appreciable amounts of free liquid. During transportation and storage, drums are subject to heating and cooling which causes vaporization and condensation. As a result, the free liquid can collect on the inside wall of the drum. Once the liquid is in contact with the wall, corrosion and breakthrough may occur. Consequently, there is a need to ensure that there is a minimum of free liquid in the cement.

The US Code of Federal Regulations (CFR) requires that the amount of free liquid be as low as reasonably achievable (ALARA) and in no case be more than 1% of the volume of the container [1, 2]. In response to this, the Department of the Energy (DOE) has requested that a nondestructive evaluation (NDE) method be developed to detect free liquid in quantities in excess of 0.5% of the volume of the container.

Current methods for determining the amount of free liquid in drums range from destructive methods, such as punching a hole in the drum, to nondestructive methods such as radiography [3]. The major problems with the hole-punch method are:
   (1) free liquid with no path to the hole will go undetected,
   (2) the hole degrades the integrity of the drum even if it is sealed after use, and
   (3) the inspection must be conducted in a place and manner that can safely handle the
      release of radioactive liquids and vapors.
Problems associated with the application of radiography (either with film or real-time techniques) to waste drum inspection include:
   (1) sensitivity to 0.5% free liquid by volume is questionable, especially if the liquid is
      dispersed in small voids throughout the cement,
   (2) for best results, free liquid detection sensitivity must be optimized for a given path

length through the drum by adjusting exposure times and other variables, and
(3) quantitative measurements of free liquid volume are difficult with radiography because it is often not possible to distinguish between changes in X-ray path length and changes in density.

Computed tomography (CT) is a highly sensitive inspection technique that can be used, free of the complications listed above, to detect free liquid within a cement-solidified waste drum. Unlike radiography (Figure 1(a)), CT measurements of X-ray attenuation are independent of X-ray path length through the material and are unaffected by surrounding structure (Figure 1(b)). Furthermore, CT sensitivity to small localized density changes is typically several orders of magnitude greater than that of radiography. For applications requiring high sensitivity, CT images are obtained one slice at a time. Each image can be thought of as a cross-sectional density map through the object in the plane of the slice. Multiple CT images can be combined to form a full 3-D view of the density distribution in the object. Consequently, multiple CT images can be used as a quantitative measurement of the total amount of free liquid in a cement solidified waste drum, independent of the location of the liquid in the drum.

The objectives of this demonstration were to: (1) use a high-energy CT scanner to detect free liquid in a standard 55-gallon (208 liter) waste drum filled with cement, (2) determine the smallest free liquid quantity that can be detected, and (3) demonstrate that CT can be used to distinguish voids filled with water and simulated radioactive liquid waste from the same sized air-voids.

METHODS AND MATERIALS

Portland Type I cement was mixed with water (one part water to two parts cement by weight) and poured into a Type 17E 208 liter (55-gallon) waste drum constructed of 18 gauge steel (57 cm diameter, 1 mm wall thickness). The bulk density of the cement was about 1.9 g/cc after drying for three days. Immediately after pouring, four sets of thin-walled glass tubes were inserted into the cement. The inside diameters of the five tubes in each set were 0.9, 2.0, 2.4, 3.4 and 4.0 mm. One set contained air, another distilled water and two sets contained concentrations of $NaNO_2$ (20% and 40%).

$NaNO_2$ was chosen because it has X-ray attenuation properties similar to that of a radioactive supernatant at West Valley, New York. Present plans are to dispose of this supernatant using the cement solidification method [4]. The percent-total solids content of the West Valley supernatant is approximately 40% and consists primarily of sodium nitrate and sodium nitrite with minor amounts of other compounds and trace amounts of radionuclides. The density of the supernatant is 1.3 g/cc. The approximate density of the 40% $NaNO_2$ solution is also 1.3 g/cc while that of the 20% solution is 1.15 g/cc.

The CT system used to scan the waste drum is an ARACOR ICT 1500 equipped with a 9 MeV linear accelerator X-ray source (Figure 2). The source and detector elevators (right and left side of scanner, respectively) are designed for a vertical scanning range of 2.3 m (92"). The specimen table can accommodate objects up to 1.3 m (52") in diameter and weighing in excess of 4500 kg (10,000 lbs). This scanner is designed for rapid inspection of stage III of the Minuteman III rocket motor. A scanner designed specifically for objects the size and weight of a cement-filled waste drum could be considerably smaller and could employ a specimen stage elevator rather than source and detector elevators.

A 10 mm slice thickness and a 0.6 millimeter pixel size were used to obtain CT images 1024 x 1024 pixels in size. Typical scan times were 6 minutes per slice. The 10 mm slice was located such that each tube extended all the way through the slice.

RESULTS

A CT image of the 57 cm diameter waste drum filled with cement (Figure 3) reveals details of the internal cross section with the photographic-like image quality typical of images produced by single-slice CT scanners. The bright ring at the periphery is the 1 mm steel wall of the drum. The out-of-round shape of this waste drum may or may not be typical but, in any case, causes no reduction in CT sensitivity to small features located anywhere in the cross section. The mottled

RADIOGRAPHY

X-RAY SOURCE

TEST OBJECT

X-RAY FILM

OVERLAPPING IMAGES OF INTERNAL PARTS

(a)

COMPUTED TOMOGRAPHY

X-RAY SOURCE

TEST OBJECT

TEST OBJECT ROTATED SO THAT MANY VIEWS ALONG A SINGLE PLANE ARE COLLECTED

DETECTOR ARRAY

VIDEO DISPLAY

COMPUTER

KEYBOARD

INTERNAL PARTS ARE SHOWN SEPARATELY

(b)
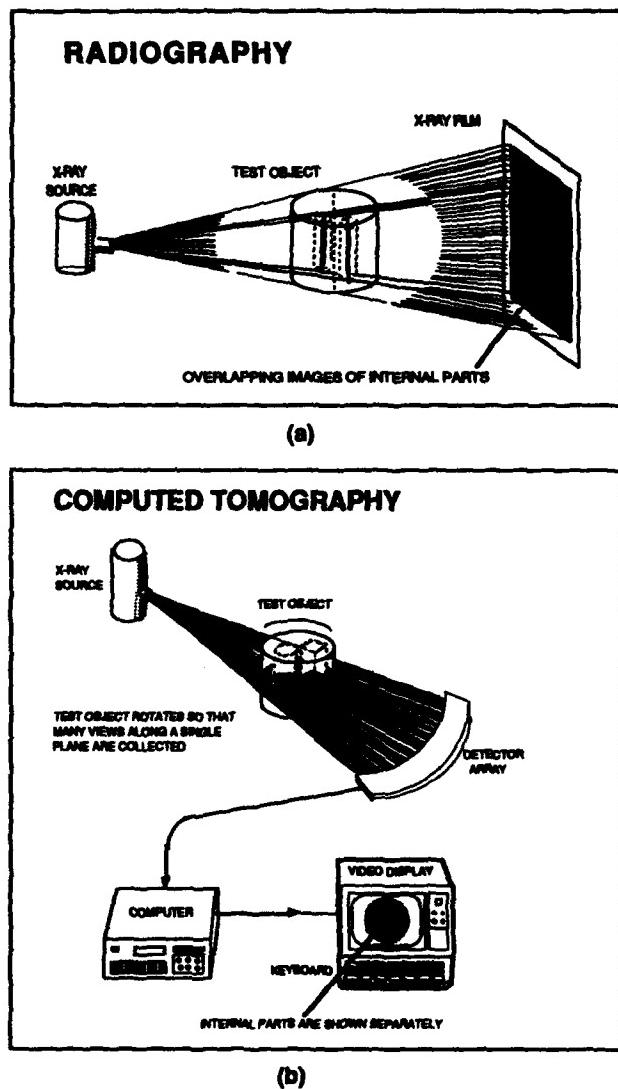
Figure 1 - Schematic diagrams contrasting (a) radiography and (b) computed tomography.

Figure 2: Industrial computed tomography scanner.
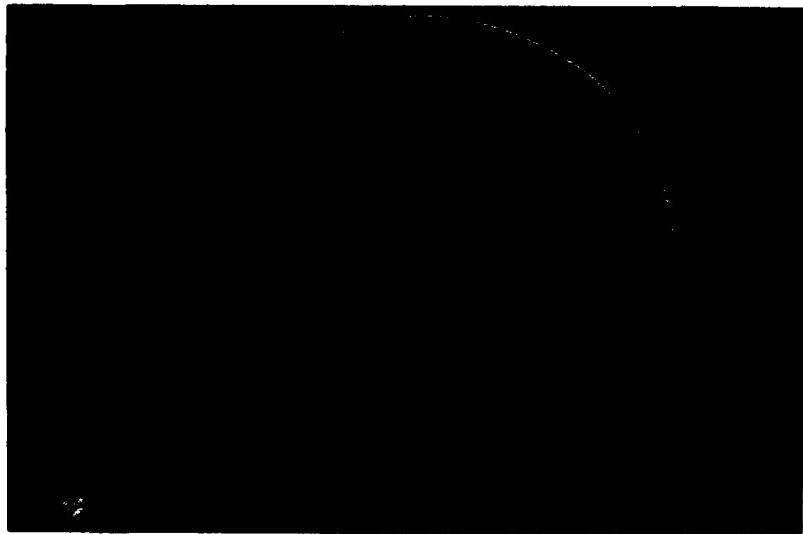
Figure 3: CT image of the 57 cm diameter waste drum.

appearance of the cement is due to a combination of statistical noise in the image and natural density variations in the cement.

The smallest air-filled tube (0.9 mm) is clearly visible and lower contrast water and $NaNO_2$-filled tubes of the same size can also just be seen in this image. The next-to-smallest tubes (2.0 mm) and all larger tubes are clearly visible regardless of contents. Several natural voids, including one against the wall at the bottom left, are apparent in the image. The shading of the image from edge to center is due to a slight beam hardening artifact.

The minimum CT density for all tubes has been measured from the CT image and plotted as a function of tube diameter (Figure 4). As evident from this graph, differences in CT density between water-filled and $NaNO_2$-filled tubes 2.4 mm and larger are measurable. For the 0.9 mm tube the difference in CT density between air-filled and fluid-filled tubes is very small and the fluid-filled tubes cannot be distinguished from one another at all.

It is remarkable that the 0.9 mm $NaNO_2$-filled tubes are detected in the CT image yet cause a change in radiographic thickness of less than 0.07% through a diameter. This is all the more surprising since natural variations in the cement and shape irregularities at the periphery also serve to mask radiographic thickness variations. The sensitivity achieved is typical of single-slice CT imaging and demands that the X-ray transmission measurements used for CT be geometrically precise and largely free of scatter. Both these requirements can be met by careful design and alignment of scanning mechanisms and collimators. Provided there is sufficient X-ray penetration, the object itself can be of any shape and composition and requires no preparation before scanning.
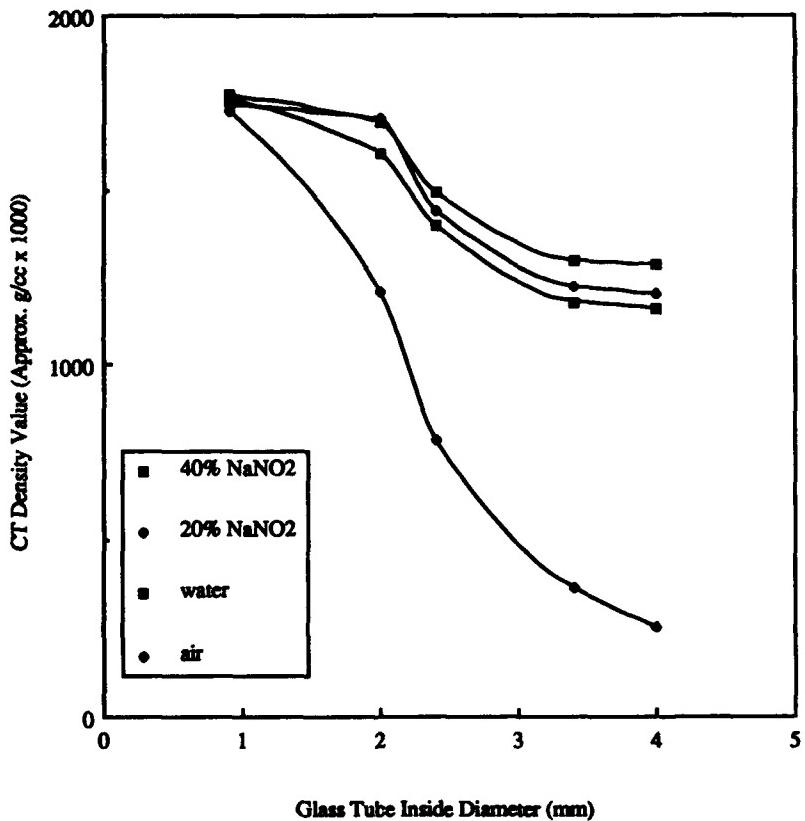
Figure 4: CT density as a function of tube diameter for various tube contents.

CONCLUSIONS

Detection of 0.5% free liquid by volume in a 208 liter (55 gallon) cement-solidified radioactive waste drum is achievable with computed tomography (CT) even if the liquid is dispersed in small voids throughout the cement. Liquid-filled voids can be distinguished from air-filled voids on the basis of CT density numbers for voids as small as 0.9 mm in diameter. Density differences between simulated supernatant and water are measurable for voids 2.4 mm and larger.

Good sensitivity is independent of the location of the free liquid in the drum and can be achieved without precise tuning of exposure times and other variables. No sample preparation is required and irregularities in the shape of the drum have no effect on sensitivity. CT density values are absolute in nature and CT data is stored in digital format on magnetic tape or optical disc for retrieval at any time. The scan quality and repeatability of the data is totally independent of the positioning of the drum on the scanner. The same drum can easily be re-scanned to reliably monitor internal changes that may occur in storage or transportation, even if the outside shape of the drum has been altered.

The CT scanner used to obtain these results is a commercially available unit designed for rocket motor scanning and employing a 9 MeV linear accelerator source. Scan times of 6 minutes per slice may be improved by factors of 2, 4 or even 8 in a custom-designed scanner. For example, the 2.8 m (9') source-to-detector distance suitable for large rocket motors could be reduced by at least a factor of 2 in a scanner designed specifically for objects the size of waste drums. This would result in a significant improvement in scan times.

Radioactive waste management is publicly perceived as a difficult problem demanding the best available inspection technology to assure environmental and public safety. Computed tomography is an exceptionally sensitive and applicable inspection technology that has been proven for other applications and is commercially available now.

Future waste drum CT research should concentrate on the optimization of the CT scanning parameters to decrease drum inspection times while maintaining an acceptable measurement sensitivity. Other radioactive waste forms should also be evaluated as candidates for CT inspection. These include compacted sludge (known to develop internal pockets of free liquid during transportation and storage) and bitumen.

With further study, application-knowledge specific to waste drums will accumulate, leading to increased confidence in the CT technique and to sophisticated uses of its uniquely quantitative capabilities. The support of applications research directed at waste drum CT and custom-scanner production will bring immediate results which will significantly advance the nuclear industry toward its goal of safe, long term disposal of radioactive waste.

ACKNOWLEDGEMENTS

REFERENCES

1. Westinghouse Electric Corporation, "TRU Waste Acceptance Criteria for the Waste Isolation Pilot Plant," WIPP/DOE - 069, Revision 3, UC - 70, January, 1989.

2. 10 Code of Federal Regulations, Part 61.56(a)(3).

3. T.L Clements, Jr., "Technologies for Sorting, Assaying, Classifying, and Certifying Transuranic Waste Within the United States," Idaho National Laboratory, EG&G Idaho Inc., Report No. EGG-M-42387 for work supported under DOE contract No. DE-AC07-76ID01570.

4. C.W. McVay, J.R. Stimmel, and S. Marchetti, "Cement Waste Form Qualification Report - WVDP Purex Decontaminated Supernatant," Topical Report DOE/NE/44139-49 for Work Performed Under Contract No. AC07-81NE44139, August, 1988, 145 p.

CONE-BEAM 3-D RECONSTRUCTION WITH DOUBLE CIRCULAR TRAJECTORY

Ph. RIZO,[+*] P. GRANGEAT,* P. SIRE,* P. LEMASSON,* S. DELAGENIERE*

+Visiting Scientist, Argonne National Laboratory
9700 South Cass Avenue, Argonne, IL 60439

*L.E.T.I./DSYS CEA/CENG 85X Avenue des Martyrs
38041 Grenoble Cedex, France

ABSTRACT

In X-ray cone-beam tomography, the only planar source trajectory that *does not produce incomplete data* is the infinite line. Such a source trajectory is not experimentally possible. To ensure complete data acquisition with cone-beam radiographs, a set of nonplanar trajectories has been studied. Among the trajectories proposed in the literature, a simple one is a set of two circular trajectories with intersection of the two trajectory axes. The angle between the two axes is related to the maximum aperture of the cone beam. We propose here an exact method for performing this reconstruction using the 3-D Radon transform of the object. The modulation transfer function of this algorithm remains identical to that for the central slice of reconstruction in a single circular trajectory. The relative mean square error for density stays within 2% for an aperture of $\pm 30°$. With a single circular trajectory, the relative mean square error may reach 20% at the same aperture. With a double circular trajectory, horizontal artifacts are nearly suppressed.

INTRODUCTION

Recently 3-D cone-beam tomography has become of interest for the nondestructive evaluation of advanced materials. The main field of application is in the evaluation of structural ceramics [1]. Study of such materials implies high density resolution and high sensitivity to cracks [2,3]. In fact, with a circular source trajectory, when the cone-beam aperture increases, density is underestimated and horizontal cracklike artifacts may appear at interfaces in the sample [4]. These artifacts limit the thickness we can examine with a planar source trajectory. To maintain optimal reconstruction accuracy with a circular source trajectory, the angular aperture must remain within $\pm 10°$ [4]. To examine greater thicknesses and to maintain resolution, we must widen the cone-beam aperture; this allows us to reduce the source/object distance, and photon noise is then reduced. If we wish to reduce the volume of the elementary voxel by 8, for example, to keep the reconstruction signal-to-noise ratio constant, we must multiply the flux in the voxel by 16. Thus, the shorter the source/object distance, the better the signal-to-noise ratio. An aperture near $\pm 30°$ allows us to examine larger volumes under good conditions.

Until now, most of the experiments presented in the literature were performed with a planar source trajectory [5,6]. Recently, a new method presented by Smith [7] has been applied to nonplanar source trajectories by Kudo and Saito [8]. The

inversion presented by Kudo uses the Hilbert transform. We present in this paper an exact reconstruction method using 3-D Radon transform inversion with a double circular source trajectory. This is an application of the work of Grangeat [9,10] who established a general mathematical relationship between X-ray transform and the first derivative of 3-D radon transform. This method requires less computation than the Kudo method [11] because Hilbert transform is not a local operation. In the Theory section of this paper, we recall that mathematical relationship. In the Method section, we show how two circular source trajectories can give access to complete information on the sample. We give the relationship between the size of the reconstructed object and the angle between the axes of the two trajectories. In the Results section, we study with simulated data the modulation transfer function (MTF) of the dual-axis reconstruction method. We provide some comparison to reconstructions obtained with single planar trajectory reconstructions.

THEORY

Grangeat [9] showed that we can link exactly the 3-D Radon transform of an object and the X-ray transform of the same object. With this relationship we can directly determine points of the first derivative of the Radon transform; this is done independently of the source trajectory. For each radiograph, the set of points filled in the Radon space forms a spherical surface (Fig. 1). Given an object function f(M) where M is a given point of the space, let us define the X-ray transform Xf(S,A), the radiographic reading at point A corresponding to a source position S, as

$$Xf(S,A) = \int_{a=0}^{a=+\infty} f(S + a\frac{\overrightarrow{SA}}{\|\overrightarrow{SA}\|})da \tag{1}$$

If we consider point P of the Radon space of origin O, the Radon transform of f in P is given by

$$Rf(P) = \int_{(\overrightarrow{OP}.\overrightarrow{PM})=0} f(M)dM \tag{3}$$

and call SYf(S,n) the integral over the line D(S,n) intersecting the detector and the plane passing through S and perpendicular to n (fig. 1)

$$SYf(S,\bar{n}) = \int_{A\in D(S,\bar{n})} Yf(S,A)dA \tag{4}$$

where

$$Yf(S,A) = \frac{\|\overrightarrow{SO}\|}{\|\overrightarrow{SA}\|}Xf(S,A) \tag{5}$$

then the Grangeat formula [9] can be written as

$$\frac{\|\vec{OS}\|^2}{\|\vec{OS}_{\wedge\tilde{n}}\|^2}\frac{\partial(SYf)}{\partial\rho'}=\frac{\partial(Rf)}{\partial\rho}(\vec{OS}.\tilde{n},\tilde{n})$$

(6)

with $\rho = OC$, $\rho' = OC'$, as defined in Fig. 1.

For reconstructing, the first derivative of the Radon transform is filled with the spheres that correspond to each source position and is inverted by two set of backprojections.

$$f(M)=-\frac{1}{8\pi^2}\int_{s^2}\frac{\partial^2 Rf}{\partial\rho^2}(\vec{OM}.\tilde{n},\tilde{n})d\tilde{n}$$

(7)

Kirillov [12] and Tuy [13] showed that in order to perform exact 3-D cone-beam tomography, all planes passing through each point of the object must cut the source trajectory at least once. Obviously, in the case of the circular trajectory, the planes that are parallel to the trajectory and cross the sample do not follow this condition. Thus, no information lying in these planes is detected.
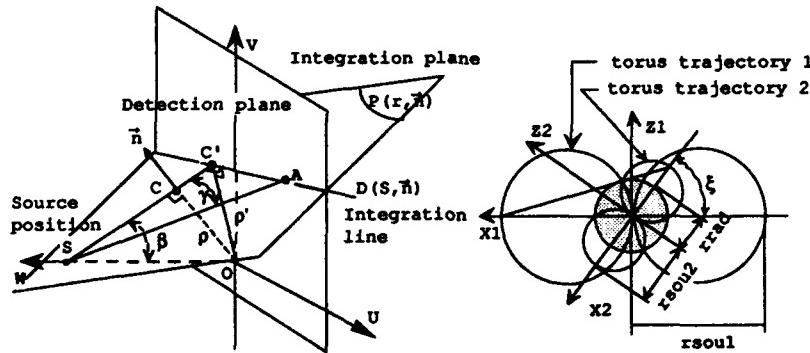
Fig. 1. Acquisition geometry for the relationship between X-ray transform and Radon transform

Fig. 2. Maximum object radius with double circular trajectory of radius rsou1 and rsou2

METHOD

The set of points of the Radon space that is addressed by a circular trajectory defines a torus [9]. The Radon transform of a spherical object is different from zero in a sphere of the same diameter as that of the object. Thus, to reconstruct an object of the same diameter as this sphere, we must measure these points in the Radon space. The principle of double circular source trajectories is definition of a second torus whose axis intersects the axis of the first and that is defined in the area where the first torus is not defined. The simplest trajectory from a mathematical point of view is achieved by constructing the second torus at 90° from the first one [8]. This trajectory provides the largest possible radius of the object to be reconstructed and allows a total angular aperture of ±45°, but is

seldom compatible with hardware problems. Usually, the possible angle between the two trajectories is less than ±45°. As shown in Fig. 2, let us assume that the angle between the two trajectories is ξ; then, if rsou1 and rsou2 are the radii of the trajectories and rrad is the maximum radius of the object that can be examined without approximation,

$$rrad = \frac{rsou1.rsou2.sin\xi}{\sqrt{rsou2^2 + 2.rsou2.rsou1.cos\xi + rsou1^2}} \qquad (7)$$

RESULTS

Using the same methods we described in Ref. [4], we have measured the MTF of the dual-axis reconstruction on a set of concentric spheres at different apertures. This MTF (Fig. 3) is identical to that of the Radon algorithm on the central slice and is independent of aperture. In the case of single-axis reconstruction, the MTF is very perturbed at large apertures no matter what algorithm is used. The uniformity of the MTF with a double circular trajectory shows that we have suppressed the entire effect of the shadow area without degrading the geometrical resolution.
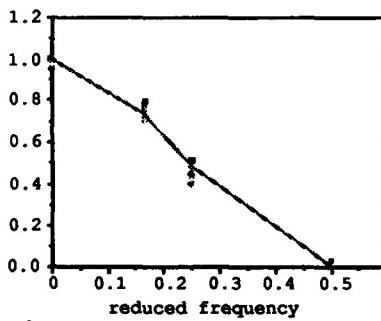
Fig. 3. Modulation transfer function of the dual axis reconstruction. All values of the MTF are very close to the apodisation function of the radon reconstruction.
━▪ Radon 1 axis central slice
━► Radon 1 axis 10° position slice
⋯ Radon 2 axis 30° position
━ Apodisation function of Radon
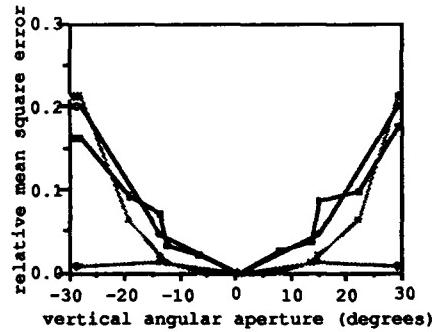
Fig. 4. Relative mean square error of the different cone-beam reconstruction codes.
━▪━ 3-D backprojection
━◆━ Radon 2 axis
━▼━ Radon 1 axis
━◆━ Radon 1 axis 0. in shadow area

Density resolution was evaluated as described in Ref [4]. A set of spheres is located on the axis of one of the two trajectories, and the average density of each sphere is compared to that of the sphere of the central slice. With a single circular source trajectory, the 3-D backprojection algorithm [5] and the Radon algorithm underestimate the density of the spheres that are not on the trajectory plane. In Fig. 4 we see that for an aperture of ±30°, with a single circular source trajectory the relative mean square error (RME) may reach 20%. With dual-axis resolution the RME is less than 2%.
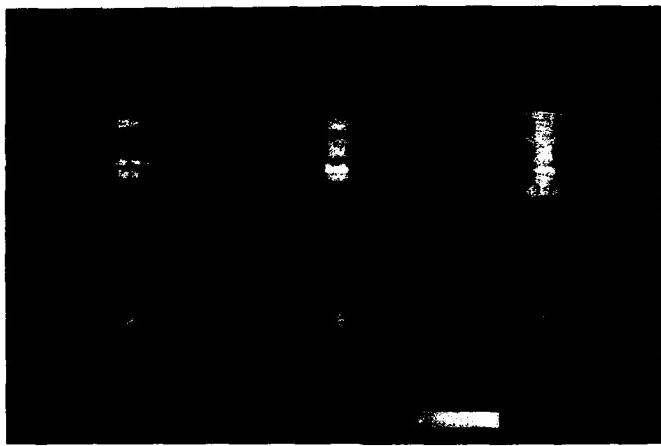
Fig. 5. Effect of double trajectory on
horizontal artifacts. The sample is a set of
cubic volumes. Each view represents a vertical
slice along the first axis of rotation. (a) 3-D
backprojection reconstruction, (b) Radon
reconstruction with single circular trajectory
(Radon 1 axis), (c) Radon reconstruction with
double circular trajectory (Radon 2 axis)

Effects of dual-axis reconstruction on horizontal artifacts
have been studied on a set of parallelipedic simulated samples.
Figure 5 shows the improveed reconstruction with a double
circular trajectory. This improvement is sensitive on each
interface and particularly at the top and bottom of the sample.

Figure 6 shows densitometer profiles taken axially along the
sections of the simulated data samples. Figure 6 a is the
densitometer profile for the entire length of the reconstructed
simulated data and Figure 6 b shows an expansion of the .7 to 1.4
density of Figure 6 a.

(a)   (b)
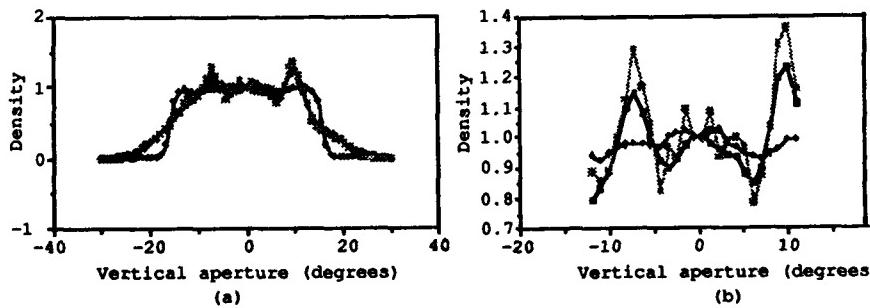
Fig. 6. Density values along the first axis of rotation
for the three reconstructions in Fig. 5. (a) plot for
all apertures. (b) central part of plot (a).
————— Radon algorithm, single circular trajectory
————— Radon algorithm, double circular trajectory
————— 3-D backprojection algorithm, single
        circular trajectory

CONCLUSIONS

We have shown that 3-D cone-beam tomography with double circular source trajectory suppresses problems of missing information encountered with single circular trajectories. Mainly, density resolution is independent of interest-area position, and streak artifacts characteristic of single circular trajectory reconstructions are suppressed. This method can be implemented without approximation using the Grangeat formula. Such a method allows the design of 3-D cone-beam tomographs for evaluation of small components with good photon efficiency. We are upgrading our experimental setup to acquire data on the double circular trajectory.

ACKNOWLEDGMENTS

REFERENCES

1. P. Rizo, P. Grangeat, in _Proc. of the Industrial Computerized Tomography Conf._ (Am. Soc. for Nondest Test., Seattle, 1989), 24-28.
2. R. W. Davidge, Br. Ceram. Trans. J., $\underline{88}$, 113-116 (1989).
3. D. R. Clarcke, K. T. Faber, J. Phys. Chem. Solids, vol 48, No. 11, 1115-1157 (1987).
4. P. Rizo, P. Grangeat, P. Sire, P. Lemasson, P. Melennec, "Comparison of two 3D X-ray cone-beam reconstruction algorithms with circular source trajectory" submitted to J. of Opt. Soc.
5. L. A. Feldkamp, L. C. Davis, J. W. Kress, J. Opt. Soc. Am. $\underline{1}$ (6),612-619 (1984).
6. P. Rizo, W. A. Ellingson, in _Proc of the Nondestructive Evaluation of Ceramics Conf._, (Am. Soc. for Nondest. Test., Columbus, OH, 1990), 121-125.
7. B. D. Smith, Ph. D. thesis, University of Rhode Island (1987).
8. H. Kudo, T. Saito, in _Proc. Topical Meeting, O.S.A., Signal Recovery and Synthesis III_, Cape Cod, MA, 1989, 174-177.
9. P. Grangeat, thèse de doctorat Ecole Nationale Supérieure des Télécommunications (1987).
10. P. Grangeat, in _Computer Assisted Radiology_, CAR'85, Springer-Verlag, Berlin (1985).
11. P. Grangeat, Lecture notes in mathematics, _Proc. of Conf. Mathematical Methods in Computed Tomography_, G. T. Herman, A. K. Louis, F. Natterer, eds., Springer-Verlag, Berlin (1990)
12. A. A Kirillov, Soviet Math. Dokl. $\underline{2}$, 268-269 (1961).
13. H. K. Tuy, SIAM J. Appl. Math. $\underline{43}$ (3), 546-552 (1983).

PROCESS CONTROL FOR COMPOSITES USING COMPUTED TOMOGRAPHY

PHILIP ENGLER*, WILLIAM D. FRIEDMAN*, MARK W. SANTANA* AND FRANK CHI**
 *BP Research, 4440 Warrensville Center Road, Cleveland, OH 44128
**The Carborundum Co., 2351 Whirlpool Street, Niagara Falls, NY 14302.

ABSTRACT

Structural information provided by computed tomography (CT) can be used for quality control and optimization of processes for manufacturing better materials. The squeeze casting method for producing metal matrix composites involves infiltrating a preform of ceramic fibers with molten metal under high pressure. Part quality can be improved if CT is used before infiltration to determine if the preforms have the desired distribution of fibers and are free of defects. Measurements do not require uniform shapes, and CT systems can even be used to obtain accurate densities on complicated part shapes that are not amenable to bulk density measurements based on weight and size. With this quantitative distribution information as a guide, preform production can be modified to produce either a more uniform fiber distribution or to selectively increase the fiber concentration in critical areas. Problems occurring during later stages of processing can be detected in CT images of the completed part. For example, CT can be used to detect unreinforced regions in metal matrix composites caused by cracking of the preform during the squeeze casting process. CT scans of completed parts can also detect and distinguish variations in structure such as microporosity.

INTRODUCTION

Ceramic fiber reinforced metal matrix composite (MMC) parts have superior mechanical and thermal properties compared to parts made from just the metal alloy. Consequently, MMC parts possess properties desired by the aerospace, automotive and consumer-goods industries [1,2]. Squeeze casting is a procedure for producing an MMC by infiltrating the open network of voids in a preform of ceramic fibers with molten metal under high pressure. The preform generally contains 10-20% fiber, by volume.

Defects, such as delaminations, porosity and non-homogeneous fiber distribution, can degrade the properties of the part and result in premature failure. By mapping the X-ray attenuation in a specimen, CT can provide an accurate reconstruction of the size, shape and distribution of such defects in cast parts. The same principles can be applied to detecting and characterizing material and density variations in preforms. The information available from CT analyses can be used for control and optimization of manufacturing processes, as well as for quality control inspection.

EXPERIMENTAL

CT images of most of the preforms and the MMC castings were obtained with a Scientific Measurement Systems (SMS) 101B series industrial CT system. The parts were scanned with an X-ray source operating at 225 kVp and filtered with 0.5 mm of brass. Scan geometry was set so that in-plane and slice thickness resolution were both either ~0.3 mm or ~0.5 mm. Images for the castings were corrected for beam hardening using transmission values obtained with an aluminum wedge. Two preforms were scanned with a Siemens DR3 medical CT system

with an X-ray source operating at 125 kVp, an in-plane resolution of ~0.7 mm
and a slice thickness of 4 mm.

In the gray scale images, white signifies greater X-ray attenuation,
which is proportional to both density and composition. For the preforms, com-
position was uniformly distributed so that the measured attenuation was di-
rectly proportional to fiber density. X-ray attenuation values were converted
to fiber density through analysis of calibration preforms having identical
composition, simple geometry (i.e, cylinder or cube), and a cross section of
similar size and shape.

RESULTS AND DISCUSSION

Fiber density in a preform affects both the casting process and the re-
sultant structure of the casting. Insufficient fiber density or cracks lead
to unreinforced or under-reinforced areas, while metal starvation can result
from too high a fiber density. In either case, premature failure of the part
may occur. For example, Figure 1a shows a photograph of the crown of a
sectioned and polished engine piston. The area containing the fiber rein-
forcement as well as a delamination that formed in the preform during casting
can be clearly seen. Figure 1b shows a CT scan of the same region. The X-ray
attenuation of the reinforced crown is less than for the unreinforced metal,
so the former appears darker. Regions in the crown having the same light gray
color as the matrix material in the rest of the piston are indicative of unre-
inforced aluminum and show where the preform had cracked.
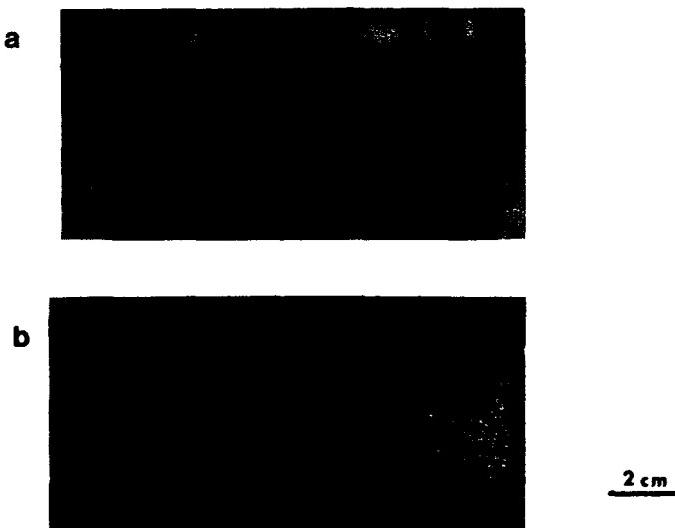
Fig. 1. Photograph (a) and CT image (b) of the top of a sectioned
Al alloy, diesel engine piston whose crown is reinforced with a
ceramic fiber. In (b), the reinforced crown appears darker than
the unreinforced metal. Regions in the crown (shown by white
arrows) having the same color as the rest of the piston are in-
dicative of unreinforced Al and show where the preform had cracked.
(Note: Black arrow and lines in (a) refer to transverse CT images
shown in Ref. 2 and should be ignored in the present paper.)

Fig. 2. CT image of a machined preform showing a
crack (indicated by arrow) and variations in
fiber distribution. CT image is parallel to and
contains preform axis.

Preforms are designed to provide the optimum distribution of fiber to
insure the needed performance of a part. Some of the defects that occur in an
MMC can be traced back to defects in the preform. There can be a significant
savings if defective or "out-of-spec" preforms can be detected and rejected
prior to the casting process. Figure 2 displays a CT image of an early gener-
ation preform, which contains a crack on the left side. While a crack such as
this may be visible from the outside, only a technique such as CT can determine
the location and extent of a crack. In another example, Figure 3a shows a CT
image of the end face of an early generation, cylindrical preform made of a
silica-alumina fiber. Two defects can be observed in this figure: a low den-
sity oval band and a square array of small, low density areas. Relating this
information to processing parameters facilitated corrective modifications that
resulted in more uniform parts (Figure 3b).

These preform images demonstrate that qualitative analysis of CT images
can make a significant contribution towards quality improvement. The fact that
CT images are digital images means that CT data is amenable to quantitative
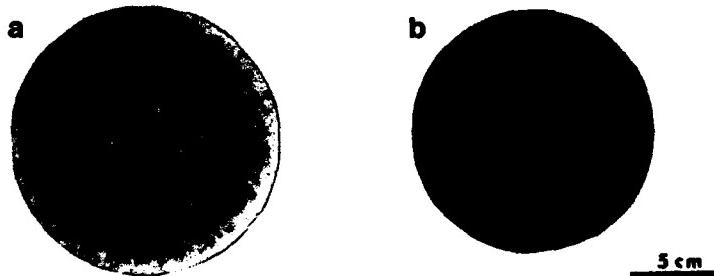
Fig. 3. CT images (obtained on a medical system) of planes
perpendicular to the the axis of cylindrical preforms: (a)
shows a low density region in the center and a square array
of small low density regions; (b) shows a more uniform pre-
form resulting from successful implementation of corrective
processing modifications.
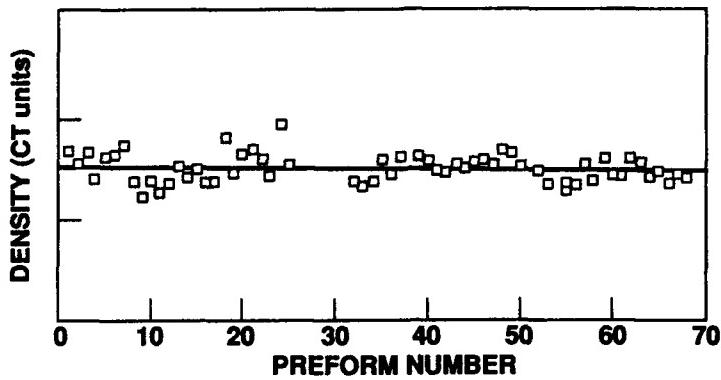
Fig. 4. Change in mean relative density of a plane in a cylindri-
cal preform during a manufacturing run as measured by CT.

analysis as well. For example, the mean X-ray attenuation for a slice from a
preform measures its average density; the standard deviation measures uniform-
ity. These quantitative parameters can be monitored during production to
determine trends. For example, Figure 4 tracks the mean density (in arbitrary
units) of a plane of a cylindrical preform during a 70-unit production run.

While the mean density or the standard deviation of an entire slice pro-
vide meaningful data, they do not necessarily reveal important structural in-
formation. For example, Figure 5 shows two preforms that have approximately
the same mean and standard deviation but significantly different structures.
The fact that a CT image is a matrix of numbers allows the data to be analyzed
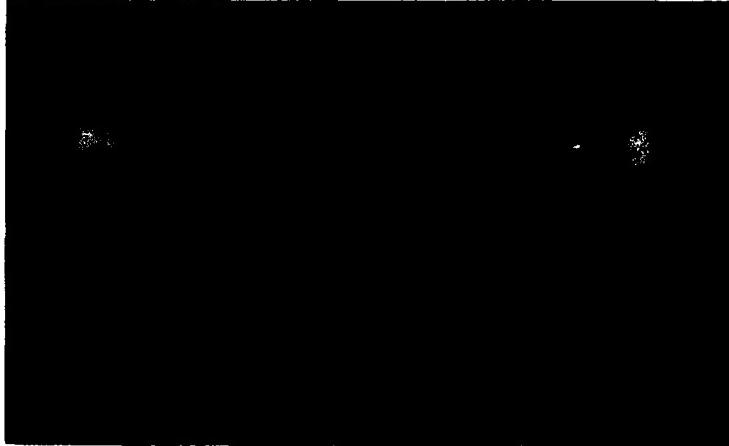
Fig. 5. CT images of two preforms having similar mean
density but different structures.

on a finer scale. In order to quantify the density gradients in shaped pre-
forms, X-ray attenuation values were obtained at regular intervals across the
CT image. These values were written to a matrix where the columns represented
points in vertical profiles, and each row represented a set of points obtained
across the part from left to right at a specified proportional distance from
top to bottom, i.e. a line following the profile of the part. Parts were
scanned at a number of fixed angular intervals about their axis to obtain in-
formation about axial symmetry. This allowed density to be plotted as a func-
tion of three parameters: radius, relative height and angle. Trends versus a
specific geometric parameter, e.g. radius, height, and angle about the part
axis, were accentuated by averaging the data with respect to the other two pa-
rameters. Figure 6 contrasts the radial density gradients of the two preforms.

These examples show the type of qualitative and quantitative information
that can be obtained by CT to guide modifications for producing preforms with
either a more uniform fiber distribution or for selectively increasing the
fiber concentration in critical areas. Even if mean part density is the only
desired parameter, CT offers an advantage: CT systems can be used to obtain
accurate densities on complicated part shapes that are not amenable to the
accurate volume measurements required for determining the bulk density.

Although certain defects appearing in metal matrix composites can be
traced back to the preform, some are caused by the metal infiltration process
itself. Information obtained from the completed part can also provide signi-
ficant structural information that can be correlated with processing problems.
For example, Figure 1b shows the detection by CT of unreinforced regions that
have formed in an engine piston. The ability to detect a preform in the metal
matrix is non-trivial. At the X-ray energies required to penetrate large cas-
tings, ceramic fibers containing alumina and typical aluminum alloys contain-
ing silicon and magnesium have very similar mass attenuation coefficients.
This means there is virtually no contrast between these components. Fortu-
nately, the alloy in this part contained about 3% copper, which increased the
attenuation coefficient of the alloy enough to provide sufficient contrast.
Nevertheless, even when contrast between the preform and alloy is absent, CT
scans of castings can provide significant information, e.g., the presence of
porosity.
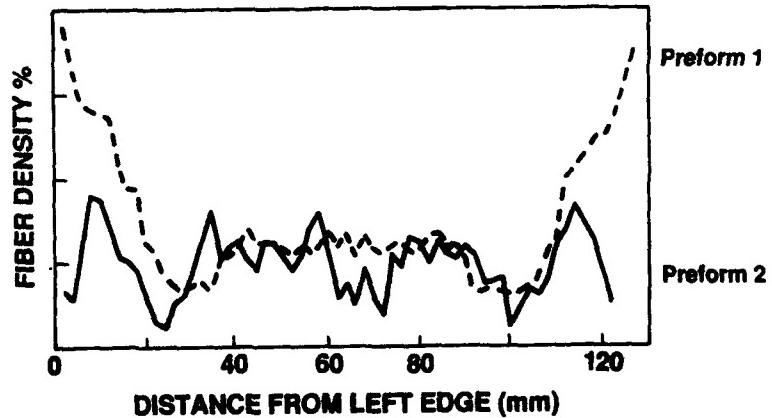
Fig. 6. Radial density profiles of preforms in Fig.5 Dashed line
(a) is profile of top preform and solid line is (b) profile of
bottom preform.

128

CONCLUSIONS

Information available from CT inspection offers the opportunity for quality control and optimization of manufacturing processes. In metal matrix composites, which are produced by infiltrating a ceramic fiber preform with metal, part quality can be improved when CT is used before infiltration to determine if preforms have the desired distribution of fibers and if they are free of defects. CT scans of cast parts can detect and distinguish unreinforced regions as well as variations in structure such as microporosity. Data can be characterized quantitatively and with this quantitative information as a guide, preform production and part casting can be modified to produce defect free composite parts having the required distribution of reinforcing fiber.

ACKNOWLEDGEMENTS

REFERENCES

1. P. Rohatgi, Adv. Mater. Processes, 1990, (2) 39-44.

2. F. K. Chi, W. Friedman, P. Engler, R. D. Maier, and T. W. Krucek in Proceedings, Twelfth Annual Discontinuously Reinforced MMC Working Group Meeting, (DOD Metal Matrix Composites Information Analysis Center No. 718, Kaman Sciences Corp., Santa Barbara, CA, 1990) paper no. 7, pp. 1-13.

NDT APPLICATIONS OF THE 3D RADON TRANSFORM ALGORITHM FOR CONE BEAM RECONSTRUCTION

P. Sire, P. Grangeat, P. Lemasson, P. Mélennec, P. Rizo[1].
LETI - Département Systèmes - SETIA, Centre d'Etudes Nucléaires de Grenoble
85 X - 38041 GRENOBLE CEDEX - FRANCE

ABSTRACT

The paper describes our 3D X-ray CT algorithm "RADON" using attenuation measurements acquired with a bidimensional detector. Our inversion diagram uses the first derivative of the Radon transform synthesis then its inversion. The potentiality of that new method, particularly for the large aperture, prompted us to develop an optimized software offering convenience and high performances on a modern scientific computer. After a brief recall of the basic principle of X-ray imaging processing, we will introduce the theoretical developments resulting in the present inversion diagram. A general algorithm structure will be proposed afterwards. As a conclusion we will present the performances and the results obtained with ceramic rotors examination.

1. INTRODUCTION

X-ray CT is used in medecine to perform body in-vivo investigation for diagnosis or therapy purpose, and also in Non Destructive Testing (NDT) to find defects into industrial products. The reconstructed characteristic parameter is proportional to the linear attenuation coefficient μ. In complement to tomographic and radiographic systems, the 3D structure apprehension prompted us to study a 3D imaging system using numeric radiography. The projections are acquired with a 2D detector. As in classic tomography : either the couple source-detector moves around the object or the object rotates into the measurement cone beam. The interest of these systems lies in the use of the total information supplied by the cone beam geometry. Then, an object may be reconstructed from a reduced acquisition set which decreases the exams length. Consequently, the 3D imaging processing has strong arguments. So we have to deal correctly with the acquisition geometry int reconstruction algorithms. This point will be the main strength of our approach resulting in an isotropic reconstruction on the three axis. In order to evaluate the performances of this new algorithm a first software development had been implemented at LETI. Readers may refer to the referencis [RIZO (1990a)], [RIZO (1990b)] for the results and more particularly for a first comparison with the Feldkamp's algorithm [FELKAMP (1984)]. This first version supplied promizing results, but the reconstructions needed a too long computation time. So we developed a software, named RADON, able to offer suppleness and high performances on a modern scientific computer.

2. RECONSTRUCTION ALGORITHM

2.1. Presentation

We set those developments into the transform methods context because they supply direct reconstruction algorithms. The measurement and the object to be reconstructed are represented by continuous space functions. The direct problem study is treated by the functional analysis. The resolution of the inverse problem leads us to find an inversion scheme consisting in expressing an object transform function then in inverting it. The numeric undertaking phasis is achieved afterwards. This implicitly implies that such sampling conditions supply a numeric formulation compatible with the analytical one.

This work is based upon a previous research done in our laboratory by P. Grangeat on the 3D cone beam tomography [GRANGEAT (1990)]. By linking the X-ray transform to the first

---

derivative of the Radon transform, Grangeat established a way to deal with the cone beam geometry. This fundamental relation resulted in the first algorithm able to treat exactly a 3D cone beam reconstruction.

2.2. First derivative Radon transform synthesis

The 3D Radon transform Rf associates a function f with the set of its space planes integrales as follows (Fig.1) :

$$Rf\left(\rho, \vec{n}\right) = \iint_{M \in P(\rho, \vec{n})} f(M) \, dM$$
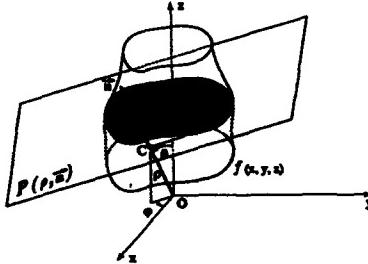
Fig. 1.

An object may be completly defined by its 3D Radon transform. This object will be reconstructed by using the following inversion formula [NATTERER (1986)].

$$f(M) = -\frac{1}{8\pi^2} \cdot \int_{S^2} \frac{\partial^2 R f}{\partial \rho^2}\left(\overrightarrow{OM}.\vec{n}, \vec{n}\right) d\vec{n}$$

The problem consists in expressing the object Radon transform from the measurement acquired with a 2D detector. We introduce the X-ray Xf transform of the function f, as the linear transform which associates f with the expression (Fig. 2) :

$$Xf(S,A) = \int_{a=0}^{+\infty} f\left(S + a.\vec{u'}_1\right) da \quad \text{for } S \in \Gamma, A \in PX \quad \text{and} \quad \text{with } \vec{u'}_1 = \frac{\overrightarrow{SA}}{\|\overrightarrow{SA}\|}.$$
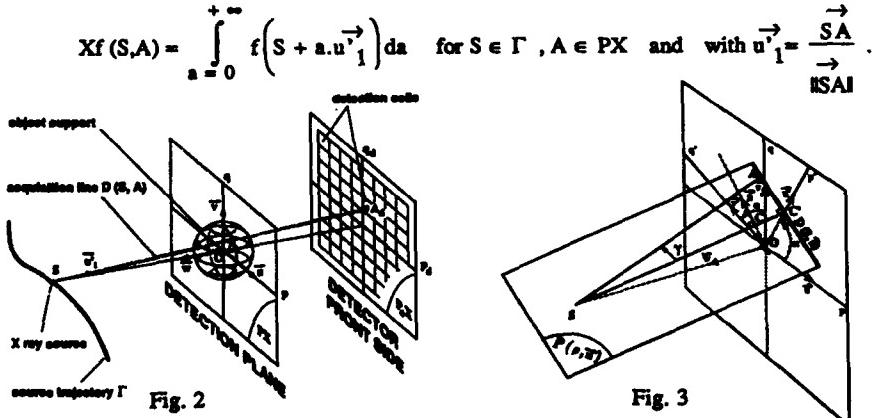
Fig. 2
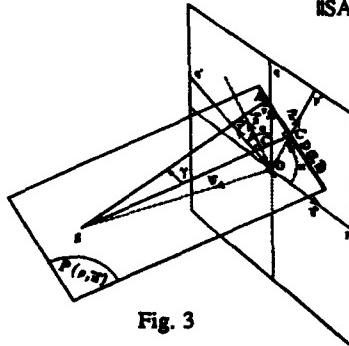
Fig. 3

After a logarithmic correction the measurement is :

$$-Log\frac{\varnothing}{\varnothing_0} = \int_S^A f(l) \, dl = Xf(S,A) \quad \text{with } l = S + a \vec{u}$$

In cone beam geometry, the X-ray transform modelizes measurements.

The theoretical difficulty, linked up to the cone beam geometry is to express a relation between the X-ray transform and the 3D Radon transform. Let us define the weighted cone beam X-ray transform Yf and its integral function SYf over the straight line D $(S_1,\vec{n})$ (Fig. 3).

$$Yf(S,A) = \frac{\|\vec{SO}\|}{\|\vec{SA}\|} \cdot Xf(S,A) \quad A \in PX, \qquad SYf\left(s,\vec{n}\right) = \int_{A \in D(S,\vec{n})} Yf(S,A) \, dA$$

The weighting coefficient expresses a magnification correction over the X-ray transform.
So the fundamental relation is [GRANGEAT (1990)].

$$\frac{\|\vec{OS}\|^2}{\|\vec{OS} \wedge \vec{n}\|^2} \cdot \frac{\partial SYf}{\partial p'}\left(s,\vec{n}\right) = R'f\left(\vec{OS}.\vec{n}, \vec{n}\right)$$

An equivalent expression may be obtained by expressing the first derivative versus p' in the (p,q) reference. So the reprojection operation splits up into two sums along p et q.
So the first derivative Radon transform synthesis is reduced to weighting, reprojecting, (sum) and filtering operations. The power of that method lies upon rigourous mathematical framework. This will subsequently avoid any validation step.

2.3. Rearrangement

The coordinates system linked up with the acquisition reference (ρ,θ,ψ) doesn't allow to regularly distribute the computized informations into the radon space. So before, they must be distributed again into a regular space sampling. The change from the acquisition coordonnates system into the Radon space one is achieved by a rearrangement operation over the circle (ρ,θ).

2.3. Shadow area

By using a circular trajectory for the source, which is the case of this first algorithm version, the cone beam X-ray transform Xf gives an incomplete description of the first derivative R'f Radon transform. This results in artefacts on the reconstructed function. To decrease these artefacts we have to fill R'f by interpolation on the shadow area. Several interpolation schemes were studied. Of course the aim is eventually the use of other source curves allowing the X-ray transform Xf to completely describe the first derivative R'f of the Radon transform. [RIZO (1990c).

2.4. Inversion of the Radon transform

The inversion formula prompts us the calculation of the second derivative R'f of the Radon transform. This is achieved by filtering operation. That inversion operation is a 3D backprojection one. In fact, this formula, as described before, is not conceivable for a practical use. A 3D backprojection operation needs too much computations which penalizes the set of the method. So in order to optimize this scheme we chose to split up into two sums the inversion formula [MARR (1980)].

$$f(M) = -\frac{1}{8\pi^2} \cdot \int_{\theta=-\frac{\pi}{2}}^{\frac{\pi}{2}} \int_{\varphi=0}^{2\pi} \frac{\partial R'f}{\partial \rho}\left(\vec{OM}.\vec{n},\vec{n}\right) \cdot |\sin\theta| \ d\theta \ d\varphi$$

Then we define the rebinned projection plane PX, with longitude , as the plane passing through the origin O and defined by the unit vectors with longitude . For each point B belonging to PX, D(B,ψ) be the straight line passing through B and perpendicular to PX. (Fig. 4).
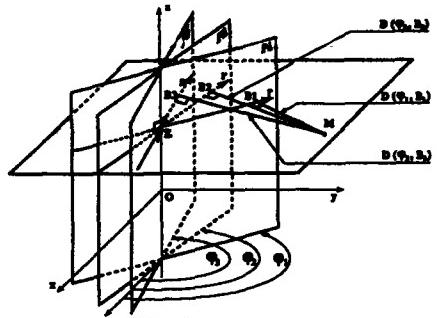
Fig. 4
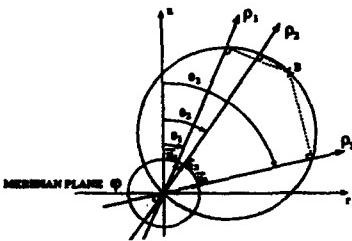
Fig. 5

We call rebinned X-ray transform the integral :

$$\widetilde{X}f(\varphi,B) = \int_{M \in D(\varphi,B)} f(M) \ dM$$

The straight line $D(B,\varphi)$ being parallel for each φ, the function $\widetilde{X}f$ may be considered as the X-ray transform in parallel geometry. The reconstruction of the function f from $\widetilde{X}f$ will be made by backprojecting the filtered rebinned projections $HD\widetilde{X}f$ on the Z planes as follows : (Fig. 5).

$$f(M) = \frac{1}{2} \cdot \int_{\varphi=0}^{2\pi} HD\widetilde{X}f\left(\varphi,B(\varphi,M)\right) d\varphi \qquad \text{HD is the classic 2D reconstruction filter.}$$

By identification with the inversion Radon transform expressed in spherical coordinates, we obtain the follows relation (Fig. 6):

$$HD\widetilde{X}f\ (\varphi,B) = -\frac{1}{4\pi^2} \cdot \int_{\theta=-\frac{\pi}{2}}^{\frac{\pi}{2}} \frac{\partial R'f}{\partial \rho}\left(\overrightarrow{OB}.\overrightarrow{n},\overrightarrow{n}\right) . \mid \sin\theta \mid \ d\theta$$
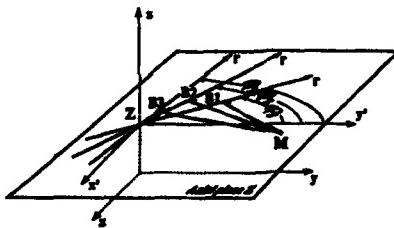
Fig 6

So the function $HD\widetilde{X}f$ is calculated by backprojecting the expression $Rf''.Sin\theta$ on rebinned projections planes. Finally we see that the use of the first derivative Radon transform and its inverse formula, defines a treatment equivalent to the backprojection on the Z planes of the parallel projections, filtered by a classic 2D reconstruction filter.

3. ALGORITHM GENERAL DIAGRAM - OPTIMISATION
The set algorithm phasis results in the following general diagram :
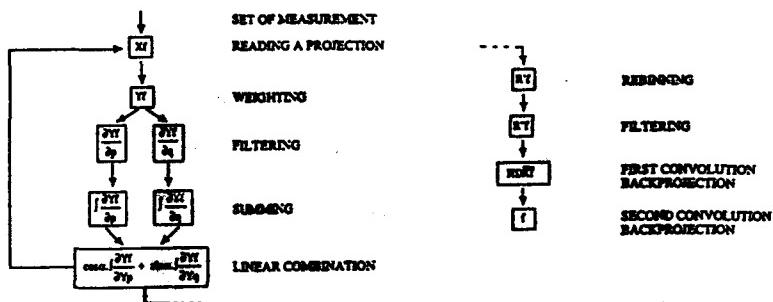
All those treatments are very used in image reconstruction processing framework. The two convolution backprojection and the summing steps are the most important ones. They require the largest part of the total reconstruction time. For the first versions, the software associated to our algorithm was two times slower than the software associated to Feldkamp's algorithm on most computer. Consequently we have work to improve the method set. According to the software use, the development and optimizations have been prompted both on a scalar computer VAX 6300 and on a supercomputer CRAY 2. It results in both the improvement of the general diagram structure in order to dicrease the scalar operations number, and the study of a software structure suited to a CRAY 2 type architecture. These developments have been achieved for our software using the Feldkamp's method too.

4. RESULTS
In order to evaluate the achieved progress on the two softwares, we executed several bench marks resulting in a reconstruction of 128^3 and 256^3. We give the results before and after the optimization.

128^3 reconstructed volume from 256 projections 128^2

	Our algorithm	Feldkamp's algorithm
VAX 6300	5 h 30 → 3 h 30	2 h 30 → 1 h 30
CRAY II*	12' → 1 ' 30	

256^3 reconstructed volume from 512 projections 256^2

	Our algorithm	Feldkamp's algorithm
CRAY II	3 h 15 → 17'	2 h 05 → 44'

* Note : that version doesn't yet use the CRAY II multitasking processing. However, first multitasking processing evaluations gave us a speed-up factor greater than 3 in a such a case, which is a promizing result. According to the computer type architecture, we obtain a great improvement after the optimization.

At last we point out that our method may be quicker than the Feldkamp's on such computers. On the over hand the necessary memory to execute our algorithm is around three times greater than the one to execute the Feldkamp's one.

134

We examined several industrial products as ceramic rotors to illustrate NDT applications of our work. We performed the following experience to evaluate our 3D X-ray CT system set to detect variation density into ceramic components. We searched various density in ceramic bits placed into 3 nock on the top of the rotor. In spite of the measurement wasn't calibrate and achieved from two different acquisitions, we detect 2.3 % various density, corresponding to 2,5 % binder content variation (Fig. 7).
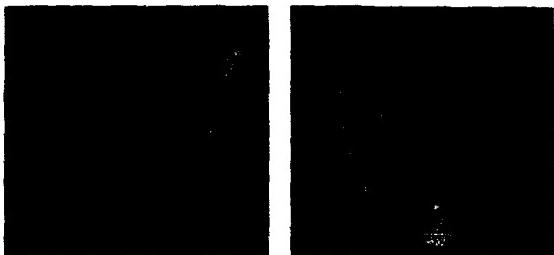
Fig. 7

Ceramic rotor surface displays

5. CONCLUSION

The new optimized algorithm we performed gives good computizing times performances, even some time better than the Feldkamp's one. The exams we achieved on modern ceramic components show that 3D X-ray CT supply repetitive results, allowing to detect lower variation density.

ACKNOWLEDGMENTS

REFERENCES

FELDKAMP L.A., DAVIS L.C., KRESS J.W. (1984). "Practical cone-beam algorithm". J. Opt. Soc. Am., 1 (6), 612 - 619.

GRANGEAT P. (1990) "Mathematical framework of cone beam 3D reconstruction via the first derivative of the RADON transform" in G.T. HERMAN, A.K. LOUIS , F. NATTERER . Mathematical Methods in Tomography. Lecture Notes in Mathematics. Springer - Verlag.

MARR R.B., CHEN C., LAUTERBUR P.C. (1980). "On two approaches to 3D reconstruction in NMR zeugmatography" in HERMAN G.T. and NATTERER F., Mathematical Aspects of Computerized Tomography, 225 - 240, Springer - Verlag.

NATTERER F. (1986). The Mathematics of Computerized Tomography. Wiley/Teubner.

RIZO Ph., ELLINGSON W.A. (1990a). "An initial comparison between two 3D X-ray CT algorithms for characterizing ceramic materials". Proc. of the conference on Non Destructive Evaluation of Modern Ceramics, Columbus, Ohio, July 9 - 12.

RIZO Ph., GRANGEAT P., SIRE P., LE MASSON P., MELENNEC P. (1990b). "Comparison of two 3D cone beam reconstruction algorithm with a circular source trajectory". Submitted to J. Opt. Soc. Am.

RIZO Ph., GRANGEAT P., SIRE P., LE MASSON P., DELAGENIERE S. (1990c). "Cone beam 3D reconstruction with a double circular trajectory". Communication at the 1990 Fall Meeting of the Material Research Society, Boston.

IMPACT OF X-RAY TOMOGRAPHIC MICROSCOPY ON DEFORMATION STUDIES OF A SiC/Al MMC.

T.M. Breunig*, S.R. Stock*, J.H. Kinney**, A. Guvenilir*, and M.C. Nichols***

*Mechanical Properties Research Laboratory and School of Materials Engineering, Georgia Institute of Technology, Atlanta, GA 30332-0245
**Chemistry and Materials Science Department, Lawrence Livermore National Laboratory, Livermore, CA 94550
***Materials Department, Sandia National Laboratory, Livermore, CA 94550.

ABSTRACT

Damage in a continuous, aligned-fiber SiC/Al metal matrix composite (MMC), e.g. fiber fracture, fiber-matrix interphase microcracking, intra-ply matrix voids and cracks, is examined with synchrotron x-ray tomographic microscopy (XTM). Quantitative three-dimensional measurements of damage are reported in as-fabricated and monotonically loaded SiC/Al. The XTM results indicate that increases in observed macroscopic structural stiffness during the first few fatigue cycles of an MMC coupon correspond to elimination of processing-related matrix porosity and to displacement of the fibers from a somewhat irregular arrangement into a more nearly hexagonal array. The XTM data also show that the carbon cores of the SiC fibers begin to fail at or below 828 MPa, that is, at loads far less than those for fracture of the entire fiber. The implications of these results and of the use of in situ loading for fatigue damage quantification are also discussed for mechanical/thermal modelling.

INTRODUCTION

Prior to utilization of metal matrix composite (MMC) materials in high performance applications, a fundamental understanding is needed of what constitutes damage and of how it initiates and accumulates. The damage and fracture initiation processes in many advanced materials are microscopic and occur in the interior of the specimen. Therefore, many of the commonly used macroscopic and surface monitoring techniques are relatively insensitive to damage initiation. High resolution, high sensitivity nondestructive evaluation is required so that internal flaws and damage development may be characterized multiple times during the course of a deformation/fracture experiment. X-ray tomographic microscopy (XTM), i.e., extremely high resolution computed tomography, provides these characteristics and is used in this study to quantify mechanically-induced damage in the SiC/Al MMC system; damage in this MMC takes the form of fiber fracture, fiber-matrix interphase microcracking, intra-ply matrix voids and cracks. The quantity, spatial distribution and evolution of each type of damage must be incorporated in realistic physically-based models before this class of materials can be used safely. Acquisition and analysis of this data for monotonic loading of the SiC/Al MMC system is discussed below.

EXPERIMENTS

The MMC material used in this study is a unidirectional, continuous-fiber SiC/Al matrix composite fabricated by Textron Corporation in 1986. The composite laminate contains eight plies of SCS-8 SiC fibers and a 6061-0 Al matrix. Each ply was fabricated by

a technique that uses a foil to support the fiber and plasma sprayed matrix material to maintain the fiber location and orientation. The SiC fibers are 142μm in diameter and have a 32μm carbon core.

The mechanical test specimens are 152 mm x 17.8 mm x 1.5 mm coupons, with the fibers oriented parallel to the longest dimension. All mechanical testing was performed in a servo-hydraulic test frame with the fibers parallel to the load axis. The monotonic tension tests were performed in load control with a loading rate of 50 kg/s (110 lbs/s). The specimen elongation was monitored with a 12 mm clip gage mounted on the largest face of the specimen. Individual specimens were monotonically loaded to 0, 207, 414, 621, 828, 1034, 1241 and 1448 MPa (0, 30, 60, 90, 120, 150, 180 and 210 ksi, respectively). Deviation from linear load-displacement response occurred at 188 MPa, and failure occurred at 1448 MPa. After mechanical testing, a specimen of each condition was examined using XTM. The specimen cross-sections examined varied from 1.5 mm x 1.5 mm to 1.5 mm x 3.0 mm and were taken from the gage sections covered by the extensometer during mechanical testing. The results presented here are a subset of the monotonic tension test sequence.

The XTM apparatus, which is described more fully elsewhere [1,2], is based on a 1320 x 1035 element, two-dimensional charged-coupled device (CCD) detector. Thus, data from multiple hundred slices can be recorded simultaneously. The CCD detector is coupled through a short-depth-of-field, variable magnification lens system to a single crystal fluorescent scintillator screen of $CdWO_4$. An optical magnification of 2.0X is used in these experiments, yielding an effective CCD pixel size of 6.8 μ.~ (2 x 2 pixel binning). The thermoelectrically-cooled CCD is operated in a charge integrating mode, and approximately 40,000 electrons are accumulated in each pixel during a single exposure.

Monochromatic synchrotron x-radiation was used for XTM; all samples described here were studied with an x-ray energy between 20 to 22 keV. Angular increments of one degree were used between projections, except for the 1448 MPa specimen where one-half degree increments were used. Exposure times for each projection varied from 5 to 25 seconds depending on the beam current of the storage ring. The reconstructions were performed with the filtered back projection method.

The three-dimensional reconstructed volumes were used to quantify the fiber separations, the linear absorption coefficients and the fiber surface area exposed by microcracks. These features were evaluated as a function of deformation level for 15 to 25 well-separated slices.

RESULTS AND DISCUSSION

Typical slices from four of the eight load levels studied are shown in Fig. 1. In the as-fabricated condition (0 MPa), there are processing defects present in the form of voids and microcracks. These voids and microcracks close as the load increases due to plastic deformation of the matrix. The fiber arrangement in the sample is also evident in Fig. 1; measurement of nearest-neighbor fiber core separations confirms this observation. Figure 2 shows the first and second nearest-neighbor fiber core separations for samples which had been loaded to 0 MPa and 828 MPa. The first-nearest neighbor separation has decreased from 236 μm to 210 μm for the 0 MPa and 828 MPa conditions, respectively. The variance has also decreased from 1048 μm² to 512 μm², respectively. The distance between second-nearest neighbors has also decreased after loading to 828 MPa. The average second-nearest neighbor separations at 828 MPa, 1241 MPa and 1448 MPa are consistent with the expected spacing for a hexagonal fiber arrangement and that of 0 MPa is between the expected separations for square and hexagonal arrays.

Some microcracking in the plies, marked M in Fig. 1a, can be seen adjacent to the fibers. These microcracks are three-dimensional, pre-existing fabrication flaws [3], and their

density is higher in the outer plies. The presence of this type of fabrication flaw has a dramatic effect on the load transfer and load carrying capability of the structure: load is transferred from the matrix to the fiber through their common interface. If this region is poorly bonded during fabrication, it can not form a reliable bond during mechanical deformation. Therefore, evaluation of the load carrying capacity of the structure requires characterization of the fiber surface area not in contact with the matrix material. In the as-fabricated structure 2.7% of the total fiber surface area is exposed, and Fig. 3 shows the distribution function for exposed surface area. The distribution of exposed fiber area for the as-fabricated structure (0 MPa) follows a three-parameter Weibull distribution to better than 95% significance (x^2 comparison of the observed distribution and a Weibull distribution, with shape parameter β = 1.783, scale parameter δ = 140 and lower limit γ = 37.7). After monotonic loading the number of processing flaws observed decreased to nearly zero as a result of plastic deformation of the matrix material.
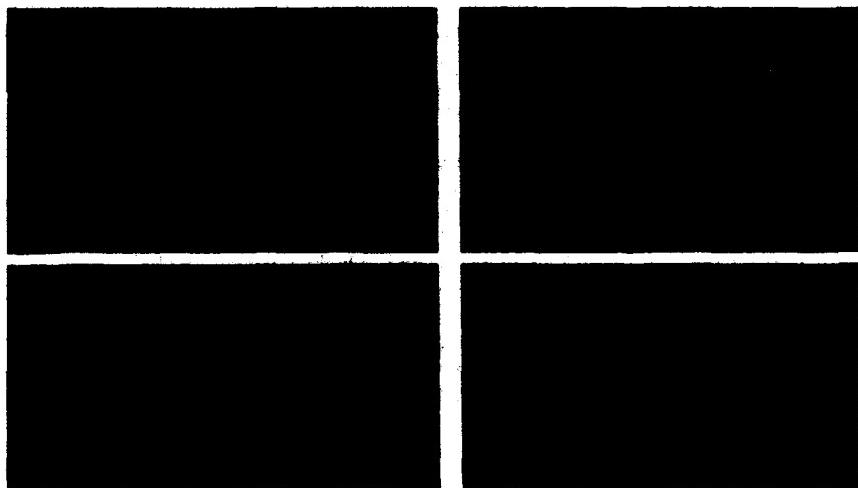
Figure 1. Typical slices at four of eight monotonic load levels studied. a) 0 MPa (as-fabricated); b) 828 MPa; c) 1241 MPa; and d) 1448 MPa (failure).
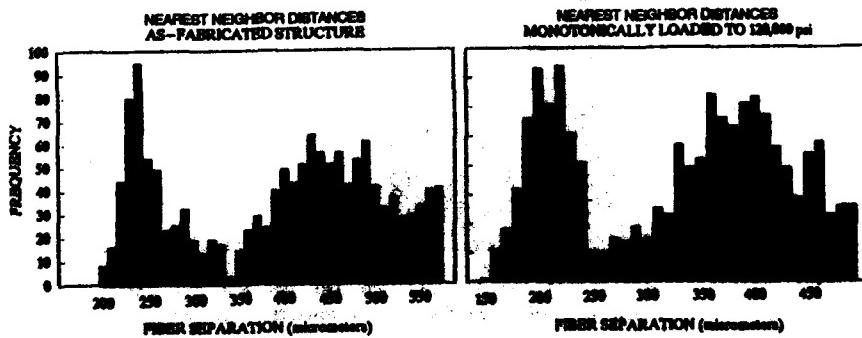
Figure 2. Distribution of first- and second-nearest neighbor fiber separations for 0 MPa and 828 MPa load conditions.

The unloading stiffness of the MMC coupons tested in this study increased with increasing load level; the observation of fiber rearrangement and of elimination of processing-related porosity with increasing load explain this effect. The change in fiber arrangement results in more uniform loading of fibers which increases the unloading stiffness. The presence of processing-related porosity may hasten the onset of fiber rearrangement and may promote homogeneity of fiber loading; viewed in this light, the processing defects might have a beneficial influence. Reduction of the volume fraction of porosity to a negligible level, however, probably does not eliminate the debonded areas of the fiber-matrix interfaces but does make this type of damage more difficult to detect.

The measured linear absorption coefficients from all samples agreed with tabulated values within 2% and are similar to previously reported results [3]. Evaluation of linear absorption coefficients in the fiber cores in samples stressed at and above 828 MPa revealed that the cores have fractured in 8 to 10% of all fibers over the 1.5 mm length of the sample examined. The specimen strain at 828 MPa is 0.67%, but the average strain-to-failure of the C cores prior to deposition of the SiC sheath is 3.1% [4]. Therefore, the average strain-to-failure of the fiber core can not be used to predict fiber fracture. Barrows [4] reported strain-to-failure of 1.04% for SiC fibers with 25.4 mm gage-lengths; increasing gage lengths decreased the strain-to-failure to 0.66%.The asymptotic limit is apparently independent of the thickness of the SiC fiber sheath. Several investigators [4,5] noted that the failure of SiC/C-core fibers initiates at the SiC/C interface but did not establish the load at which initiation occurred. This indicates that fiber fracture is controlled by flaws in the C core and/or interface layers between the SiC and C. These flaws could result from the SiC deposition process, elastic modulus mismatch, thermal residual strains, etc.

In Fig. 4 the low absorption features have been highlighted with air being the darkest and Al and SiC being the lightest pixels. The C core marked C is missing over a length of $40\mu m$. Figure 5 is an SEM micrograph of a fracture surface showing the core fractured and pulled-out approximately $40\mu m$. If the core fractures and elastically relaxes, the SiC portion of the fiber becomes a thick-walled cylinder with flaws on the internal surface. These internal flaws initiate fracture from the combined axial loading and Poisson contraction.
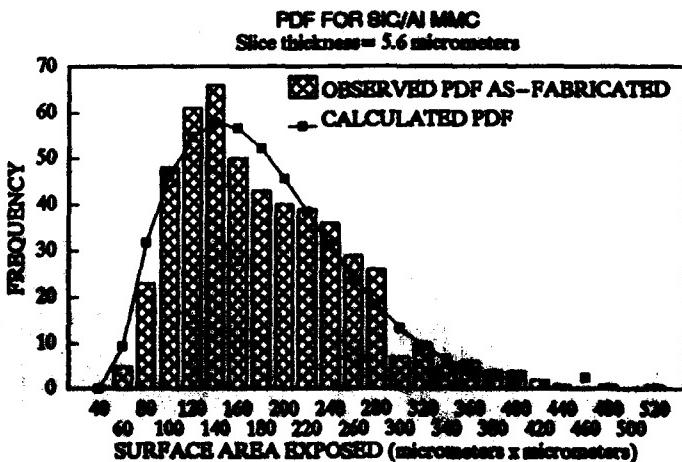
Figure 3. Fiber surface area exposed in square micrometers for the 0 MPa and 828 MPa. (The sample average is 164 μm^2 and the variance is 7,252 μm^2.)

Fracture of the overall MMC structure is controlled by fracture of the fibers. When a fiber breaks, the load it carried must be redistributed to the surrounding fibers, and a significant amount of strain energy is released. Many fibers fracture in more than one location due to the initiation of fracture in their cores; this fragmentation of the fibers, marked F, is shown in Fig. 6. The locations of individual fiber fractures are often widespread and far below the fracture surface. The fracture surfaces of the SiC fiber are not planar due to multiple initiation sites on the inside surface of the SiC sheath. Because of the multiple initiation sites at the C/SiC interface, fibers can shatter into multiple segments, marked MS in Fig. 6. The fibers also pull-out of the Al matrix, PO, because the matrix can not carry the high shear loads required for load transfer. Figure 7 shows enlarged regions from a cut parallel to the plies. In these images the contrast has been stretched to highlight the carbon core pull-outs and fiber fragmentation.

MODELLING

The mechanical/thermal response of a composite material can only be modelled realistically after damage initiation and accumulation phases are understood quantitatively. From the results presented above, a preliminary model of the fiber strength distribution could be developed. The model needs to account for core fracture events and their spatial distribution along the length of unit cell fiber segments. Since load transfer to the fiber is through the interface, the distribution of exposed surface area would be required to

0 μm   20.4 μm   40 μm
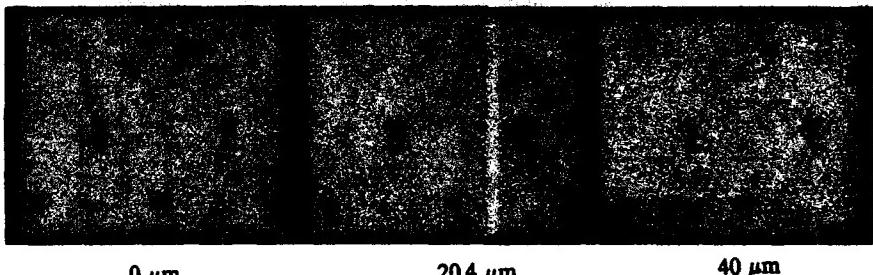
Figure 4. Carbon core fracture and pull-out. (Al and SiC are white and air is black.)

80 μm

Figure 5. SEM micrograph of a typical SiC fiber fracture surface. The carbon core extends about 40 μm from the SiC sheath.

determine the load distribution pattern on the fiber. The fiber arrangement would be used to determine unit cell sizes (each containing one fiber and its surrounding matrix). An incremental load would be applied to the model structure; the unit cell displacements and local load distributions are then calculated and, finally, specimen stiffness would be determined from the applied load and summation of displacements.

SUMMARY AND FUTURE TRENDS

This work demonstrates that nondestructive XTM can quantify the three-dimensional internal damage state of MMC specimens as a function of the macroscopic deformation level. Since XTM measures the x-ray absorption coefficients of the materials in a structure, the location of damage is related directly to the material/structure initiating the flaw.

In this study, damage was identified and quantified in a SiC/Al continuous aligned-fiber MMC for monotonic tensile loading from 0 MPa (as-fabricated) to 1448 MPa (fracture). In the as-fabricated state the principal form of damage is porosity at the fiber-matrix interface or between adjacent fibers: the exposed fiber surface area appears to follow a Weibull distribution with a mean of 164 μm^2 and a variance of 7,252 μm^2. As the applied load is increased the pre-existing processing voids disappear and the SiC fibers change from an arrangement intermediate between a square and hexagonal array to a hexagonal array.
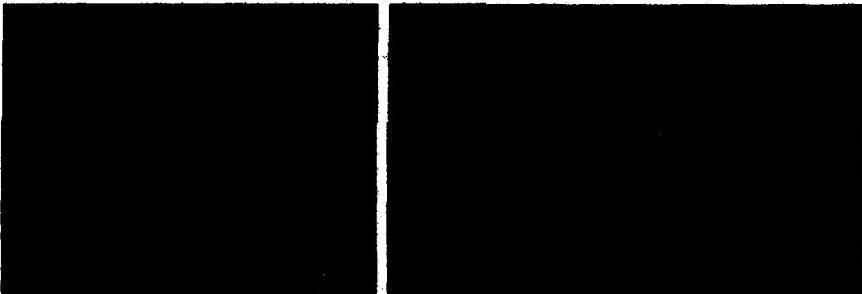
Figure 6. a) Slice normal to the fibers and loading axis and which contains shattered fibers, MS, and pulled-out fibers, PO. b) Cut parallel to the fibers and plies, showing fragmented fibers, F.
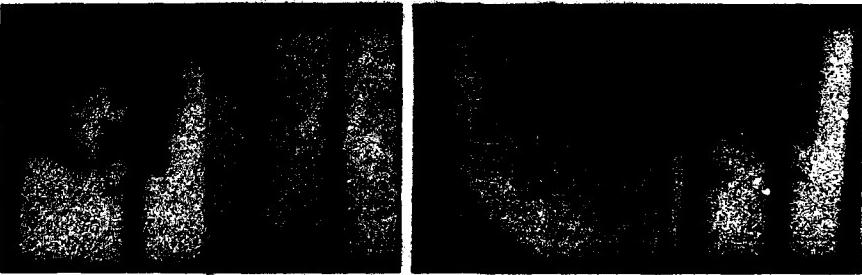
Figure 7. Enlarged view of two portions of the cut in Fig 6. showing a) fiber core pull-out and b) SiC fiber fragmentation. The low absorption features in a) and b) have been highlighted by stretching the contrast in these images.

This change in fiber arrangement results in more uniform loading of all fibers in the structure and appears to account for the increase in structural stiffness observed during unloading. The first indications of fiber failure were at 828 MPa (57% of the fracture stress). Carbon core fractures appears to initiate failure of the SiC sheath. The SiC sheath can break at multiple locations of each fiber, and the SiC fracture surface is irregular due to multiple initiation sites.

Future applications of XTM to damage studies in MMC will need to incorporate region-of-interest data acquisition, in-situ evaluation of structures and sub-micrometer spatial resolution. The region-of-interest sampling allows much larger samples to be examined, with high resolution data being collected only from the portion of the volume containing the feature(s) of interest. In-situ XTM will allow dynamic evaluation of material processes such as: crack face interaction during fatigue crack growth; damage development as a function of applied load, temperature, fatigue, etc.; environmental degradation; consolidation during sintering or other densification processes and liquid flow patterns in porous media. A compact in situ load frame has been constructed at Georgia Tech and its use for in situ XTM of SiC/Al MMC is anticipated in the first half of 1991. Region-of-interest data collection will allow in situ loading of larger specimens while preserving spatial resolution better than 5 μm; use of much larger specimens will eliminate concerns about edge effects and will allow the identical volume of material to be examined repeatedly. Improving spatial resolution of XTM to the sub-micrometer level is a definite possibility and will be of inestimable value in interpreting fiber-matrix debonding in composites, in identifying interphases at fiber-matrix boundaries and in characterizing crack face interactions during fatigue.

ACKNOWLEDGEMENTS

REFERENCES

1. U. Bonse, Q.C. Johnson, M.C. Nichols, R. Nusshardt, S. Krasnicki, and J.H. Kinney: *Nucl. Instrum. Methods*, A246, 644 (1986).
2. J.H. Kinney, R.A. Saroyan, M.C. Nichols, T.M. Breunig, and S.R. Stock: this volume.
3. J.H. Kinney, S.R. Stock, M.C. Nichols, U. Bonse, T.M. Breunig, R.A. Saroyan, R. Nusshardt, Q.C. Johnson, F. Busch, and S.D.Antolovich: *J. Mater. Res.*, 5, (5),112 (1990).
4. R.G. Barrows, in Failure Modes in Composites IV, edited by J.A. Cornie and F.W. Crossman (The Metallurgical Society of AIME Publishers, 1979), pp. 45-72.
5. K.D. McHenry, and R.E. Tressler: *J. Compos. Mat.*, 9, 73 (1975).

PREPROCESSING OF ION MICROTOMOGRAPHY DATA FOR IMPROVED RECONSTRUCTION QUALITY

DAVID L. WEIRUP*, ARTHUR E. PONTAU**, ARLYN J. ANTOLAK**,
DAN H. MORSE**, G. BENCH***, M. CHOLEWA***, A. SAINT***,
AND G.J.F. LEGGE***
  *Lawrence Livermore National Laboratory, Livermore, CA 94550
 **Sandia National Laboratories, Livermore, CA 94551
***Micro Analytical Research Centre, University of Melbourne,
Melbourne, Australia

ABSTRACT

In Ion Microtomography (IMT), material densities are determined
from the energy lost by ions as they pass through a specimen.   For fine-
scale measurements with micron-size beams, mechanical stability and
precision of motion can impact the quality of the reconstruction. We
describe several preprocessing procedures used to minimize imperfect
specimen manipulation, including adjustment of the center of mass
motion in sinograms and correction for vertical translations. In
addition, the amount of noise in the reconstruction is reduced by
utilizing median (as opposed to mean) ion energy loss values for
density determinations. Furthermore, particular portions of the
sampled image can be enhanced with minimal degradation of spatial
resolution by a judicial choice of spatial filter in the reconstruction
algorithm. The benefits and limitations of these preprocessing
techniques are discussed.

INTRODUCTION

Ion Microtomography (IMT), unlike x-ray computed tomography
methods, measures the energy lost by each ion rather than the fraction
of the radiation absorbed [1,2]. A number of residual ion energies,
typically 5 to 100 are measured for each sampled point. The incident
ion energy is chosen to ensure the primary source of energy loss is due
to interactions with specimen electrons and the charged ion. The mean
or median value of the energy loss distribution is used as the energy
loss value of the sampled point. The energy loss is then converted to a
density value using tabulated electronic stopping powers[3]. A single

projection is made by scanning the beam across the specimen, or translating the specimen through the beam for larger specimens. After each projection the specimen is rotated slightly to prepare for a new projection. Projections are acquired until the specimen has been rotated through 180 or 360 degrees. The density data are then reconstructed using a filtered backprojection technique. Multiple reconstructed slices may then be combined to form a 3-dimensional density image of the specimen.

A number of parameters can affect the ultimate resolution in the reconstructed density image. In this paper, we describe methods to preprocess the IMT data in order to improve the image quality. One parameter influencing the reconstruction is acquiring erroneous data due to ion damage in the detector. We describe changes made in the energy loss-to-density conversion code to help correct this problem. As beam sizes decrease, the accuracy and precision of the specimen movement system become important. Small scale perturbations in positioning alter the results so preprocessing adjustments must be made in the data. Another parameter is using the median, rather than the mean, residual ion energy to compute the line integrated density. We consider the trade-offs of using the median to eliminate spurious data but at the price of greater calculation times to evaluate. We also discuss the effects of using different filters with the reconstruction algorithm. Edge definition enhancement and density gradients are sensitive to the particular filter implemented.

PREPROCESSING TECHNIQUES TO CORRECT FOR MOTION ERRORS

With improvement in focusing ion beams to smaller sizes and the accompanying increase in image resolution, staging instabilities which could once have been safely ignored begin to have a large impact on reconstruction quality. Figure 1 shows tomographic data taken with a 0.25 micron proton beam of a 25 micron diameter glass pipette at the Micro Analytical Research Centre (MARC) of the University of Melbourne. Two hundred fifty-six contiguous slices were made of this pipette. To our knowledge, this is currently the highest resolution ion beam tomogram.

There were, however, a number of problems with this data which required preprocessing. The top row of images in Figure 1 shows several of the raw sinograms from the 256 slices. Each projection is

Figure 1   Sinograms and reconstructed images of a 25 micron pipette. This data was
            acquired at the Micro Analytical Research Centre (MARC) of the University of
            Melbourne. Row one contains three raw pipette sinograms displaying 1 to 5
            micron bearing wobble along the edges. Row two displays reconstructions of
            these sinograms. In row three the center-of-mass of each projection has
            been aligned to the center of rotation of the rotary manipulator. The
            reconstructions of the corrected sinograms are displayed in row 4.
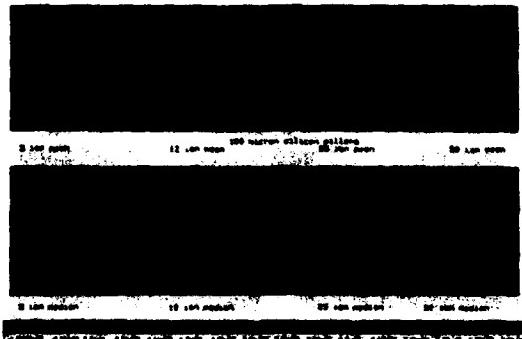
Figure 2   Reconstructed images of a silicon specimen using different numbers of ions
            and either the mean or median value of the residual energy loss distribution.

made up of 256 rays with a projection taken every degree over 180
degrees. The effect of 1 to 5 micron bearing wobble in the manipulator
rotation is seen along the edges of the sinograms. The second row of
images display the reconstructions of the raw sinograms. Because of
the bearing wobble effect, the reconstruction code could not correctly
reconstruct the data about any one center of rotation. The third row of
the figure shows the sinograms after making center of mass
corrections[4]. In the image the center of mass of each projection has
been shifted to a position equivalent to having the pipette perfectly
aligned at the manipulator's center of rotation. The fourth row of
images are the reconstructions of the corrected sinograms. As
resolution increases this technique or similar techniques which
preserve correct spot spacing will become more important in acquiring
and presenting useful data.

MEDIAN VS MEAN ENERGY LOSS VALUES FOR DENSITY DETERMINATION

The transmitted ion energy loss at each sampled point can be
calculated with either a mean or median value The mean value is
faster computationally since the processing can be done as each ion is
detected. On the other hand, calculation of the median value is more
time consuming, but is less sensitive to extraneous data points[5]. Fig.
2 shows reconstructed images of a silicon pillars specimen using
different numbers of ions and either the mean or median value from the
residual energy distributions. As can be seen in the figure the median
produces a less noisy image. The improvement in image quality using
the measured median energy loss greatly outweighs its additional
computational expense even in large data sets.

ION DETECTOR CALIBRATION

IMT measurements are also conducted at the Sandia Microbeam
Analysis Laboratory in Livermore (SMALL)[1] collaboratively with the
Lawrence Multi-user Tandem Laboratory[6]. Our data acquisition
system utilizes a silicon surface barrier detector to measure residual
ion energy. The detector is subject to damage from the ions depending
upon their energy and fluence. We raster the detector to reduce the
exposure time that the beam hits any given spot. The damage causes a
shift in the measured energy and thus produces erroneous values in the
IMT data file. In early reconstructions, the detector calibration was

determined with only one energy value. The associated sinograms
reflected this shift in energy due to the detector damage. To account
for this, the energy loss-to-density conversion code was modified to
calculate individual detector calibrations for each row of IMT data.
Fig. 3 shows sinograms of a silicon specimen using 100 protons per
sampled spot. The first image shows the sinogram using one value for
the calibration. The second shows the same sinogram when a separate
calibration is computed for each projection. The third image is their
difference. The reconstruction average density increases by 0.08%
with the modified version of the code and the image noise decreases by
1.6% in standard deviation.

SPATIAL FILTERS

The choice of filter used with the backprojection algorithm can also
affect the final reconstructed image[7]. Figure 4 shows four
reconstructions of the silicon pillar data. Each is reconstructed from a
data set made with 100 protons per spot using median data. The top
two images are filtered with a Hamming filter, the bottom two use a
6th order Butterworth approximation for a ramp filter. The Hamming
filter tends to accentuate the lower frequencies in the reconstruction,
and is used for enhancing density gradients in the specimen. The
Butterworth filter amplifies the higher frequency components. This
type of filter is used in edge definition studies or for examining
machined surfaces. It is very important that the experimenter is aware
of the variations a filter selection will make to his reconstruction. It
is quite possible to hide or smear the exact feature of interest if an
improper filter selection is made.

SUMMARY

The improvement in resolution of IMT systems has brought about
problems related to specimen manipulation and detector damage caused
by the resolution related increase in sampling time. This paper has
described preprocessing techniques developed by the authors to solve
these problems.

Figure 3   This figure displays the effect of ion damage to a silicon surface barrier
detector. The first image displays a sinogram of a silicon specimen acquired
using 100 ions and the median value of the residual energy loss distribution
when one value is chosen to calibrate the detector. The second image shows
the same sinogram when a separate calibration is computed for each
projection. The final image is their difference.
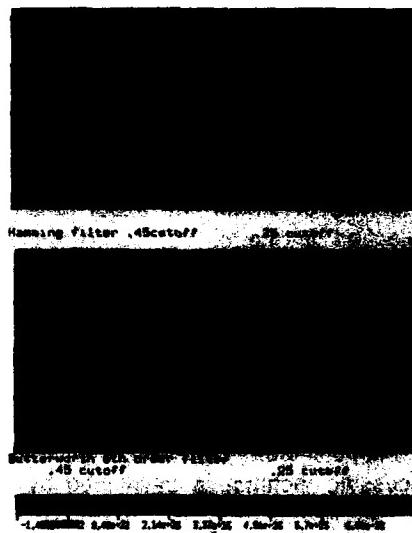
Figure 4   The top row displays reconstructed images of a silicon specimen filtered
using a Hamming filter at two different cutoff frequencies. The bottom row
displays the same data reconstructed using Butterworth 6th order filters at
cutoffs corresponding to those of the top row.

ACKNOWLEDGEMENTS

REFERENCES

1. A. E. Pontau, A. J. Antolak, D. H. Morse, A. A. Ver Berkmoes, J. M. Brase, D. W. Heikkinen, H. E. Martz and I. D. Proctor, Nuc. Inst. Meth. B40.41 (1989) 646.

2. A. E. Pontau, A. J. Antolak, D. H. Morse, Nuc. Inst. Meth. B(1990) in press.

3. F. Ziegler, Handbook of Stopping Cross-sections for Energetic Ions in all Elements,Pergamon Press, New York, 1980.

4. S. G. Azevedo, D. J. Schneberk, J. P. Fitch, H. E. Martz, LLNL Report UCRL-102615, IEEE Trans. Nuc. Sci., Vol.37, #4 (Aug. 90), 1525-1540.

5. J. C. Overly, R. M. S. Schofield, J. D. MacDonald, and H. W. Lefevre, Nucl. Inst. Meth. B30 (1988) 337.

6. I. D. Proctor, J. C. Davis, M. R. Eaton, J. I. Garibaldi, T. L. Moore, B. J. Schumacher, J. R. Southon, and T. A. Zimmerman, Nucl. Inst. Meth. A268 (1988) 344.

7. D. J. Schneberk, H. E. Martz, S. G. Azevedo, M. Skeate, LLNL Report UCRL-101264, (1989), and The American Society for Nondestructive Testing Topical Conference on Industrial Computerized Tomography Topical Proceedings, July 25-27, Seattle, WA, Am.Soc.for NDT, Columbus OH (1989)609.

ADVANCES IN CONE-BEAM RECONSTRUCTION
FOR THE ANALYSES OF MATERIALS

BRUCE D. SMITH
University, Dept. of Electrical & Computer Engineering, Mail Location 30, Cincinnati, OH 45221

INTRODUCTION

The utility of cone-beam tomography in the analysis of material has been demonstrated by Feldkamp et al [1]. Recent advances in cone-beam tomography will enhance its usefulness in the analysis of material.

Review of literature

Improvements in the theory of cone-beam tomography was made in [2,3]. In [2] the so-called "completeness condition" was developed. When cone-beam data is collected, the vertex of the cone is moved in some fashion about the object. The completeness condition specifies whether enough information to produce an artifact-free three-dimensional reconstruction can be collected from a given geometry of vertices as the vertex is moved about the object. Additionally, two novel reconstruction methods were developed [2].

Further improvements followed in [3]. The theory presented in [3] eliminated the need to form the homogeneous extension of the cone-beam data. This made possible improvements in efficiency in two methods in [2] and the development of a third reconstruction method. Since [3] is not widely available, a derivation of these results was published in [4].

The scope of this paper

An abridged non-mathematical review of three novel reconstruction methods proposed by the author will be presented in this paper. Additionally, a comparison is made of a method, which is based upon these three methods, and the method first proposed by Feldkamp. In section 2 the necessary theoretical background is presented. In section 3 the three novel reconstruction methods are presented. Finally, in section 4 the results of the comparison are discussed.

BACKGROUND THEORY

New functions for cone-beam tomography

In cone-beam reconstruction, the Fourier transform does not play such a key role as it does in parallel tomography. It seems the three-dimensional divergence of the cone-beam data does not lend itself to Fourier transform theory. Rather the function F, defined in [3] and [4], will play a role in cone-beam reconstruction similar to the role played by the Fourier transform in parallel tomography. It can be directly involved in the reconstruction process just as the Fourier transform is involved in the "Direct Fourier Method" as described in [5]. Or it can be used as an intermediate step in the development of more efficient inversion formulas. More importantly, the function F can be used to describe all the information that is contained within the cone-beam data collected from some geometry of vertices and what information, if any, is missing.

A second new function has to be defined as well. As explained in [3] and [4], the function G plays an intermediate role in computing F from the cone-beam data. By its definition the function G is closely related to the cone-beam data. Since cone-beam data is divergent, the function G can be thought of as "something divergent". In contrast, since the function F is closely related to the three-dimensional Radon transform, it can be thought of as "something parallel".

A "generalized rebinning" formula that relates the function G to F is developed in [3] and [4]. This makes the connection between something that is divergent to something parallel. This rebinning allows all the information contained within the divergent cone-beam data to be described in terms of "something parallel", namely, the function F. Since parallel-beam tomography is well understood, describing the information contained in the cone-beam data in terms of the function F makes the analysis and inversion of cone-beam data possible.

The "completeness condition" for vertices geometries

It can now be determined whether the information that results from some geometry of vertices is enough to perform an artifact-free reconstruction. The formula which inverts F to obtain the object, specifies what information needs to be obtained. If for a given geometry it is possible to obtain this information by rebinning the function G, then an artifact-free reconstruction can, at least in theory, be obtained using the data collected. If for a given geometry it is not possible to obtain the information, then without using extrapolation, it is not possible to obtain an artifact-free reconstruction of an arbitrary object. (There exists "special" objects that can be reconstructed without the use of extrapolation, e.g., a spherically symmetric object, but these objects are not of practical importance and will not be considered here.) Resulting from the above argument is the following simple rule, referred to as the "completeness condition", which specifies whether enough information can be measured from a given geometry to produce an artifact free reconstruction.

> If on every plane that intersects the object there lies a vertex, then one has complete information about the object.

The "sine on the cylinder" geometry, which is discussed in [4], is an example of a complete geometry. A circle is an example of a geometry that is not complete.

THREE NOVEL RECONSTRUCTION METHODS

Knowing whether a given geometry of vertices could possible yield enough information to produce an artifact free reconstruction is clearly of importance. This in itself, however, will not invert the data. Computer algorithms for inverting cone-beam data are clearly needed. Toward this end, three novel exact reconstruction methods are developed in the [3] and [4]. A number of attributes are desirable of a reconstruction method. How each of the three novel reconstruction methods fare with respect to many of these attributes is now discussed.

One novel reconstruction method

The most computationally inefficient of the three novel cone-beam methods, since both the functions G and F have to be computed. It is flexible as to what data collection geometries can be used with it. A priori information is easily incorporated for extrapolation.

A second reconstruction method

This method is more computationally efficient than the first, since only G needs to be computed. It also may be applied to any data collection geometry.

A third reconstruction method

This method is extremely computationally efficient, since neither F nor G needs to be computed. The reconstruction is exact if the vertex geometry intersects almost every plane that intersects the object exactly n times. The only geometry which is know that satisfies this condition is an infinitely long straight line.

A COMPARISON WITH A STANDARD CONE-BEM ALGORITHM

Using computer generated data, a comparison was made between the algorithm first proposed by Feldkamp and an algorithm that is based upon the three methods presented. Although the grey levels near the bottom and top are low, the results indicated the algorithm based upon the novel methods eliminate the z directional blurring associated with Feldkamp's algorithm. Moreover, same number of computer operations are required for both algorithms.

CONCLUSION

Three novel reconstruction methods have been discussed along with the necessary background theory. Using computer simulated data, a comparison was made between a standard cone-beam algorithm and an algorithm which is based upon the three novel reconstruction methods presented here. It was seen that the novel algorithm eliminates the z directional blurring and required the same number of computer operations.

References

[1]   L.A. Feldkamp, L.C. Davis, and J.W. Kress, "Practical cone-beam algorithm," J. Opt. Soc. Amer. A, vol. 1, pp. 612, 1984.

[2]   B.D. Smith, "Image reconstruction from cone-beam projections: Necessary and sufficient conditions and reconstruction methods," IEEE Trans. Med. Imag., vol. MI-4, pp. 14, 1985.

[3]   B.D. Smith, Computer-Aided Tomographic Imaging from Cone-Beam Data, (Ph.D. Dissertation) University of Rhode Island, 1987.

[4]   B.D. Smith, "Cone-beam tomography: recent advances and a tutorial review," Optical Engineering Journal, vol. 29, pp. 524-534, May 1990.

[5]   H. Stark, "Direct Fourier reconstruction in computer tomography," IEEE Trans. Acoust., Speech Sig. Process., vol. ASSP-29, pp. 237-245, 1981.

PART III

Diffraction

ULTRASONIC COMPUTED TOMOGRAPHY FOR IMAGING BONES AND ADJOINING SOFT TISSUES

C. M. SEHGAL[*] and J. F. GREENLEAF[**]
[*]Department of Radiology, University of Pennsylvania, Philadelphia, PA 19104
[**]Department of Physiology & Biophysics, Mayo Clinic, Rochester, MN 55905

INTRODUCTION

The skeletal system of bones and cartilage forms a framework that supports and protects soft tissues. It also provides surfaces to which muscles, ligaments and tendons attach and coordinate movement of bones. Since such musculoskeletal system serves as a "structural" element of the body it is easy to see that its functional capabilities are closely related to it mechanical strength. Consequently, there have been numerous attempts to characterize the properties of bones. Currently, several sophisticated diagnostic procedures and radiographic imaging techniques are available for quantitative purposes. Virtually all the available methods are based on the measurement of mineral content of the bone. It is well known that it is the combination of the organic and the inorganic components that determine the strength of the bones. Thus, in principle, the traditional methods can provide only part of the information about the bone tissues. With this shortcoming in view an effective case can be made for the development of a technique that measures both the components. Many researchers have looked at ultrasonic energy to fulfill this role. The rationale for the choice of this energy is that ultrasound is a "mechanical radiation" and its propagating properties provide a direct measure of mechanical strength or related property of the medium.

Velocity of sound transmission and its attenuation during propagation are the most widely studied properties to characterize bones. In an early study Anst et al. [1] reported measurement of ultrasound velocity across fracture sites in human and experimental animals. Since then there has been periodic activity in using sound speed to determine the strength of bones. More recently it has been shown that sound speed can be used as an indicator for fragility of bone due to osteoporosis [2], and to assess the quality of bone in the human newborns [3]. It has also been observed that ultrasound velocity of bones correlates with the performance of marathon runners [4].

ULTRASOUND FOR MONITORING BONE HEALING

One of the problems often faced during the fracture healing process is the determination of bone stability after fracture. The radiographic technique in many cases does not provide sufficient evidence to determine the point when the functional capacity of bone has returned to normal. There have been various attempts in the past to identify the union of bones by using ultrasound.

Abendschein and Hyatt [5] measured transmission speed of ultrasound through human femoral and tibial diaphyseal cortices obtained immediately after lower-extremity amputation

and showed that their sound speed values varied with the pathology of bones. From their measurements they also calculated modulus of elasticity, E_l, by the following equation,

$$E_l = \rho c^2, \tag{1}$$

where ρ and c represent density and sound speed of the bone sample. Elasticity measurements were also made by the static method and compared with E_l. The two parameters were found to be linearly correlated but showed deviation from the line of identity. This difference was attributed to the fact that bones are viscoelastic and not elastic as assumed by the Equation 1. Nevertheless, the linear correlation shows that sound speed can be used as an index to observe changes in the properties of bones. These results have provided basis for belief that ultrasound could potentially be used for diagnosing and evaluating healing of bones after fracture.

ONE DIMENSIONAL TECHNIQUES

One dimensional techniques are simple and easy to implement. The results from several in vivo studies reported in the literature have been very encouraging. Yet the ultrasonic techniques have not yet been accepted in clinical medicine for routine use. One of the prime reasons is the significant fluctuation in the measured data. This could be due to biological variability of tissues, but also due in part to the method of measurement which in the majority of cases is made by placing collinear transducers on the limbs. First the sites of measurement at different times of bone healing are not identical. Secondly, by one line measurement it is difficult to account for the variable lengths of overlying soft tissue. This is further complicated by the fact that the measurements are generally made in the near field at relatively low frequencies, 20 – 200 kHz, at which there is significant diffraction.

To get around the problem of poor reproducibility an interesting approach was proposed by Leitgeb [6]. This was based on the analysis of properties of soft tissues around bone fracture rather than the crack. It is well known that if fracture occurs, in most cases, a fairly annular hematoma is formed around the fracture. As the fracture heals the composition of hematoma changes. In the early stages there is increasing collagen. This is followed by increasing amounts of calcium. The formation of callus can be regarded as an indica, r of stability of fracture. The transformation of hematoma which is blood-like to bone-like callus, can in principle be used to monitor bone healing by observing the difference in echo times from the hematoma and the bone surface. This preposition assumes that dimensions of callus remain constant through-out the healing process. This may not be always true. Moreover, the measurements must be taken at the same site and with the same inclination and so this method suffers from the same limitation as the conventional methods.

ULTRASONIC CT IMAGING

The problems listed above can be significantly minimized by using computed tomography (CT). The application of ultrasonic energy to CT methods was first proposed by Greenleaf et al. to image breast. The prototype developed for such imaging consists of a pair of transducers mounted on an assembly that moves linearly in steps of one millimeter; executes rotation about center axis; and can move up or drop down to scan different planes.

The assembly is enclosed in a water tank . At each position the transducer transmits a shock excited narrow pulse. The transmitted energy is received by the second collinear transducer. The signal is received and amplified. By integrating and thresholding the signal the transmitted energy and travel time profiles are determined. Such profiles collected from different angles of view (60 in general) are used for CT reconstruction by assuming straight line propagation. At the imaging frequency of 3 to 5 MHz, sound truly does not travel in straight line and there is noticeable diffraction which leads to image artifacts. Recently, another feature has been added to the CT scanner. In addition to transmission there is now provision to gather reflected energy simultaneous to transmission measurements. Each of these signals is time gain compensated and used to reconstruct a linear B-scan. The scans obtained from all the angles of views are added to yield a compound B-scan. Such averaging of back scatter from different angles of view reduces speckle and provides a high quality image. Thus, three images of a given cross-section are obtained, each representing a different property of the tissue. The attenuation images represents the energy loss due to scatter and transformation of sound energy to heat; the sound speed tomogram represent a measure of compressibility of tissues; and, the compound B-scan represents a map of acoustic impedance mismatch, or inhomogeneities and boundaries. With this powerful technique at hand our first aim was to determine if this methodology can be used for reconstructing images of bones and the soft tissue that surrounds it.

Animal bones of turkey and dog limbs, and cadaveric human excised limb were scanned by suspending the tissue in the water scanner. Examples of these images for human limb are shown in the Figures 1 and 2.
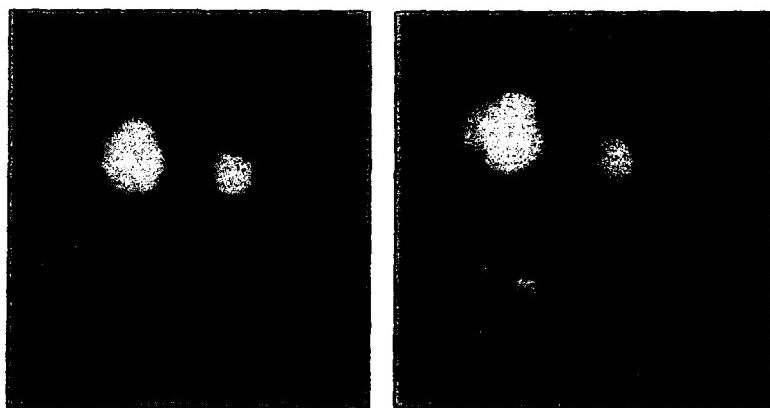
Figure 1. Ultrasonic CT image reconstructed from attenuation data measured across a plane of cadaveric leg. The bright regions indicate high attenuation and represent bones.

In all our scans soft tissue and the skin was kept in tact. In all cases we were able to transmit enough energy to obtain attenuation images. However, the transmitted signal was weak and the use of threshold method to determine arrival time lead to significantly noisy speed image. This problem can probably overcome by using an alternate approach of

measuring travel time. The refraction effects that are very dominant in breast imaging were not observed significantly in any of the studied cases. One probable explanation for this is that the limbs do not offer as strong a curvature across the beam as the breasts. The near perpendicular incidence minimizes the refraction effects. In the back scatter image shown in Figure 2 the internal structure of bones is difficult to visualize, but the structure of soft tissue can be seen in great detail.
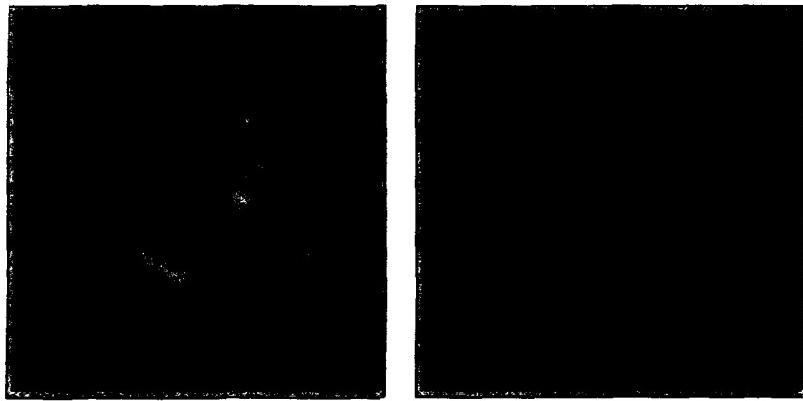
Figure 2. Compound B-scan of another plane of human leg. The dark regions represent bones.

VOLUMETRIC IMAGING

Two dimensional reconstructions of the type shown in Figures 1 and 2 show information on the shape of any particular structure and its relationship to other structures in a given plane. Additional information on the shape of the structure like hematoma and its relationship to other structures in the other adjacent planes is often needed. Three dimensional information is obtained by constructing 2D images in multiple contiguous planes in the third dimension and stacking them serially as indicated in Figure 3.

Once the data are mapped into a volumetric matrix composed of cubical voxels it can be numerically dissected in any plane; projected or volume rendered from different angles of view. To see if the data collected from the ultrasonic scanner had sufficient integrity for such a synthesis, data from 80 cross-sections were gathered by dropping the scanner in 2mm steps. The data were stacked and interpolated to obtain a volume composed of cubical voxels. The cubical data of animal bones when dissected in orthogonal planes provide high resolution images [7].
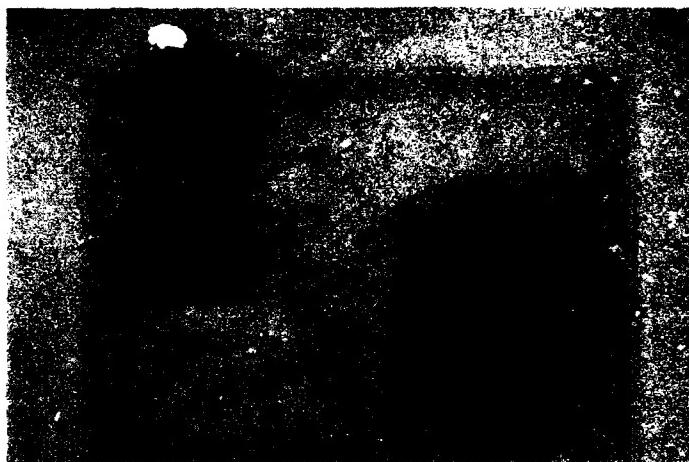
Figure 3. Schematics of numerical synthesis of volumetric images by stacking two dimensional images.
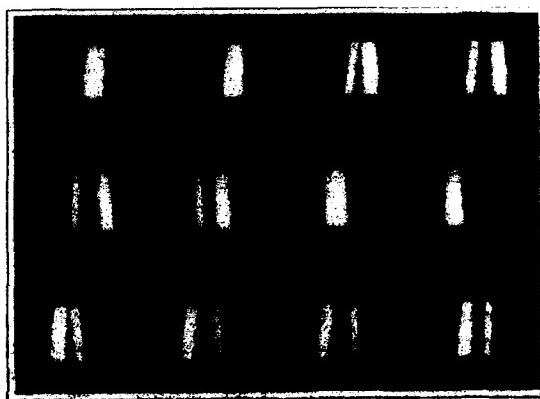
Figure 4. Projection images constructed by numerically transmitting rays through the imaged volume from different volumes and projecting the brightest pixel.

162

By using Mayo developed software ANALYZE [10], the data from human leg was projected by selecting the brightest pixel along the ray tracings. The projection images of attenuation data from different angles of view are shown in Figure 4. The surface display of the same data is shown in Figure 5.

Figure 5. Surface display of imaged excised leg.

The markings as seen on the images represent sutures on the skin of the cadaveric limb. Both Figures 4 and 5 show that the data collected from the ultrasonic scanner can be used for three dimensional imaging of bones and the surrounding tissues.

MEASUREMENTS FROM VOLUMETRIC IMAGES

After obtaining evidence in support of the hypothesis that ultrasound data can be used for volumetric imaging our next aim was to make some measurements. Although as mentioned earlier the sound speed images were most noisy this parameter is best understood. Therefore, it was our first aim to make measurements of this parameter. The speed image data was organized into volumetric matrix and the brightest pixel projected on to planes from different angles of views. This procedure got rid of noisy points and provided a means of measurements. Regions of interest were chosen by outlining bone and soft tissues in the images synthesized from different angles of view. Measurements were made on the areas enclosed within an outlined region. One example of such measurement is shown in Figure 6.
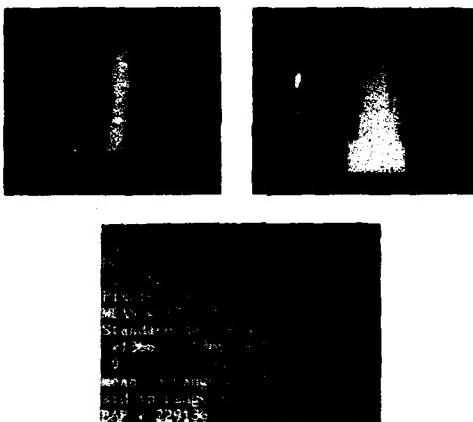
Figure 6. Illustration of sound speed measurement made on bone. Region of interest was outlined. The histogram of this measurement is shown in the right panel. The bottom panel shows printout of measurement. The measurements were made by using ANALYZE software.

Excised hind legs of a new born, a 13 week puppy and an adult dog were scanned. The preliminary measurements of sound speeds are shown in the table below.

	New born	13 Wk old puppy	Adult dog
Bone	1573 (18)	1641 (17)	1790 (45)
Soft tissue	1541(5)	1551 (19)	1575 (20)

Table 1. Measured sound speed (m/sec) in dog bones from animals of different ages. The numbers in parenthesis represent standard deviation. The temperature of measurement was room temperature (approximately 25 degrees Centigrade).

Though the sample size is small to make definitive conclusion, our initial investigation reveals sound speed of bone as well as the surrounding soft tissue to increase monotonically with age. This is consistent with the expectation from the relationship between tissue

composition of bones of animals and their age. Studies of Simonet et al. [8] showed water content of cortical and cancellous bones decrease with age. If one regards bone to be a made up of water and a second component consisting of high speed material like minerals or collagen the sound speed will be represented by [9],

$$\frac{1}{c} \simeq \frac{1}{c_w} - \left(\frac{1}{c_w} - \frac{1}{c_m}\right)\chi \tag{2}$$

where χ is the volume fraction; c the sound speed and subscripts w and m representing water and mineral components of the tissue. A decrease in water and an increase in mineral content (higher sound speed) as is observed with the age of the animal will result in higher sound speed. This is in accordance with the measurements.

CONCLUSIONS

The application of ultrasonic CT method is still in the early stages of development. Although there are several attractive features about using ultrasound several key questions need to be further answered before the technique can find application in clinical medicine. The results shown here demonstrate that it is technologically feasible to obtain high resolution images without using ionizing radiation. The data can be used for reconstructing three dimensional images and thus overcome the problems accompanying single line measurements. Further validation and quantification of this technique is now under progress.

REFERENCES

1. G.T. Anst, T. Fields and I.M. Siegel. Ultrasonic technique for the evaluation of bone fractures, Amer. J. Phys. Med. 37:157 (1958).

2. R.P. Heaney, L.V. Avioli, C.H. Chestnut III, J. Lappe, R.R. Recker, and G. H. Brandenburger. JAMA, Vol. 261:2987-2990 (1989).

3. L.L. Wright, M.J. Glade, and J. Gopal. Pediatr. Res., 22:541-544 (1987).

4. C.T. Rubin, G.W. Pratt Jr., A.L. Porter L.E. Lanyon and R. Poss. The use of ultrasound in vivo to determine acute changes in the mechanical properties of bone following intense physical activity. J. Biomechanics, 20:723-727 (1987).

5. W. Abendschein and G.W. Hyatt. Ultrasonic and selected physical properties of bone. Clin. Orthopaedics Research and Related Res. 69:294-301 (1970).

6. L. Leitgeb. A new noninvasive quantitative method for fracture diagnosis. Medical Progress through Technology. 11:185-190 (1986).

7. C.M. Sehgal, D.G. Lewallan, J.A. Nicholson, R.A. Robb and J.F. Greenleaf. Ultrasound transmission and reflection computerized tomography for imaging bones. IEEE Ultrasonic Symposium, Chicago, IL Vol. 2:849-852 (1988).

8. W.T. Simonet, J.T. Bronk, M.R. Pinto, E.A. Williams, T.H. Meadows, P.J. Kelly. Cortical and cancellous bone: Age-Related changes in morphologic features, fluid spaces and calcium homeostasis in dogs. Mayo Clinic Proc. 63:154–160 (1988).

9. C.M. Sehgal, G.M. Brown, R.C. Bahn and J.F. Greenleaf. Measurement and use of acoustic nonlinearity and sound speed to estimate composition of excised livers. Ultrasound in Medicine and Biology, 12:865–874 (1986).

10. R.A. Rob, P.B. Heffernan, J.J. Camp and D.P. Hanson. Workstation for interactive display and quantitative analysis of 3D and 4D biomedical images. IEEE Proceedings of Computer Applications in Medical Care, 240-256 (1986).

PART IV

Multi-Modality

THREE-DIMENSIONAL NUCLEAR MAGNETIC RESONANCE AND X-RAY MICROTOMOGRAPHIC IMAGING OF COMPOSITE MATERIALS

S.L. DIECKMAN,* P. RIZO,‡ N. GOPALSAMI,* R.E. BOTTO#
*Materials and Components Technology Division, Argonne National Laboratory, 9700 S. Cass Ave., Argonne, IL 60439
‡L.E.T.I./Départment Systèmes, C.E.A./ C.E.N.G. 85X Avenue des Martyrs 38041 Grenoble Cedex, France.
#Chemistry Division, Argonne National Laboratory, 9700 S. Cass Ave., Argonne, IL 60439.

ABSTRACT

This paper presents a new, three-dimensional (3-D) nuclear magnetic resonance (NMR) imaging technique for spatially mapping proton distributions in green-state ceramic composites. The technique is based on a 3-D back-projection protocol for data acquisition, and a reconstruction technique based on 3-D Radon transform inversion. In principle, the 3-D methodology provides higher spatial resolution of solid materials than is possible with conventional slice-selection protocols. The applicability of 3-D NMR imaging has been demonstrated by mapping the organic additive distribution (2.5 wt.%) in cold-pressed Si_3N_4 whisker-reinforced Si_3N_4 ceramic composites. Three-dimensional X-ray computed tomography (CT) also has been employed for mapping voids and inclusions within the composite specimen. Combining information from both imaging modalities provides an extremely powerful nondestructive evaluation tool for materials characterization.

INTRODUCTION

Process development in the mass production of high-performance structural ceramics and ceramic composites requires a detailed understanding of the macro- and micro-structural characteristics of the ceramic materials in relation to the processing conditions. The origin, nature, and effect of flaws (such as voids, cracks, inclusions, and density variations) must be understood in order to ensure the continuing technological development of advanced processing techniques. Nondestructive evaluation techniques, such as nuclear magnetic resonance (NMR) imaging and X-ray computed tomography (CT), can play a key role in this endeavor by providing detailed diagnostic measurements on selected specimens before, during, and after various processing stages.

Application of X-ray CT techniques to the study of advanced structural materials has been under development in recent years [1,2]. The use of 3-D X-ray CT for interrogation of ceramic components has been demonstrated and has quickly become an accepted NDE method. X-ray CT provides detailed information on the spatial distribution of internal voids, cracks, inclusions, and density gradients. However, heterogeneous materials are less amenable to analysis by conventional X-ray CT techniques because local compositional differences and density variations cannot readily be distinguished.

NMR imaging, on the other hand, is sensitive to local chemical environments in complex molecular solids. Moreover,

the technique has the unique capability of spatially mapping a sample's chemical or physical properties independently. Two-dimensional NMR imaging has proven to be an extremely versatile tool for the chracterization of numerous solid materials [3-10], including mapping the organic distributions in green-state ceramics [3-6]. However, a major difficulty in obtaining adequate spatial resolution in the third dimension rests with the intrinsic NMR properties, i.e., broad linewidths, that are characteristic of many solids.

In this paper, we describe a 3-D NMR method that is based on a back-projection protocol in combination with image reconstruction techniques based on 3-D Radon transform inversion. Similar techniques have been described previously for imaging of liquid samples [11,12]. The method incorporates the experimental flexibility to overcome the difficulties which are presented by broad-line materials. This method has been applied to the analysis of specimens consisting of cold-pressed Si_3N_4-whisker-reinforced Si_3N_4 composites. X-ray microtomographic imaging techniques were used in combination with NMR to provide a map of the intrinsic density of the samples. The information obtained from the two modalities allows a complete analysis of both the organic and inorganic distributions within these materials.

MATERIALS AND METHODS

The NMR imaging system used in this study consisted of a Bruker CXP-100 NMR spectrometer fitted with a home-built imaging accessory which is described in detail elsewhere [5]. The accessory, designed specifically for examining solid materials, consists of a versatile home-built IBM/PC based pulse programmer, three (X,Y,Z) Techron audio range 1-kW gradient amplifiers, a RF shaping unit, and a home-built, singly-tuned imaging probe capable of operating at 1-kW RF levels. The probe also contains forced-air-cooled gradient coils capable of operating with duty cycles in excess of 20% while producing a highly linear magnetic field gradient of 58 G/cm over a spherical space of 30 mm in diameter.

In a conventional 2-D NMR back-projection tomographic experiment, one applies a linear magnetic field gradient in a plane at numerous projection angles. For each angle, the Fourier transform of the data represents a planar integral of the proton density normal to the gradient vector. Similarly, in the 3-D back-projection experiment, by varying the gradient vector in order to sample the entire 3-D space, one obtains a 3-D Radon transform of the proton density. Let Rf(P) be the Radon transform of the object function f(M), where P and M are discrete points in the Radon and object space, respectively (Fig. 1):

$$Rf(P) = \int_{(OP.OM)=0} f(M)dM$$

$$(1)$$

The inversion of this transform can be obtained by double differentiation and back projection. Marr et al. [13] have shown that the fastest way to invert the Radon transform is to use two sets of back projections, one along the meridian planes

and the other along planes of constant latitude. The inversion can then be written as (Figure 2):

$$f(M) = \frac{1}{4\pi} \int_{\theta=0}^{\theta=\pi} \int_{\phi=0}^{\phi=\pi} \frac{\partial^2 Rf}{\partial \rho^2}(\rho(M,\theta,\phi),\theta,\phi)\sin\theta \, d\theta \, d\phi \tag{2}$$

where ρ,θ,ϕ are the classical parameters of spherical coordinates, and $\rho(M,\theta,\phi) = OM \cdot n$, where O is the origin and n is the unit vector in the direction (θ,ϕ). The reconstruction algorithm of the 3-D Radon transform inversion was implemented as proposed by Grangeat and coworkers [15].

Three-dimensional NMR imaging data were acquired on specimens using 128 complex data points, and a total of 1024 projections (16 θ angles over $\pi/2$ radians x 64 ϕ angles over 2π radians). A gradient strength of 35 G/cm and a sweep width of 100 kHz were used. A total of 128 averages were acquired by using an approximate 90° pulse and a recycle delay time of 0.25 s. A spectroscopic resolution of 175_x x 175_y x 175_z μm^3 was achieved. A total of 18 hours was required for data acquisition using these parameters.
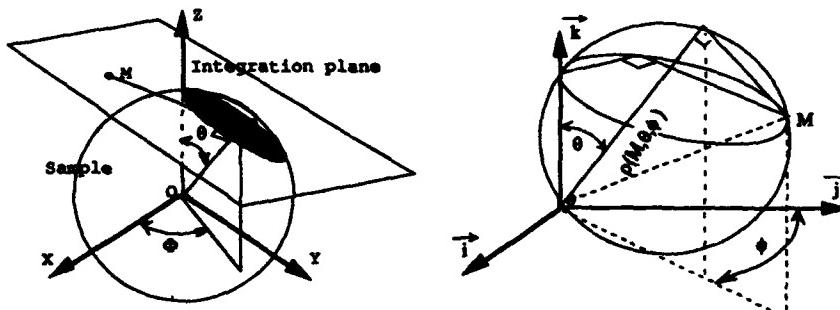
Fig. 1. Definition of 3-D Radon transform. Value of 3-D Radon transform in P is the integral of points M in plane defined by OP⊥MP.

Fig. 2. Decomposition of integral over a sphere in two series of back-projections.

The 3-D X-ray microtomograph system used in these experiments consists of a microfocus source, a image intensifier, a CCD (512^2) camera, manipulation stages (X,Y,θ), and an IBM/PC/AT compatible computer [16]. Image reconstruction was performed on a local VAX 8700 with either of two analytical codes (Radon [15] or Feldcamp [14]). For small apertures, it has been shown that both codes provide similar results in reconstructed images [16]. The X-ray data of the composite specimen were acquired using X-ray source settings of 39 kV, and 0.9 mA of flux. The number of projections equaled 185, and 128 averages were acquired per projection. A final spatial resolution of 124_x x 124_y x 124_z μm^3 per volume element (voxel) was achieved in the reconstructed image.

Si_3N_4-whisker-reinforced Si_3N_4 matrix composites were prepared by conventional ceramic processing techniques. Si_3N_4 powder (UBE Chemical Ind. UBE-SN-E10, α), 2.5 wt.% MgO (in form of $Mg(NO_3)_2 \cdot 6H_2O$), and 2.5 wt.% Carbowax 400 (Union Carbide - polyethylene glycol), were suspended in ethyl alcohol and ball-milled for 16 h. Si_3N_4 whiskers 10 wt.% (UBE Chemical Ind. UBE-SN-WB β) were added and ball milling was continued for 3 h. The sample was pan-dried to remove the alcohol before pressing. The pressed specimens were stored under desiccant until the imaging experiment. The sample chosen for examination in this work measured 7 x 7 x 3 mm.

RESULTS AND DISCUSSION

Three-dimensional NMR and X-ray images displayed via surface rendering techniques are presented in Fig. 3. Surface rendering is performed by applying a user-adjusted threshold intensity to define a minimum intensity that is used to calculate the contiguous surface. The particular threshold chosen for the X-ray image resulted in an accurate representation of the sample's topology. The NMR surface, however, was reconstructed with a minimal threshold intensity that was chosen to suppress structures having low proton density near the sample surface. This threshold level essentially eliminated two corners of the sample from the rendered object (as indicated in Fig. 3A). The remainder of the NMR image, however, is similar to the one acquired by X-ray, Fig. 3B.

Thin 2-D sections (or "slices") of the 3-D NMR and X-ray CT reconstructed images taken from identical spatial locations within the specimen is shown in Figure 4. Because the NMR and X-ray signals arise from completely different mechanisms and thus have different filtering functions, scaling constants, signal-to-noise ratios, and intrinsic image contrast, quantitative image measurements must be determined for both methods independently using known concentration and density phantoms. Even in the absence of the necessary intensity calibrations, qualitative indications from identical geometric positions in the images can still be discussed. For example, a lack of intensity in X-ray image could indicate either a void or a low density inclusion (area of high organic concentration) in a green ceramic composite. NMR imaging would clearly distinguish between these two possibilities, since a void will appear as an area of low intensity while an organic inclusion will appear as a high intensity indication.

Three types of localized intensity indications can be observed in Figure 4: (a) areas of low NMR and low X-ray intensity stemming from voids, cracks, or low-density inclusions having little or no discernible protons; (b) areas of high ceramic density; and (c) areas of high organic concentrations. Efforts are presently underway to calibrate image intensities with appropriate proton density and intrinsic density standards. Dual-modality experiments performed in this manner will allow a quantitative evaluation of flaws (voids, cracks, etc.), as well as mapping binder and density variations throughout the green component.

While the experimental NMR imaging times reported here are lengthy, it should be pointed out that significant reductions in data acquisition time can be expected for commercial components.

Given the concentrations of binder used in commercial green-state composites, significant increases in signal-to-noise ratios of five to seven can be expected. Additionally, a further gain in sensitivity of ≈12 may be realized by increasing the magnetic field strength from 2.3 T (100 MHz) to 9.2 T (400 MHz). These factors would account for a time savings of nearly two orders of magnitude while improving the signal-to-noise ratio throughout the image.
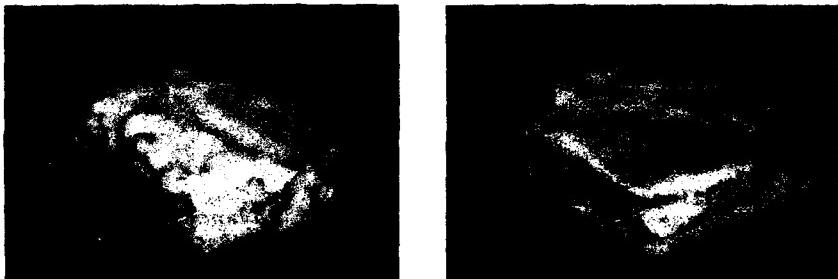
Figure 3.   Surface reconstructed (A) 3-D NMR image and (B) 3-D X-ray CT image of a green-state Si_3N_4-whisker reinforced Si_3N_4 composite specimen.

Figure 4.   Internal thin 2-D sections of 3-D (A) NMR image and (B) X-ray CT image of the composite specimen shown in Fig. 3.

CONCLUSIONS

We have demonstrated the feasibility of performing microtomographic NMR imaging on solid materials in three spatial dimensions. Methods were developed which combined 3-D dual back-projection protocol with image reconstruction using a Radon transform inversion technique. Using this methodology, we were able to spatially map low-concentration (2.5 wt.%) organic additive distributions in green-state Si_3N_4-whisker reinforced Si_3N_4 ceramic composites. Additionally, intrinsic density variations were determined via 3-D X-ray microtomography. The results obtained from both methods are complementary and thus provide the necessary information to distinguish flaws stemming from voids, areas of high ceramic content, and areas of high organic concentration in these samples.

174

REFERENCES

1. W. A Ellingson, and M. W. Vannier, *X-ray Computed Tomography for Nondestructive Evaluation of Advanced Structural Ceramics*, Argonne National Laboratory Report ANL-87-52 (1988).
2. B. London, R. N. Yancey, and J. A. Smith, Materials Evaluation, **48** [5], 604 (1990).
3. L. Garrido, J. L. Ackerman, and W. A. Ellingson, J. Magn. Reson., **88**, 340 (1990).
4. L. Garrido, J. L. Ackerman, W. A. Ellingson, and J. D. Weyand, Ceram. Eng. Sci. Proc., **9** [9–10] 1465 (1988).
5. N. Gopalsami, G. A. Foster, S. L. Dieckman, W. A. Ellingson, and R. E. Botto, *Development of NMR Imaging Probes for Advanced Ceramics*, Rev. Prog. in QNDE, edited by D. O. Thompson and D. E. Climenti (Plenum Press, 1990).
6. N. Gopalsami, S. L. Dieckman, W. A. Ellingson, R. E. Botto, and H. Yeh, *Quantitative MRI Measurement of Binder Distributions in Green-State Ceramics*, Proc. of Rev. Prog. in QNDE, edited by D. O. Thompson and D. E. Climenti (Plenum Press; in press, 1991).
7. K. Hayashi and K. Kawashima, J. Phys. D., Appl. Phys., **21** [6], 1037 (1988).
8. S. L. Dieckman, N. Gopalsami, and R. E. Botto, Energy and Fuels, **4** [4], 417 (1990).
9. J. B. Miller and A. N. Garroway, J. Magn. Reson., **85**, 255 (1989).
10. E. Rommel, S. Hafner, and R. Kimmich, J. Magn. Reson., **86**, 264 (1990).
11. P. C. Lauterbur and C.-M. Lai, IEEE Trans., **27**, 1227 (1980).
12. C.-M. Lai and P. C. Lauterbur, J. Phys. E, **13**, 747 (1980).
13. R. B. Marr, C. Chen, and P. C. Lauterbur, in *Aspects of Computerized Tomography*, edited by G. T. Herman and F. Natterer (Springer-Verlag, 1980).
14. L. A. Feldkamp, L. C. Davis, and J. W. Kress, J. Opt. Soc Amer. **1**, 612 (1984).
15. P. Grangeat, G. Hatchadourian, P. Le Masson, and P. Sire, *Logiciel Radon, Notice Descriptive Des Algorithmes Et Des Programmes*, Version 2.1 du 13-04-1990, LETI/DSYS/SETI/90-180 PS, Grenoble, le 11 Mai, 1990.
16. P. Rizo and W. A. Ellingson, in *Proceedings of the Nondestructive Evaluation of Ceramics Conference*, (Am. Soc. for Nondest. Test., Columbus, OH, 1990), 121.

COMPARATIVE IMAGING OF LIQUIDS IN ROCKS
BY NMR AND DIFFERENTIAL X RAY CT*

C. JEANDEY[a], J.M. CASAGRANDE[b], A. BRIGUET[c], T. NTOUTOUME[c], G. GUILLOT[d]

a   LETI, division of CEA, CENG – 85 X – 38041 GRENOBLE
b   INTERCONTROLE, CENG – 85 X – 38041 GRENOBLE
c   Université Claude Bernard LYON I, 69622 VILLEURBANNE
d   Université Paris Sud, IEF, CNRS URA 22, 91405 ORSAY (FRANCE)

ABSTRACT

We have applied NMR Imaging and X_Ray Computerized Tomography to the study of the structural properties of rocks. Samples from different porous rocks ; sandstones, granites, limestones have been successively examined by both techniques. NMR images have been obtained on water saturated samples. The spatial distribution of liquid indicates the effective porosity. By constrast, X_Ray images display the mineral content of rocks. Standard tomographs do not have the required resolution to see pores smaller than 100 μm. We used water as a constrast agent to localize porosities by "differential" CT. Comparative results are shown.

1. INTRODUCTION

The presence and migration of water in rocks play an important role in the selection of a safe site for the disposal of hazardous chemical or nuclear waste materials [1]. A good description of the rock hosting the waste is needed, since an adequate computer modeling of the site is hoped. One important problem is the characterization of heterogeneities in porous media, which may largely influence their hydrogeological properties ; for instance the hydraulic conductivity and permeability [2]. In stratified or fractured rocks, more generally in porous media presenting a large distribution of pore sizes, the variations of petrophysical properties are defined on characteristic lengths scale much larger than the microscopic length scales, as obtained by the flow velocity or the flow of electric current in an homogeneously connected pore network. For example, in a rock formed of parallel strata of different permeabilities, the length and the width of strata become the two characteristic lengths. Otherwise, near the percolation threshold, the trajectory of fluids through a sealed pore network become very complex and tortuous leading to a correlation length much larger than the microscopic

lengths, i.e. the pores or grains sizes. Finally, dispersion of tracers and pollutants depend sharply on the characteristic sizes and amplitude of heterogeneities which must be considered in the computer modeling of the site.

We have attempted to characterize these large scale heterogeneities using tomographic methods.

2. METHODS

2.1. X Ray computerized tomography

CT is now extensively used in the Non Destructive Testing of materials [3], and only recently X_Ray medical scanners have been diverted from their primary clinical objective to the characterization of rocks [4]. For petrophysical studies their spatial resolution is not high enough (typically 1 mm) and we took the opportunity to use a tomograph specially designed for NDT and developed by a joint team LETI and INTERCONTROLE (typical spatial resolution 100 μm, and density resolution 10^{-3}), commercially available.

CT principles are well known and based on the absorption of X_Rays. Under well defined circumstances, a density map of a slice of the object can be obtained.

Experimental setup

The X_Ray photons originate from at 420 kV X_Ray tube (PANTAK/HF 200). First the X_Ray beam is collimated in a flat fan beam geometry with a 15° aperture angle and 2 mm height at the detector inlet. This beam is further separated into 31 cords having a beam width of 0.4 mm. Each cord is associated with a BGO detector which presents numerous advantages over Xe gas detectors [5]. The object (here a rock core) is installed on a positioning device and can be displaced in rotations of 14.4° angular and 200 μm translations steps, providing 775 projections in less than 10 minutes. Positioning, signal multiplexing data processing and graphical display (SEIKO hard copy) are controlled in real time by a μVAX computer.

Experimental procedure

Samples were simply implemented on a vertical shaft allowing the 3D image reconstruction of fissures within the cores. Most of the samples had max 6.2 cm diameter, and therefore the tube was operated at 300 kV and 3 mA. In order to reduce the beam hardening artefact, 3 mm Cu filters were used. Total acquisition time including image reconstruction was roughly 6 mins.

For differential tomography, the procedure is straightforward. The sample is first examined in the dry state within a low absorbing beaker. The sample was then allowed to wet within 1 hour. After removal of water, the sample kept at the same place, is reexamined.

2.2. NMR Imaging

At present, the major application of NMR imaging is in medical and biological sciences, where it provides spatial images of tissues and organs with valuable anatomical details. However, applications in other areas have also been demonstrated in material sciences. For instance, NMR Imaging of porous systems began in 1979 when Gummerson et al [6] used this technique to

study unsaturated water flow in building materials. NMR Images of water within porous rocks [7] and composites materials [8] and of protons in ceramics [9] were also reported. More recently, most advanced MRI techniques were introduced into the field of core analysis by a joint team Shell—oil company and General Electric [10, 11].

In the present study we use low field imagers (0.1 T and 0.13 T), and show that despite the sensitivity loss, useful informations can be obtained.

Experimental setup

First attempts were tried out on a 4.7 T machine, where most of the available hardware has been designed for imaging studies of molecules in the liquid state with T_1 and T_2 relaxation times of the order of 100 ms. Usually, typical pulse sequence operate on this time scale. Moreover the shortest echo time is limited by the time required for the settling of the encoding gradients ($\geq$ 6 ms).

At 4.7 T, T_2 times were measured by spin echo and found to range between 1 and 3.5 ms in water saturated samples. T_1 times were measured by inversion recovery between 0.4 and 0.5 s.

In a standard spin echo sequence, the signal intensity in each pixel is given by :

$$I = I_0 \left[1 - \exp\left(- T_r/T_1\right)\right] . \exp\left(- T_e/T_2\right)$$

where I_0 is the maximum amplitude after a 90° pulse, T_r the repetition time and T_e the spin echo time. Several strategies can be adopted to enhance echo signal I : (1) use a solid state NMR machine, with special pulse narrowing sequence [12], (2) use 3D back projection without slice selection [this conference Botto, Rizo], (3) construct a shielded [11] or at least a reduced size gradient system, (4) increase T_2 by raising the temperature, taking another proton rich liquid or working at lower magnetic field. The latter was chosen as low field machines were available to us at LYON (B_0 — .13 T) and ORSAY (0.1 T). Indeed, T_2 were considerably longer at low field jumping from 1 to 3.5 ms to 20 to 50 ms. T_1 values decrease as expected with B_0 power 0.24. The often mentioned explanation is that magnetic impureties or susceptibility changes at pore boundaries generate large local gradient fields. It is interesting to note that no T_2 lengthening of time was obtained replacing water by cyclohexane which has the same viscosity but is less polar.

Experimental procedure

The saturation was done as follows : the sample was placed inside a dessicator, first evacuated with a vacuum pump. Then, water was allowed to immerse the sample. The pumping above water level was repeated until the weight became almost constant.

T_e was chosen as short as compatible with the gradient switching time. T_r was chosen long enough for the magnetization to recover a sizeable amount and short enough to reduce the total imaging time. Machines parameters were optimized performing 1D—FT. The acquisition parameters are listed in table I.

178

	LYON	ORSAY
Magnet	0.13 T	0.1 T
Method	2D-FT	3D-FT
Repetition time	Tr - 1 s	Tr - 0.4 s
Echo time	Te - 25 ms	Te - 7 ms
Number of acquisitions	Nacq - 28	Nacq - 4
Total acquisition time	60 min	55 min
Bandwidth	Δf - 10 kHz	Δf - 20 kHz
Slice	e - 5 mm	e - 6 mm (16 slices)

Table I - Parameters used for water NMR imaging

3. RESULTS AND DISCUSSIONS

Two examples have been selected to illustrate the different properties
of the two imaging techniques.

3.1. Episyénite granite stone

Figure 1 shows a typical water image obtained at 0.1 T (see table I for
acquisition parameters) without slice selection. This corresponds to a
projection of all the protons on the plane where the two remaining encoding
gradients are applied. The rectangle seen at the bottom corresponds to a
moistered supporting synthetic foam spacer. The distribution of water is far
from being homogenous as the CT image would suggest. This finding is a proof
that this granite suffered an intense hydrothermal activity favourable to the
deposit of valuable minerals (Uranium) but perhaps not for the containment of
waste.

Figure 2 shows the corresponding slice obtained by CT. The resolution is
higher. Bright spots may indicate high density minerals deposit (Fe oxides,
etc...).

3.2. Stratified porous limestone

Figure 3 shows a NMR cross section of a porous limestone (porosity 15 %)
performed at 0.13 T. Stratification is clearly resolved on this picture (see
table I).

Figure 4 shows a differential CT image obtained following the procedure
discribed above. Provided the object has not moved, the image is generated on
a pixel to pixel substriction basis. Here, statistical noise and tomograph
stability are the major concerns. Thereafter the integration was lengthened up
to 20 mins. The X_Ray tue operated at maximum anode current (7 mA) and the
copper filter removed.

4. CONCLUSIONS

NMR gives a better water contrast than differential CT in a comparable
acquisition time (30 min).
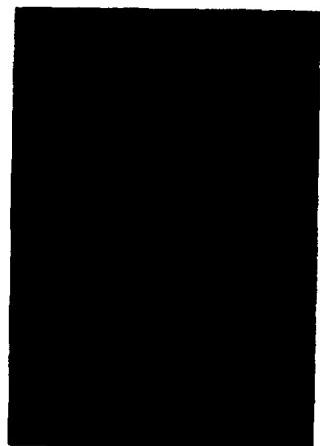
Figure 1 : Water image in granite
at .1 T (effective porosity : 5 %)
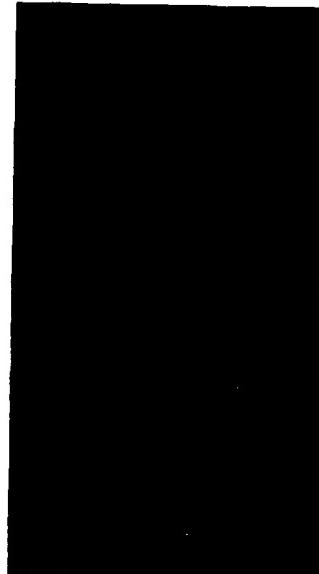
Figure 2 : CT image of granite
(same cross section as fig. 1)

Figure 3 : Water image in limestone
at .13 T (effective porosity : 15 %)

Figure 4 : Differentiel CT image
of limestone (same cross section
as figure 3)

Conventional 2DFT and 3DFT spin echo NMR imaging can be performed on rocks at low magnetic field strengths. This modality enables the observation of the connected pore network, in a full 3D representation.

Relaxation times T_1 and T_2 as a function of field (relaxometry) could be used as a marker of the chemical and physical protons environment. However it is important to notice that more data are needed for a clearcut interpretation of the observed values.

New NMR techniques introduced in medical imaging (flow and diffusion imaging) could be, if adapted, profitably used.

CT is a straightforward technique to visualize rocks due to the ease of implementation comparatively to NMR. It gives higher spatial resolution in a given time (less than 10 min).

For permeability studies, we suggest differential CT. If the fluid migration is slow enough (1 or 2 days), the progression of fluid could be monitored. For this purpose, an hydraulic press could be installed on the tomograph, provided that its absorption is not too high.

REFERENCES

[1]   FAUSSAT A., La technique moderne, 21–25 (oct 1989).

[2]   OGER L., GAUTHIER C., HULIN J.P. and GUYON E., Entropie n° 152, 29–42 (1989)

[3]   Proceedings of the Industrial Computerized Tomography Topical, July 25–27, 1989, Seattle, published by the American Society for Nondestructive Testing, Inc. (Columbus, OH 43228).

[4]   FABRE D., MAZEROLLE F. and REYNAUD S., Rocks at great depth, 1989, published by Balkema, Rotterdam (ISBN 906191 9754) 297–304.

[5]   GLASSER F., THOMAS G., GAGELIN J.J. and CUZIN M., Proceedings of the Industrial Computerized Tomography Topical.

[6]   GUMMERSON R.J., HALL C., HOFF W.D., HAWKES, R. HOLLAND G.N. and MOORE W.S., Nature, 281,56 (1979)

[7]   GUILLOT G., TROKINER A., DARASSE L. and SAINT JALMES H., J. Phys. D, Applied Physics 22, 1546–1549 (1989)

[8]   ROTHWELL W.P., HOLECEK D.R. and KERSHAW J.A., J. polymer Sci. Polym Lett Ed 22, 241 (1984)

[9]   GARRIDO L., ACKERMAN J.L. and ELLIGSON W.A., J. of Magnetic Resonance, Vol. 88, 340–353 (1990)

[10] VINEGAR H.J., TUTUNJAN P.N., EDELSTEIN W.A. and ROEMER P.B., Society of petroleum engineers journal (oct 1989)

[11] EDELSTEIN W.A., VINEGAR H.J., TUTUNJAN P.N., ROEMER P.B. and MULLER O.M., SPE 18272, 101–111 (1988)

[12] MILLER J.B., GARROWAY A.N. J. of magnetic resonance, Vol. 82, 529–538 (1989)

PART V

Neutron and Protons

THE STUDY OF MATERIALS USING WAVELET IMAGE PROCESSING TECHNIQUES

L. BELTRÁN-DEL-RÍO, A. GÓMEZ AND M. JOSÉ-YACAMÁN

Instituto de Física, Universidad Nacional Autónoma de México, México D.F. 01000, P.O. Box 20-364.

ABSTRACT

In this work the wavelet transform is used to process high- and medium resolution electron micrographs from small particles and their substrates. It is concluded that the edge sensitivity of the technique and its contrast enhancement capabilities are most useful in the processing of electron micrographs.

THE WAVELET TRANSFORM

The wavelet transform, introduced by Morlet [1] for seismic signal analysis can be defined as

$$Wf(s,\omega) = \int_{-\infty}^{\infty} f(x) \sqrt{s} \; \psi^*(s(x-\omega)) \, dx \qquad (1)$$

where W stands for the transform, f is the function ("image" or "signal") to be analyzed, s and u are real parameters ($s\neq0$), and ψ is an auxiliary function to perform the analysis (the so-called "wavelet").

The wavelet must satisfy the admissibility condition

$$\int_{0}^{\infty} \frac{|\hat{\psi}(\omega)|^2}{|\omega|} d\omega < \infty \qquad (2)$$

where $\hat{\psi}$ stands for the Fourier transform of ψ. In most cases the admissibility condition is equivalent to requiring that

$$\int_{0}^{\infty} \psi(x) \, dx = 0 \qquad (3)$$

The wavelet transform can be written as a convolution product

$$Wf(s,\omega) = [f * \bar{\psi}_s^{-\mathrm{M}}](\omega) \qquad (4)$$

where $\bar{\psi}_s(x) = \sqrt{s} \; \psi(-sx)$.

In reciprocal space the transform can be written taking the Fourier transform of equation 4

$$\hat{Wf}(s,\omega) = \hat{f}(\omega)(s^{-1/2})\hat{\psi}^*(\omega/s) \qquad (5)$$

All these concepts can be extended to two dimensions. In the present work all the transforms are bi-dimensional. The

wavelet used is the so-called Mexican hat (of course!) as described by Daubechies [2].

A mathematical microscope

From equation 4 it can be seen that the transform acts as if one were to form an image of the "object" $f(x)$ with a microscope with point spread function $\vec{\psi}_s^{-x}$. The various ψ_s correspond, then, to microscopes of different resolutions. The transform of $\vec{\psi}_s^{-x}$ can be likened to a transfer function. In this way it can be seen that if $\vec{\psi}_s^{-x}$ is very localized (high resolution) then the transform will be similar to the original function f. If $\vec{\psi}_s^{-x}$ is, on the other hand, very spread out, then the transform will resemble the wavelet itself.

Wavelets as filters

From equation 5 it can be appreciated that the wavelet transformation is a filter whose passing band can be selected with the parameter s. It can be shown that the center of the passing band of the filter and the bandwidth are both proportional to s.

Edge enhancement

The wavelet transform is ideally suited to the purpose of detecting intensity gradients in any direction, enhancing peaks, borderlines, edges, even lines suggested by aligned peaks. In addition the wavelet transform can be used to perform a simple contrast enhancement that can emphasize details of interest.

TRANSFORMS OF MICROGRAPHS

In order to illustrate the main features of the wavelet transform we show in figures 1-a to 1-e an image of $CoMoS_2$ hexagonal domains. The unprocessed image (1-a) was transformed with a narrow wavelet producing an image (1-b) very nearly undistinguishable from the original . Subsequent figures (1-c to 1-e) show the effect of increasingly larger wavelets yielding images in which the resolution diminishes. But in the case of fig. 1-c, the new resolution seems to coincide with the different distances related to the hexagonal structure.

In figure 2 the edge detection features are illustrated with a synthetic image. In fig. 2-a the unprocessed object can be seen to consist of circular peaks forming a circular particle and, choosing the adequate wavelet, in fig. 2-b it can be appreciated how the edges of the small circles are surrounded by a double contrast line.

In some instances the transform can be used to focus the attention on the particle as a whole rather than on its
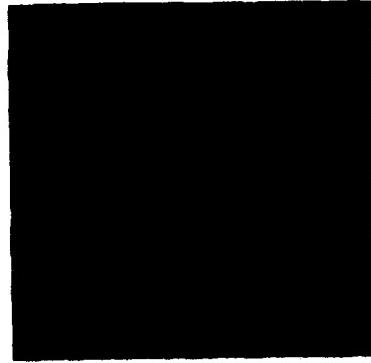
figl a) Original, unprocessed, image of CoMoS$_2$ catalyst.
b) Image transformed with a very thin wavelet. The
digitalization process fails to yield a null image,
instead presents the original image.
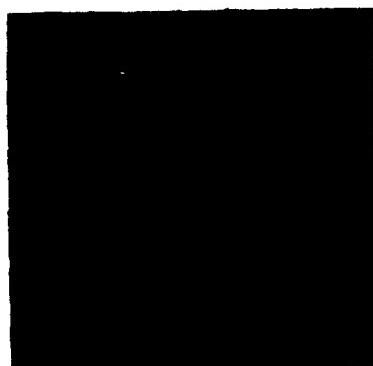
fig.1c) Transformed image
with s=37.

fig.1d) Transformed image
with s=26.
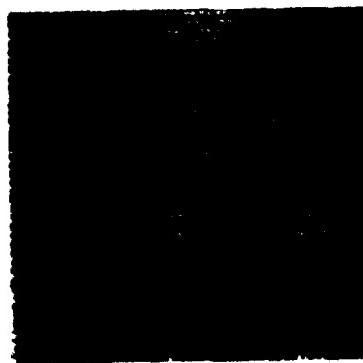
fig.1e) Transformed image with s=21.
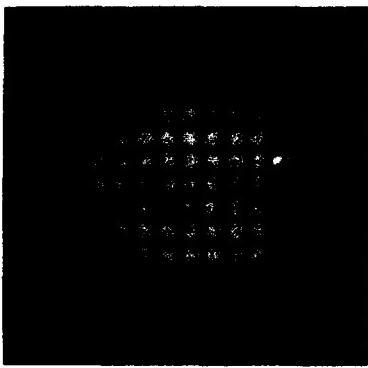
fig.2a Synthetic object
composed of circular peaks.
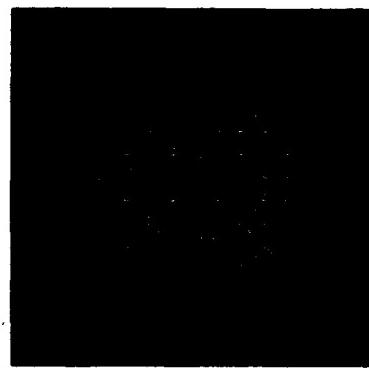
fig.2b) Same object, but
transformed with s=37. The
emphasis on the edges is
to be noticed.
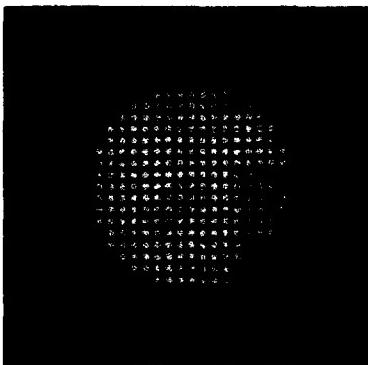
fig.3a) Synthetic object with
small "atoms".
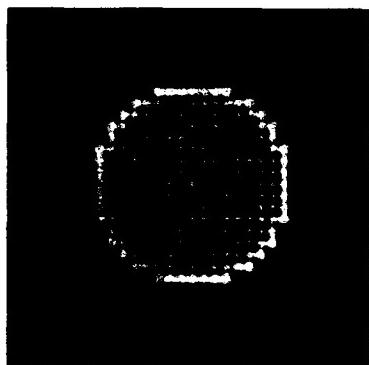
fig.3b) Same object, but
transformed with s=18. The
particle's edge is to be
noticed.
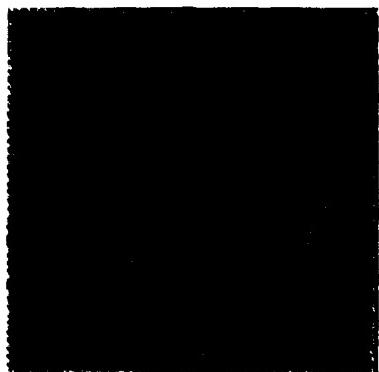
fig.4a) Processed image with s=25, threshold 65%.
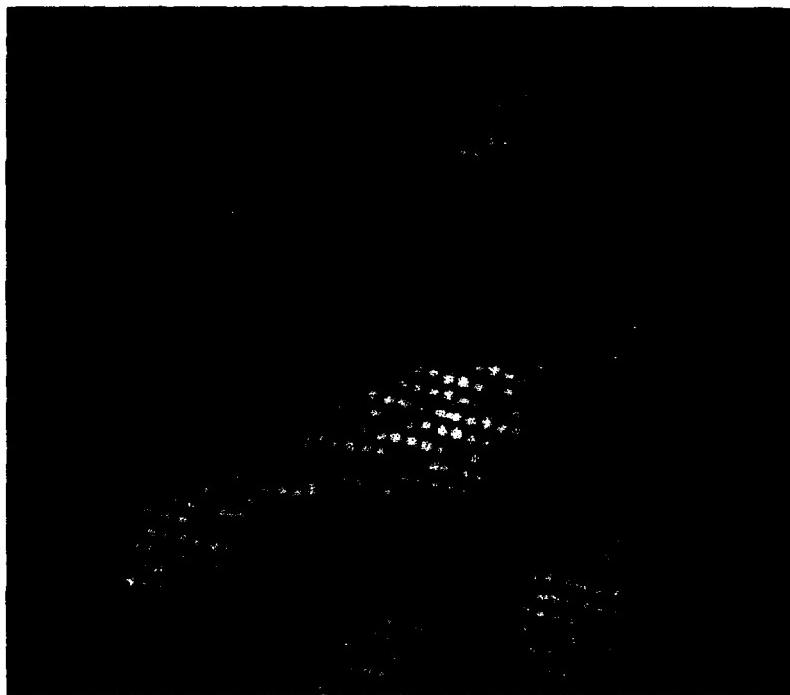
fig.4b Same image processed with appertures in the
reciprocal space, on the lattice peaks. Best
threshold posible, 30%.

details as shown in fig. 3 in which an unprocessed image (3-a) was transformed with a broad wavelet (3-b) so the atomic details are lost but the overall shape and extension of the cluster are now apparent.

WAVELET TRANSFORM ANALYSIS OF BOUNDARIES

In the image (fig. 1-a), in which a net of hexagonal domains is apparent, by applying a simple threshold the domains can be seen more clearly and can be extracted for further analysis(fig.4-a).

The boundary domains correspond to antiphase boundaries and, probably, to some chemical disorder induced by the cobalt impurity. For the sake of comparison we show in fig. 4-b the result of processing the same image using standard Fourier techniques. As it can be seen, the processing introduces unwanted distortions in the shape of the domains. This shows how the wavelet transform can be a most powerful technique.

ACKNOWLEDGEMENTS

References

1. A. Grossmann, J. Morlet and T. Paul, J. Math. Phys. 22, 2473 (1985)

2. Ingrid Daubechies, IEEE Transactions on information theory 39, 961 (1990)

NEUTRON TOMOGRAPHY: A SURVEY
AND SOME RECENT APPLICATIONS

E. A. RHODES*, J. A. MORMAN*, AND G. C. McCLELLAN**
*Argonne National Laboratory, 9700 S. Cass Ave., Argonne, IL 60439
**Argonne-West, P. O. Box 2528, Idaho Falls, ID 83403-2528

ABSTRACT

A survey is given of recent developments in selected areas of neutron tomography, within the context of several applications Argonne is involved in, including high penetration of reactor-fuel bundles in thick containers (involving TREAT and NRAD facilities), dual-energy hydrogen imaging (performed at IPNS), dynamic coarse-resolution emission tomography of reactor fuel under test (a proposed modification to the TREAT hodoscope), and an associated-particle system that uses . eutron flight-time to electronically collimate transmitted neutrons and to tomographically image nuclides identified by reaction gamma-rays.

INTRODUCTION

Unlike gamma-rays, neutrons transmitted through materials react with nuclei rather than electrons. Neutrons can deeply penetrate many materials (allowing tomographic radiography of thick objects), neutron transmission cross-sections often vary strongly with energy and nuclide (yielding "fingerprints" for various nuclides), and neutron reactions often occur that produce gamma-rays having distinct spectra (giving wide-range identification of specific nuclides). Neutrons provide a uniquely useful diagnostic probe for characterization of materials, and examples are given that illustrate these properties.

Traditionally neutron tomography is performed at a reactor using film measurements of thermal-neutron transmission at many orientations, followed by microdensitometer film scans and computer reconstruction from projections. However many aspects of neutron tomography are changing. Within the context of some applications Argonne is involved in, a survey is given of related recent developments in source, detection, data acquisition, and computer reconstruction technologies that are making neutron tomography more accessible, in the sense of new applications, less expensive and more transportable equipment, and faster measurements. The Argonne applications focus on penetration of thick objects and comprehensive materials identification. Minimization of measurement times is more important than high spatial resolution in most of the applications discussed, and medium to low (mm to cm) spatial resolution is adequate in most cases.

EPITHERMAL RADIOGRAPHY OF REACTOR FUEL

At the TREAT (Transient Reactor Test facility) reactor at Argonne-West, prototypic reactor fuel assemblies heated by fission inside capsules or coolant loops are driven to destruction by transient overpower and/or coolant flow coastdown conditions designed to simulate HCDA's (Hypothetical Core Disruptive Accidents). During the actual test, a fast-neutron hodoscope dynamically records a 2D image of the fuel as it melts and relocates [1]. For analysis of HCDA progressions and consequences, it is also important to examine the final distribution of fuel, clad, and coolant and determine metallurgical material changes. The standard technique for this is laborious remote post-test destructive examination of the irradiated assembly at HFEF (Hot Fuel Examination Facility) at Argonne-West, where transverse sections are cut, polished, and studied macroscopically and microscopically.

Neutron tomography is now being developed to complement post-test destructive examinations, by providing a guide to locate optimal sectioning positions and reduce the number of section cuts necessary, as well as by yielding many more transverse section images than possible with destructive sectioning. The goal is to provide more comprehensive and quantitative post-test material distributions. The test fuel has a high gamma-ray radiation level that fogs direct X-ray or neutron-sensitive films, so the indirect process of neutron activation of foils is used, with subsequent activity transfer to film. The high-density test fuel strongly absorbs thermal neutrons. Also, in order to preserve the distribution of materials, in some cases the test fuel is radiographed prior to disassembly from an outer (mostly steel) container ~ 15 mm thick. Thus epithermal neutron radiography is required.

The neutron radiographs are produced at the north beam tube of the NRAD 250-kW TRIGA reactor at HFEF [2]. The tube extends from the core face to obtain a relatively hard spectrum containing many epithermal neutrons. L/D ratios of 185, 300, and 700 are available, for radiographs up to 43 cm x 36 cm in size. The radiographing process is illustrated in Fig. 1. A fuel-pin bundle is suspended on a precision rotator for the many views required. At each view a packet of foils is irradiated for 30-60 min., a cadmium foil in front to attenuate thermal neutrons and an indium imaging foil to capture epithermal neutrons at the 1.45 eV indium resonance. The indium foils are removed and placed in contact with photographic film (usually type T). After the decaying indium exposes the films, they are developed and then digitized on a scanning microdensitometer.

A computer program aligns each view image and calibrates the density from a step wedge image in each view. Then a computed tomography transverse cross-section is reconstructed for each desired elevation. As an illustration of the penetration and imaging capability of indium resonance tomography, Fig. 2 shows a reconstructed cross-section of a 91-pin EBR-II fuel bundle using only 36 views [3]. Each pin is U metal 3.68 mm in diameter. Spiral spacer wires are also evident. The image has been high-pass filtered and clipped.

Shown in Fig. 3 are a series of transverse reconstructions of the remains of an assembly containing seven mixed Pu-U oxide fuel pins after TREAT test LO7, compared to cut and polished sections at the same elevations [4]. Seventy-six views were used and the densitometer aperture was set at 0.1 mm horizontally and 0.2 mm vertically. The 7 originally intact fuel pins are 5.84 mm in diameter and are supported in a close-packed hexagonal arrangement by grid spacers inside the 26-mm diameter fluted tube. Unfortunately the transverse reconstructions in Fig. 3 are from pseudocolor images and cannot be compared easily in density to the cut section images, in which steel is light-shaded and fuel and voids are dark, but the spatial details are similar (in some cases material present during radiography has been lost during destructive examination). Not shown are useful axial reconstructions obtained by stacking the transverse reconstructions and slicing through them computationally, providing length-wise views of the test pins.

At the present stage of development, the reconstructions identify relocated fuel and steel, flow tube blockages, and pin displacement, but do not reliably distinguish between fuel and steel in very irregular geometries or where fuel porosity changes substantially and provide little information on cladding condition. To go further into quantitative analysis of materials distributions and to separate boundary features of hex cans, grid spacers, porous fuel, and cladding, improved spatial and density resolution are required. This will necessitate higher resolution film digitization, which will increase the already long 3 films/day microdensitometer scanning times. However modern digitizers are available that can scan a radiograph in 30 s with sufficient spatial and density resolution, and there are plans to buy one. Possibly many more that the present 76 views will be needed, leading to much longer reactor operation. Around an hour will be required for each radiograph, due to low indium foil activation, and 2 to 5 radiographs will be needed for each view to cover the test-fuel length.
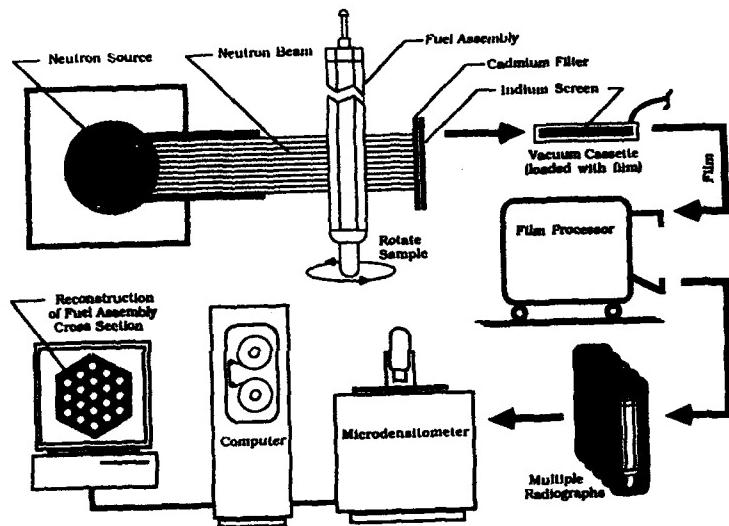
Fig. 1. NRAD indium-resonance neutron radiography process.
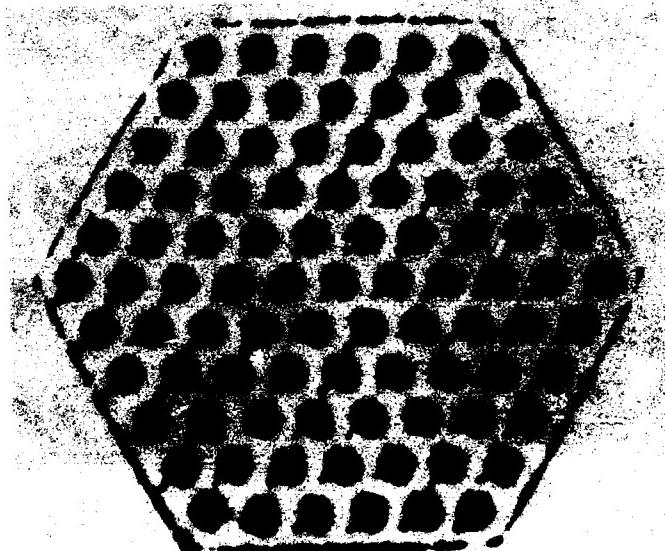
Fig. 2. NRAD reconstruction of an EBR-II 91-pin fuel bundle.
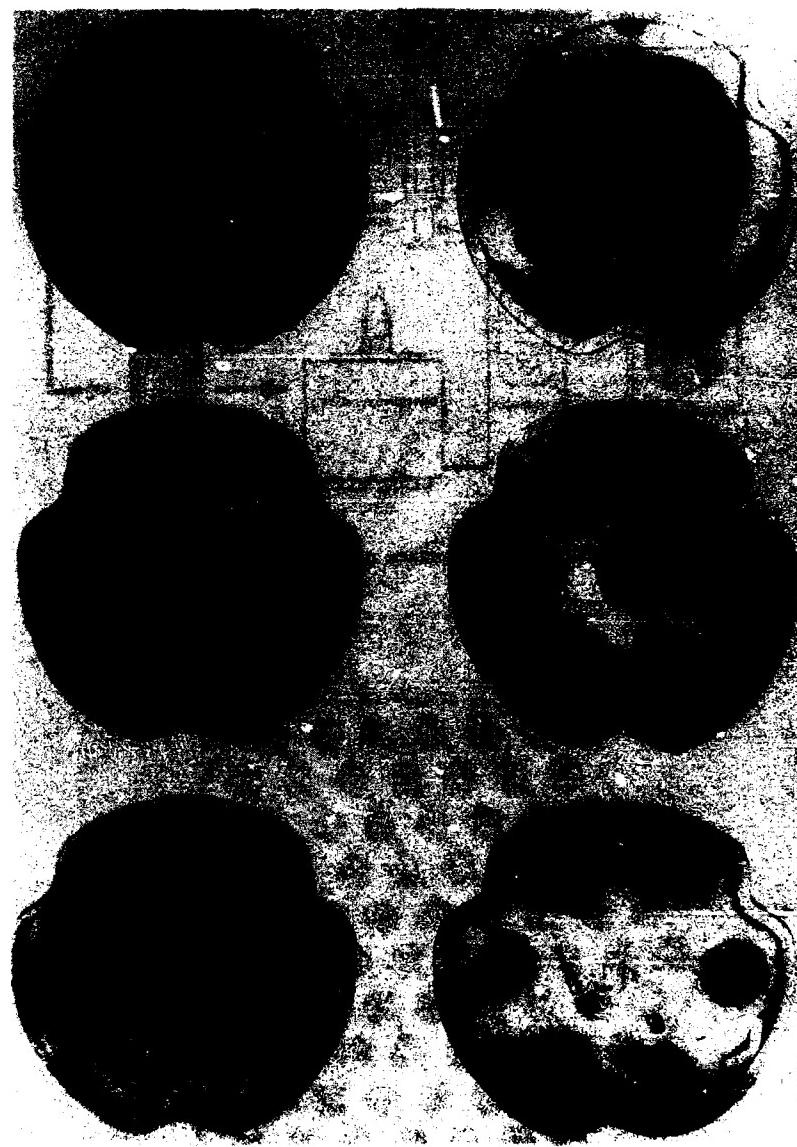
Fig. 3. Comparison of LO7 transverse reconstructions (left) with cut sections (right) at elevations of 97 mm (top), 71 mm (center), and -3 mm (bottom).

Perhaps a tomographic algorithm can be found that will provide good reconstructions with fewer views, minimizing reactor time. The currently used filtered backprojection allows quick calculation but requires trial-and-error filter optimization. Other linear algorithms are available that implement gradient, convolution, minimum variance, and regularization methods, among others [5,6]. Nonlinear tomographic methods that provide positive-definite image constraints, such as MART [6], maximum entropy [7], and maximum likelihood (EM) [8], may hold more promise for use of fewer views. Figure 2 was reconstructed from only 36 views using a maximum entropy algorithm. The nonlinear methods are less susceptible to noise and are less prone to image artifacts, but require intensive iterative computations that can be particularly consumptive of computer time and memory on the large data base required for high spatial resolution. Such computations will likely pose little problem for modern high-speed computers, but it remains to be seen how accurately nonlinear reconstruction algorithms preserve spatial and density resolution in asymmetric geometries.

MULTIPLE-ENERGY NEUTRON TOMOGRAPHY

In multiple-energy neutron tomography, specific nuclides are imaged or their images are enhanced by using the differences in cross-section variation with neutron energy of the nuclides present, by either subtracting tomographic images or by producing several different sets of radiographs at different neutron energies, often by simultaneously distinguishing different neutron energies during one exposure. Use of a pulsed accelerator and active neutron detectors time-gated to the beam allows simultaneous selection of desired neutron energies by flight-time measurement. In this manner, resonance radiography has been performed at the NIST electron linac from 1 to 40 eV [9] and at the Argonne IPNS (Intense Pulsed Neutron Source) from 0.3 to 10 eV [10], in which separate images are formed at discrete resonance energies where there are strong increases in neutron absorption for nuclides of interest (actinides, rare earths, and fission products for $Z > 40$, at these energies). Images of each nuclide are unfolded from the resonance patterns.

Another technique is dual-energy hydrogen imaging, in which the increase in hydrogen neutron cross-section at subthermal neutron energies is used to enhance the imaging of small amounts of hydrogen against a background of other absorbing materials by subtracting a tomographic image obtained for higher energy neutrons from that obtained for subthermal neutrons (picking energies such that the other absorbing materials have nearly the same cross-sections at both energies). This technique was used to provide dual-energy imaging of water in tuffaceous rock [11], with the goal being to track water flow through porous rock for site risk analysis of permanent disposal of radwaste. A feasibility experiment was conducted at the IPNS facility with coarse spatial resolution, collecting neutrons at 15 and 85 meV in a scanned ^{3}He detector. The setup is shown in Fig. 4. At IPNS, 30 intense pulses of 500 MeV protons per second strike a U target, where spallation produces fast neutrons that are moderated to low energies. Neutron energies are simultaneously selected by measuring moderator flight time.

Measurements were taken at 4 scan positions for 3 views of a tuff sample that was 7 cm in diameter, as sketched in Fig. 5. The crack shown contained water, particularly at the outer rim. Coarse-resolution reconstructions were performed using the convolution algorithm. The image obtained by subtracting the reconstruction at 85 meV from that at 15 meV is shown in Fig. 6. The darker regions indicate the strongest absorption and are consistent with expected presence of water (the sample in Fig. 6 is rotated from the sketch in Fig. 5). Absorption differences due to rock boundaries, ie. the sample rim and the crack (except for water), are nearly invisible, so that a clean enhanced image of water is obtained.

194
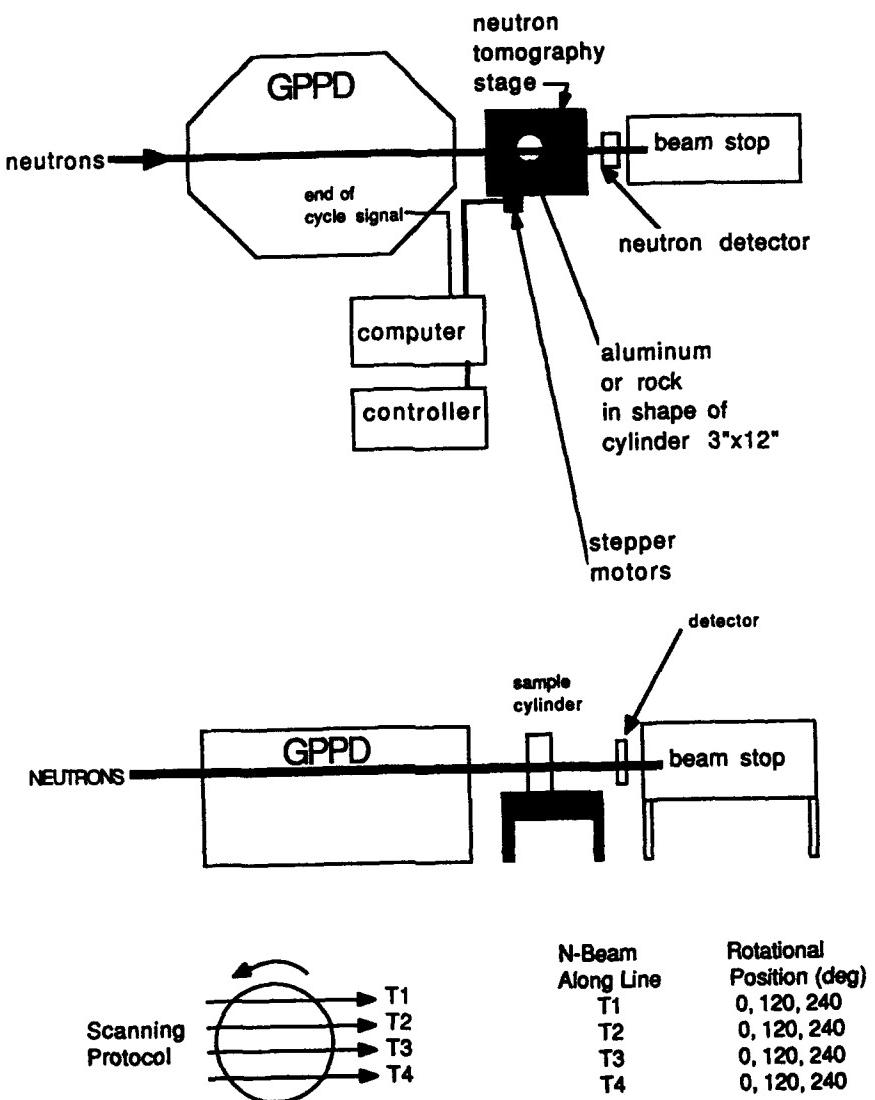
Fig. 4. IPNS setup for dual-energy imaging of water in tuff.
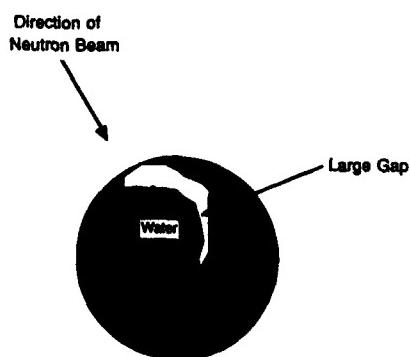
Fig. 5. Approximate sketch of tuff cross-section.
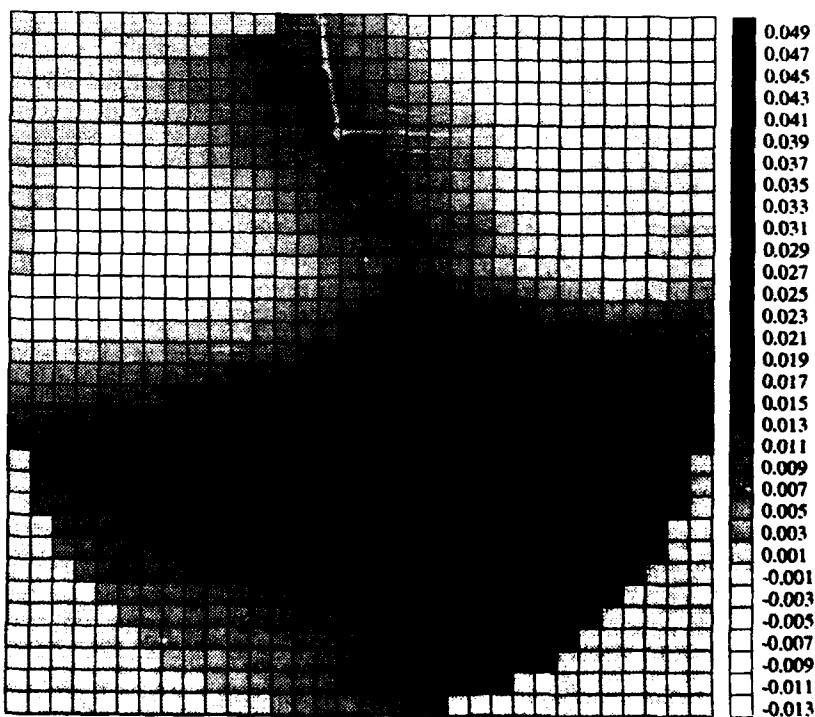
Fig. 6. Subtractive dual-energy reconstruction of tuff cross-section (rotated from sketch in Fig. 5).

SOME RECENT HARDWARE DEVELOPMENTS

Recent hardware developments have led to progress in some areas of neutron tomography. In the past few years, relatively high resolution active 2D (two-dimensional) position-sensitive detectors have been developed that are efficient for thermal and epithermal neutrons. Wide-area detectors include a 5 cm x 5 cm crossed-wire proportional counter of 1-mm resolution containing a high-pressure gas mixture [12], and a 22-cm diameter neutron Anger camera of 2-mm resolution, based on a glass scintillator optically coupled by a light guide to 19 close-packed photomultipliers [13].

The most prevalent detectors use a 2D image intensifier of some type, the simplest being a ZnS (or other) converter screen of arbitrary size viewed through a lens by a low-light-level TV camera containing an intensifier [14]. One image intensifier tube has a 23-cm diameter Gd_2O_2S converter screen and electrodes that focus the electrons onto a scintillation screen that is viewed by a TV camera [15]. A third type of intensified detector is a Lixiscope fronted by a 5-cm diameter neutron-sensitive scintillator, with fibre optics, a photocathode, and a microchannel plate. The output can be either a phosphor screen for TV camera viewing [16] or a resistive anode for electronic interfacing [12]. Intensified detectors are capable of resolutions from around 50 to 500 microns, depending on detection area.

The availability of these detectors has aided development of new neutron radiography applications. Dynamic 2D radiography has become possible for large (reactor) and medium (accelerator) neutron sources, with applications in fluid flow [17] and mechanical motion [18]; although the images tend to be somewhat noisy and resolution and contrast are substantially lower than attainable in static neutron radiography, useful motion is observed. For small (^{252}Cf and deuteron-on-tritium, or D/T, generator) neutron sources, transportable 2D radiography systems have been built for applications such as aircraft inspection [19]. Intense transportable sources are being developed, including a high-output D/T generator [20] and accelerators based on bombardment of Be by protons or deuterons, such as a superconducting cyclotron [21] and small rf linacs [22].

These neutron detector and source developments lead one to contemplate the potential for dynamic 3D (three-dimensional) neutron tomography. Key features of any system capable of this would be the use of efficient 2D detectors, the attainment of 2D and depth resolution simultaneously, and stationary sources and detectors. Coded apertures (for emission, or auto-radiography), such as any of a number of arrangements of multiple pinholes or a Fresnel zone plate, and corresponding coded sources (for transmission radiography) come to mind, since they cast shadows on the detectors that vary in size with distance of objects from the detector and that can be decoded to yield depth information. However they have not been successful for neutron radiography when a substantial number of voxels is desired in the 3D image, because of neutron penetration of and scattering in the structure of the coded aperture or source and resulting low contrast and image artifacts.

Another possibility might be a stereoscopic pair of sources and detectors. Although this would allow determination of the order in depth of well-separated objects, little detailed depth resolution would result. The use of simultaneous views around the object to be radiographed, with a source/detector combination for each view, would be more likely to provide successful dynamic 3D tomography, but much hardware would be involved unless a small number of views will yield adequate 3D resolution. As an example of a system for dynamic 3D neutron tomography, a tomographic fast-neutron has been proposed that is based on a reactor source and massively parallel arrays of detectors; this concept evolved from the present 2D TREAT hodoscope mentioned earlier.

Elevation and plan views of the present TREAT hodoscope [1] are shown in Fig. 7. It provides dynamic 2D emission radiography by detecting fission neutrons emitted by test fuel in a capsule or loop at the center of the TREAT reactor core, using time-resolved readouts of a 2D detector array. Test fuel is driven to destruction during a reactor transient, in order to simulate an HCDA, and the hodoscope captures the resulting fuel motion for later analysis. The test fuel is viewed through a large steel collimator, which contains 360 channels, 36 rows x 10 columns. Fast-neutron detectors are located behind each channel, and all detectors read out in parallel to a computer data acquisition system. This system emphasizes time resolution, rather than spatial resolution, as required by the experiments: the data collection interval is 0.3 ms to several ms and interchannel spacing at the test plane is 6.6 mm horizontally and 34.5 mm vertically.

There was a desire to provide depth resolution for proposed future STF (Safety Test Facility) tests of large fuel bundles. The possible arrangements proposed to perform dynamic 3D neutron tomography, two 2D hodoscopes at 90 deg. or three at 120 deg., are illustrated in Fig. 8. It was found in a study of computer-generated phantoms and reconstructions [23] that a substantial amount of tomographic resolution could be attained using specialized reconstruction methods for 2 and 3 views.

ASSOCIATED-PARTICLE TOMOGRAPHY

Recently Argonne has been involved with the associated-particle tomography method, a potentially powerful diagnostic tool. In this method, a special D/T generator containing an alpha-particle detector irradiates the object of interest with 14-MeV neutrons. As shown in the schematic layout in Fig. 9, deuterons are accelerated into a tritium target, producing 14-MeV neutrons isotropically. Each neutron is accompanied by an associated alpha-particle travelling in the opposite direction. The gamma-ray and neutron detectors are time-gated by pulses from the alpha detector, which forms a cone of flight-time-correlated neutrons through the object. Detector pulses are time-resolved by CFD's (constant-fraction discriminators). Flight times are determined by TAC's (time-to-amplitude converters), digitized by an ADC (analog-to-digital converter), and recorded. When a reaction occurs in the object along the cone that results in a detected gamma-ray, the time-delay from the alpha pulse yields the position (depth) along the cone where the reaction occurred, since the source neutron and gamma-ray speeds are known. By scanning the alpha detector horizontally and vertically (or by using a 2D position-sensitive multipixel alpha detector), transverse and depth coordinates of reaction sites can be mapped, providing 3D emission imaging of reaction densities.

Pulses from the gamma detectors are digitized by ADC's and their energy spectra are recorded. Fast-neutron (prompt) inelastic scattering reactions in the object provide spectra that can identify many nuclides. By choosing gamma lines of specific nuclides, a 3D image of each identifiable nuclide can be mapped. By choosing appropriate nuclide intensity ratios, 3D images of compounds can be made. Slow-neutron capture is not prompt and thus not time-correlated with the alpha pulses, but provides nonimaging gamma-ray spectra that can aid nuclide identification. (If fissionable materials are present, neutron reaction detectors may be used to detect emitted fission neutrons).

As shown in Fig. 9, by discarding detected neutrons not having the proper flight time to be uncollided, one can perform fast-neutron 2D transmission imaging without a collimator (by scanning or using 2D neutron detectors), since scattered neutrons are removed by "electronic collimation". By measuring at a sufficient number of views around 180 deg., 3D tomography is feasible. Transmission imaging can be done along with or instead of emissive reaction-density imaging.
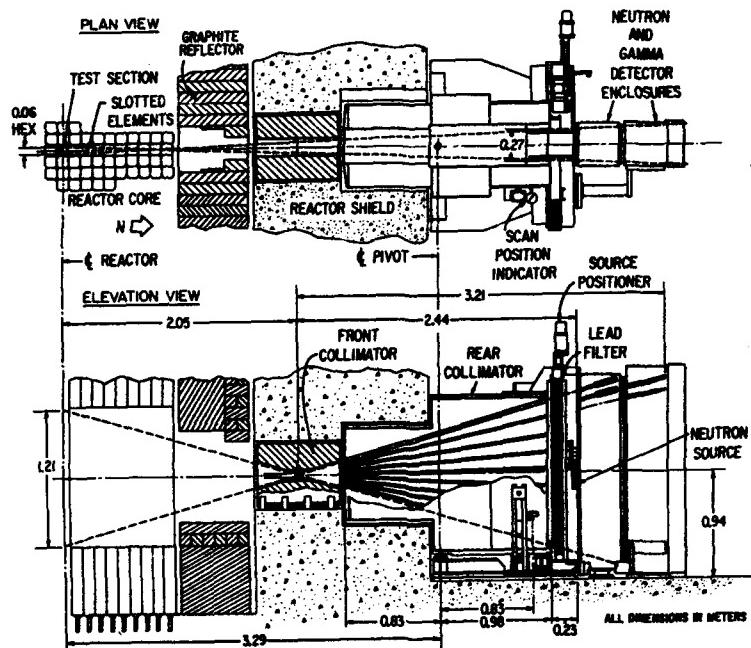
Fig. 7. Diagram of TREAT fast-neutron hodoscope.
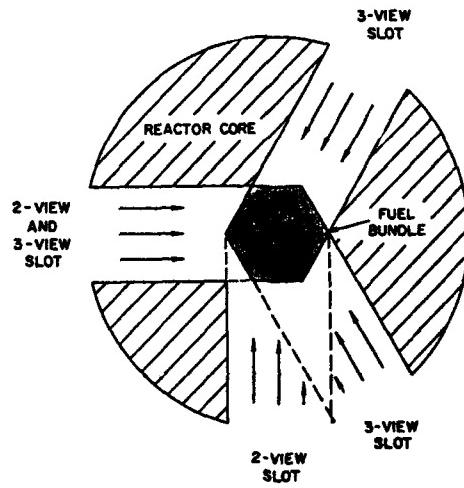
Fig. 8. Plan view of hodoscope arrangements for tomographic resolution in STF.
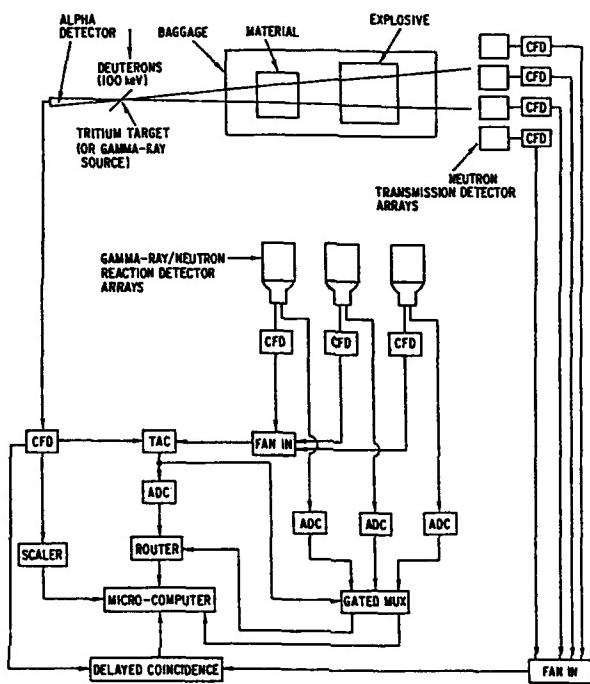
Fig. 9. Schematic layout of associated-particle interrogation system.
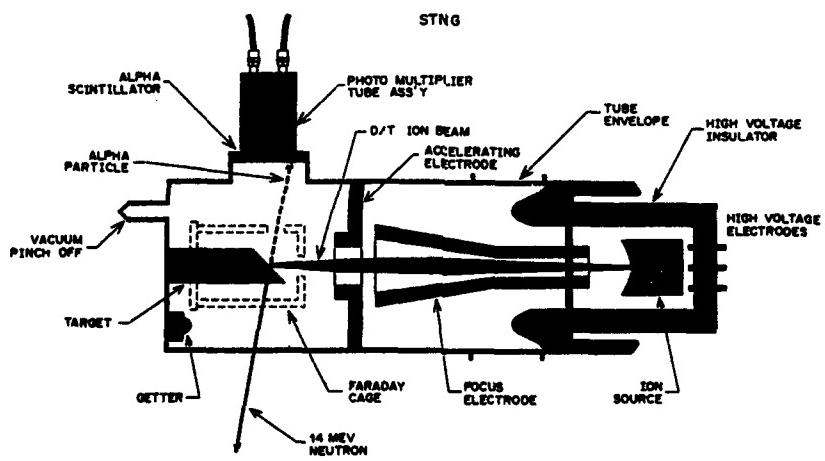
Fig. 10. Diagram of APSTNG (Associated-Particle Sealed-Tube Neutron Generator).

200
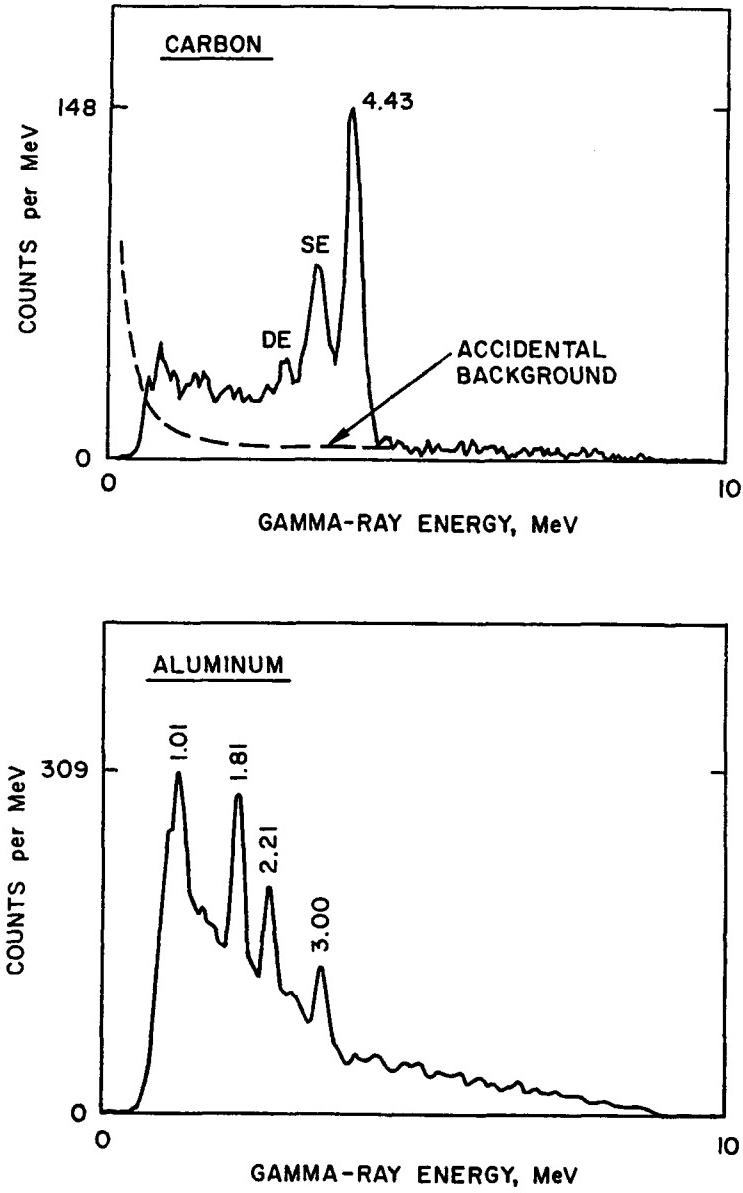
Fig. 11. APSTNG system gamma-ray energy spectra of C and Al targets.
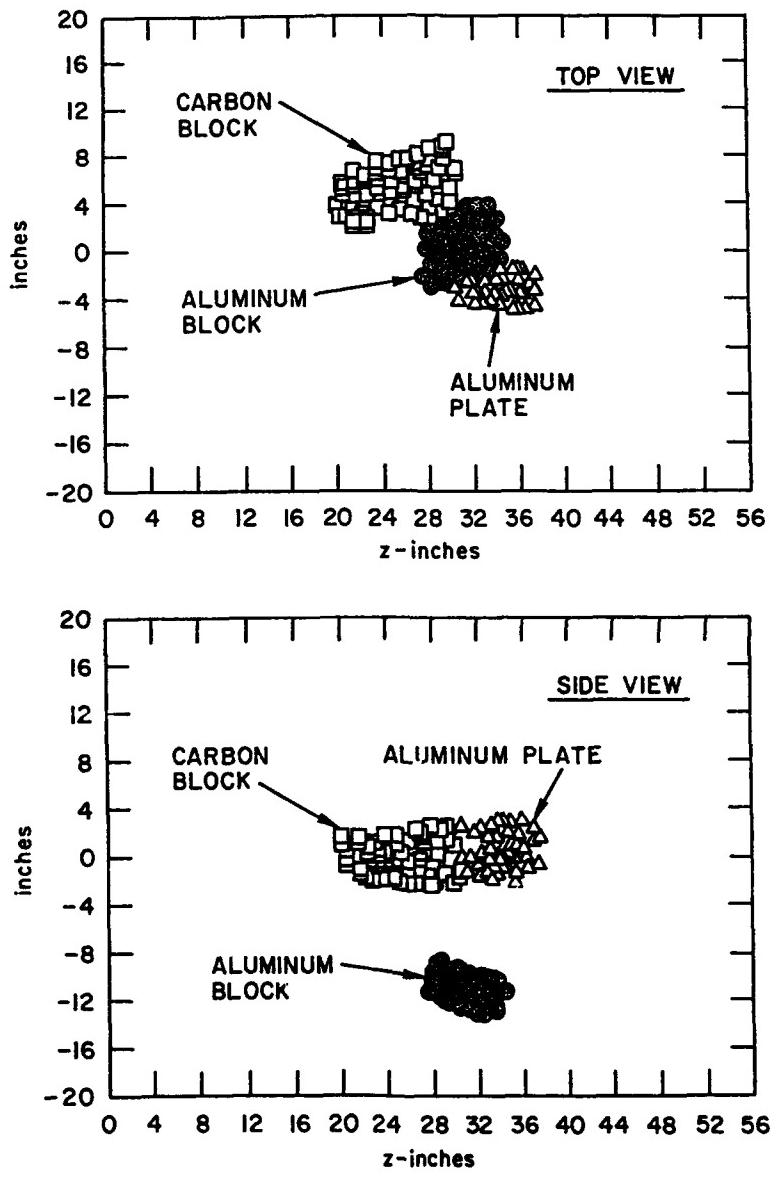
Fig. 12. Top and side views of 3D location of C and Al targets as mapped from APSTNG gamma-ray emission data. Points indicate mapped reaction sites.

In the actual system, a PC controls the experiment, collects flight-time and energy data, calculates positions, and displays data and images. The heart of the system is the state-of-the-art APSTNG (Associated-Particle Sealed-Tube Neutron Generator) developed with considerable effort by C. Peters, manager of the Advanced Systems Division of Nuclear Diagnostic Systems. As diagrammed in Fig. 10, a Penning ion source emits a mixed beam of deuterium and tritium ions that is accelerated and focused on a small spot on the target, tritiating the target and producing neutrons and alpha particles. The alpha detector consists of a ZnS screen and a photomultiplier. The APSTNG is an inexpensive small sealed module with low-bulk support equipment. It has a long MTBF (around 2000 hours at a million n/s or 200 hours at 10 million n/s), is easily replaced by a remanufactured module (allowing simple field operation), and presents low radiation exposure.

A proof-of-principle experiment on gamma-ray emission reaction-density imaging was performed on an interrogation volume containing a carbon block and an aluminum block and plate. Shown in Fig. 11 are the gamma-ray energy spectra for neutron inelastic scattering obtained for C and Al. By scanning a single-pixel alpha detector over one side of the volume (x and y coordinates) and mapping reaction sites from flight-time along the correlation cone (z coordinate) for energy windows enclosing C and Al gamma lines, the objects were correctly identified and 3D-imaged, as shown in Fig. 12. Proof-of-concept experiments have been successfully done for a number of applications: chemical ordnance identification, explosive detection and identification, contraband drug detection, uranium borehole logging, corrodent detection on turbine blades, kerogen analysis of shale, and contents of coals (sulfur, minerals, and btu).

APSTNG technology has the capabilities for identification and 3D imaging of many individual nuclides and compounds, with flexible positioning of reaction detectors with respect to the neutron source (on the same side, perpendicular, or opposite side), as well as capability for fast-neutron transmission imaging. The source and emitted radiation are high-energy and penetrate highly absorbing objects. But there are some limitations that can be significant in certain applications of this technology. With regard to transmission imaging, development of a 2D fast-neutron detector having sufficient efficiency will involve resolution tradeoff. With regard to emissive reaction-density imaging, images will be significantly attenuated with depth into the interrogated object if it is strongly absorbing, presently attainable depth resolution is limited to 5 cm (because the system has an overall time resolution of ~ 1 ns and a 14-MeV neutron travels 5 cm in 1 ns), and measurement times can be rather long to obtain sufficient gamma counts.

The gamma signal count rate is limited by reaction cross-sections, solid angles subtended by the alpha detector and gamma detectors, gamma detector efficiency, and source strength, but usable source strength is limited by detector accidental counts and pileup. Two developments are underway for reducing measurement time. The use of a relatively large array of small gamma detectors or a relatively small array of large flight-time sensitive gamma detectors is being investigated for increasing the count rate while maintaining depth resolution for emissive imaging. The fabrication of a relatively large 2D alpha detector is also being considered, for increasing the signal rate while maintaining transverse resolution and eliminating scanning.

REFERENCES

1. A. DeVolpi, C. L. Fink, G. E. Marsh, E. A. Rhodes, and G. S. Stanford, Nucl. Tech. **56**, 141 (1982).

2. W. J. Richards, G. C. McClellan, and D. M. Tow, Matl. Eval. **40**, 1263 (1982).

3. D. M. Tow, Neutron Radiography: Proceedings of the First World Conference (San Diego, CA, Dec. 7-10, 1981), 425.

4. J. A. Morman, P. H. Froehle, J. W. Holland, and J. D. Bennett, Proceedings of the 1990 International Fast Reactor Safety Meeting (Snowbird, UT, Aug. 12-16, 1990) I, 441.

5. R. H. Huesman, G. T. Gullberg, W. L. Greenburg, and T. F. Budinger, Users Manual: Donner Algorithms for Reconstruction Tomography, Pub. 214, Lawrence Berkeley Laboratory, Univ. of California, Berkeley CA, (Oct. 1977).

6. G. T. Herman, R. M. Lewitt, Dewey Odhner, and S. W. Rowland, SNARK89: A Programming System for Image Reconstruction from Projections, Medical Image Processing Group Tech. Rpt. No. MIPG160, Dept. of Radiology, Univ. of Pennsylvania, Philadelphia, PA (Nov. 1989).

7. G. Minerbo, Comput. Biol. Med. 9, 29 (1979).

8. K. Lange and R. Carson, J. of Computer Assisted Tomography 8, 306 (1984).

9. C. D. Bowman, R. A. Schrack, J. W. Behrens, and R. G. Johnson, ibid Ref. 3, 503.

10. M. G. Strauss, G. H. Lander, R. Brenner, and C. T. Roche, ibid Ref. 3, 519.

11. D. S. Kupperman, R. L. Hitterman, and E. Rhodes, Proceedings of the 17th Annual Review of Progress in Quantitative NDE (San Diego, CA, July 1990).

12. R. A. Schrack et al, ibid Ref. 3, 495.

13. M. G. Strauss, R. Brenner, F. J. Lynch, and C. B. Morgan, IEEE Trans. Nucl. Sci. NS-28 (1), 800 (Feb. 1981).

14. W. E. Dance and S. F. Carollo, Neutron Radiography: Proceedings of the Second World Conference (Paris, France, June 16-20, 1986), 415.

15. Vijay Alreja and Leonard Corso, ibid Ref. 14, 625.

16. J. T. Lindsay, J. D. Jones, C. W. Kaufman, and B. Van Pelt, Nucl. Instr. A242, 525 (1986).

17. John M. Cimbala, Dhushy Sathianathan, Stephen A. Cosgrove, and Samuel H. Levine, Neutron Radiography: Proceedings of the Third World Conference (Osaka, Japan, May 14-18, 1969), 497.

18. Koichi Sonoda, Atsuo Ono, Eiichi Hiraoka, Ryoichi Taniguchi, Shuichi Tazawa, and Takehiko Nakanii, ibid Ref. 17, 539.

19. V. J. Orphan, T. Maung, and R. Polichar, ibid Ref. 17, 749.

20. Serge Cluzeau and Michel Dubouchet, ibid Ref. 17, 205.

21. M. R. Hawkesworth, ibid Ref. 14, 183.

22. Robert W. Hamm, ibid Ref. 17, 231.

23. A. DeVolpi and E. A. Rhodes, Matl. Eval. 40, 1273 (1982).

CHARACTERIZATION OF LOW DENSITY CARBON FOAMS BY X-RAY
COMPUTED TOMOGRAPHY (CT) AND ION MICROTOMOGRAPHY (IMT)

W. E. Moddeman[*], D. P. Kramer[*], D. W. Firsich[*], P. D.
Trainer[*], R. N. Yancy[**], D. L. Weirup[***], C. M.
Logan[***], A. E. Pontau[***], A. J. Antolak[****] and D. H.
Morse[****]
[*]EG&G Mound Applied Technologies, Miamisburg, OH 45343
[**]ARACOR, Wright-Patterson Air Force Base, Dayton, OH 45433
[***]Lawrence Livermore National Laboratory, Livermore, CA 94551
[****]Sandia National Laboratory/Livermore, Livermore, CA 94551

ABSTRACT

Two NDT techniques were used to characterize low-density,
microcellular, carbon foams fabricated from a salt replica
process. The two techniques are x-ray computed tomography (CT)
and ion microtomography (IMT); data are presented on carbon
foams that contain high-density regions. The data show that
densities which differ by <10% are easily observable for these
low density (<100 mg/cm^3) materials. The data reveal that
the carbon foams produced by this replica process have small
density variations; the density being ~30% greater at the outer
edges than when compared to the interior of the foam. In
addition, the density gradient is found to be rather sharp,
that is the density drops-off rapidly from the outer edges to a
uniform one in the interior of the foam. This edge build-up in
carbon density was explained in terms of polymer concentrating
on the foam exterior during drying which immediately followed a
polymer infusion processing step. Supporting analytical data
from other techniques show the foam material to be >99.9 %
carbon.

INTRODUCTION

EG&G Mound Applied Technologies has produced carbon foams
from a salt replica process that has been developed at Lawrence
Livermore National Laboratory.[1,2] The uses of such carbon
foams are described elsewhere by Williams et al[3] and will
not be addressed in this paper. In the replica process, salt
particles are pressed into a bar and then infused with a
polymer. The polymer is then cured and the salt removed. This
creates small voids, microcells, within the cured polymer.
Finally the cured polymer is carbonized primarily into an
amphorous carbon. The carbon foams are light in weight and can
be produced to a designed density between 15 and 100 mg/cm^3.

In this paper, we are interested in determining the density
distribution throughout the light-weight carbon foams. Two NDT
techniques are used to measure the density variation; they are
x-ray CT (computed tomography) and IMT (ion microtomography).
The first measures the distribution of carbon atoms in the foam
from x-ray absorption[4] and the latter determines the
electron distribution from ion energy loss due to small angle
scattering.[5]

EXPERIMENTAL

All of the carbon foams examined in this study are made by the salt replica process.[1,2] Details of the process can be obtained from reference 2. In order to identify the contaminants and also to determine the purity of the carbon produced by this replica process, the foams are characterized by several analytical techniques. The residual organic materials that might be present after pyrolysis are found by exchanging the foams with several polar and non-polar organic solvents; the extracted solvent is concentrated and then analyzed by gas chromatography/mass spectroscopy (GC/MS). No extractable contaminants, >10 ppm, are detectable. In addition, foams are weighed and burned in O_2, and the weight of the residual ash is determined. The measured weight loss is >99.9%. Most ash, but not all, dissolved in aqua regia. The composition of the acid-soluble ash is determined by inductively coupled plasma (ICP) spectroscopy. The results are given in Table I. They show the major constituents to be Ca and P, and

TABLE I

Inductively Coupled Plasma (ICP) Data (in ppm) on Ashed
Samples of Carbon Foams Made From Replica Process

	Element										
	Al	Ca	Cr	Cu	Fe	Mg	Mn	Na	Si	Ti	P
Elemental Concentration	23	385	13	10	95	21	105	10	140	3	168

the total concentration of the impurties to be <1000 ppm. That part of the ash that is not soluble in the strong acid is measured by energy dispersive spectroscopy (EDS) and found to be primarily alumina, which is only very slightly soluble in aqua regia. A JEOL 840 spectrometer is used to record the electron images and the EDS measurements.

The CT studies were performed at the Wright Research Development Center, Materials Laboratory x-ray Computed Tomography facility located at Wright-Patterson AFB, OH. The LAM/DE operates with a 420-kV bremsstrahlung x-ray source and has a spatial resolution of ~0.25 mm. Because of the low-density of these carbon foams, the x-ray source was not filtered and detectors only used a 1.5 mm thick aluminum filter. The LAM/DE machine has two sets of detectors for each line of sight, a thin front detector to monitor low-energy x-ray attenuation and a thick back detector to monitor the higher energy x-ray attenuation. This study used the front detector and utilized a detector preamp setting which assumed low x-ray attenuation through the material. This allowed for accumulation of CT data with high signal to noise ratios while still operating at the 420-kV level with the x-ray source.

The IMT data were collected using a 200 micron square, 8 MeV proton beam at the Sandia Microbeam Analysis Laboratory at Livermore.[5] The specimens were translated and rotated through the stationary beam, with the median of 100 proton energy loss determinations used to determine each line density (ray) through each specimen. Energy losses, measured with a solid state detector, were converted to density values using tabulated stopping powers for protons in carbon. Approximately 10,000 line density determinations were used for each tomographically reconstructed slice.

RESULTS AND DISCUSSION

Figure 1 illustrates a typical, high purity (>99.9%) carbon foam produced at Mound. A high-magnification secondary electron photomicrograph (SEM), Figure 2, shows the typical microcellular structure within a foam. The carbon manifests itself as the cell walls; the wall thickness is typically 0.1 micron or less. The diameter of the microcells is on the average a few microns and corresponds to the diameter of the salt particles. Some contaminants are dispersed throughout the foam as very small particulates. These can be seen as tiny bright spots in the backscatter electron (BSE) image shown in Figure 3. These spots are examined with EDS and are found to consist of Ca, P, Si, Mn, Fe and S. These impurities are likely present in the original salt and are left behind in the salt extraction process.
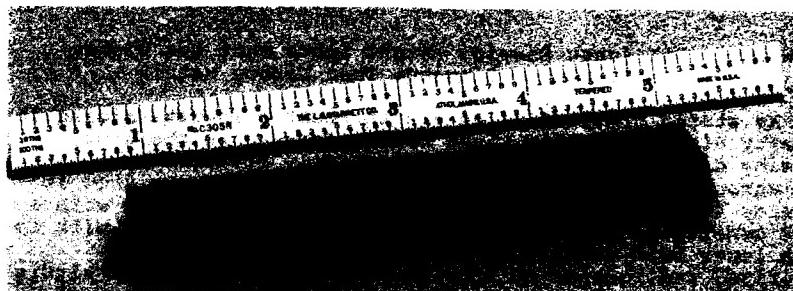
Figure 1.   Optical Photograph of a Typical Carbon Foam Produced at EG&G Mound Applied Technologies.

Figure 2.   High-Magnification SEM Photomicrograph Showing Typical Cell Structure in Carbon Foam.
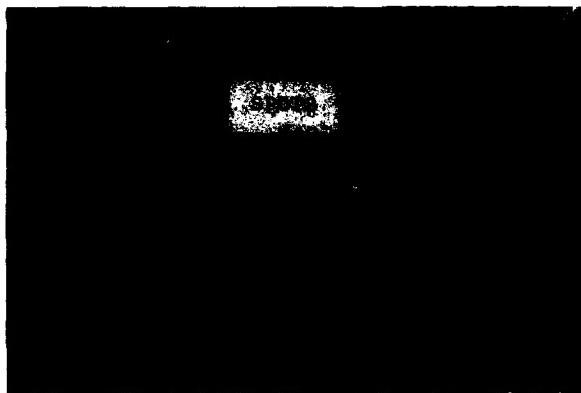
Figure 3. BSE Image Showing Bright Spots That Are Higher
Atomic Number Elements Than Carbon Matrix

As stated previously, we are interested in determining the
density distribution in these carbon foams. In the past,
density distributions have been routinely obtained by
radiography. Two typical digitized radiographs are show in
Figures 4a and 4b; the first is of a low-density foam with a
bulk density of 38 mg/cm^3 and the second is of a foam with an
even lower bulk density of 16 mg/cm^3. In each of the
digitized radiographs an area as been 'boxed' in for analysis.
A plot of grey level versus distance for this area is also
shown for each foam. The first radiograph shows a variation in
carbon density in the foam, that is Figure 4a shows the density
to be higher at the outer edges when compared to the interior.
The second radiograph, Figure 4b, shows no obvious high and low
density regions. The foam represented in Figure 4a was
prepared with the polymer infusion step and the one in Figure
4b was not. Radiography, or digitized radiography, has very
good spatial resolution (x and y) but very poor depth of field
(z), since the density is summed over a large volume element
that extends the length (or width) of a foam. Therefore, it is
impossible to quantify where on the edge the density gradient
is the highest. Two techniques, CT and IMT, are able to give
density information with a volume resolution of $\leq$0.125 and
$\leq$0.008 mm^3, respectively. In addition, these two techniques
are quantitative. The next paragraphs discuss the CT and IMT
results on the same two foams.

Several CT slices are recorded on each specimen; all give
similar results, thus, the data given in Figures 5a and 5b can
be considered as representative of what would be expected for
the 38 mg/cm^3 foam and 16 mg/cm^3 foams. For the former
material (Figure 5a), the CT slice shows the "outside" edge to
have a higher carbon density than the interior of the foam.
This was not the case for the low-density one (Figure 5b) where
"no" carbon build-up on the "outside" surfaces could be
detected. In fact, all foams that have been examined with CT
that have bulk densities $\geq$30 mg/cm^3 exhibit similar
high-density "outside" edges. However, no high density edges
are detected in foams with bulk densities of <20 mg/cm^3.

RADIOGRAPH →

LINE SCAN

GRAY
LEVEL

205

200

DISTANCE (TOTAL = 19 mm)

(b)

RADIOGRAPH →

LINE SCAN

GRAY
LEVEL

184

163

DISTANCE (TOTAL = 19 mm)

(a)
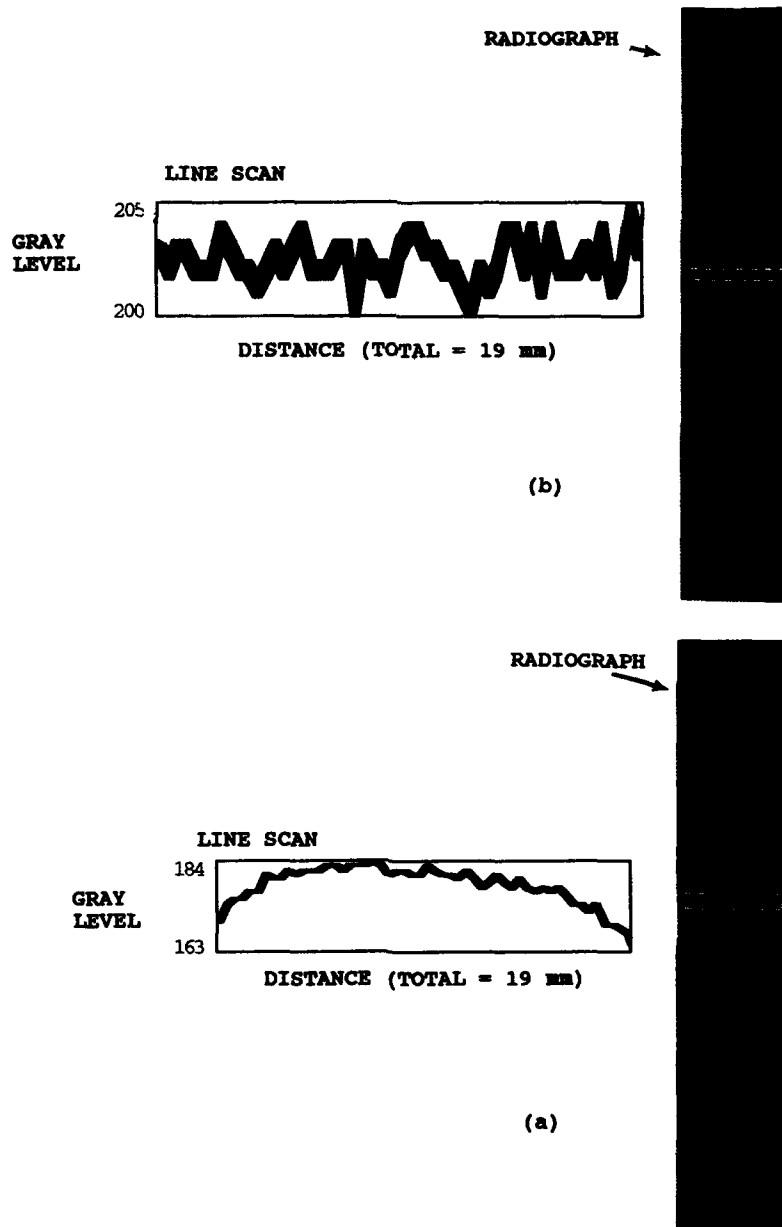
Figure 4. Digitized Radiographs and Line Scans of Carbon Foams
of: (a) Bulk Density of 38 mg/cm^3 and (b) Density
of 16 mg/cm^3.
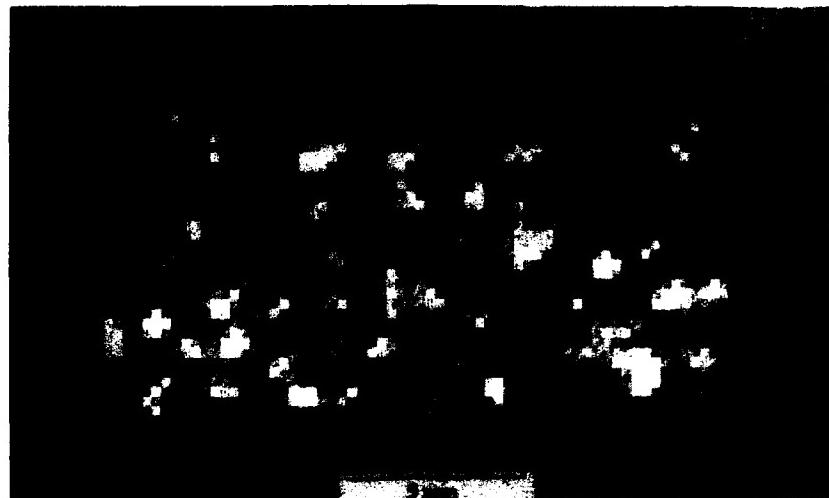
(b)
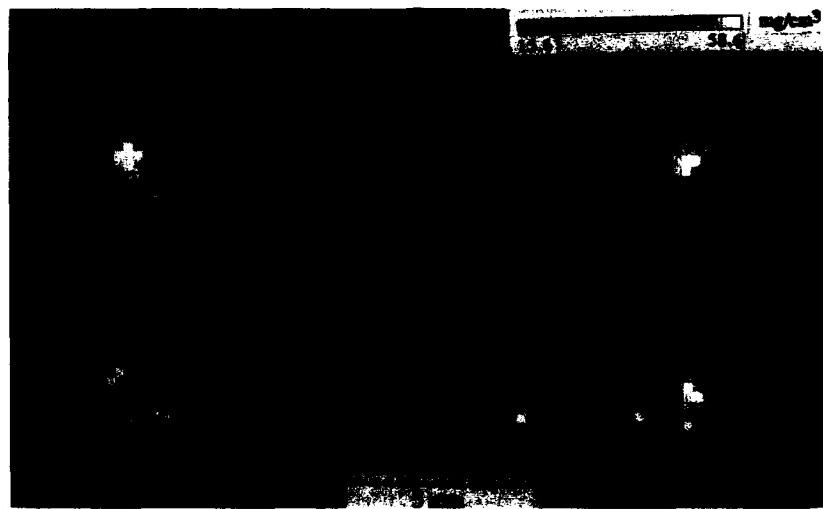
(a)

Figure 5.   Typical CT Slices of Carbon Foams With: (a) Bulk
            Density of 38 mg/cm^3 and (b) Very Low Bulk Density
            of 16mg/cm^3.

From the line scans of the CT slice for the 38 mg/cm^3 material (Figure 6a), densities on the periphery are found to be ~30% higher than the densities on the inside of the foam. In fact, the corners show the greatest density of carbon. These results can be explained by examining more closely the polymer infusion step of the replica process. Polymer is dissolved in a solvent. The salt bars are placed in the solution and the polymer diffuses into the center of the bars. After equilibrium, the wet bars are allowed to dry. The solvent evaporation begins on the outside surface of the bar. As the solvent evaporates, more solvent migrates from the interior of the bar to the surface. In doing so, some of the polymer is dragged towards the edges of the foam causing an enrichment of the polymer on the outside surfaces. After curing, salt removal and pyrolysis, the CT images show these high density regions on the edges and the corners. Figure 6b depicts a CT line scan from the very low-density foam. Since this foam does not include a polymer infusion step in its production, a high density edge region would not be expected. The CT data support this finding. From a practical point-of-view, these CT results suggest that machining ~1.5 mm from each side of the 38 mg/cm^3 would produce a foam with a reasonably uniform density.

The IMT examinations of the same two specimens discussed above are given in Figures 7a and 7b. Since IMT measures the energy loss of monoenergetic protons that have scattered from the electrons of a material, the line scans are a measure of variations in electron density in the foam. For the energy range used with the CT scans, the amount of x-ray attenuation is primarily due to Compton scattering which in turn is also proportional to electron density. The former is a very highly probable process whereas the latter is not. Although the probablities of the scattering events are much different between the two techniques, similar conclusions can be drawn from the IMT data, that is a high-density edge is observable for the 38 mg/cm^3 foam but is not present in the very low density one. Also the IMT data show the increase in electron density at the edge to be ~30% over that of the interior, the same value extracted from the CT line scans.

SUMMARY

Analytical data from various techniques that were taken on carbon foams produced by the salt replica process are shown to be very pure, >99.9% carbon. The density distributions are determined with two NDT techniques, x-ray CT and IMT; data from both techniques showed carbon enrichment at the edges and corners of a foam with a bulk density of 38 mg/cm^3. The density increase at the edges are determined to be ~30% when compared to the bulk density. This density variation is explained in turns of a polymer infusion processing step. A foam that was prepared without the polymer infusion step, which subsequently results in a very low density of only 16 mg/cm^3, showed no build-up of carbon on the periphery of the material.
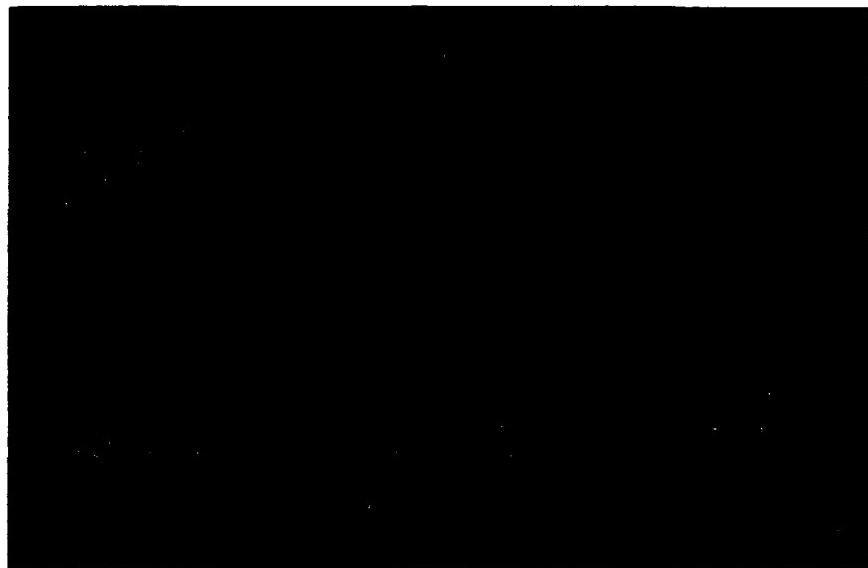
(b)

(a)

Figure 6. CT Line Scans Showing: (a) Density Variation in 38 mg/cm^3 and (b) Uniform Distribution in 16 mg/cm^3 Carbon Foams.
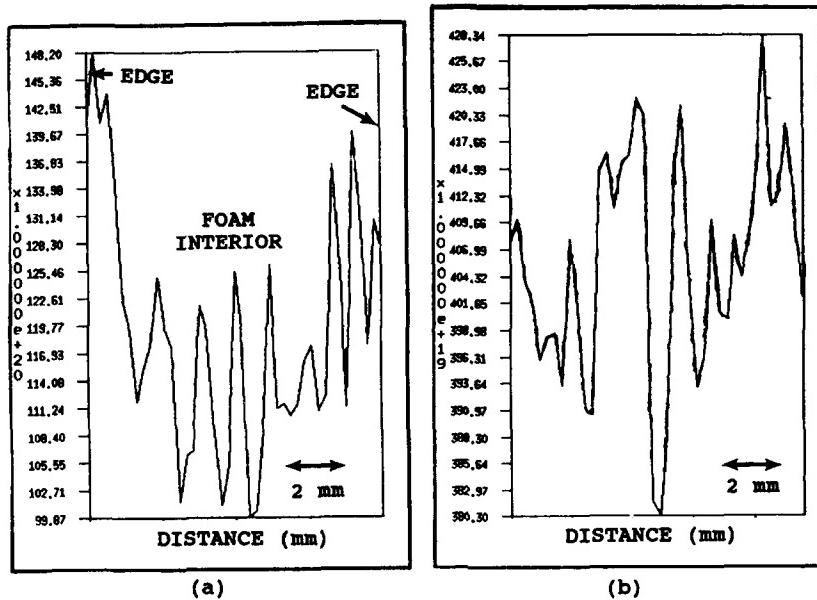
Figure 7.   IMT Line Scans for: (a) 38 mg/cm^3 and (b) 16 mg/cm^3 Carbon Foams.

REFERENCES

1. R. W. Hopper and R. W. Pekala, U. S. Patent Nos. 4756898, July 12, 1988 and 4806290, February, 21 1989.
2. R. W. Pekala and R. W. Hopper, J. Materials Sci., 22, 1840 (1987).
3. D. A. Wrobleski, K. H. Abel, A. J. Gray and J. M. Williams, "Potential foams and metal foil for cosmic dust capture", Report No. LA-11271-MS, Los Alamos National Lab., NM, July 1988.
4. T. H. Newton and D. G. Potts, ed "Technical Aspects of Computed Tomography," in Vol 5, "Radiology of the Skull Brain," 1981. C. V. Mosby Co., St Louis, MO.
5. A. E. Pontau, A. J. Antolak, D. H. Morse, et al, Nucl. Instr. and Meth. B40/41, 646 (1989).

Author Index

Subject Index

218

MATERIALS RESEARCH SOCIETY SYMPOSIUM PROCEEDINGS

MATERIALS RESEARCH SOCIETY SYMPOSIUM PROCEEDINGS

MATERIALS RESEARCH SOCIETY SYMPOSIUM PROCEEDINGS

MATERIALS RESEARCH SOCIETY SYMPOSIUM PROCEEDINGS

MATERIALS RESEARCH SOCIETY SYMPOSIUM PROCEEDINGS

MATERIALS RESEARCH SOCIETY SYMPOSIUM PROCEEDINGS

MATERIALS RESEARCH SOCIETY SYMPOSIUM PROCEEDINGS

MATERIALS RESEARCH SOCIETY SYMPOSIUM PROCEEDINGS

Recent Materials Research Society Proceedings listed in the front.